Understanding the mechanical behaviour of novel liquid crystal elastomers

Thomas Raistrick

Department of Physics and Astronomy

University of Leeds

Submitted in accordance with the requirements for the degree of

Doctor of Philosophy

March 2022

The candidate confirms that the work submitted is his own, except where work which has formed part of jointly authored publications has been included. The contribution of the candidate and the other authors to this work has been explicitly indicated below. The candidate confirms that appropriate credit has been given within the thesis where reference has been made to the work of others.

Chapter 8 includes content which has been published in the paper by Thomas Raistrick, Zhaopeng Zhang, Devesh Mistry, Johan Mattsson and Helen F. Gleeson in Physical Review Research 3 (2), 023191. All the work and the majority of the writing of this paper was performed by T. Raistrick. Z. Zhang, D. Mistry, J. Mattsson and H. F. Gleeson provided edits and comments during drafting.

Chapter 9 and 10 include content which has been published in the paper by Thomas Raistrick, Matthew Reynolds, Helen F Gleeson and Johan Mattsson in Molecules 26 (23), 7313. M. Reynolds performed χ^4 analysis on the dielectric data obtained by T. Raistrick. Rheological measurements were performed in collaboration with M. Reynolds. The majority of the writing of this paper was performed by T. Raistrick. M. Reynolds, H. F. Gleeson and J. Mattsson provided edits and comments during drafting.

Acknowledgements

I would like to thank my supervisors Prof. Helen Gleeson and Dr. Johan Mattson for their guidance and support throughout my PhD. Our discussions were always useful and informative. I would also like to acknowledge Dr. Daniel Baker for his continual support for our group and Dr. Matthew Reynolds for his expertise in rheology and dielectric measurements.

I would like to thank the people at the Jožef Stefan Institute, who made me feel most welcome during my visit and provided with many useful discussions.

I would like to thank everyone in the University of Leeds Soft Matter group, I have made some wonderful memories and met some wonderful people throughout this PhD.

Finally, I would like to thank my family and friends.

Abstract

Liquid crystal elastomers (LCEs) are a class of materials which combine the orientational order and anisotropic properties of liquid crystals with the rubber-like elasticity of conventional elastomers. This thesis investigates the behaviour of an all acrylate LCE which displays a molecular auxetic response when deformed in the direction perpendicular to its nematic director. Auxetic materials have negative Poisson's ratios meaning they expand in one or both of their transverse axes when a longitudinal elongational strain is applied. In addition to a molecular auxetic response, the LCE also deforms via the mechanical Fréedericksz transition (MFT) which is characterised by a sharp rotation of the nematic director once a critical strain is reached. This behaviour appears to be quite different from the 'semi-soft elastic' (SSE) response observed in other LCEs. The SSE is characterised by a continuous rotation of the nematic director, and a low energetic cost of deformation.

The molecular auxetic response and MFT in the LCE is investigated using polarised Raman spectroscopy (PRS), broadband dielectric spectroscopy (BDS), and the rheological techniques 'dynamic mechanical analysis' (DMA) and 'small amplitude shear rheology' (SAOS). PRS provides insight into the state of the nematic order. The PRS measurements reveal that when the LCE is strain perpendicular to the nematic director there is a decrease in the uniaxial order and the emergence of biaxial order. Additionally, at strains near the onset of the molecular auxetic response, the order parameter data suggests that the mesogenic units rotate into the axis that also displays the negative Poisson's ratio. BDS, DMA and SAOS provide insight into

glass-formation and the molecular dynamics of the LCE. This LCE is particularly interesting in this regard as chemically identical nematic or isotropic samples can be synthesised. The glass transition temperatures are similar in both the nematic and isotropic phase. For both phases of the LCE, a cross-over in the dynamic behaviour of $\tau_\alpha(T)$ is observed at $T^* \approx 330$ K. However, above T^*, $\tau_\alpha(T)$ is Arrhenius for the nematic LCE whereas $\tau_\alpha(T)$ is non-Arrhenius for the isotropic sample. The difference in $\tau_\alpha(T)$ is argued to be related to the presence of pretransitional nematic domains in the isotropic LCE.

The effect of strain on the relaxation dynamics and mechanical response of the nematic LCE is investigated to better understand the molecular auxetic response and the MFT. It is found that the complex Young's modulus, E^* and the characteristic time-scale of the α relaxation, τ_α remain constant during small deformations. However, for strains close to the onset of the molecular auxetic response an increase in both E^* and τ_α is observed. Based on these findings it is suggested that the observed molecular auxetic response, which is related to out-of-plane rotations of the mesogenic units, is in turn driven by an effect of constraints on polymer configurations, and the finite extensibility of the network, at large imposed strains.

Abbreviations

BDS	broadband dielectric spectroscopy
CC	Cole-Cole function
DMA	dynamic mechanical analysis
HN	Havriliak-Negami function
LC	liquid crystal
LCE	liquid crystal elastomer
LVR	linear viscoelastic regime
MCLCE	main-chain LCE
MFT	mechanical Fréedericksz transition
MS	Maier-Saupe
ODF	orientational distribution function
PRS	polarised Raman spectroscopy
PVA	polyvinyl alcohol
SAOS	small-amplitude oscillatory shear
SSE	semi-soft elastic
SCLCE	side-chain LCE
SCLCP	side-chain liquid crystalline polymer
TTS	time-temperature superposition
VFT	Vogel-Fulcher-Tammann
WLF	Williams-Landel-Ferry
D	strength parameter
ΔE_A	activation energy
ϵ	strain
ϵ_{t}	true strain
ε^*	complex dielectric permittivity
E^*	complex Young's modulus
G^*	complex shear modulus
k_{B}	Boltzmann constant

m	fragility parameter
M^*	complex dielectric modulus
ν	Poisson's ratio
$\langle P_{L00} \rangle$	uniaxial order parameters
$\langle P_{Lm0} \rangle$	phase biaxial order parameters
r	backbone anisotropy
$R(\theta)$	depolarisation ratio
σ	engineering stress
σ_{t}	true stress
σ_{DC}	DC conductivity
τ	relaxation time-scale
T_{ni}	nematic to isotropic transition temperature
T_{g}	glass transition temperature
ω	angular frequency

Publications

First author publications

- T. Raistrick, Z. Zhang, D. Mistry, J. Mattsson and H. F. Gleeson., Understanding the physics of the auxetic response in a liquid crystal elastomer., *Physical Review Research* 3 (2), 023191, (2021).
- T. Raistrick, M. Reynolds, H. F. Gleeson and J. Mattsson., Influence of liquid crystallinity and mechanical deformation on the molecular relaxations of an auxetic liquid crystal elastomer. *Molecules* 26 (23), 7313, (2021).

Contributing author

- D. Mistry, M. Nikkhou, T. Raistrick, M. Hussain, E. I. L. Jull, D. L. Baker and H. F. Gleeson., Isotropic liquid crystal elastomers as exceptional photoelastic strain sensors. *Macromolecules* 53, 10, 3709–3718, (2020)
- M. Hussain, E. I. L. Jull, R. J. Mandle, T. Raistrick, P. J. Hine and H. F. Gleeson., Liquid crystal elastomers for biological applications. *Nanomaterials* 11, 3, 813, (2021).
- L. A. Mihai, D. Mistry, T. Raistrick, H. F. Gleeson and A. Goriely., A mathematical model for the auxetic response of liquid crystal elastomers. *Philosophical Transactions of the Royal Society of London* (accepted), (2022).
- E. I. L. Jull, R. J. Mandle, T. Raistrick, Z. Zhang, P. J. Hine, and H. F. Gleeson., Toward In Silico Design of Highly Tunable Liquid Crystal Elastomers.*Macromolecules* (accepted), (2022).

Contents

Acknowledgements ii

Abstract iii

Abbreviations v

Publications vii

Contents viii

List of Figures xiii

1 Introduction 1

1.1 Liquid crystalline phases . . . 1

1.1.1 What is a liquid crystal? . . . 1

1.1.2 The nematic phase . . . 3

1.2 Polymers and conventional elastomers . . . 5

1.2.1 Static conformation of a polymer chain . . . 6

1.2.2 Rouse model . . . 8

1.2.3 Entanglements . . . 11

1.3 Glass formation . . . 13

1.3.1 Dynamics of the glass transition . . . 13

1.3.2 Cross-over in dynamic behaviour . . . 15

1.4 Liquid crystal elastomers . . . 17

1.4.1 Polymer conformation and anisotropy in liquid crystal elastomers . . . 17

1.4.2 Types of liquid crystal elastomers and alignment 19
1.4.3 Stress-optical coupling and nematic order induced actuation 20
1.4.4 Mechanical deformations in mono-domain nematic liquid crystal elastomers 20
1.4.5 Semi-soft elasticity 21
1.4.6 Mechanical Fréedericksz transition 21
1.4.7 The auxetic response in liquid crystal elastomers 22
1.5 Summary 25
1.6 Thesis outline 26

2 Theory I: Orientational distribution functions and liquid crystal phases 28
2.1 The orientational distribution function (ODF) 29
2.2 The uniaxial ODF 30
2.2.1 Exponential approximation 32
2.2.2 The significance of $\langle P_4 \rangle$ 34
2.3 The phase biaxial ODF 40
2.4 Non-cylindrically symmetric molecules 42
2.5 Summary 43

3 Theory II: Mechanical deformation of LCEs 45
3.1 Derivation of the 'Trace formula' 46
3.1.1 Isotropic case 46
3.1.2 Nematic case 48
3.2 Spontaneous distortion under the isotropic to nematic transition . 50
3.3 Soft elasticity 51
3.4 Mechanical Fréedericksz transition 56
3.5 Summary 58

4 Experimental I: Materials and LCE synthesis 60
4.1 Cell assembly 60
4.2 LCE synthesis 62
4.3 Summary 65

5 Experimental II: Raman spectroscopy **66**
5.1 Raman scattering . . . 67
5.1.1 Scalar case . . . 67
5.1.2 Tensorial case . . . 69
5.2 Selection of Raman peaks for calculation of order parameters in liquid crystal phases . . . 70
5.3 Polarised Raman spectroscopy and the orientational distribution function (ODF) . . . 71
5.4 Determination of order parameters from polarised Raman spectroscopy . . . 73
5.4.1 Full depolarisation method . . . 73
5.4.2 Two point method . . . 75
5.4.3 Phase biaxial order parameters from PRS . . . 76
5.4.4 Molecular biaxial order parameters from PRS . . . 78
5.5 Experimental set-up . . . 79
5.6 Summary . . . 81

6 Experimental III: Broadband dielectric spectroscopy **82**
6.1 The dielectric response of materials . . . 83
6.1.1 Static response . . . 83
6.1.2 Dynamics . . . 86
6.1.3 Debye single relaxation model . . . 87
6.1.4 Empirical fitting: The Havriliak-Negami function . . . 89
6.1.5 DC conductivity . . . 90
6.2 Experimental set-up . . . 91
6.3 Summary . . . 94

7 Experimental IV: Rheology **95**
7.1 Viscoelasticity . . . 95
7.2 The complex Young's modulus . . . 96
7.3 DMA testing procedures . . . 98
7.3.1 Strain sweep . . . 98
7.3.2 Frequency sweep . . . 99
7.3.3 Time temperature superposition . . . 99

7.4 Experimental set-up . . . 101
7.4.1 Dynamic mechanical analyser . . . 101
7.4.2 Shear rheometer . . . 102
7.5 Summary . . . 103

8 Results I: Order parameters of LCEs under strain: Insight into the auxetic response 104
8.1 Introduction . . . 104
8.1.1 Predicted emergence of biaxiality . . . 106
8.2 Experimental set-up . . . 110
8.3 Results of the uniaxial model . . . 113
8.3.1 Strain parallel to the director . . . 113
8.3.2 Strain perpendicular to the director . . . 116
8.3.3 The behaviour of different moieties in the LCE . . . 118
8.4 Discussion . . . 119
8.4.1 Uniaxial case: Insight into the mechanical Frèedericksz transition . . . 119
8.4.2 Uniaxial case: Deviation from Maier-Saupe theory . . . 122
8.4.3 The emergence of biaxiality . . . 125
8.4.4 Relating biaxiality to the auxetic behaviour . . . 127
8.5 Conclusion . . . 131

9 Results II: Influence of phase on the molecular dynamics of LCEs 134
9.1 Introduction . . . 134
9.2 Nomenclature of molecular relaxations in LCEs . . . 135
9.3 Experimental set-up . . . 137
9.3.1 Sample preparation . . . 137
9.3.2 Broadband dielectric spectroscopy . . . 137
9.3.3 Rheology . . . 138
9.4 Results: Broadband dielectric spectroscopy . . . 138
9.4.1 Relaxation dynamics of the isotropic and nematic LCE . . . 138
9.4.2 Existence of the δ relaxation? . . . 140
9.4.3 T-dependant behaviour of observed relaxations . . . 142
9.4.4 Dynamic cross-over of the α relaxation . . . 145

9.4.5 Suggested cause of the dynamic cross-over in this LCE . . 148
9.4.6 Ionic Conductivity Behaviour of the Isotropic and Nematic LCE 151
9.5 Results: Rheological behaviour of LCEs 155
9.6 Conclusion 160

10 Results III: Effect of applied strain on the molecular dynamics of LCEs 163
10.1 Introduction 163
10.2 Experimental methods 164
10.3 Effect of applied strain on the complex elastic modulus 166
10.3.1 Effect of applied strain on DMA master curve data 166
10.3.2 Effect of applied strain on E^* at fixed frequency and temperature 168
10.4 Effect of applied strain on the α relaxation 172
10.4.1 Effect of applied strain on $\tau_\alpha(T)$ 173
10.4.2 Effect of applied strain on τ_α at a fixed temperature 175
10.5 Conclusion 178

11 Conclusion and outlook 180

A Raman Spectroscopy: Jen *et al.* [104] method 186

References 214

List of Figures

1.1 Chemical structure of 5CB (4-Cyano-4′-pentylbiphenyl). 5CB contains a biphenyl group which is often represented by a rigid rod and a flexible chain with a length of 5 carbons. 2

1.2 (a) Illustration of an isotropic phase with no positional or orientational order. (b) Illustration of the nematic phase with only orientational order but no positional order. (c) Illustration of the smectic A phase with orientational and positional order. 3

1.3 (a) Illustration of rod-like liquid crystal molecules forming a nematic phase. The average molecular orientation is known as the nematic director ($\hat{n}$). The angular deviation of a given molecule from $\hat{n}$ is defined by β. (b) The variation of the orientational order parameter, Q, as a function of reduced temperature showing a nematic to isotropic transition at 1. Before the transition Q decreases continuously, whereas at the transition Q jumps from ∼0.43 to 0. 4

1.4 Illustration of a nematic phase with a negative order parameter. . 5

1.5 Illustration of a polymer, with freely rotating bonds, behaving as a random walk. $\vec{R}$ is the end-to-end vector, $\vec{u}_i$ is the vector between the i_{th} freely rotating bond and the $i_{\text{th}+1}$ freely rotating bond. . . 6

1.6 Schematic of a Rouse chain. 9

1.7 Different modes of motion for a Rouse chain. 10

1.8 Schematic of the tube model. A polymer is held within an effective tube (dotted black line) of diameter a due to entanglements (blue line). The polymer can leave a tube via longitudinal motions (reptation) along the primitive path (red line). 12

1.9 (a) Arrhenius plot ($\log(\tau)$ against $1000/T$) showing the behaviour of the α relaxation (VFT-like) and the β and γ relaxation (Arrhenius-like). (b) Shape of $\tau_\alpha(T)$ for various values of m. 13
1.10 Illustration of (a) main-chain attachment, (b) end-on side-chain attachment and (c) side-on side-chain attachment. 17
1.11 Illustration of (a) an isotropic (spheroid) polymer conformation, (b) a prolate (elongated along the nematic director) polymer conformation and (c) an oblate (elongated perpendicular to the nematic director) polymer conformation. 18
1.12 Schematic showing the geometries and length changes when defining the Poisson's ratio. The sample is elongated along x and contractions occur in the transverse axis to conserve volume. Note, that for an auxetic material we expect an expansion in one or more of the transverse axes. 23
1.13 Sample thickness as a function of applied strain. The partial auxetic response observed in the nematic LCE happens after a strain threshold is reached. Data taken from Mistry *et al.* [1] 24

2.1 Euler angles (α,β,γ) of a single molecule within the reference frame of the nematic director (z_{D}). z_{M} is the molecular long axis which defines the orientation of the longest axis of the molecule. 29
2.2 b_2 values as a function of $\langle P_4 \rangle$ and $\langle P_2 \rangle$ determined by numerically solving equations 2.12. 33
2.3 b_4 values as a function of $\langle P_4 \rangle$ and $\langle P_2 \rangle$ determined by numerically solving equations 2.12. 34
2.4 ODF of 5CB at 23°C using information theory (black line) and the truncated form (red line). In both cases $\langle P_2 \rangle = 0.63$, $\langle P_4 \rangle = 0.31$. For the exponential approximated ODF, $b_2 = 2.7860$ and $b_4 = 0.4467$ which is determined by solving the system of equations 2.12. 35
2.5 [$\langle P_2 \rangle$, $\langle P_4 \rangle$] phase space showing the absolute limits of P_4 (black lines), the $\langle P_4 \rangle$ model (red line), prediction of P_4 from Maier-Suape theory (green line) and the cone model (blue line). 36

2.6 Normalised ODFs from various models, showing the 3 distinct regions in the $[\langle P_{200}\rangle, \langle P_{400}\rangle]$ phase space. Black line: MS theory distribution of molecules using order parameters predicted by Maier-Saupe theory ($\langle P_{200}\rangle = 0.5$, $\langle P_{400}\rangle = 0.178$). Red line: Large distribution of molecules at $\beta = 90°$ using $\langle P_{200}\rangle = 0$, $\langle P_{400}\rangle = 0.178$. Blue line: Cone model showing a distribution of molecules peaking at $\beta_c = 31.8°$ using $\langle P_{200}\rangle = 0.5$, $\langle P_{400}\rangle = -0.041$. 39

3.1 Initial geometry involved in the semi-soft elastic response and the mechanical Fréedericksz transition. In both cases the initial nematic director is orientated along z and a perpendicular strain is applied along x. 46

3.2 Change in probability distribution of the polymer chains under an affine deformation. The shape of the probability remains unchanged however the centre of the distribution is now shifted from $\vec{R}$ to $\vec{R}'$. 47

3.3 Schematic of the soft elastic response in LCEs. The LCE has access to an isotropic conformation (top) and upon cooling will form a nematic conformation with an arbitrary director angle. The nematic conformations have equal energies. Thus λ_{soft} deformations have no energetic cost. 52

3.4 Schematic of the stress-strain behaviour and the director rotation of a nematic LCE strained perpendicular to the initial director and undergoing the semi-soft elastic response 55

3.5 Free energy (F_{el}) against extension of an LCE in the unrotated state (F_{el}^A) and the rotated state (F_{el}^B). The free energies cross-over at λ_{c}. 56

4.1 Schematic of an assembled cell. The steps required to assemble the cell are described in section 4.1. 62

4.2 Structures of the constituent chemicals of the LCE. 63

4.3 Schematic of the polymerised LCE network showing the constituent chemicals. 65

5.1 Typical Raman spectra for the acrylate LCE studied herein. The phenyl-stretching mode (1606 cm^{-1}) and the cyano-stretching (2250 cm^{-1}) are shown. These particular Raman modes are prevalent in many liquid crystalline systems. 71

5.2 (a) Schematic showing the Euler angles (α, β, γ) of a liquid crystal molecule with its long axis (z_M) at an angle (β) from the director (z_D). z_M corresponds to the molecular long axis. (b) Shows the laboratory frame relating the angle between the incident laser polarisation and the director of nematic director (θ). In this case the laser travels along the y_L axis. 72

5.3 $R(\theta)$ of 5CB at 23°C determined from the 1606cm^{-1} peak. The red line shows the fitting to the data (black crosses) using the full depolarisation method; values of $\langle P_{200} \rangle = 0.63 \pm 0.05$, $\langle P_{400} \rangle = 0.30 \pm 0.05$ and $p = -0.24$ are deduced from the full depolarisation method. The blue line shows the fitting to the data using the '2 point method' where a value of $p = -0.04$ has been used as this is the value of p in the isotropic phase of 5CB; incorrect values of $\langle P_{200} \rangle = 0.53 \pm 0.05$, $\langle P_{400} \rangle = 0.11 \pm 0.05$ and $p = -0.04$ are deduced from the 2 point method. 75

5.4 Schematic of the Raman spectrometer. The green line denotes the laser and the black arrows are the direction of the laser path which is in a back-scatter geometry. The whole Raman spectrometer as depicted is encapsulated in an polarised optical microscope. 80

6.1 Schematic of a dielectric material placed between two capacitors with a charge build up, q_0, and a potential difference across the plates of V. There is a net polarisation, P, of dipoles in the dielectric material of and a build of bound charges, q_b, at the boundary of the dielectric material. 83

6.2 Frequency dependence of ε' and ε'' for the Debye single relaxation model. 87

6.3 ε'' against frequency for (a) the Cole-Cole function ($p \neq 1, q = 1$) for various values of p and (b) the Cole-Davidson function ($p = 1, q \neq 1$) for various values of q. 89
6.4 Simplified circuit diagram of a dielectric measurement. The sample is shown in blue and is sandwiched between the two electrodes. . . 92

7.1 An oscillatory strain is applied to a sample. The resultant oscillatory stress is out of phase with the applied strain by the value δ. 96
7.2 Strain sweep performed at 18°C and 1 Hz on a nematic LCE strained parallel to the director. The grey dashed line separates the linear viscoelastic regime and the non-linear viscoelastic regime. 98
7.3 (a) Unshifted E' (solid circles) and E'' (empty triangles) data for the nematic LCE strained perpendicular to the director for a temperature range of 10°C - 50°C (b) Rheological master curve constructed with the TTS principle using $T_{\text{ref}} = 40$°C. 100
7.4 Schematic of rheological measurements on a sample using (a) the DMA performed with the tension film clamps attachment and (b) the shear rheometer in a parallel plate geometry. 102

8.1 (a) Non auxetic parallel geometry refers to strain applied parallel to the initial nematic director (along z). (b) Auxetic perpendicular geometry refers to the strain being applied perpendicular to the initial nematic director (along x). The sample 'thickness' is in the y axis. 110
8.2 Schematic of the bespoke straining rig which is housed within the Raman spectrometer which allows one to determine order parameters of an LCE as a function of strain. 111

8.3 (a) Raman spectrum of the LCE film. Showing the symmetric phenyl stretch (a: 1606cm^{-1}), the carbonyl stretch (b: 1730cm^{-1}) and the cyano group stretch (c: 2250cm^{-1}). (b) Depolarisation ratio of an unstrained sample determined from the 1606cm^{-1} peak. The red line shows the fitting to the data (black crosses) with the values of $\langle P_{200} \rangle = 0.59 \pm 0.05$, $\langle P_{400} \rangle = 0.29 \pm 0.05$, $p = -0.23 \pm 0.05$ and $\theta = -5 \pm 0.5^{\circ}$ deduced from the fit. 112

8.4 (a) Order parameters $\langle P_{200} \rangle$ and $\langle P_{400} \rangle$ as a function of strain applied parallel to the nematic director; error bars in order parameter data are the tolerances of the fitting procedure and error bars in strain are standard errors in measurements. (b) The stress-strain data for the LCE strained parallel to the director is taken from [2]. 114

8.5 $\langle P_{400} \rangle$ against $\langle P_{200} \rangle$ for the LCE strained parallel to the nematic director; error bars in order parameter data are the tolerances of the fitting procedure. Maier-Saupe predictions of $\langle P_{400} \rangle$ for a given value of $\langle P_{200} \rangle$ is shown by the green line. The blue dot denotes the values of the order parameters for the unstrained LCE. 115

8.6 (a) $\langle P_{200} \rangle$ and $\langle P_{400} \rangle$ as a function of strain for the LCE strained perpendicular the initial nematic director; error bars in order parameter data are the tolerances of the fitting procedure and error bars in strain are standard errors from repeated measurements. (b) Reorientation of the director, determined from fitting to the full depolarisation Raman data, showing an MFT at a strain of 1.16; error bars are instrumental errors. (c) The stress-strain curve of the LCE showing a softening response between the strains of 0.2 and 0.9 and (d) Fractional sample thickness of the LCE sample showing the auxetic response emerging at strains near the MFT. The dotted grey lines show points of interest. The first line is the beginning of the softening of the stress response which coincides with the reduction in order clearly demonstrating the coupling of the nematic order and the polymer network. The second line shows the crossing of $\langle P_{400} \rangle$ and $\langle P_{200} \rangle$ and the end of the softened stress plateau. Director rotation occurs between the second and final line. The final line shows the re-emergence of $\langle P_{200} \rangle$ order and a sharp rotation of the director. See Mistry *et al.* [1, 2] for more details on stress-strain and thickness measurements. 117

8.7 Proposed mechanism for an auxetic response in a liquid crystalline polymer. [155] (a) the LCP contains two types of repeating mesogenic units: one attached end-on and one attached laterally. (b) the LCP is strained which causes the laterally attached mesogenic unit to rotate. 118

8.8 $\langle P_{400} \rangle$ plotted as a function of $\langle P_{200} \rangle$ for the LCE strained perpendicular to the initial director; error bars in order parameter data are the tolerances of the fitting procedure. The blue dot highlighted with the asterisk denotes the order parameters in unstrained state. The black dots signify the values of the order parameters on approach to the MFT (region I-III in figure 8.6). The red dots denote the order parameter values after the MFT (region IV in figure 8.6). Various models for $\langle P_{400} \rangle$ and $\langle P_{200} \rangle$ are included on the diagram which are discussed in detail in chapter 2 by Pottel *et al.*[94] 123

8.9 ODFs for the perpendicularly strained LCE constructed from the order parameter data deduced with the assumption of a uniaxial distribution of molecules (figure 8.6a.). Line colour corresponds to the strain. Increasing strain results in an increasing distribution of molecules perpendicular to the nematic director (i.e. $\beta = 90^{o}$) . 124

8.10 (a) Uniaxial order parameters ($\langle P_{200} \rangle$: black squares, $\langle P_{400} \rangle$: red circles) used in the fitting of the biaxial order parameters. The values for $\langle P_{400} \rangle$ are obtained using Maier-Saupe predictions. (b) Biaxial order parameters ($\langle P_{420} \rangle$: purple diamonds, $\langle P_{440} \rangle$: blue downwards triangles $\langle P_{220} \rangle$: green upwards triangles) as a function of strain. (c) Instantaneous Poisson's ratio of the auxetic LCE as a function of strain which becomes negative at a strain of $\sim$1.00. See Mistry *et al.* [1, 2] for more details on stress-strain and thickness measurements. 128

8.11 Truncated ODF plot showing distribution of molecules in the unstrained state (a) and at the beginning of the auxetic response (b). The initial director orientation is along z and the strain axis is in the x direction. The macroscopic sample's 'thickness' occurs is in the y-dimension. The red regions correspond to the highest density of molecules and black/blue the lowest. 130

9.1 Schematic of possible dielectric relaxations in a side-chain liquid crystalline polymer. 135

9.2 Dielectric loss (ε'') versus frequency (f) for the isotropic (a, c, e) and nematic (b, d, f) LCE samples at $T = 315$ K, $T = 248$ K and $T = 163$ K. The overall fits to the data are shown in solid red lines, and the individual contributions from the α, β and γ relaxations, as well as the DC conductivity (σ) are labelled and shown in dashed lines. Errors associated with equipment ($\Delta\varepsilon''\pm < 1\%$) are smaller than the symbol size. 139

9.3 A slow Debye-like relaxation is observed in (a) the $\varepsilon''_{\text{der}}$ and (b) the M'' representation for selected temperatures. 141

9.4 An increase in (a) ε' coincides with the presence of the Debye-like relaxation in the (b) M'' representation. The is evidence that the observed relaxation is the 'conductivity relaxation'. 142

9.5 Characteristic relaxation times for the α (squares), β (circles) and γ (triangles) relaxations identified for the isotropic (black) and nematic (red) LCE samples. The results of a VFT fit to the α relaxation data, and Arrhenius fits the β and γ relaxation data are shown in solid lines. Errors associated with the fitting tolerances are smaller than the symbol size. 143

9.6 Stickel analysis of $\tau_\alpha(T)$ data of the isotropic (black) and nematic (red) LCE samples. A crossover behaviour is observed at T^* ≈333 K, as shown with a dashed line. Linear fits of the data are shown both for temperatures above and below T^*. For the nematic samples the data for $T > T^*$ can be well described using a horizontal line (corresponding to Arrhenius behaviour). (b) Arrhenius plot of $\tau_\alpha(T)$ vs. inverse temperature for the isotropic and nematic samples. For $T < T^*$, the VFT fits to the data are shown in solid lines. For $T > T^*$ VFT fits are shown in dashed lines for the isotropic (black) and nematic (red) sample. An Arrhenius fit is also applied to the nematic data before $1000/T$=3.0 (blue solid line). 145

9.7 Volume of correlated molecular motions for the isotropic LCE sample as a function of inverse temperature. [169] 150

9.8 Plot of $\log(\sigma_{DC})$ vs. $\log 1/\tau_\alpha$ for the isotropic and nematic LCE samples. Also shown is the γ_w coupling coefficient from the equation σ_{DC}, which is related to the extent of coupling between the α relaxation and the ionic conductivity. 153
9.9 (a) van Gurp-Palmen plots of the SAOS (filled circles) and DMA (hollow circles) data for the isotropic LCE. (b) van Gurp-Palmen of the SAOS data for the polydomain nematic LCE. 155
9.10 TTS master curves of the isotropic LCE for shear storage modulus (G', green circles), shear loss modulus (G'' , blue circles), unshifted storage modulus (E', hollow black circles), unshifted loss modulus (E'', hollow red circles), shifted storage modulus (E', black circles) and shifted loss modulus (E'', red circles). A vertical shift of -0.37 (on the log-scale) is applied between G^* and E^* demonstrating a very good agreement between the two data sets. Approximate power-law scalings of $\omega^{0.5}$ and $\omega^{0.25}$ discussed in the text are illustrated. Inset: phase angle, $\tan(\delta)$, against TTS shifted angular frequency ($a_T.\omega$) for the SAOS data. 157
9.11 TTS master curves of the polydomain nematic LCE for shear storage modulus (G', green circles), shear loss modulus (G'' , blue circles). Approximate power-law scaling of $\omega^{0.5}$ discussed in the text is illustrated. Inset: phase angle ($\tan(\delta)$) against TTS shifted angular frequency ($a_T.\omega$) for the SAOS data. 158
9.12 Arrhenius plot showing the α relaxation time, $\tau_\alpha(T)$ vs. inverse T for the (a) isotropic LCE and (b) polydomain nematic LCE as measured via BDS (filled black circles) and SAOS (filled blue circles). Also shown is the SAOS vertically shifted (hollow blue circles) to show good agreement between $\tau_\alpha(T)$ between the BDS and SAOS measurements. 159

10.1 Schematic showing how DMA measurements were performed under strain. (a) The nematic LCE sample in the DMA with the nematic director perpendicular to the axis of oscillatory strain. The sample is elongated to the desired strain and stress-relaxed. (b) an oscillatory strain is applied to the sample and the complex elastic modulus is measured E^*. 164

10.2 (a) E', (b) E'', (c) $\tan(\delta)$ master curves constructed from DMA measurements for the nematic LCE as a function of perpendicularly applied strain (see legend in (b)). (d) horizontal shift factors (a_T) against $T - T_{\text{ref}}$ where $T_{\text{ref}} = 22^{\text{o}}\text{C}$. The grey dashed line is a fit to the WLF model with $C_1 = 9 \pm 1\text{K}$ and $C_2 = 50 \pm 10\text{K}$. . . . 167

10.3 Storage and loss moduli determined at 1 Hz and T = 23°C, as a function of true-strain applied perpendicular to the nematic director; errors in E', E'' and ϵ_t are standard errors from multiple measurements. Inset: non-dynamic tensile tests showing the true-stress (hollow circles) σ_{t} [MPa] as function of true strain ϵ_{t} (raw data taken from [2]). The grey dashed line marks the threshold for the onset of the molecular auxetic response. 170

10.4 $\tan(\delta)$ as a function of true-strain applied perpendicularly to the nematic director; errors in $tan(\delta)$ and strain are standard errors from multiple measurements. 171

10.5 $\tau_\alpha(T)$ against $1000/T$ for the nematic LCE under strain. The solid lines are fits to the data with the VFT equation. Errors associated with the fitting tolerances are smaller than the symbol size. 174

10.6 Normalised BDS loss data taken at T =23°C as a function of applied true-strain (ϵ_{t}) ranging from (a) 0.00 to 0.44 and (b) 0.00 to 0.86. (c) and (d) the corresponding α relaxation times from fitting with a HN function; errors in τ_α are fitting tolerances and errors in strain are standards errors from multiple measurements. 176

10.7 Normalised α-relaxation times, τ_α, versus applied true-strain; errors in τ_α are fitting tolerances and errors in strain are standards errors from multiple measurements. The grey dashed line marks the threshold for the onset of the molecular auxetic response. . . . 177

10.8 Storage modulus, E' and normalised α-relaxation times, τ_α, versus applied true-strain. The grey dashed line marks the threshold for the onset of the molecular auxetic response. 178

11.1 Schematic of the proposed auxetic mechanism, due to the lack of a δ relaxation, the mesogenic units are constrained to follow the distortions of the polymer network. The network is deformed perpendicular to the nematic director which results in a biaxial conformation of the polymer. The overall configurational entropy of the polymer is reduced. Configurations in which there are out-of-plane rotations of the mesogenic become increasingly likely due to a reduction in the overall configurational states available. The out-of-plane rotations drive the auxetic behaviour. 185

Chapter 1

Introduction

The aim of this thesis is to understand the mechanical behaviour of recently discovered liquid crystal elastomers (LCEs) which display an auxetic response when strains are applied perpendicular to the nematic director. [1, 2] To achieve this, polarised Raman spectroscopy is used to determine the order parameters of the strained LCEs. Models are applied to the order parameter data to investigate whether there is a link between the ordering of the LCE and the auxetic response. Complementary techniques are used to investigate the dynamic behaviour of LCEs under strain. In particular, broadband dielectric spectroscopy and rheology are used to probe the molecular relaxation processes in LCEs, and comparisons with conventional polymeric and elastomeric materials are discussed. The strain-dependant response of the dielectric and rheological data is investigated to better understand the auxetic behaviour. The relevant experimental techniques are introduced later in chapters 5-7. Since LCEs bridge the gap between liquid crystal and polymers, this chapter will outline the relevant fundamental physics of liquid crystals, polymers and liquid crystal elastomers.

1.1 Liquid crystalline phases

1.1.1 What is a liquid crystal?

Liquid crystal (LC) phases are mesophases meaning they are intermediate states of matter. An LC phase will typically flow, much like a viscous liquid, whilst

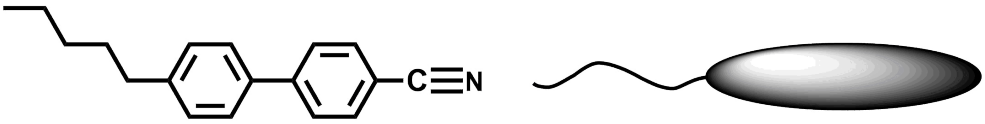

Figure 1.1: Chemical structure of 5CB (4-Cyano-4′-pentylbiphenyl). 5CB contains a biphenyl group which is often represented by a rigid rod and a flexible chain with a length of 5 carbons.

still possessing long-range orientational order much like a solid crystal. An LC phase generally has anisotropic properties which can include: optical anisotropy which leads to birefringence; electrical anisotropy which allows for alignment with electrical fields; and anisotropic shear viscosity, to name but a few. [3] Figure 1.1 shows the chemical structure of the LC molecule 4-Cyano-4′-pentylbiphenyl (5CB) which forms a nematic LC phase between 22 °C $< T <$ 35 °C. [4] Also shown in figure 1.1 is a typical idealisation of a liquid crystal molecule consisting of a rigid rod connected to a flexible chain. Often, the flexible chain is not included in this idealisation. Examples of LC phases are: the nematic (Nem) phase which has long-range orientational order but no positional order; and the smectic-A (SmA) and smectic-C (SmC) phases which have both long-range orientational and positional order. Schematics of the Iso, Nem and SmA phases are shown in figure 1.2. Thermotropic LC phases are only stable (or metastable) within a specific temperature range. [5] Above the temperature of LC phase stability the material will form an isotropic (Iso) phase and below the temperature of LC phase stability the material will, typically, form a crystalline (Crys) or amorphous solid phase. [6] It is not uncommon for LC materials to exhibit various LC phases in different temperature ranges. The order in which the phases form is known as the phase sequence. A typical example is that of 4-cyano-4′-octylbiphenyl (8CB) which has the following phase sequence upon cooling: Iso $\rightarrow$ Nem $\rightarrow$ SmA $\rightarrow$ Crys. [4] 8CB is chemically very similar to 5CB albeit with a carbon chain of length 8 instead of length 5, however, 5CB does not form a SmA phase; thus demonstrating the sensitivity of the bulk phase behaviour to the molecular structure. The isotropic and nematic phases are a particular focus for this thesis as they are the most relevant phases for the investigated LCEs.

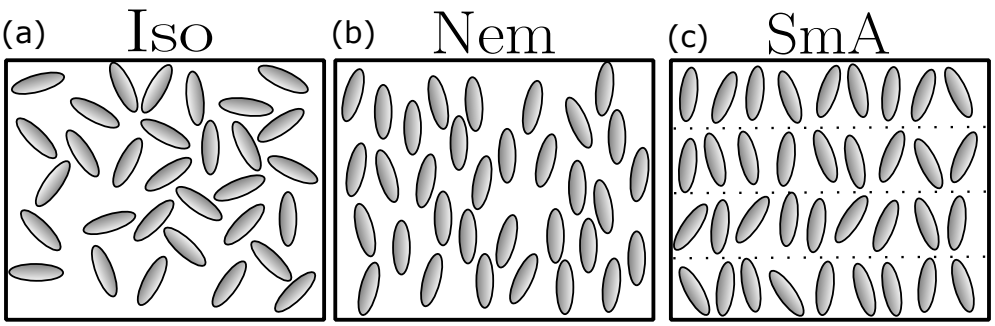

Figure 1.2: (a) Illustration of an isotropic phase with no positional or orientational order. (b) Illustration of the nematic phase with only orientational order but no positional order. (c) Illustration of the smectic A phase with orientational and positional order.

1.1.2 The nematic phase

The nematic phase, shown in figure 1.3(a), is the simplest of the LC phases. The nematic phase has no positional order but has long-range orientational order. It is important to be able to quantify the orientational order of a liquid crystal phase as many of the macroscopic properties of the bulk material come from the microscopic ordering of the phase. [5] Quantification of an ordered system can be achieved by defining an order parameter. A correctly defined orientational order parameter should be non-zero in the nematic phase but have a value of 0 in the isotropic phase. [7] Additionally, one expects a suitably defined order parameter to decrease upon increasing temperature (or any relevant thermodynamic variable). [8, 9]

The orientational order parameter of the nematic phase was first suggested by Tsvetkov [10] as:

$$Q = \langle P_2(\cos\beta)\rangle = \left\langle \frac{1}{2}(\cos^2\beta - 3)\right\rangle, \tag{1.1}$$

where $\langle ...\rangle$ represents an ensemble average, P_2 is the 2^{nd} rank Legendre polynomial, β is the angle of a molecule with respect to the overall average orientation of the molecules, or the nematic director, represented by $\hat{n}$. Q is commonly referred to as the ***scalar orientational order parameter***. Equation 1.1 assumes

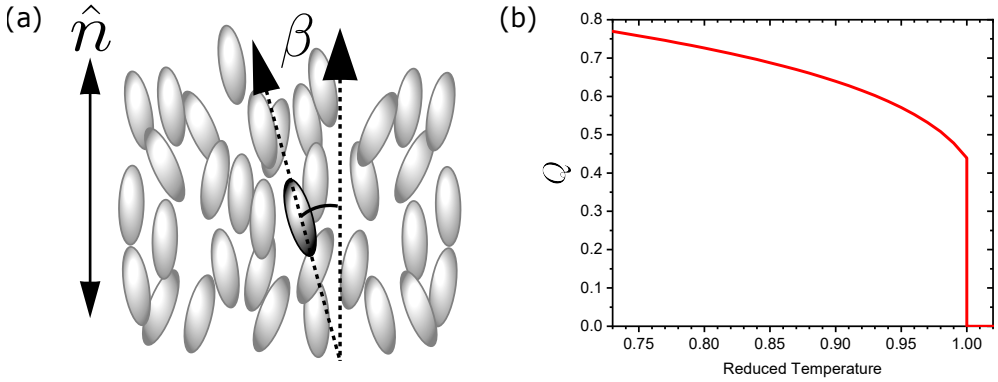

Figure 1.3: (a) Illustration of rod-like liquid crystal molecules forming a nematic phase. The average molecular orientation is known as the nematic director ($\hat{n}$). The angular deviation of a given molecule from $\hat{n}$ is defined by β. (b) The variation of the orientational order parameter, Q, as a function of reduced temperature showing a nematic to isotropic transition at 1. Before the transition Q decreases continuously, whereas at the transition Q jumps from ∼0.43 to 0.

that the phase (i) has cylindrical (uniaxial) symmetry and (ii) is apolar so that $\hat{n} = -\hat{n}$. [7, 10] Both these assumptions are true for conventional nematic phases. Shown in figure 1.3(b) is the typical evolution of Q as a function of temperature as predicted by Maier-Saupe theory and observed experimentally. [11] In molecular LC nematics the transition from the nematic phase to the isotropic phase is weakly first order with the transition from the nematic to the isotropic phase occurring at T_{ni}.

The order parameter, defined in equation 1.1, has limits of $-0.5 \leq Q \leq 1.0$. [12] These limits occur at $\beta = 90°$ and $\beta = 0°$ respectively. A value of $Q = 1$ describe a phase with perfect ordering along the nematic director. A value of $Q = 0$ describes a randomly ordered (isotropic) phase. Values of Q between 0 and 1 describe a phase which has ordering along the director and as $Q \to 1$ the angular deviation of the molecules from the overall nematic director reduces. Negative values of Q describe a phase where, on average, the molecules are randomly aligned in the plane 90° to the nematic director; an illustration of this is shown in figure 1.4. [7, 12] Whilst a negative order parameter ($Q < 0$) is mathematically possible, there are few experimental studies investigating negative order parameters in low molar mass liquid crystals. However, evidence

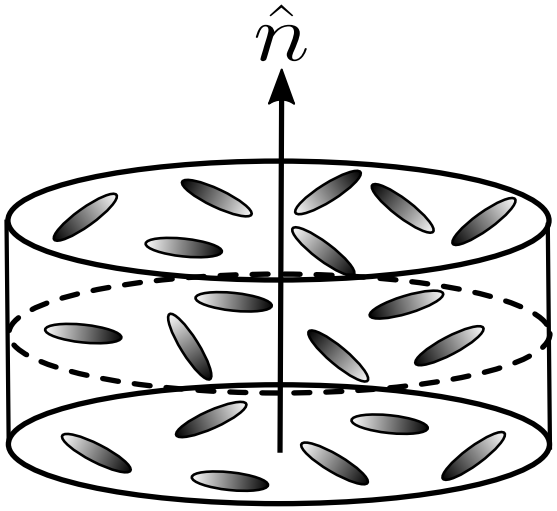

Figure 1.4: Illustration of a nematic phase with a negative order parameter.

of a negative order parameter has been observed in liquid crystal elastomers. [1, 13]

The scalar order parameter, Q, provides a reasonably good description of the state of order for most low molar mass nematic liquid crystals. However, it is often useful to introduce higher rank order parameters to more fully describe the true distribution of the molecules in a phase. These higher rank order parameters, along with the biaxial order parameters, will be discussed in chapter 2.

1.2 Polymers and conventional elastomers

Polymers are long flexible chains comprised of repeating units called 'monomers'. [14] The physical behaviour of polymeric materials is vast and depends on many parameters, including but not limited to: chain length; backbone chemistry; crystallinity and molecular orientation. [15] Consistently polymeric materials are 'viscoelastic', and in addition to the many structural and chemical considerations outlined above, the physical behaviour of a polymeric material is dependent on environmental factors such as temperature, frequency, pressure, and the magnitude of the imposed stress or strain. [15] Polymeric materials can be considered macromolecules, consisting of monomers, with complex dynamic behaviour. [16]

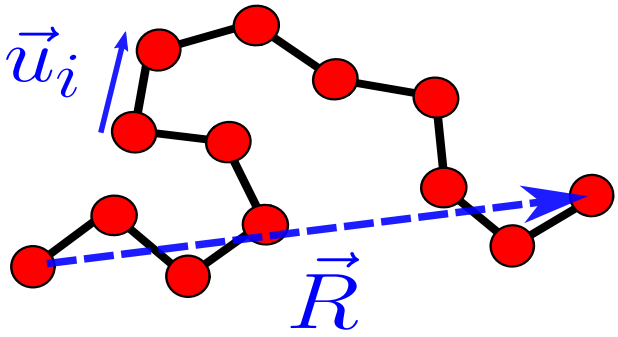

Figure 1.5: Illustration of a polymer, with freely rotating bonds, behaving as a random walk. $\vec{R}$ is the end-to-end vector, $\vec{u}_i$ is the vector between the i_{th} freely rotating bond and the $i_{\text{th}+1}$ freely rotating bond.

An 'elastomer' is a network of polymers formed either via chemical or physical cross-links. The presence of cross-links in the network prevent the polymeric chains from flowing relative to each other and generally allows elastomeric materials to have large recoverable (i.e. elastic) strains. [17] Models describing the dynamic behaviour of polymeric and elastomeric materials are discussed below. These are introduced as they are relevant to understanding some of the dynamic behaviour of LCEs.

1.2.1 Static conformation of a polymer chain

An 'ideal' polymer chain is a chain in which there are no interactions between the segments within the chain. Let us consider an ideal chain consisting of freely jointed segments a shown in figure 1.5. In the 'freely jointed chain' model the vector between two freely jointed segments is given by $\vec{u}_i$ and the end-to-end vector, $\vec{R}$, is the distance between the two ends of the ideal chain which is given by: [14]

$$\vec{R} = \sum_{i=1}^{n} \vec{u}_i, \tag{1.2}$$

where n is the number of freely jointed segments of length a in the ideal chain. The ensemble average of the end-to-end vector, $\langle \vec{R} \rangle$, for the freely jointed chain

is 0, however, the mean square of the end-to-end vector is non-zero: [14]

$$\langle \vec{R}^2 \rangle = \sum_{i=1}^{n} \sum_{j=1}^{n} \langle \vec{u}_i \cdot \vec{u}_j \rangle = a^2 \sum_{i=1}^{n} \sum_{j=1}^{n} \langle \cos \theta_{ij} \rangle, \tag{1.3}$$

where θ_{ij} is the angle between i_{th} and j_{th} chain segment. In the freely jointed chain model, it is assumed that the segments can take any angle and there are no interactions between segments. Therefore, there are no correlation between the angle of i_{th} and $i_{\text{th}+1}$ bond; that is to say that $\langle \cos \theta_{ij} = 0 \rangle$ for $i \neq j$ and $\langle \cos \theta_{ij} \rangle = 1$ for $i \neq j$. [14] The mean square end-to-end vector, $\langle \vec{R}^2 \rangle$, is therefore given by:

$$\langle \vec{R}^2 \rangle = a^2 n = aL, \tag{1.4}$$

where $L = an$ is the 'contour length' of the polymer. Note that a real isotropic polymer occupies 3D space, therefore, the end-to-end vector in the i_{th} dimension is given by $\langle \vec{R}_i^2 \rangle = \frac{1}{3} \langle R^2 \rangle = \frac{1}{3} aL$.

For an ideal chain is it assumed that there are no correlations between segments, however, in reality the bond angles of neighbouring segments have some correlations. [14] Therefore, for the i_{th} segment the summation of $\langle \cos \theta_{ij} \rangle$ over all over segments converges to a finite value, C_i': [14]

$$C_i' = \sum_{j=1}^{n} \langle \cos \theta_{ij} \rangle, \tag{1.5}$$

and the mean square end-to-end vector can be rewritten as: [14]

$$\langle \vec{R}^2 \rangle = a^2 \sum_{i=1}^{n} C_i' = a^2 n C_n, \tag{1.6}$$

where C_n is the average value of C_i' over all segments also known as 'Flory's characteristic number': [14]

$$C_n = \frac{1}{n} \sum_{i=1}^{n} C_i', \tag{1.7}$$

which converges to a steady value of C_∞ for an infinitely long chain. The value of C_∞ quantifies the local chain stiffness of the polymer.

Over long enough distances the bond angles of segments are uncorrelated as is assumed in the freely jointed chain model. The 'equivalent freely jointed chain' model divides the chain into N segments of length b known as the *Kuhn length*. The Kuhn length is comparable to the length scale at which bond angle correlations are negligible. The contour length of the polymer remains the same and can be defined in terms of the Kuhn length: [14]

$$L = Nb. \tag{1.8}$$

The mean square end-to-end vector of the polymer chain is: [14]

$$\langle \vec{R}^2 \rangle = Nb^2 = a^2 n C_\infty, \tag{1.9}$$

and the Kuhn length b is: [14]

$$b = \frac{a^2 n C_\infty}{L} = \frac{\langle \vec{R}^2 \rangle}{L}. \tag{1.10}$$

It is useful to define the end-to-end distance of the chain:

$$R_\mathrm{d} = \sqrt{\langle \vec{R}^2 \rangle} = bN^{1/2}. \tag{1.11}$$

1.2.2 Rouse model

The Rouse model attempts to describe the dynamic behaviour of a polymer, in a melt, by picturing the polymer as a collection of beads connected in series by Hookean springs as shown in figure 1.6. In the Rouse model hydrodynamic interactions between the beads are ignored. [14, 18] The beads in a Rouse chain move via Brownian motion and the motion of bead is resisted by a drag force, from the neighbouring beads, dictated by a coefficient of friction (ζ). [14, 16] The total coefficient of friction of the Rouse chain is the sum of the coefficients of friction of each bead. Hence for a Rouse chain of N beads, the coefficient friction is: [14]

$$\zeta_R = N\zeta. \tag{1.12}$$

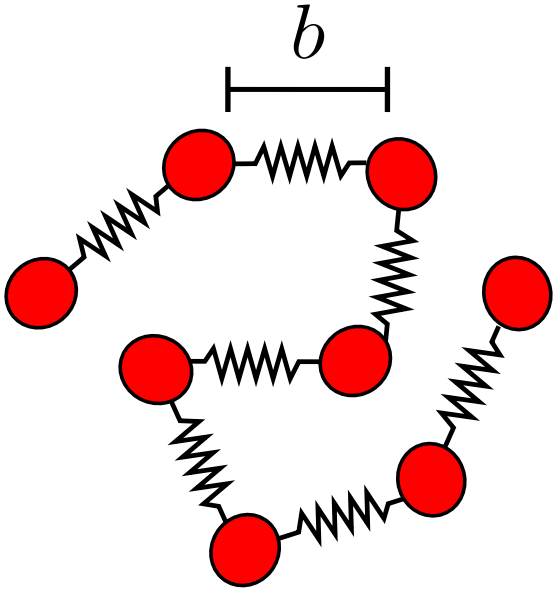

Figure 1.6: Schematic of a Rouse chain.

The beads follow the Einstein relationship for diffusion via Brownian motion thus the diffusion coefficient of the chain is defined as: [14]

$$D_R = \frac{k_B T}{\zeta_R}, \tag{1.13}$$

where $k_B T$ is thermal energy. The self-diffusion time of the Rouse chain (i.e. the time taken for the Rouse chain to diffuse a distance equal to its end-to-end distance, R_d) is given by: [14]

$$\tau_R = \frac{L^2}{D_R} = \frac{\zeta}{k_B T} N R_d^2, \tag{1.14}$$

where R_d is the end-to-end distance of the Rouse chain. τ_R is often called the 'Rouse time'. Substituting $R_d = bN^{1/2}$ into equation 1.14 leads to the following: [14]

$$\tau_R = \frac{1}{6\pi^2} \frac{\zeta b^2}{k_B T} N^2, \tag{1.15}$$

where the $1/6\pi^2$ term comes from the complete derivation of the Rouse model for an ideal chain by Rouse. [14, 18]

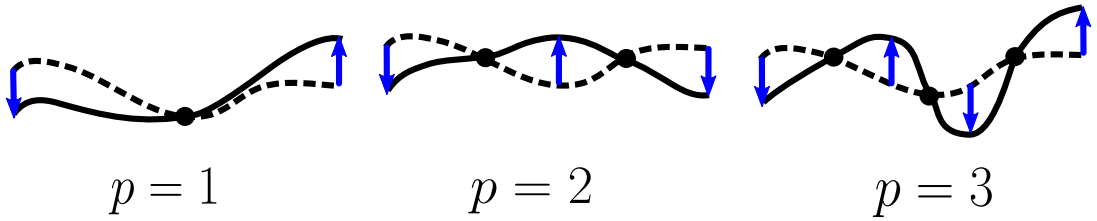

Figure 1.7: Different modes of motion for a Rouse chain.

The Rouse chain can move in p modes of motion, with different time-scales of relaxation, the longest time-scale being τ_R. A depiction of the Rouse modes is seen in figure 1.7; the physical nature of the modes is related to the number of segments involved in the motion i.e. when $p = 1$ the ends of the rouse chain move in opposite directions (normal to the molecular backbone) and the centre of the polymer chain is stationary. [19] For the p_{th} mode there are $p+1$ segments involved in a motion. The shortest time-scale for the Rouse-chain, τ_0, or the 'molecular relaxation time' occurs when $p = N$:

$$\tau_0 = \frac{1}{6\pi^2}\frac{\zeta b^2}{k_{\text{B}}T}, \tag{1.16}$$

and the time-scale of the p_{th} relaxation is therefore given by:

$$\tau_p = \tau_0 \left(\frac{N}{p}\right)^2. \tag{1.17}$$

Hence, the Rouse model predicts that on time-scales longer than τ_R, the whole chain diffuses and the behaviour is that of a fluid. [14] On time-scales shorter than τ_0 even the smallest units of the chain cannot move diffusively and instead the chain displays an elastic response. [14] A viscoelastic regime is therefore predicted by the Rouse model for $\tau_0 < t < \tau_R$. The viscoelastic behaviour will be dictated by how many relaxed modes are in the Rouse chain. At $t = \tau_p$ there will be p unrelaxed modes which contribute to the elastic modulus. It is assumed that each unrelaxed mode contributes equally to the elastic modulus and that each mode is of the order of $3k_{\text{B}}T$. [14, 20] Hence, at τ_p the elastic modulus of

the Rouse chain is: [14, 20]

$$E(\tau_p) = \frac{3k_{\mathrm{B}}T}{b^3}\phi\frac{p}{N}. \tag{1.18}$$

where ϕ is the volume fraction of N/p molecules. Rearranging equation 1.17 for p and substituting into equation 1.18 leads to:

$$E(t) = \frac{3k_{\mathrm{B}}T}{b^3}\phi\frac{p}{N}\left(\frac{t}{\tau_0}\right)^{\frac{1}{2}} \quad \text{for} \quad \tau_0 < t < \tau_R. \tag{1.19}$$

where $E(t)$ is the elastic modulus in the time-domain. $E(t)$ can be transformed into the frequency domain, [14, 21] leading to the following power-law scaling:

$$E'(\omega) \approx E''(\omega) \propto \omega^{\frac{1}{2}} \quad \text{for} \quad \frac{1}{\tau_R} < \omega < \frac{1}{\tau_0}, \tag{1.20}$$

where ω is the angular frequency and E' and E'' are the storage and loss elastic modulus which, as discussed in chapter 7, quantify the energy stored and lost in a material during an oscillatory motion, respectively. Thus, the Rouse model predicts that the dynamic response of an unentangled polymer is of the form $E' \approx E'' \propto \omega^{0.5}$. [14]

1.2.3 Entanglements

The Rouse model introduced in section 1.2.2 describes an unentangled ideal polymer with no hydrodynamic interactions. [14, 18] However, sufficiently long and concentrated polymers will experience topological constraints imposed by neighbouring polymers in the form of entanglements. In the tube model, these complicated topological constraints are modelled as an effective tube surrounding the polymer. [22, 23] See figure 1.8 for a schematic of the tube model. In order to move over large distances the polymer must move out of the tube in a snake-like motion. This snake-like motion is often referred to as '*reptation*'. Reptation occurs through fluctuations of the entrapped chain along a primitive path through the tube, shown in red on figure 1.8. Additionally, the shape of the effective tube can change by two mechanisms: [24] (i) the polymer reptates along a path leaving part of the old tube and entering part of a new tube; (ii) the tube itself

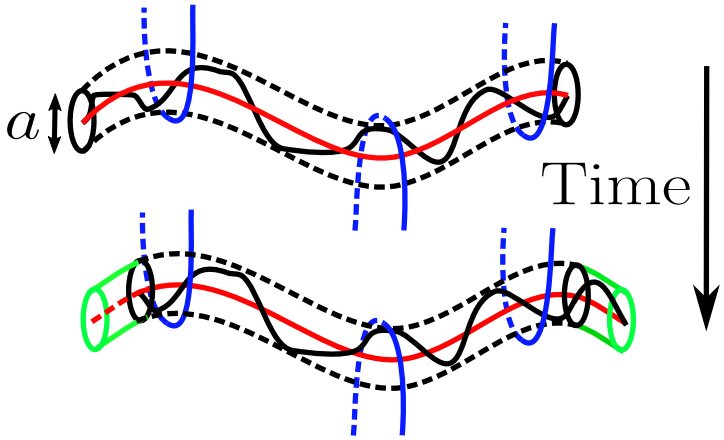

Figure 1.8: Schematic of the tube model. A polymer is held within an effective tube (dotted black line) of diameter a due to entanglements (blue line). The polymer can leave a tube via longitudinal motions (reptation) along the primitive path (red line).

fluctuates due to the thermal fluctuation of the neighbouring polymers which form the tube. The motion of the chain within the effective tube is Rouse-like. The diffusion coefficient is equivalent to that of the Rouse model and in the case of the reptation model is called the 'curvilinear diffusion coefficient' due to the motion occurring along the curved primitive path. [14] The curvilinear diffusion coefficient is therefore:

$$D_c = \frac{k_b T}{\zeta_R} = \frac{k_B T}{N\zeta}. \tag{1.21}$$

The relevant-time scale for entanglements is the time it takes for the polymer to reptate the length of the tube that surrounds it, τ_{rep}, which is predicted by the tube model as:

$$\tau_{\text{rep}} \propto N^3, \tag{1.22}$$

which is a slightly weaker prediction than the $\tau_{\text{rep}} \propto N^{3.4}$ found experimentally. [14, 23] This discrepancy is thought to be related to: [21] (i) the fluctuations of the tube length due to the contracting and stretching of the chain ends of the reptating chain and (ii) motion of the tube itself which results in the release of some of the topological constraints on the reptating chain. In linear concentrated

polymers, the presence of the power law scaling:

$$E'' \propto \omega^{-a_{\text{rep}}} \quad \text{with } 0 < a_{\text{rep}} < 1/4, \tag{1.23}$$

in the low frequency dynamic response is evidence of reptation behaviour. [23] For elastomeric materials, due to the presence of cross-links, relaxation of the pendant chains occurs through arm retraction which modifies the power-law scaling in equation 1.23. [25]

1.3 Glass formation

A 'glass' or 'glassy state' is a non-equilibrium amorphous state of matter which is typically formed by super-cooling a liquid (i.e. avoiding crystallisation). [26] The glass transition is a kinetic process which can be observed by the rapid divergence of the viscosity, η, of a liquid on cooling. In section 1.3.1 the dynamic processes involved in glass formation are discussed.

1.3.1 Dynamics of the glass transition

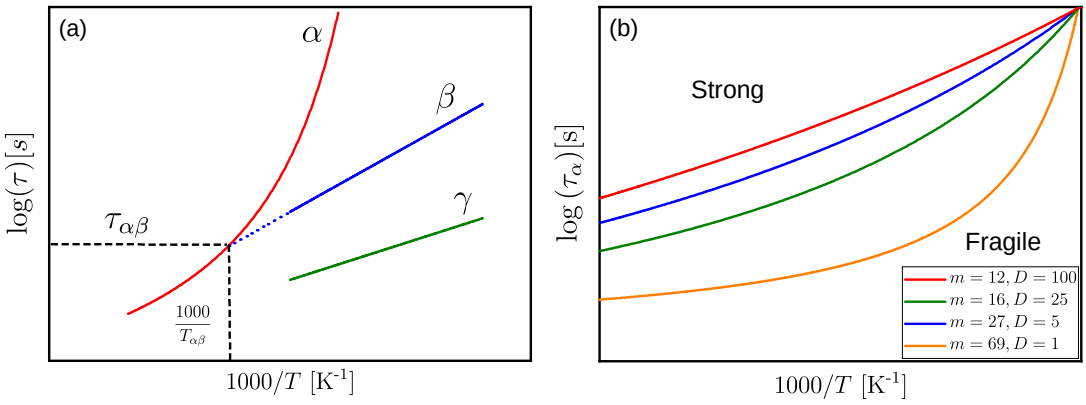

Figure 1.9: (a) Arrhenius plot ($\log(\tau)$ against $1000/T$) showing the behaviour of the α relaxation (VFT-like) and the β and γ relaxation (Arrhenius-like). (b) Shape of $\tau_\alpha(T)$ for various values of m.

The glass transition can be discussed in terms of the molecular relaxations involved in glass formation. The α relaxation, or often the 'structural relaxation', of a glass-forming material, slows down dramatically upon cooling. The α relaxation is the primary relaxation in glass formation. For molecular liquids, the time-scale of the α relaxation, τ_α, is related to the viscosity of the material by the equation: [16]

$$\eta = G_\infty \tau_\alpha, \tag{1.24}$$

where G_∞ is the high frequency shear modulus. Traditionally the glass transition temperature, T_g, for molecular liquids is defined as the point at which $\eta \sim 10^{12}$ Pa·s. [16] For molecular liquids G_∞ is of the order of 10 GPa, therefore, the characteristic time-scale of the α relaxation at T_g is $\tau_\alpha(T_\mathrm{g}) \approx 100$s. [16] The definition of the glass transition as $\tau_\alpha(T_\mathrm{g}) \approx 100s$ is used for polymeric materials as the relationship between η and τ_α depends on the molecular weight of the polymer. [16]

Glass forming materials will typically show, in addition to the α relaxation, other secondary molecular relaxations which are named with Greek letters in order of decreasing relaxation time-scale (i.e. $\tau_\alpha > \tau_\beta > \tau_\gamma$). The presence of the 'Johari-Goldstein' β relaxation is often believed to be a generic feature of glass formation. [16] The characteristic time-scale of the β relaxation, in the glassy state, is well-described by an Arrhenius equation:

$$\tau_\beta = \tau_0 e^{\Delta E_\mathrm{A}/k_\mathrm{B}T}, \tag{1.25}$$

where, τ_0 is a microscopic relaxation time, ΔE_A is the activation energy and k_B is the Boltzmann constant. Thus, within the glassy state, the β relaxation can be characterised by a single energetic barrier. [27] For simple molecular glass formers it is found that the activation energy of the Johari Goldstein β relaxation is $\Delta E_A \approx 24\, R\, T_\mathrm{g}$, where R is the universal gas constant. [28, 29] The γ relaxation (and the further secondary relaxations) are also typically well described by an Arrhenius equation in the glassy state. [27, 30] In polymeric materials the β relaxation has been attributed to intramolecular motion. [19] However, the β relaxation was also present in studies of molecular glass-formers

for which there is no intramolecular motion, therefore, at least in these systems the β relaxation must be related to intermolecular motion. [16, 31]

The temperature dependence of τ_α is typically non-Arrhenius and the energy barrier of the α relaxation increases on decreasing T. $\tau_\alpha(T)$ is often described using the empirical Vogel-Fulcher-Tammann (VFT) equation: [16, 27]

$$\tau_\alpha = \tau_0 e^{DT_0/(T-T_0)} \tag{1.26}$$

where τ_0 is a microscopic relaxation time, T_0 is the temperature at which τ_α tends to infinity and D is a parameter which controls the extent of deviation of τ_α from Arrhenius behaviour. The temperature dependent behaviour of α, β and γ are shown in figure 1.9(a). Approaching T_g, on cooling, the molecular motions of the α relaxation become increasingly cooperatively and there is an increase in the number of molecules involved in this motion. [30] At T_g the size of the cooperative motion is of the order of a few hundred polymer segments. [32] Additionally, upon cooling the motions of the α relaxation are markedly more 'dynamically heterogeneous'; [30] dynamic heterogeneity referring to spatial regions within a glass-forming material with different characteristic time-scales of relaxation. [30]

It is often useful to determine the fragility parameter, m, of a glass-former which is defined as: [27]

$$m = \left.\frac{d(\log \tau_\alpha)}{d(T_g/T)}\right|_{T=T_g}. \tag{1.27}$$

A 'fragile' glass former has a large value of m (small D) and is highly sensitive to changes in T near T_g while a 'strong' glass former has a small value of m (large D) and is typically Arrhenius-like at $T \approx T_g$. [33] A plot of $\tau_\alpha(T)$ for various fragilities is shown in figure 1.9(b).

1.3.2 Cross-over in dynamic behaviour

The characteristic time-scale of the α relaxation, $\tau_\alpha(T)$, can be described with a VFT equation for extended temperatures. However, a cross-over in dynamic behaviour of the α relaxation is often observed. [27] To study the subtle changes in dynamics it is useful to perform derivative analysis, first suggested by Stickel

et al. [34, 35], on the $\tau_\alpha(T)$ data. Stickel analysis linearises a VFT behaviour by plotting the derivative of $\tau_\alpha(T)$, Z: [34, 35]

$$Z = \left(\frac{d \log \left(\tau_\alpha(T) \right)}{d \left(1000/T \right)} \right)^{-\frac{1}{2}}, \tag{1.28}$$

against $1000/T$. The gradient in a 'Stickel plot' describes the evolution of the slope of $\tau_\alpha(T)$ with T in an Arrhenius plot; [34, 35] $\tau_\alpha(T)$ with behaviour closer to Arrhenius behaviour has a small (negative) gradient and $\tau_\alpha(T)$ with significant non-Arrhenius behaviour has a large (negative) gradient, therefore, a change in the gradient in a Stickel plot represents a change in VFT behaviour. When the gradient of the Stickel plot is 0, τ_α is described by the Arrhenius equation.

In molecular glass-formers there are typically two cross-overs of $\tau_\alpha(T)$ observed. [27] The first, upon heating from the glassy phase, is a cross-over from one VFT dependence to another VFT dependence with a greater deviation from Arrhenius behaviour. The temperature of this cross-over is typically defined as T_B and often occurs at a similar temperature as the bifurcation of the α relaxation and the β relaxation, $T_{\alpha,\beta}$. [27, 36] Note that $T_{\alpha,\beta}$ is typically determined by extrapolating $\tau_\beta(T)$ as the β relaxation is often not observable at these temperatures. [16] In addition to the dynamic cross-over occurring close to the bifurcation of the α relaxation and Johari-Goldstein β relaxation, T_B is found to scale with the glass transition temperature with typical values $T_\mathrm{B} = 1.2 - 1.6 \times T_\mathrm{g}$ (depending on the fragility of the system [37]) and is also found to signify a change in diffusion behaviour in materials. [27] The second cross-over in dynamic behaviour occurs at $T_\mathrm{A} > T_\mathrm{B} > T_\mathrm{g}$ and is a cross-over from VFT behaviour to Arrhenius behaviour which occurs at high temperatures. [27] This cross-over in behaviour is associated with a reduction in the need for cooperative motions in the α relaxation. In polymeric glass formers the cross-over behaviour is similar to that of molecular glass formers. However, for sufficiently long polymers the cross-over behaviour at T_B is reduced or completely lost. [32, 38] Additionally, whilst in principle T_A (i.e. the cross-over from VFT to Arrhenius behaviour at high T) should be observed in polymeric materials, this is often a higher temperature than the polymeric samples degradation temperature and therefore not experimentally observable. [39]

1.4 Liquid crystal elastomers

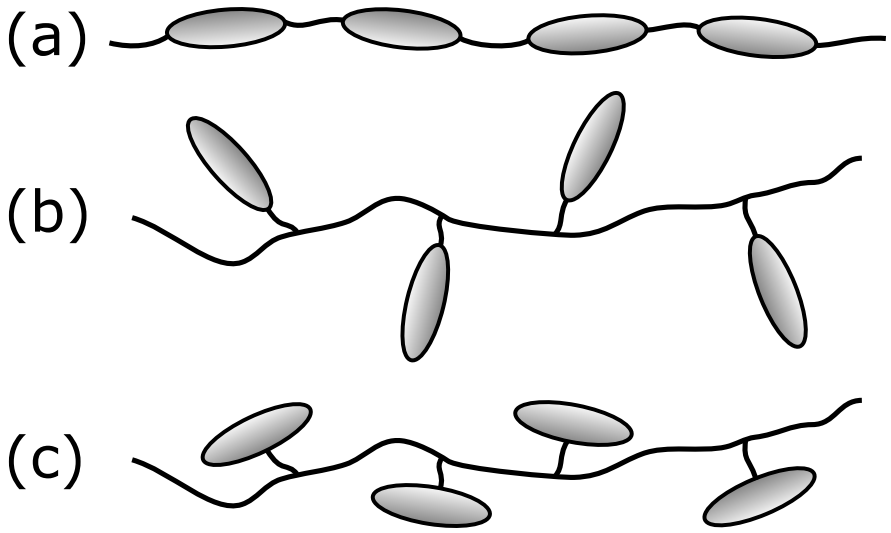

Figure 1.10: Illustration of (a) main-chain attachment, (b) end-on side-chain attachment and (c) side-on side-chain attachment.

Liquid crystal elastomers (LCEs) are a class of materials which combine the orientational order and anisotropic properties of LCs with the rubber-like elasticity of conventional elastomers. [40] LCEs are weakly cross-linked networks containing mesogenic units and, unlike low molar mass liquid crystals, LCEs do not flow. The incorporation of mesogenic units into a rubbery network leads to an array of remarkable properties observed in LCEs, [40, 41] some of which are outlined in sections 1.4.3-1.4.7. There is a particular focus on the mechanical behaviour of LCEs under deformation, the theories relating to this behaviour will be introduced more formally in chapter 2.

1.4.1 Polymer conformation and anisotropy in liquid crystal elastomers

Mesogenic units can be incorporated within the polymer chain (main-chain attachment) or dangling off the polymer chain as a pendant chain (side-chain attachment). [40] A side-chain attachment can occur at the end of the mesogenic unit

(end-on attachment) or on the side of the mesogenic unit (side-on attachment). Illustrations of a polymer chain containing mesogenic units for the different attachments is show figure 1.10; when cross-linked these will form a main-chain LCE (MCLCE), an end-on side-chain LCE (SCLCE) or a side-on SCLCE, respectively.

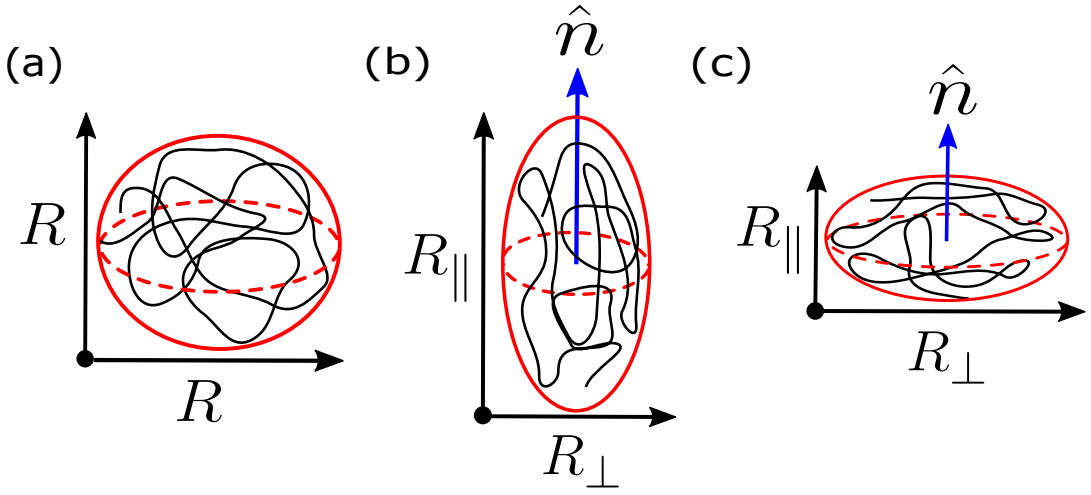

Figure 1.11: Illustration of (a) an isotropic (spheroid) polymer conformation, (b) a prolate (elongated along the nematic director) polymer conformation and (c) an oblate (elongated perpendicular to the nematic director) polymer conformation.

The incorporation of mesogenic units causes the average polymer conformation to elongate in a preferential direction. [40] The elongation of the polymer conformation can occur parallel (prolate conformation) or perpendicular (oblate conformation) to the nematic director, both these conformations are shown in figure 1.11. A prolate polymer conformation typically occurs in MCLCEs and side-on SCLCEs, an oblate polymer conformation typically occurs in end-on SCLCEs, and an isotropic polymer conformation is typically seen in conventional isotropic elastomers and LCEs in the isotropic phase. [42–45] The extent of anisotropy in the network can quantified through the backbone anisotropy parameter, r:

$$r = \left(\frac{R_{\parallel}}{R_{\perp}}\right)^2 = \frac{l_{\parallel}}{l_{\perp}}, \tag{1.29}$$

where $R_{\parallel/\perp}$ is the radius of gyration parallel or perpendicular to the nematic di-

rector and $l_{\parallel/\perp}$ is the step length parallel or perpendicular to the nematic director. For a prolate conformation $r > 1$, for an oblate conformation $r < 1$, and for an isotropic conformation $r = 1$. [40] The elongation of the polymer backbone can also be quantified through the backbone order parameter, Q_b, which is similar to the nematic order parameter, Q; however, Q_b is a measurement of averaged preferential ordering of the individual backbone units in a given direction with respect to the backbone director. [40] The interplay between the state of the mesogenic units, the average conformation of the polymer and the behaviour of the macroscopic material is often referred to as 'LC-backbone coupling'. [40] As a general rule, MCLCEs have greater LC-backbone coupling than SCLCEs as the mesogenic units are incorporated directly into the backbone. Because of this, main-chain LCEs typically have large values of r. [46] In SCLCEs, side-on SCLCEs typically have greater LC-backbone coupling than end-on SCLCEs, however, this is dependent on the spacer length amongst other things. [44, 46]

1.4.2 Types of liquid crystal elastomers and alignment

Important to many of the physical properties of the LCEs is the type and extent of nematic alignment present in the sample. An isotropic LCE is one which is cross-linked in the isotropic phase, or elevated above T_{ni}, there is no nematic ordering and the averaged polymer conformation is spherical. [45] Polydomain LCEs have domains of nematic ordering; however, macroscopically these domains are randomly ordered. Polydomain LCEs can be considered either nematic genesis polydomain LCEs (nPLCEs) or isotropic genesis polydomain LCEs (iPLCEs). [47, 48] nPLCEs are formed when an LCE is cross-linked in the nematic phase with no attempts to align the mesogenic units. iPLCEs are formed when an LCE is cured in the isotropic phase and cooled below T_{ni}. A monodomain nematic LCE has nematic alignment with a single macroscopic director. Generally, a monodomain nematic LCE can be formed in one of two ways: (i) cross-linking of an aligned nematic liquid, for example, via UV polymerisation [49, 50]; (ii) the partial cross-linking of an isotropic liquid to form an isotropic gel which is then aligned further before completion of cross-linking. [51] The (ii) synthesis route was used, for example, in the 'Finkelmann' procedure which was the first

example of a monodomain nematic LCE. [51] In certain nematic LCEs, elevating the temperature will not result in a narrow-temperature ranged, weakly-first order transition from a nematic phase to an isotropic phase as is observed in low molar mass LC materials. Instead, the transition is a continuous 2^{nd} order transition from an ordered nematic state to a very low order state with some inherent nematic ordering known as the 'paranematic' phase. [52, 53] This is very similar to a conventional LC which is held in a large magnetic or electric field and elevated above T_{ni}. [54–56] The cause of the nematic-paranematic transition is thought to be due to the existence of a 'mechanical field' in the LCE due to internal stresses and heterogeneities within the LCE sample. [57, 58] An LCE sample which exhibits a paranematic phase is said to be 'supercritical'. [57]

1.4.3 Stress-optical coupling and nematic order induced actuation

Coupling between the backbone order and the nematic order means that macroscopically straining an LCE sample causes a change in the ordering of the mesogenic units which is often observed as change or emergence of birefringence colours. [59–62] The change in optical properties (or the nematic order parameter) of an LCE with the application of external mechanical stresses is known as stress-optical coupling. Conversely, changing the nematic order of the mesogenic units will cause a macroscopic change in the shape of the LCE. Changing the nematic order of the LCE is typically achieved by changing temperature or by inducing the cis-to-trans isomerisation of azo-benzene functionalised mesogenic units with the application of a specific wavelength of light. [42, 63]

1.4.4 Mechanical deformations in mono-domain nematic liquid crystal elastomers

Of particular interest to this thesis is the behaviour of nematic LCEs under mechanical deformation. When an LCE is strained perpendicular to the director the LCE deforms via the semi-soft elastic (SSE) response [40, 64] or via a mechanical

Fréedericksz transition (MFT). [2, 40, 65] These two behaviours are introduced below and discussed in more detail in 3.

1.4.5 Semi-soft elasticity

When a strain is applied perpendicular to the nematic director some LCEs will display semi-soft elasticity, whereby there is a very low cost of elastic deformation accompanied by the continuous rotation of the nematic director to align with the axis of strain. [40] The low cost of elastic deformation is due to the ability for the polymer chains to rotate without changing configurational entropy. [66] In the ideal soft elastic response, the rotation of the director begins the instant that a strain is applied and cost of deformation (i.e. the gradient of the stress-strain curve) is 0. [40, 67] However, early experiments by Küpfer revealed the response in LCEs is actually 'semi'-soft elastic (SSE). [68] In the SSE response, the gradual rotation of the director occurs only after a threshold strain is reached. Before the threshold strain is reached, the director remains perpendicular to the strain axis and the load curve has a positive and linear gradient. At the threshold strain, the director begins to rotate and the stress-strain curve has a small (but none 0) gradient (i.e. low cost of deformation). [40] Once the director has completed its rotation towards the strain axis, there is a re-stiffening of the stress-strain response. The SSE response observed in LCE is due to 'non-idealities' in the LCE. [40] Verway *et al.* suggested that the 'non-idealities' can arise from compositional fluctuations within the LCE or due to the presence bulky mesogenic-like cross-linkers. [67] The rotation of the nematic director often occurs via counterrotating domains parallel to the stain axis, known as 'stripe domain', which minimise shear effects at the clamped regions of the LCE sample. [40, 69]

1.4.6 Mechanical Fréedericksz transition

In addition to the SSE, an LCE when strained perpendicular to the nematic director may deform via the 'mechanical Fréedericksz transition' (MFT). The MFT is characterised by a sharp rotation of the nematic director at a specific critical strain. [2, 66] Originally, the MFT was only reported by the Mitchell group and the stress-strain curve associated with this behaviour was unknown

[65, 70]; however, there was evidence of a change in the nematic order of the LCE, Q, as a function of applied strain. [71] Later, Mistry *et al.* reported the stress-strain response of an LCE deforming via the MFT revealing it to be non-linear elastic behaviour similar to the shape of the stress-strain curve of the SSE response. [2]

1.4.7 The auxetic response in liquid crystal elastomers

Auxetic materials are materials that have a negative Poisson's ratio. The auxetic response is a thickening of one or more of the transverse axes of the material that occurs when a longitudinal elongation is applied. Strictly, a material is said to be *strongly auxetic* if the thickening occurs in *both* transverse axes or *partially auxetic* if the thickening occurs in just *one* its transverse axis. [72, 73] The change in the dimensions of a material under deformation can be quantified via the Poisson's ratio (ν) which is defined as: [74]

$$\begin{aligned} \nu_{xz} &= \frac{\epsilon_z}{\epsilon_x} = \frac{\Delta L_z \times L_x}{L_z \times \Delta L_x}, \\ \nu_{xy} &= \frac{\epsilon_y}{\epsilon_x} = \frac{\Delta L_y \times L_x}{L_y \times \Delta L_x}, \end{aligned} \tag{1.30}$$

where ϵ_i is the strain, L_i is the initial length of the material and ΔL_i is the change in length in the i_{th} dimension, respectively. For an isotropic material $\nu_{xz} = \nu_{xy} = \nu$; the limits of ν for an isotropic material are $-1 < \nu < 0.5$ with the ideal isotropic response being $\nu = 0.5$ (i.e. volume conserving). [74] For an anisotropic material $\nu_{xz} \neq \nu_{xy}$ and the value of ν_{ij}, in an ideal anisotropic elastic material, has no limits provided the ν_{ji} value acts to conserve volume. [72]

Auxetic materials can be synthesised by designing patterns into conventional materials (i.e. positive Poisson's ratio in bulk) to elicit a negative Poisson's ratio response; such auxetic materials are known as 'structural auxetic materials' and often incorporate porosity into the material or re-entrant structures. [75–77] Structural auxetic materials, due to their porous nature, have an inherent reduction in mechanical integrity when compared to its constituent materials in bulk. [76] Naturally occurring molecular auxetic materials (i.e. intrinsic negative Poisson's ratio in bulk) exist, however, they are typically crystalline solids [75–77]

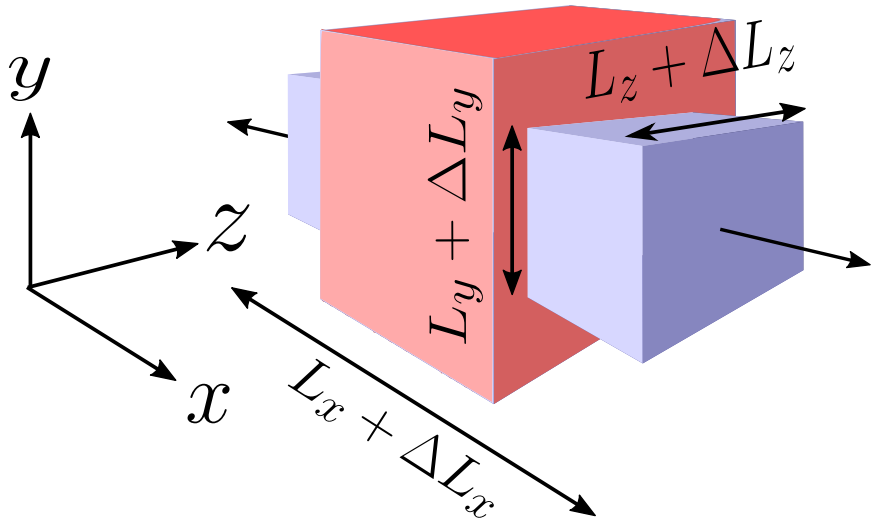

Figure 1.12: Schematic showing the geometries and length changes when defining the Poisson's ratio. The sample is elongated along x and contractions occur in the transverse axis to conserve volume. Note, that for an auxetic material we expect an expansion in one or more of the transverse axes.

and, as such, have limitations in regard to their operational strain range and have large Young's moduli thus limiting potential applications.

Mistry *et al.* was the first to report a *partial* auxetic response in an LCE which occurred when the LCE was strained perpendicular to its nematic director. [1] The observed auxetic response in the nematic LCE occurs in only one axis and beyond a threshold strain (the initial response at low strains is not auxetic) making the LCE a *partial auxetic*. Figure 1.13 shows the fractional thickness of the LCE under-strain, taken from Mistry *et al.*, showing the partially auxetic response. The onset of the *synthetic molecular auxetic* response coincided with the discontinuous rotation of the nematic director during the MFT, thus, suggesting that these two behaviours are somehow related. [1, 2] Insight into the change in nematic ordering was investigated by the change in birefringence colours, as a function of applied strain, via cross-polarised microscopy. This revealed that the MFT response is associated with a decrease in birefringence colours and therefore a decrease in nematic ordering. [1, 2] It was found that the region where the auxetic response occurs coincides with a region of zero birefringence observed in

the plane of investigation. This could suggest that the mesogenic units are in a state of negative ordering. [1, 2] Additionally, whilst not reported at the time, re-analysis of data from the Mitchell group also appears to suggest a *partial* auxetic response occurring. [70] In the case of the Mitchell group, a decrease in nematic order was confirmed via X-ray diffraction. Both LCEs displaying an auxetic response (confirmed in the case of Mistry, suggested by the Mitchell group) have acrylate backbones, display an MFT response and have evidence of a change in the nematic ordering as a function of strain. [1, 70] It therefore appears that the MFT response is related to the auxetic response in LCEs.

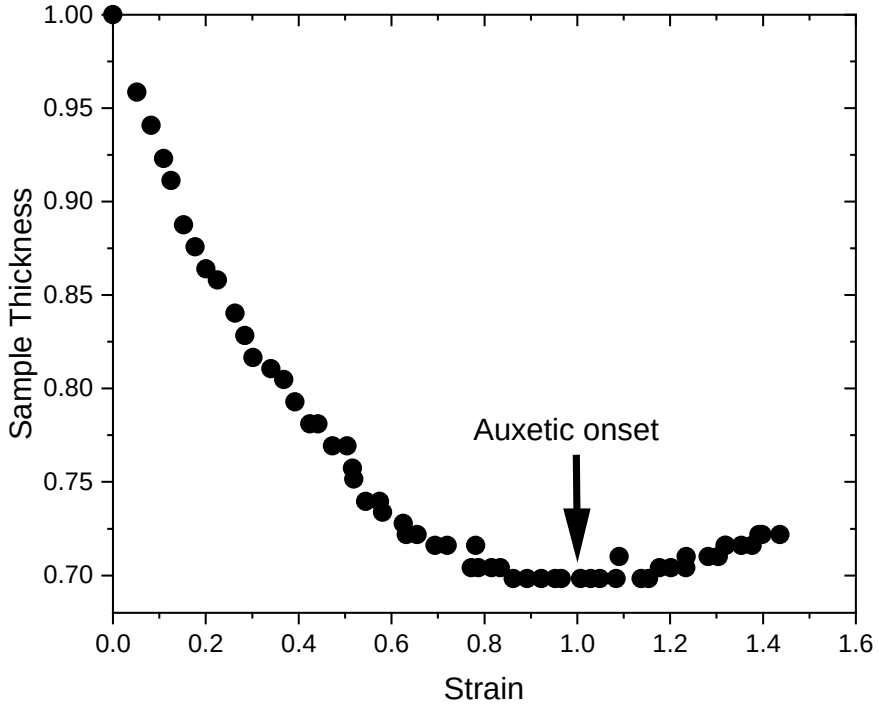

Figure 1.13: Sample thickness as a function of applied strain. The partial auxetic response observed in the nematic LCE happens after a strain threshold is reached. Data taken from Mistry *et al.* [1]

1.5 Summary

Liquid crystal elastomers combine the behaviours of the liquid crystalline phase with the behaviours of cross-linked polymeric materials. In this chapter the liquid crystal phases are introduced with particular focus on the nematic phase and the 'scalar order parameter' is defined. The dynamic behaviour of polymeric and elastomeric materials, in the form of the Rouse model and the tube model, is discussed. The glassy phase and the molecular relaxations involved in glass formation are introduced. Finally, LCEs are discussed with a particular focus on their mechanical deformation behaviour when a strain is applied perpendicularly to the nematic director. The two key behaviours are the semi-soft elastic (SSE) response and the mechanical Fréedericksz transition (MFT) which are introduced more formally in chapter 3.

1.6 Thesis outline

Chapter 2: Orientational distribution functions and liquid crystal phases In this chapter, the orientational distribution function for the uniaxial phase and biaxial phase are described. The shape of the orientational distribution function for various values of uniaxial order is discussed.

Chapter 3: Mechanical deformation of LCEs The theoretical description of the SSE and MFT is outlined and the Trace formula is introduced in this chapter.

Chapter 4: Materials and LCE synthesis Materials and LCE synthesis The materials and synthesis steps required to produce LCEs are outlined in this chapter.

Chapter 5: Raman spectroscopy The key principles of Raman spectroscopy are described in this chapter. The experimental set-up required to determine the order parameters of liquid crystals is outlined.

Chapter 6: Broadband dielectric spectroscopy The key principles of broadband dielectric spectroscopy are described. The experimental set-up required to study dipole relaxations with broadband dielectric spectroscopy is outlined. The connection between dipole relaxations and the dynamics of glass formation is described.

Chapter 7: Rheology The key principles of rheology are described. The experimental set-up required to perform both dynamic mechanical spectroscopy and small amplitude oscillatory shear rheology are described. The time-temperature superposition principle is introduced.

Chapter 8: Order parameters of LCEs under strain: Insight into the auxetic response In this chapter, Raman spectroscopy is used to investigate the change in the order parameters of a nematic LCE under strain. A possible mechanism for the molecular auxetic response is discussed.

Chapter 9: Influence of phase on the molecular dynamics of LCEs In this chapter, the molecular dynamics of the LCE are investigated with broadband dielectric spectroscopy and rheology. The glass formation behaviour of the LCE in the isotropic and nematic phase is discussed. Additionally, the molecular relaxations present in both phases of the LCE are discussed.

Chapter 10: Effect of applied strain on the molecular dynamics of LCEs In this chapter, the effect of applied strain on the viscoelastic behaviour and the characteristic time-scale of the α relaxation of the nematic LCE is investigated. Based on the findings the proposed mechanism for the molecular auxetic response is discussed.

Chapter 11: Conclusion and outlook The overall conclusions of this thesis are discussed in this chapter. Potentially interesting future work is outlined.

Chapter 2

Theory I: Orientational distribution functions and liquid crystal phases

In section 1.1.2, the nematic LC phase is introduced and the nematic scalar order parameter, Q, is defined in equation 1.1. However, if only the Q order parameter is used the LC phase is constrained to be cylindrically symmetric with the molecule distribution following a Gaussian distribution centred about $\beta = 0$. [8] Therefore using only Q (often called 'S') to describe the order in an LC phase does not encapsulate the full orientational information of required for many materials such as smectic phases and biaxial phases. [8] It is therefore often necessary to introduce higher order terms through the orientational distribution function (ODF).

In this chapter, the ODF is defined for both uniaxial and biaxial phases and the higher rank order parameters are introduced. In particular, the significance of the 4^{th} rank uniaxial order parameter $\langle P_4 \rangle$ (or $\langle P_{400} \rangle$) on the shape of the ODF is discussed. The approach, to derive the ODF, developed by van Gurp [78] and discussed in detail by Zannoni [8, 9] is used. The ODFs in the form presented herein have been utilised by Jones *et al.* [79, 80], Southern *et al.* [81–84] and Zhang *et al.* [85–88] to determine order parameters via Raman spectroscopy. In sections 2.2 and 2.3, only cylindrically symmetric rigid molecules are considered and molecular biaxility is ignored.

2.1 The orientational distribution function (ODF)

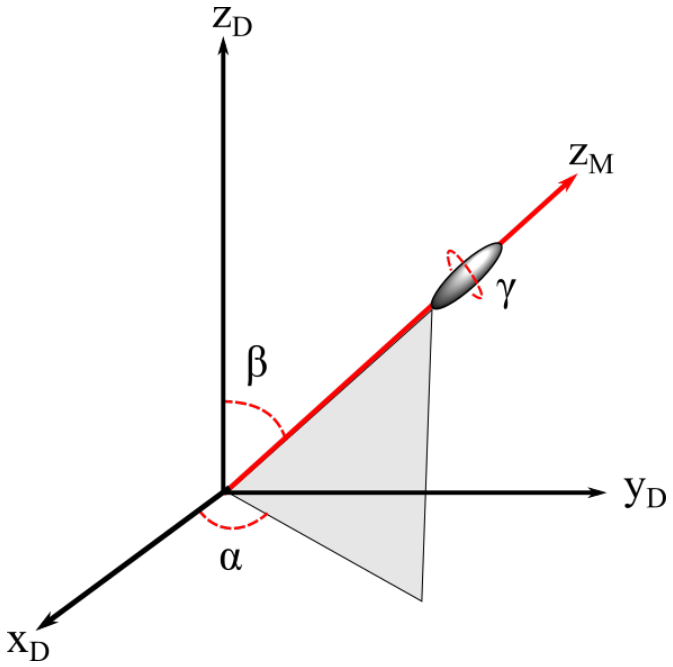

Figure 2.1: Euler angles (α,β,γ) of a single molecule within the reference frame of the nematic director (z_{D}). z_{M} is the molecular long axis which defines the orientation of the longest axis of the molecule.

Assuming that the molecules in a LC phase are completely rigid so as to not account for fluctuations in molecular shape, the orientation of a single molecule can described completely by a set of angles (α, β, γ) known as the Euler angles (figure 2.1). The orientational distribution function (ODF) is a probability distribution function which quantifies the probability of finding a molecule between (α, β, γ) and ($\alpha + d\alpha$, $\beta + d\beta$,$\gamma + d\gamma$). For the constructed ODF to be valid, the ODF must be normalised and positive for all angles such that: [8, 9, 78]

$$\begin{gathered} f(\alpha,\beta,\gamma) \geq 0 \ \text{ for all } \ (\alpha,\beta,\gamma), \\ \int_0^{2\pi}\int_0^{\pi}\int_0^{2\pi} f(\alpha,\beta,\gamma)\sin\beta d\alpha d\beta d\gamma = 1. \end{gathered} \tag{2.1}$$

On this basis, an experimentally relevant ODF can be constructed.

2.2 The uniaxial ODF

First, let us consider the cylindrically symmetric uniaxial phase consisting of cylindrically symmetric molecules. This is the simplest form of the ODF, as it is invariant to rotations in both α and γ, and can be described fully by β. Typically, in the nematic state, the ODF will be maximum at $\beta = 0$ and be greater than or equal to 0 for $\beta \neq 0$, a natural choice for the ODF is therefore a series of $\cos^{2n}\beta$ functions [8, 9, 78]. The Legendre polynomials are a set of functions with the form of $\cos^{2n}\beta$ and are given by:

$$P_L(\cos(\beta)) = \frac{1}{2^L L!}\frac{d^L}{d(\cos\beta)^L}(\cos^2\beta - 1)^L, \tag{2.2}$$

where $L = 0, 1, 2, ..., N$. The first 5 terms of the Legendre polynomials are shown below.

$$\begin{aligned} P_0 &= 1, \\ P_1 &= \cos\beta, \\ P_2 &= \frac{1}{2}(3\cos^2\beta - 1), \\ P_3 &= \frac{1}{2}(5\cos^3\beta - 3\cos\beta), \\ P_4 &= \frac{1}{8}(35\cos^4\beta - 30\cos^2\beta + 3). \end{aligned} \tag{2.3}$$

The ODF can then be written as a normalised series of the Legendre polynomials:

$$f(\beta) = \sum_{L=0}^{\infty} a_L P_L(\cos\beta), \tag{2.4}$$

where a_L is a normalisation constant.

When a measurement of a parameter is made which is dependent on molecular orientation the value recorded will be an average over all contributions. Consider a quantity $A(\beta)$ which is related to the molecular distribution by the function

$g(\beta)$, the ensemble average, $\langle A \rangle$, can be found by integrating over β: [78]

$$\langle A \rangle = \int_0^{\pi} A(\beta) g(\beta) \sin \beta d\beta. \tag{2.5}$$

$\langle A \rangle$ is therefore the ***order parameter*** associated with the parameter (or function) $A(\beta)$. This definition of an order parameter can be applied to the ODF for the uniaxial phase, equation 2.4, which is shown below.

$$\langle P_J \rangle = \int_0^{\pi} P_J(\cos \beta) \sum_{L=0}^{\infty} a_L P_L(\cos \beta). \tag{2.6}$$

A benefit of using the Legendre polynomials is that they are 'orthonormal' thus following the relationship: [8, 9, 78]

$$\int_0^{\pi} P_L(\cos \beta) P_J(\cos \beta) \sin \beta d\beta = \frac{2}{2J+1} \delta_{LJ}, \tag{2.7}$$

where δ_{LJ} is the Kronecker-delta function; with $\delta_{LJ} = 1$ for $L = J$ and $\delta_{LJ} = 0$ for $L \neq J$. Equation 2.6 can therefore be solved using the orthonormality condition in equation 2.7: [8, 9, 78]

$$\langle P_J \rangle = \frac{2}{2J+1} a_J \delta_{LJ}. \tag{2.8}$$

The order parameters, $\langle P_J \rangle$, can therefore be incorporated into the ODF by rearranging for a_L: [8, 9, 78]

$$f(\beta) = \sum_{L=0}^{\infty} \frac{2L+1}{2} \langle P_L \rangle P_L(\cos \beta) \text{ with } L = \text{even}, \tag{2.9}$$

where only even terms of L are considered as the liquid crystalline molecules, and resulting phases, are assumed to be apolar.

Whilst the ODF in equation 2.9 is an infinite sum of Legendre polynomials and their relevant order parameters, the ODF is generally truncated to the number of order parameters relevant to the experimental technique used. For example, determination of order from birefringence measurements is truncated to the 2^{nd} rank and for Raman spectroscopy the ODF is truncated to the 4^{th} rank. [79–82,

86–88] (note that x-ray diffraction can, in principle, determine order parameters greater than $\langle P_4 \rangle$ [89]). Truncation of the number of terms in the ODF can result in observations that are not necessarily representative of the exact ODF. This could include regions of the ODF with negative values, which is unphysical, and non-zero values at $\beta = 90^o$, which is unexpected for conventional nematic phases. [81] The problems with truncation of the ODF arise because, when defining the ODF, it is assumed that the functions are orthogonal. This orthogonal approach is exact for terms included but does not make assumptions for the value of the higher order terms thus, when truncated to the 4^{th} rank, 6^{th} rank and higher terms are assumed to be 0. [8] To rectify some of the problems with truncation of the ODF the ***exponential approximation*** is sometimes used. This approach, which is outlined in section 2.2.1, makes best guesses for the shape of the ODF given that the order parameters are known.

2.2.1 Exponential approximation

To remove some of the problems associated with truncation of the ODF one can use '***information theory***' to estimate the least biased distribution of molecules for a set of known order parameters. [8] In the information theory approach, the most probable distribution of molecules is defined as the one which maximises the entropy (h) of the system given by the equation: [90–92]

$$h(f(\beta)) = -\int f(\beta) \ln\left(f(\beta)\right) \sin(\beta) d\beta. \tag{2.10}$$

The solution for the ODF which maximises equation 2.10 for a given set of pre-determined order parameters is known [8, 9] and follows the form:

$$f(\beta) = \frac{\exp(\sum_L b_L P_L(\cos\beta))}{\int_0^\pi \sin\beta \exp\left(\sum_L b_L P_L(\cos\beta)\right) d\beta}, \tag{2.11}$$

where P_L is the L^{th} order Legendre polynomial as before and b_L is a new normalisation constant yet to be determined. The ODF in equation 2.11 is sometimes referred to as the '***exponential approximation***' of the ODF. The general form of an order parameter, $\langle A \rangle$, for an arbitrary distribution function $g(\beta)$ is given in

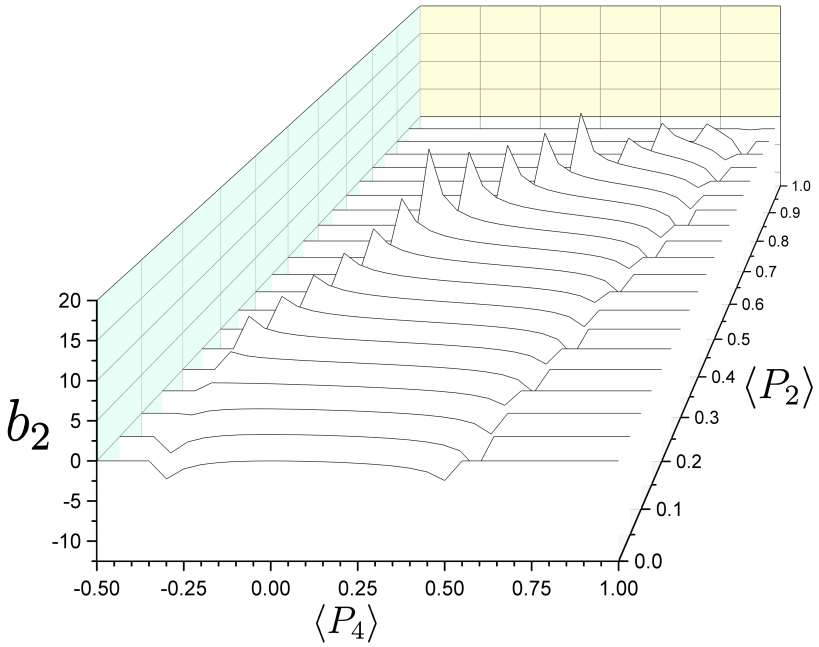

Figure 2.2: b_2 values as a function of $\langle P_4 \rangle$ and $\langle P_2 \rangle$ determined by numerically solving equations 2.12.

equation 2.5. Using the exponential approximation (equation 2.11) of the ODF, the order parameters up to $\langle P_4 \rangle$ are given by: [8, 9, 93]

$$\begin{aligned} \langle P_2 \rangle &= \frac{\int_0^\pi P_2(\cos\beta) \exp\left[b_2 P_2(\cos\beta) + b_4 P_4(\cos\beta)\right] \sin\beta d\beta}{\int_0^\pi \exp\left[b_2 P_2(\cos\beta) + b_4 P_4(\cos\beta)\right] \sin\beta d\beta}, \\ \langle P_4 \rangle &= \frac{\int_0^\pi P_4(\cos\beta) \exp\left[b_2 P_2(\cos\beta) + b_4 P_4(\cos\beta)\right] \sin\beta d\beta}{\int_0^\pi \exp\left[b_2 P_2(\cos\beta) + b_4 P_4(\cos\beta)\right] \sin\beta d\beta}. \end{aligned} \tag{2.12}$$

Having the ODF in the form of equation 2.11 means that the orthonormality of the Legendre polynomials (equation 2.7) can no longer be used to determine values for b_L. Instead, the system of equations 2.12 needs to be solved numerically to determine b_2 and b_4, for a given set of $\langle P_2 \rangle$ and $\langle P_4 \rangle$, so that the ODF can be constructed. [8, 9] The values of b_2 and b_4 in this thesis were determined using the `fsolve` in *Matlab* for $0.0 < \langle P_2 \rangle < 1.0$ and $-0.5 < \langle P_4 \rangle < 1.0$ and are shown in figures 2.2 and 2.3. The ODFs for 5CB at 23 °C ($\langle P_2 \rangle = 0.63$ and $\langle P_4 \rangle = 0.31$) using the orthogonal approach and information theory can be seen in figure 2.4

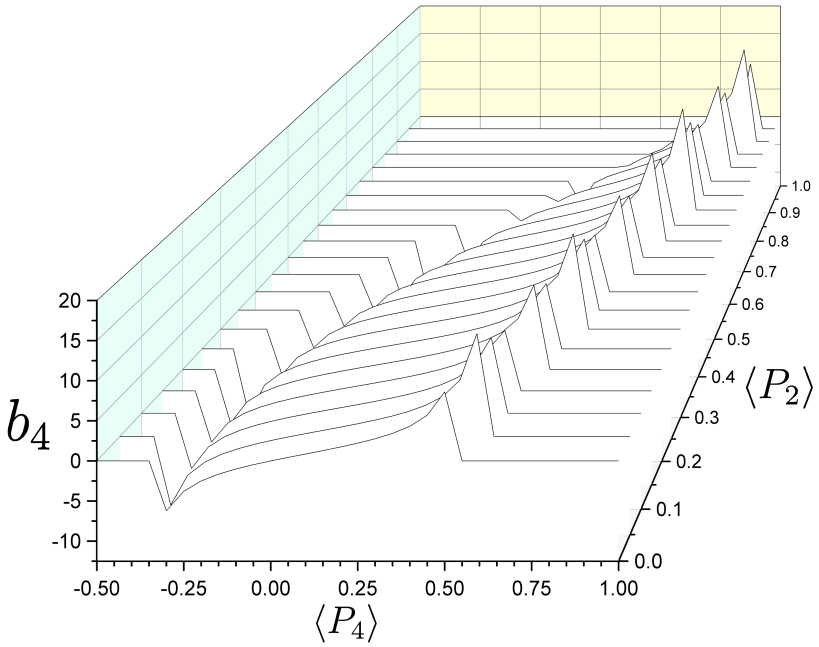

Figure 2.3: b_4 values as a function of $\langle P_4 \rangle$ and $\langle P_2 \rangle$ determined by numerically solving equations 2.12.

where is is clear that the orthogonal approach results in regions of negative values and non-zero values of the ODF at $\beta = 90°$.

2.2.2 The significance of $\langle P_4 \rangle$

In section 2.2 the 4$^{\text{th}}$ rank uniaxial order parameter $\langle P_4 \rangle$ is introduced. The addition of $\langle P_4 \rangle$ in the ODF provides more information about the distribution of molecules in a phase and can result in behaviour not encapsulated when only $\langle P_2 \rangle$ (or 'Q') is used. The shape of the ODF for positive values of $\langle P_2 \rangle$ (and various values of $\langle P_4 \rangle$) has been discussed in detail in Pottel *et al.* [94]; key sections of distributions were defined by lines within the [$\langle P_2 \rangle$,$\langle P_4 \rangle$] phase space and their physical meanings were discussed. The lines defining key ODF behaviours are shown in figure 2.5 and outlined below.

For a fixed $\langle P_2 \rangle$ the value $\langle P_4 \rangle$ is constrained, by trigonometric relations, to

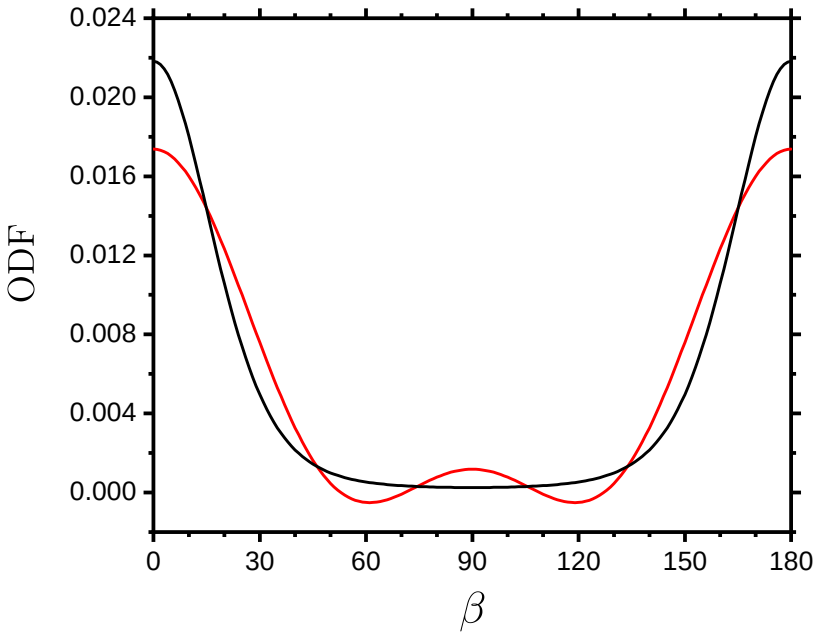

Figure 2.4: ODF of 5CB at 23°C using information theory (black line) and the truncated form (red line). In both cases $\langle P_2 \rangle = 0.63$, $\langle P_4 \rangle = 0.31$. For the exponential approximated ODF, $b_2 = 2.7860$ and $b_4 = 0.4467$ which is determined by solving the system of equations 2.12.

values following the inequality:

$$\frac{35}{18}\langle P_2 \rangle^2 - \frac{5}{9}\langle P_2 \rangle - \frac{7}{18} \leq \langle P_4 \rangle \leq \frac{5}{12}\langle P_2 \rangle + \frac{7}{12}. \tag{2.13}$$

The minimum and maximum values of $\langle P_4 \rangle$ are shown as black lines in figure 2.5. Within the physical limits of the $[\langle P_2 \rangle, \langle P_4 \rangle]$ there are, broadly speaking, 3 distinct regions of ODF behaviour shown in figure 2.5 as areas of orange, green and blue colours. [94, 95] These are discussed below:

1. In the blue area of figure 2.5 the ODF is singly peaked at a conic angle, β_c, which is not centred at $\beta = 0°$. On the $\langle P_4 \rangle_{\min}$ line, shown in black, the ODF is a singly peaked delta function centred at an conic angle of $\beta = \arccos\left(\frac{2}{3}\langle P_2 \rangle + \frac{1}{3}\right)^{1/2}$. Due to the delta-function distribution of molecules on the $\langle P_4 \rangle_{\min}$ line it is sometimes referred to as the 'hollow cone' line. The 'cone model', or sometimes the 'diffuse cone' line, shown as a blue dotted

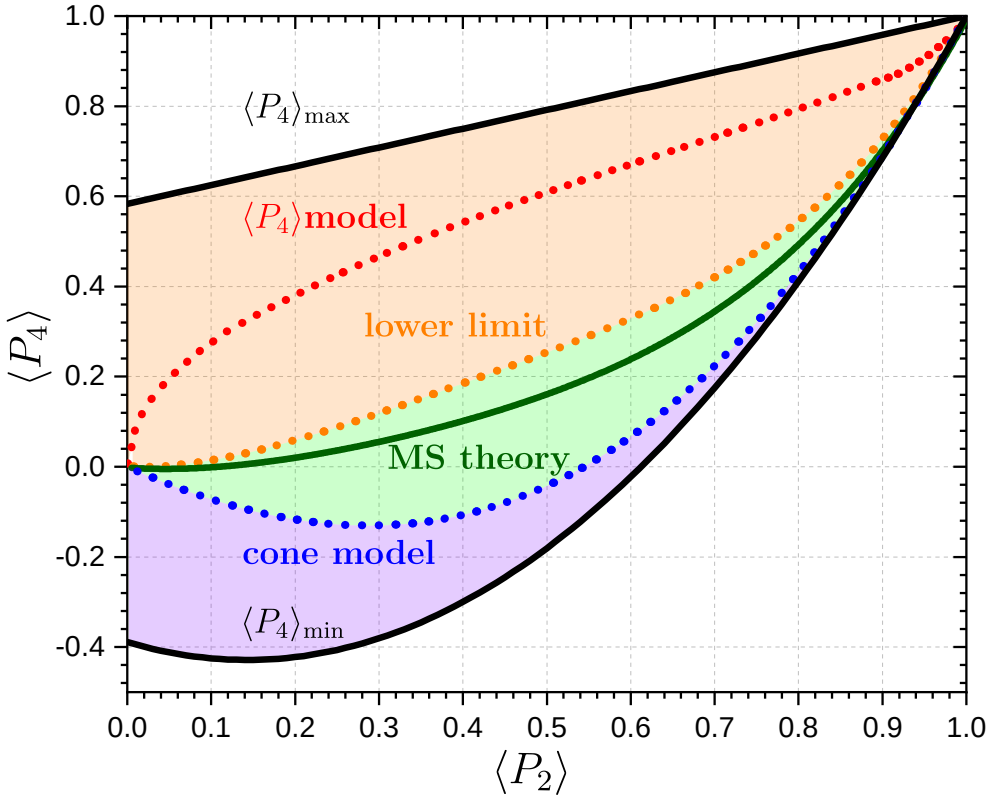

Figure 2.5: $[\langle P_2\rangle, \langle P_4\rangle]$ phase space showing the absolute limits of P_4 (black lines), the $\langle P_4\rangle$ model (red line), prediction of P_4 from Maier-Suape theory (green line) and the cone model (blue line).

line describes a distribution of molecules with a single peak centred at β_c (See figure 2.6 for an example of the ODF on the 'cone model' line). The 'cone model' line can be determined using the relationship:

$$\begin{aligned}\langle P_2\rangle &= \frac{1}{2}\cos\beta_c(1+\cos\beta_c),\\ \langle P_4\rangle &= \frac{1}{8}\cos\beta_c(1+\cos\beta_c)(7\cos^2\beta_c-3).\end{aligned} \tag{2.14}$$

The values of $\langle P_2\rangle$ and $\langle P_4\rangle$ of the de Vries type SmA phase will typically fall on the 'cone model' line. [96]

2. In the orange area of figure 2.5 the ODF is doubly peaked at $\beta = 0°$ and

$\beta = 90°$. On the $\langle P_4 \rangle_{\max}$ line, the ODF is a doubly peaked *delta* function centred at $\beta = 0°$ and $\beta = 90°$. The orange line defines the lower limit of values of $\langle P_2 \rangle$ and $\langle P_4 \rangle$ in which the ODF will be doubly peaked.

3. In the green area of figure 2.5 the ODF is singly peaked at $\beta = 0°$. The values of $\langle P_2 \rangle$ and $\langle P_4 \rangle$ predicted by Maier-Saupe theory fall within the $[\langle P_2 \rangle, \langle P_4 \rangle]$ phase space bounded by the green area.

Included in figure 2.5 are the Maier-Saupe theory (MS theory) line [97] and the '$\langle P_4 \rangle$ model' line of Zannoni *et al.* [8, 98] Both the MS theory and '$\langle P_4 \rangle$ model' are examples of 'mean-field theories'; both Maier-Saupe theory and the '$\langle P_4 \rangle$ model' consider long range anisotropic dispersion forces whilst short range intermolecular forces are assumed to be the same in the isotropic and nematic phases and are generally ignored. [11, 98, 99] Within the mean-field approach the energy between two molecules, U, is defined by a Pseudo potential given by the equation: [97, 100]

$$U = \sum_{L:n} \langle u_L \rangle \langle P_L \rangle P_L(\cos\beta), \tag{2.15}$$

where $\langle u_L \rangle$ is the statistical average of the expansion coefficient. The key difference between the classical MS theory and '$\langle P_4 \rangle$ model' is that MS theory considers only a 2nd rank pair potential whilst the $\langle P_4 \rangle$ considers only a 4^{th} rank pair potential. Hence the pseudo-potential of MS theory is: [98]

$$U(\cos\beta) = \langle u_2 \rangle \langle P_2 \rangle P_2(\cos\beta), \tag{2.16}$$

and for the '$\langle P_4 \rangle$ model': [98]

$$U(\cos\beta) = \langle u_4 \rangle \langle P_4 \rangle P_4(\cos\beta). \tag{2.17}$$

The value of $\langle P_4 \rangle$ for a given $\langle P_2 \rangle$ predicted by both MS theory and '$\langle P_4 \rangle$ model' can be determined using information theory (section 2.2.1). The set of equations

to be solved numerically for MS theory and '$\langle P_4 \rangle$ model' are, respectively:

$$\begin{aligned} f(\beta) &= \frac{\exp(b_2 P_2(\cos\beta))}{\int_0^\pi \sin\beta \exp\left(P_2(\cos\beta)\right)}, \\ \langle P_2 \rangle &= \frac{\int_0^\pi P_2(\cos\beta) \exp\left[b_2 P_2(\cos\beta)\right] \sin\beta d\beta}{\int_0^\pi \exp\left[b_2 P_2(\cos\beta)\right] \sin\beta d\beta}, \\ \langle P_4 \rangle &= \frac{\int_0^\pi P_4(\cos\beta) \exp\left[b_2 P_2(\cos\beta)\right] \sin\beta d\beta}{\int_0^\pi \exp\left[b_2 P_2(\cos\beta)\right] \sin\beta d\beta}. \end{aligned} \tag{2.18}$$

and

$$\begin{aligned} f(\beta) &= \frac{\exp(b_4 P_4(\cos\beta))}{\int_0^\pi \sin\beta \exp\left(P_4(\cos\beta)\right)}, \\ \langle P_2 \rangle &= \frac{\int_0^\pi P_2(\cos\beta) \exp\left[b_4 P_4(\cos\beta)\right] \sin\beta d\beta}{\int_0^\pi \exp\left[b_4 P_4(\cos\beta)\right] \sin\beta d\beta}, \\ \langle P_4 \rangle &= \frac{\int_0^\pi P_4(\cos\beta) \exp\left[b_4 P_4(\cos\beta)\right] \sin\beta d\beta}{\int_0^\pi \exp\left[b_4 P_4(\cos\beta)\right] \sin\beta d\beta}. \end{aligned} \tag{2.19}$$

The MS theory line can be closely approximated by the following equation: [8]

$$\begin{aligned} \langle P_4 \rangle &= \frac{5}{7}\langle P_2 \rangle^2 - \frac{2}{539}\langle P_2 \rangle^3 + \frac{35650}{49049}\langle P_2 \rangle^4 + \cdots, \\ &\approx \frac{5}{7}\langle P_2 \rangle^2. \end{aligned} \tag{2.20}$$

Maier-Saupe theory is an incredibly successful theory which can predict the nematic-isotropic transition temperature and the value of the Q order parameter for conventional nematic LC materials within agreement to experiments. [97] Note that the 'MS theory' line shown in figure 2.5 gives values of $\langle P_4 \rangle$ for $0 < \langle P_2 \rangle < 0.43$. Values in this range would not typically be observed in Maier-Saupe theory as a first order transition for nematic to isotropic is predicted whereby $\langle P_2 \rangle$ jumps from 0.43 to 0 at a given temperature. Instead, the MS theory line in figure 2.5 predicts values of $\langle P_4 \rangle$ for a given $\langle P_2 \rangle$ when the interaction potential is that of Maier-Saupe theory and makes no predictions of the thermodynamic behaviour of the LC phase.

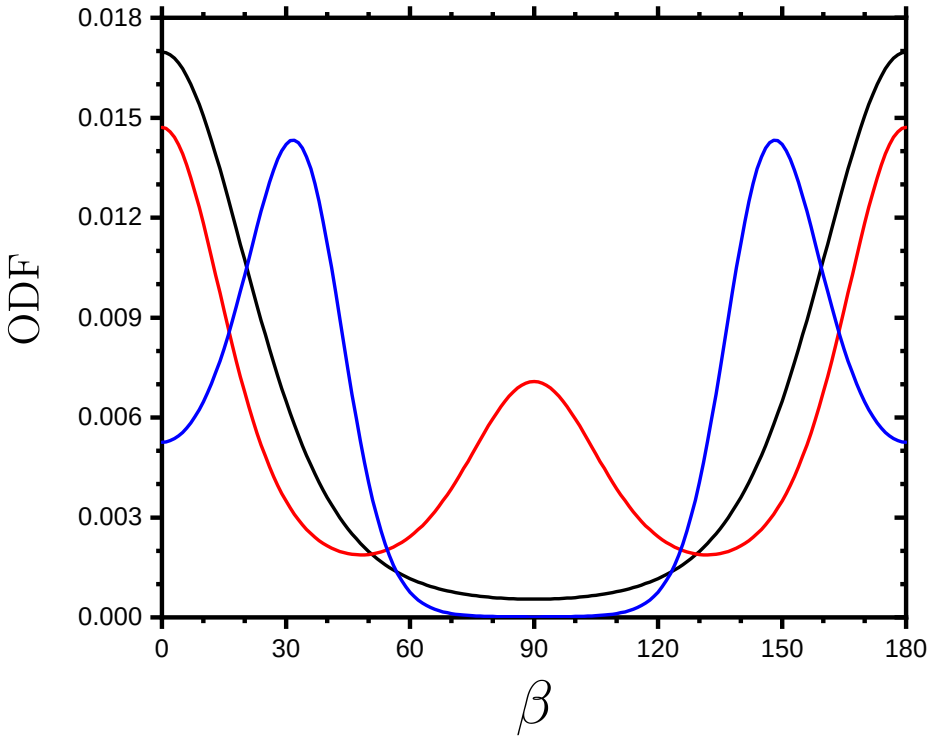

Figure 2.6: Normalised ODFs from various models, showing the 3 distinct regions in the $[\langle P_{200}\rangle, \langle P_{400}\rangle]$ phase space. Black line: MS theory distribution of molecules using order parameters predicted by Maier-Saupe theory ($\langle P_{200}\rangle = 0.5$, $\langle P_{400}\rangle = 0.178$). Red line: Large distribution of molecules at $\beta = 90°$ using $\langle P_{200}\rangle = 0$, $\langle P_{400}\rangle = 0.178$. Blue line: Cone model showing a distribution of molecules peaking at $\beta_c = 31.8°$ using $\langle P_{200}\rangle = 0.5$, $\langle P_{400}\rangle = -0.041$.

The '$\langle P_4\rangle$ model' can be closely approximated by the following equation: [8]

$$\langle P_4\rangle = \sqrt{\frac{77}{90}}\langle P_2\rangle^{\frac{1}{2}} - \frac{69}{260}\langle P_2\rangle + \frac{7794479}{1007760\sqrt{770}}\langle P_2\rangle^{\frac{3}{2}} + \cdots . \tag{2.21}$$

The $\langle P_4\rangle$ model predicts regions in the $[\langle P_2\rangle, \langle P_4\rangle]$ phase space where $\langle P_4\rangle > \langle P_2\rangle$ [101, 102] which have been found in lipid membranes by Florescence depolarization measurements of probe molecules. [93] An example ODF can be seen in figure 2.6 where $\langle P_4\rangle$ has been selected to be greater than $\langle P_2\rangle$. We can see this describes a probability function that has a large contribution of molecules perpendicular to the nematic director. A situation which cannot be described when

only $\langle P_2 \rangle$ is considered (or when considering Maier-Saupe theory). [8]

2.3 The phase biaxial ODF

So far, only uniaxial cylindrically symmetric phases consisting of cylindrically symmetric molecules have been considered. However, certain LC phases can have biaxial symmetry. [103] It is therefore necessary to define an ODF which contains phase biaxial order parameters, as discussed in detail by van Gurp and Zannoni. [8, 9, 78] To do this, it is useful to construct the ODF with a set of orthogonal functions which are dependent on α, β and γ; much like in the uniaxial case. The Wigner functions satisfy both these conditions. Using the definition of the Wigner functions the general ODF can be constructed: [8, 9, 78, 104]

$$f(\alpha, \beta, \gamma) = \sum_{L=0}^{\infty} \sum_{m,n=-L}^{L} a_{mn}^{L} D_{mn}^{L}, \tag{2.22}$$

where the indices L, m and n represent the symmetry conditions of rotations in β, α and γ respectively, a_{mn}^{L} is the normalisation constant and D_{mn}^{L} are the Wigner functions. The Wigner functions are orthogonal and thus follow the relationship: [78]

$$\int_0^{2\pi} \int_0^{\pi} \int_0^{2\pi} D_{m_i n_i}^{L_i *}(\alpha, \beta, \gamma) D_{m_j n_j}^{L_j}(\alpha, \beta, \gamma) \sin\beta d\alpha d\beta d\gamma = \frac{8\pi^2}{2L_i + 1} \delta_{L_i L_j} \delta_{m_i m_j} \delta_{n_i n_j}, \tag{2.23}$$

where $D_{m_i n_i}^{L_i *}$ is the complex conjugate of $D_{m_i n_i}^{L_i}$ and $\delta_{x_i x_j}$ is the Kronecker-delta function in which $\delta_{x_i x_j} = 1$ for $i = j$ and $\delta_{x_i x_j} = 0$ for $i \neq j$. As with the uniaxial case, order parameters can be introduced into the ODF through the normalisation constant (a_{mn}^{L}). First, the order parameters are defined as in equation 2.29 by integrating over α, β and γ: [78]

$$\langle D_{mn}^{L*} \rangle = \int_0^{2\pi} \int_0^{\pi} \int_0^{2\pi} D_{mn}^{L*} f(\alpha, \beta, \gamma) \sin\beta d\alpha d\beta d\gamma. \tag{2.24}$$

Substituting equation 2.22 into equation 2.24 and using the orthogonal condition in equation 2.23 it follows that:

$$\langle D^{L*}_{mm} \rangle = \frac{8\pi^2}{2L+1} a^L_{mn}, \tag{2.25}$$

and the general ODF becomes:

$$f(\alpha, \beta, \gamma) = \sum_{L=0}^{\infty} \sum_{m,n=-L}^{L} \frac{2L+1}{8\pi^2} \langle D^{L*}_{mn} \rangle D^L_{mn}. \tag{2.26}$$

Assuming that the molecules are rigid and have cylindrical symmetry (i.e. invariant to rotations in γ) the Wigner functions, and their complex conjugates, are related to the associated Legendre polynomials: [78, 105]

$$\begin{aligned} D^L_{m0}(\alpha, \beta, \gamma) &= \sqrt{\frac{(L-m)!}{(L+m)!}} P^m_L(\cos(\beta)) e^{im\alpha}, \\ D^{L*}_{m0}(\alpha, \beta, \gamma) &= (-1)^m \sqrt{\frac{(L-m)!}{(L+m)!}} P^m_L(\cos(\beta)) e^{-im\alpha}. \end{aligned} \tag{2.27}$$

Uniaxial molecules in a uniaxial phase For cylindrically symmetric molecules in a uniaxial phase only even terms of L are required and m and $n = 0$. The imaginary components of the Wigner functions vanish due to symmetry arguments and the generalised ODF for cylindrically symmetric molecules in a uniaxial phase is exactly as described in section 2.2 and can be represented with Legendre polynomials.

Uniaxial molecules in a biaxial phase For cylindrically symmetric molecules in a biaxial phase only even terms of L and m are necessary as the phase is apolar and achiral. [8, 9, 78, 83] If the phase has mirror symmetry in the xz, xy and yz plane the imaginary components of the Wigner functions disappear and Wigner functions collapse into to the generalised Legendre polynomials, $P^m_L(\alpha, \beta)$. [8, 9, 78, 83, 85] Hence, we can define the truncated ODF for uniaxial molecules

forming a biaxial phase as:

$$\begin{aligned} f(\alpha,\beta) = \frac{1}{8\pi^2}[1 &+ \frac{5}{2}\langle P_{200}\rangle(3\cos^2\beta - 1) \\ &+ \frac{30}{2}\langle P_{220}\rangle(1-\cos^2\beta)\cos 2\alpha \\ &+ \frac{9}{8}\langle P_{400}\rangle(3 - 30\cos^2\beta + 35\cos^4\beta) \\ &+ \frac{540}{8}\langle P_{420}\rangle(-1 + 8\cos^2\beta - 7\cos^4\beta)\cos 2\alpha \\ &+ \frac{630}{8}\langle P_{440}\rangle(1 - 2\cos^2\beta + \cos^4\beta)\cos 4\alpha], \end{aligned} \tag{2.28}$$

with the order parameters defined as:

$$\begin{aligned} \langle P_{200}\rangle &= \langle\frac{1}{2}(3\cos^2\beta - 1)\rangle, \\ \langle P_{400}\rangle &= \langle\frac{1}{8}(35\cos^4\beta - 30\cos^2\beta + 3)\rangle, \\ \langle P_{220}\rangle &= \langle\frac{1}{4}(1-\cos^2\beta)\cos 2\alpha\rangle, \\ \langle P_{420}\rangle &= \langle\frac{1}{24}(-1 + 8\cos^2\beta - 7\cos^4\beta)\cos 2\alpha\rangle, \\ \langle P_{440}\rangle &= \langle\frac{1}{16}(1 - 2\cos^2\beta + \cos^4\beta)\cos 4\alpha\rangle, \end{aligned} \tag{2.29}$$

where all the Legendre polynomials are of the form P_{Lm0} due to the invariance of the system to γ. $\langle P_{200}\rangle$ and $\langle P_{200}\rangle$ are the uniaxial order parameters as defined in section 2.2 and $\langle P_{220}\rangle$, $\langle P_{420}\rangle$ and $\langle P_{440}\rangle$ are the phase biaxial order parameters.

2.4 Non-cylindrically symmetric molecules

In sections 2.2 and 2.3 the ODF and order parameters are defined assuming that the LC phase consists of cylindrically symmetric rigid molecules. However, for non-cylindrically symmetric molecules, the ODF has a dependence with respect to γ and the molecular biaxial order parameters need to be included. The ODF in the case of a uniaxial phase consisting of board-like (i.e. non-cylindrically symmetric) molecules is given by: [85, 88]

$$
\begin{aligned}
f(\alpha,\gamma) = \frac{1}{8\pi^2}[1 + \frac{5}{2}\langle P_{200}\rangle(3\cos^2\beta - 1) \\
+\frac{30}{2}\langle P_{202}\rangle(1-\cos^2\beta)\cos 2\gamma \\
+\frac{9}{8}\langle P_{400}\rangle(3 - 30\cos^2\beta + 35\cos^4\beta) \\
+\frac{540}{8}\langle P_{402}\rangle(-1 + 8\cos^2\beta - 7\cos^4\beta)\cos 2\gamma \\
+\frac{630}{8}\langle P_{404}\rangle(1 - 2\cos^2\beta + \cos^4\beta)\cos 4\gamma],
\end{aligned}
\tag{2.30}
$$

where $\langle P_{L0n}\rangle$ are the molecular biaxial order parameters. Many conventional LCs show evidence of molecular biaxiality (for example 5CB as investigated by nuclear magnetic resonance has shown evidence of slight molecular biaxiality [106]) whilst still forming uniaxial nematic phases. [103] As will be discussed in chapter 5, it is assumed that the vibrational Raman mode selected has cylindrical symmetry. Therefore, typically, only the uniaxial ($\langle P_{200}\rangle$, $\langle P_{400}\rangle$) and phase biaxial ($\langle P_{220}\rangle$, $\langle P_{420}\rangle$, $\langle P_{440}\rangle$) are determined. Throughout this thesis the phenyl-stretching mode (1606 cm^{-1}) is selected, which has been reported to have near-cylindrical symmetry [88], and therefore the molecular biaxial order parameters are not considered in the Raman analysis of order parameters.

2.5 Summary

To summarise, the orientational distributions function (ODF) of the uniaxial and biaxial phase are introduced. In addition, the concept of an ***order parameter*** is discussed and the uniaxial ($\langle P_{200}\rangle$ and $\langle P_{400}\rangle$) and phase biaxial ($\langle P_{220}\rangle$, $\langle P_{420}\rangle$ and $\langle P_{440}\rangle$) order parameters, relevant to Raman scattering, are introduced. Since Raman spectroscopy can resolve order parameters to 4^{th} rank the issues with truncation of the ODF is discussed and the exponential approximation of the ODF from ***information theory*** is introduced to resolve these.

The significance of the value of the $\langle P_{400}\rangle$ order parameter on the uniaxial phase is discussed. It is revealed that there are 3 distinct regions in the [$\langle P_{200}\rangle$, $\langle P_{400}\rangle$] phase space: (1) a region defined by a doubly peaked ODF centred at $\beta = 0°$ and $\beta = 90°$; (2) a region defined by a singly peaked ODF centred at

$\beta = 0°$; (3) a region defined by a singly peaked ODF centred at a conic angle β_c. The predictions of $\langle P_{400} \rangle$ for a given $\langle P_{200} \rangle$ from the mean field 'Maier-Saupe' and '$\langle P_4 \rangle$ model' theories are discussed. In chapter 8, the various uniaxial models, as discussed in section 2.2.2, will be used to describe the orientational distribution of molecules in an nematic LCE strained either parallel and perpendicular to the nematic director. It is shown that, for the perpendicularly strain LCE, the ODF deviates from that predicted by Maier-Saupe theory and converges towards the $\langle P_4 \rangle$ model line. A full investigation of this behaviour leads to exploring the emergence of biaxial order in the LCE.

Chapter 3

Theory II: Mechanical deformation of LCEs

In chapter 1, LCEs as a class of materials, which combine the anisotropic behaviour of liquid crystals and the rubbery elasticity of conventional elastomers, are introduced. Remarkable behaviours, unique to LCEs, such as 'stress optical coupling' and 'soft elasticity' are discussed. Herein, the concepts introduced in chapter 1 are discussed in greater detail and some of the key theoretical descriptions of the mechanical behaviour of LCEs are outlined. As the mechanical behaviour of LCEs is incredibly rich [40, 107], only the behaviour of nematic LCEs under strains applied perpendicular to the nematic director will be considered. This deformation geometry is relevant to the later results chapters in this thesis as it is the geometry for which the MFT and molecular auxetic response are observed in certain LCEs.

This chapter begins with a derivation of the free energy of an isotropic rubber under strain. Following on from this, the free energy of a nematic LCE under strain is derived which results in the *neo-classical Trace formula*. The neo-classical Trace formula is fundamental to the two theories considered in this chapter; the theory of 'semi-soft elasticity' (SSE) and the theory of the 'mechanical Fréedericksz transition' (MFT). In the case of the SSE, the director rotates continuously towards the strain axis and there is a softening in the stress-strain response. In the case of the MFT, the director remains perpendicular to the applied strain until there is a sharp rotation of the director at a critical strain. The

geometry, shown in figure 3.1, is the same in both cases with the initial nematic director orientated along the z axis and a strain imposed along the x axis. Deformation of all known nematic LCEs occurs either via the SSE or the MFT; the MFT is most relevant to the experiments within this thesis as all measurements are performed on an LCE deforming by this mechanism. [40] The majority of this chapter is formed from the discussions in '*Liquid Crystal Elastomers*' by Warner & Terentjev [40] and in the PhD thesis by Mistry. [108]

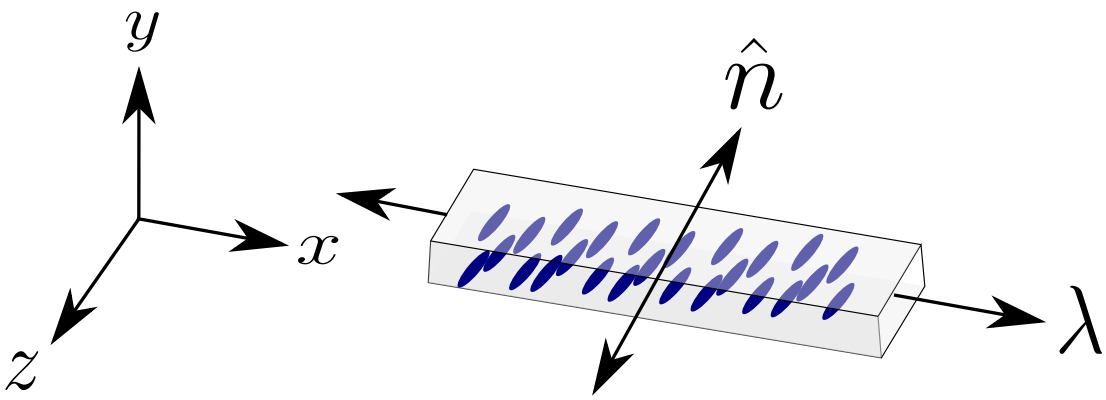

Figure 3.1: Initial geometry involved in the semi-soft elastic response and the mechanical Fréedericksz transition. In both cases the initial nematic director is orientated along z and a perpendicular strain is applied along x.

3.1 Derivation of the 'Trace formula'

3.1.1 Isotropic case

In chapter 1 the random walk behaviour of an isotropic polymer chain is introduced. It is shown that whilst the end-to-end vector $\langle \vec{R} \rangle = 0$, the mean square end-to-end vector $\langle \vec{R}^2 \rangle = a^2 n = aL$ where a is the segment length, n is the number of segments in the chain and L is the 'contour length' of the chain. In the limit of large n the probability distribution of the end-to-end vector is a Gaussian

function given by the equation: [14, 40]

$$p(\vec{R}) = \left(\frac{3}{2\pi aL}\right)^{\frac{3}{2}} \exp\left(-\frac{3\vec{R}\cdot\vec{R}}{2aL}\right). \tag{3.1}$$

The probability distribution function in equation 3.1 is valid for cross-linked systems provided that the cross-link density is low enough such that the number of molecules in a network strand is large. [14, 109] The free energy of the network strand is given by $F_s = U - TS$ where U is internal energy and S is entropy, however, since only entropic effects are considered $F_s = -k_{\mathrm{B}}T \ln Z_n$ where $Z_n \propto p(\vec{R})$ is the partition function [14], therefore:

$$F_s = \frac{3}{2}\left(\frac{k_{\mathrm{B}}T}{aL}\right)\vec{R}\cdot\vec{R} + C, \tag{3.2}$$

where C is an arbitrary constant which is ignored. Let us consider the deformation

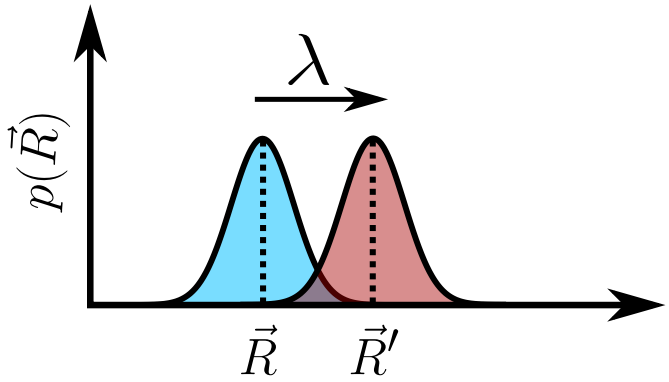

Figure 3.2: Change in probability distribution of the polymer chains under an affine deformation. The shape of the probability remains unchanged however the centre of the distribution is now shifted from $\vec{R}$ to $\vec{R}'$.

of a selected network strand with the end-to-end vector of $\vec{R}$ into a new end-to-end vector:

$$\vec{R}' = \underline{\underline{\lambda}} \cdot \vec{R}, \tag{3.3}$$

where $\underline{\underline{\lambda}}$ is the deformation tensor or deformation gradient. We assume that the deformation is affine which means that all network strands in the network deform

by the same amount. The shape of the probability distribution therefore remains the same albeit shifted (see figure 3.2) and the free energy of the deformed strand is determined by substitution of equation 3.3 into 3.2:

$$\begin{aligned} F_s' &= \frac{3}{2}\left(\frac{k_\mathrm{B}T}{aL}\right)\vec{R}'\cdot\vec{R}' \\ &= \frac{3}{2}\left(\frac{k_\mathrm{B}T}{aL}\right)\vec{R}\cdot\underline{\underline{\lambda}}^T\cdot\underline{\underline{\lambda}}\cdot\vec{R}. \end{aligned} \tag{3.4}$$

The average free energy of the network, or the free energy density, can be determined by taking the ensemble average of equation 3.4:

$$\langle F_s'\rangle = \frac{3}{2}\left(\frac{k_\mathrm{B}T}{aL}\right)\langle\vec{R}\cdot\underline{\underline{\lambda}}^T\cdot\underline{\underline{\lambda}}\cdot\vec{R}\rangle, \tag{3.5}$$

where $\underline{\underline{\lambda}}^T$ is the trace of $\underline{\underline{\lambda}}$. Since the deformation is affine, the deformation gradient $\underline{\underline{\lambda}}$ is the same for all strands in the network, therefore, averaging occurs over $\langle\vec{R}\cdot\vec{R}\rangle$ only. The free energy density of the deformed network is therefore given by the equation:

$$\langle F_s'\rangle = \frac{3}{2}k_\mathrm{B}T\ \mathrm{Tr}\left(\underline{\underline{\lambda}}^T\cdot\underline{\underline{\lambda}}\right), \tag{3.6}$$

where the definition $\langle\vec{R}^2\rangle = aL$ (equation 1.4) has been used. The total free energy of the deformed network, F_el, is simply the free energy density equation multiplied by the number of network strands:

$$F_\mathrm{el} = \frac{3}{2}\mu\ \mathrm{Tr}\left(\underline{\underline{\lambda}}^T\cdot\underline{\underline{\lambda}}\right), \tag{3.7}$$

where $\mu = n_s k_\mathrm{B}T$ is the shear moduli of the material with n_s the number of molecules in a network strand.

3.1.2 Nematic case

For an LCE in the nematic phase the random walk of the polymer chain is anisotropic. Therefore, assuming uniaxial symmetry with the nematic director ($\hat{n}$) orientated in the z direction, $\langle\vec{R}_x^2\rangle = \langle\vec{R}_y^2\rangle \neq \langle\vec{R}_z^2\rangle$. In each dimension the polymer chain has an associated step-length which can be represented in tensorial

form: [40]

$$\underline{\underline{l}} = \begin{bmatrix} l_x & 0 & 0 \\ 0 & l_y & 0 \\ 0 & 0 & l_z \end{bmatrix}. \tag{3.8}$$

There are now 3 mean square end-to-end vectors in the principal frame defined by the equation $\langle \vec{R}_i \cdot \vec{R}_j \rangle = \frac{1}{3} l_{ij} L$. [40] The mean square end-to-end vector, in 3D space, is the sum of the three principle mean square end-to-end vectors in x, y and z:

$$\langle \vec{R}^2 \rangle = \frac{L}{3}(l_x + l_y + l_z) = \frac{1}{3} L \mathrm{Tr}(\underline{\underline{l}}). \tag{3.9}$$

The 3D probability distribution function of a network strand is given by $p(\vec{R}) = p(\vec{R}_x)p(\vec{R}_y)p(\vec{R}_z)$ with the probability distribution in the i_{th} dimension given by: [40]

$$p(\vec{R}_i) = \left(\frac{3}{2\pi L l_i}\right)^{\frac{1}{2}} \exp\left(-\frac{3\vec{R}_i \cdot \vec{R}_i}{2 L l_i}\right). \tag{3.10}$$

The 3D probability distribution function is therefore: [40]

$$\begin{aligned} p(\vec{R}) &= \left(\frac{3}{2\pi L}\right)^{\frac{3}{2}} \left(\frac{1}{\mathbf{det}(\underline{\underline{l}})}\right)^{\frac{1}{2}} \exp\left(\frac{-3}{2L}\left(\frac{\vec{R}_x^2}{l_x} + \frac{\vec{R}_y^2}{l_y} + \frac{\vec{R}_z^2}{l_z}\right)\right) \\ &= \left(\frac{3}{2\pi L}\right)^{\frac{3}{2}} \left(\frac{1}{\mathbf{det}(\underline{\underline{l}})}\right)^{\frac{1}{2}} \exp\left(\frac{-3}{2L}\left(\vec{R} \cdot \underline{\underline{l}}^{-1} \cdot \vec{R}\right)\right), \end{aligned} \tag{3.11}$$

where the definition $\mathbf{det}(\underline{\underline{l}}) = l_x l_y l_z$ has been used. As before, using the definition of the free energy of a strand, $F_s \propto -k_{\mathrm{B}} T \ln p(R)$:

$$F_s = \frac{3 k_{\mathrm{B}} T}{2L} \vec{R} \cdot \underline{\underline{l}}^{-1} \cdot \vec{R} + \frac{k_{\mathrm{B}} T}{2} \ln\left(\frac{\mathbf{det}(\underline{\underline{l}})}{C}\right), \tag{3.12}$$

where C is a constant. The '$\ln(\mathbf{det}(\underline{\underline{l}})/C)$' term contains the nematic order in the step-length tensor $\underline{\underline{l}}$. If the magnitude of the nematic order is unchanged during a deformation the $\ln(\mathbf{det}(\underline{\underline{l}})/C)$ term will be a constant.

As before, an affine deformation is applied to the network such that $\vec{R}' = \underline{\underline{\lambda}} \vec{R}$. Following the arguments of the isotropic case, the free energy density of the

network is related to $\langle \vec{R} \cdot \underline{\underline{\lambda}}^T \cdot \underline{\underline{l}}^{-1} \cdot \underline{\underline{\lambda}} \cdot \vec{R} \rangle$, which due to the nature of the affine deformation is related to $\langle \vec{R}^2 \rangle$ only. Hence, the free energy density in the nematic case is determined by substituting equation 3.9 into equation 3.12:

$$\begin{aligned} \langle F_s' \rangle &= \frac{3k_{\mathrm{B}}T}{2L} \langle \vec{R} \cdot \underline{\underline{\lambda}}^T \cdot \underline{\underline{l}}^{-1} \cdot \underline{\underline{\lambda}} \cdot \vec{R} \rangle + \frac{k_{\mathrm{B}}T}{2} \ln \left(\frac{\mathbf{det}(\underline{\underline{l}})}{C} \right) \\ &= \frac{1}{2} k_{\mathrm{B}}T \, \mathrm{Tr}(\underline{\underline{l_0}} \cdot \underline{\underline{\lambda}} \cdot \underline{\underline{l}}^{-1} \cdot \underline{\underline{\lambda}}) + \frac{k_{\mathrm{B}}T}{2} \ln \left(\frac{\mathbf{det}(\underline{\underline{l}})}{C} \right), \end{aligned} \tag{3.13}$$

where $\underline{\underline{l_0}}$ is the unstrained step-length tensor with $\mathrm{Tr}(\underline{\underline{l_0}}) = (l_{x,0} + l_{y,0} + l_{z,0})$. The total free energy of the network is the free energy density multiplied by the number of strands, n_s, therefore:

$$F_{\mathrm{el}} = \frac{1}{2} \mu \mathrm{Tr}(\underline{\underline{l_0}} \cdot \underline{\underline{\lambda}} \cdot \underline{\underline{l}}^{-1} \cdot \underline{\underline{\lambda}}) + \frac{1}{2} \mu \ln \left(\frac{\mathbf{det}(\underline{\underline{l}})}{\mathbf{det}(\underline{\underline{l_0}})} \right), \tag{3.14}$$

where $\mu = n_s k_{\mathrm{B}} T$ and C has been set to $\mathbf{det}(\underline{\underline{l_0}})$ so that F_{el} is equal to that of an isotropic rubber in the undeformed state. [40] Equation 3.14 is known as the ***'Trace formula'*** for a nematic rubber and forms the basis for understanding the SSE and MFT behaviours.

3.2 Spontaneous distortion under the isotropic to nematic transition

Much like a conventional low molecular mass liquid crystal, an ideal LCE will undergo a transition from an isotropic phase to a nematic phase upon cooling through T_{ni}. However, due to the coupling between the nematic order and the macroscopic shape of the LCE, the transition from the isotropic phase to the nematic phase will be accompanied by a spontaneous distortion of the polymer conformation of the LCE. [40] Consider an LCE formed in the isotropic phase and cooled into a mono-domain nematic phase. The step-length tensors associated

with this transition are:

$$\begin{aligned} \underline{\underline{l_0}} &= \text{Diag}[a, a, a] = a \cdot \underline{\underline{\delta}}, \\ \underline{\underline{l}} &= \text{Diag}[\lambda_\perp, \lambda_\perp, \lambda_\parallel], \end{aligned} \tag{3.15}$$

and the deformation tensor of the spontaneous distortion, assuming no change in volume, accompanying the transition from the isotropic phase to the nematic phase is given by:

$$\underline{\underline{\lambda_\text{m}}} = \text{Diag}\left[\frac{a}{\sqrt{\lambda_\text{m}}}, \frac{a}{\sqrt{\lambda_\text{m}}}, a\lambda_\text{m}\right]. \tag{3.16}$$

Substituting the relevant step-length tensors (equation 3.15) and deformation tensor (equation 3.16) into the the Trace formula (equation 3.14) leads to the following free energy:

$$F_\text{el} = \frac{1}{2}\mu\left(\frac{2a}{\lambda_\text{m} l_\perp} + \frac{2a\lambda_\text{m}^2}{l_\parallel}\right). \tag{3.17}$$

The value of the spontaneous deformation is determined by minimising equation 3.17 with respect to λ_m:

$$\lambda_\text{m} = \left(\frac{l_\parallel}{l_\perp}\right)^{1/3} = r^{1/3}, \tag{3.18}$$

and the spontaneous deformation tensor is therefore determined by substituting equation 3.18 into equation 3.16:

$$\underline{\underline{\lambda_\text{m}}} = \text{Diag}[r^{-1/6}, r^{-1/6}, r^{1/3}]. \tag{3.19}$$

Therefore the transition from an isotropic LCE to a mono-domain nematic LCE is accompanied by the spontaneous deformation $\underline{\underline{\lambda_\text{m}}} = \text{Diag}[r^{-1/6}, r^{-1/6}, r^{1/3}]$. As will be apparent in the following section, the existence of $\underline{\underline{\lambda_\text{m}}}$ is important to the theory of the soft elastic response.

3.3 Soft elasticity

The concept of semi-soft elasticity is first mentioned in section 1.4.5 to describe the plateau-like stress-strain behaviour of certain LCEs after a threshold strain

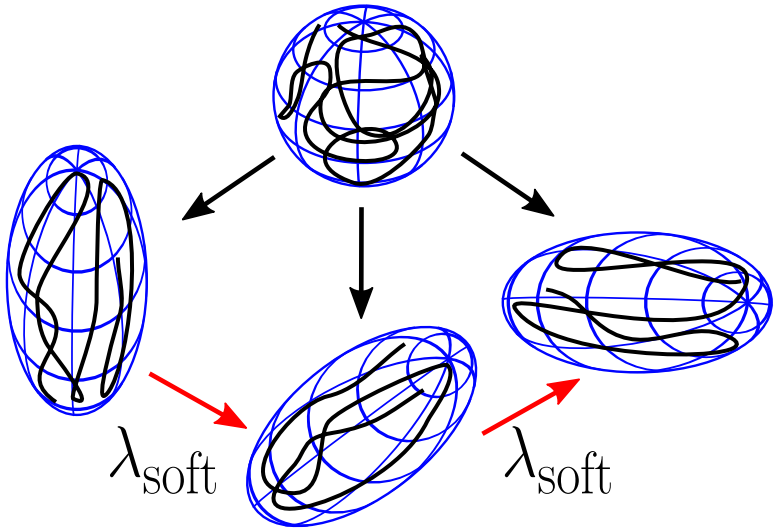

Figure 3.3: Schematic of the soft elastic response in LCEs. The LCE has access to an isotropic conformation (top) and upon cooling will form a nematic conformation with an arbitrary director angle. The nematic conformations have equal energies. Thus λ_{soft} deformations have no energetic cost.

is reached. [40, 64, 67, 69] The requirement for a threshold strain to be reached is observed in real LCEs and is a consequence of non-idealities, as discussed in further in this section, however, first let us consider the ideal thresholdless soft elasticity. In the theoretical description of soft elasticity outlined herein it is assumed that (a) the LCE has access to an isotropic reference state and (b) that the nematic order remains unchanged during deformation. The approach of this chapter closely follows that of Warner & Terentjev [40] and begins with the deformation gradient of Olmsted: [110]

$$\underline{\underline{\lambda}}_{\text{soft}} = \underline{\underline{l}}^{\frac{1}{2}} \cdot \underline{\underline{W}}_{\phi} \cdot \underline{\underline{l_0}}^{-\frac{1}{2}}, \tag{3.20}$$

where $\underline{\underline{W}}_{\phi}$ is an arbitrary body rotation by an angle 'ϕ'. By substituting equation 3.20 into equation 3.14 and assuming that the nematic order remains constant:

$$
\begin{aligned}
F_{\text{el}} &= \frac{1}{2}\mu \text{Tr}\left(\underline{\underline{l_0}} \cdot \underline{\underline{l_0}}^{-\frac{1}{2}} \cdot \underline{\underline{W}}_{\phi}^{T} \cdot \underline{\underline{l}}^{\frac{1}{2}} \cdot \underline{\underline{l}}^{-1} \cdot \underline{\underline{l}}^{\frac{1}{2}} \cdot \underline{\underline{W}}_{\phi} \cdot \underline{\underline{l_0}}^{-\frac{1}{2}}\right) \\
&= \frac{1}{2}\mu \text{Tr}\left(\underline{\underline{l_0}} \cdot \underline{\underline{l_0}}^{-\frac{1}{2}} \cdot \underline{\underline{W}}_{\phi}^{T} \cdot \underline{\underline{I}} \cdot \underline{\underline{W}}_{\phi} \cdot \underline{\underline{l_0}}^{-\frac{1}{2}}\right) \\
&= \frac{1}{2}\mu \text{Tr}\left(\underline{\underline{l_0}} \cdot \underline{\underline{l_0}}^{-\frac{1}{2}} \cdot \underline{\underline{l_0}}^{-\frac{1}{2}}\right) \\
&= \frac{1}{2}\mu \text{Tr}\left(\underline{\underline{I}}\right) = \frac{3}{2}\mu,
\end{aligned}
\tag{3.21}
$$

which is the elastic free energy of an unstrained isotropic rubber, hence, there exists a set of deformations of the type in equation 3.20 for which there is no energetic cost of deformation.

To understand the form of the soft deformation, $\underline{\underline{\lambda}}_{\text{soft}}$, let us consider the behaviour of the director assuming that the nematic order remains constant. The soft response begins with the nematic director perpendicular to the initial strain axis so that the initial step-length tensor is $\underline{\underline{l_0}} = \text{Diag}\left[l_\perp, l_\perp, l_\parallel\right]$. The $\underline{\underline{l_0}}^{-\frac{1}{2}}$ term in equation 3.20 can therefore be rewritten using the definition $r = l_\parallel / r_\perp$: [40]

$$
\begin{aligned}
\underline{\underline{l_0}}^{-\frac{1}{2}} &= \text{Diag}\left[l_\perp^{-\frac{1}{2}}, l_\perp^{-\frac{1}{2}}, l_\parallel^{-\frac{1}{2}}\right] \\
&= l_\perp^{-\frac{1}{2}} r^{-\frac{1}{6}} \text{Diag}\left[r^{\frac{1}{6}}, r^{\frac{1}{6}}, r^{-\frac{1}{3}}\right] \\
&= l_\perp^{-\frac{1}{2}} r^{-\frac{1}{6}} \underline{\underline{\lambda_{\text{m}}}}^{-1},
\end{aligned}
\tag{3.22}
$$

where $\underline{\underline{\lambda_{\text{m}}}} = \text{Diag}\left[r^{-1/6}, r^{-1/6}, r^{1/3}\right]$ is the spontaneous distortion of an LCE during the isotropic to nematic transition. [40] The soft response ends when the director been rotated fully towards the strain axis, therefore, $\underline{\underline{l}} = \text{Diag}\left[l_\parallel, l_\perp, l_\perp\right]$. Once again, the $\underline{\underline{l}}^{\frac{1}{2}}$ term in equation 3.20 can be rewritten using the definition $r = l_\parallel / r_\perp$: [40, 108]

$$
\begin{aligned}
\underline{\underline{l}}^{\frac{1}{2}} &= \text{Diag}\left[l_\parallel^{\frac{1}{2}}, l_\perp^{\frac{1}{2}}, l_\perp^{\frac{1}{2}}\right] \\
&= l_\perp^{\frac{1}{2}} r^{\frac{1}{6}} \text{Diag}\left[r^{\frac{1}{3}}, r^{-\frac{1}{6}}, r^{-\frac{1}{6}}\right] \\
&= l_\perp^{\frac{1}{2}} r^{\frac{1}{6}}\, \underline{\underline{U}}^{T} \cdot \underline{\underline{\lambda_{\text{m}}}} \cdot \underline{\underline{U}},
\end{aligned}
\tag{3.23}
$$

where $\underline{\underline{U}}$ is a rotation matrix. From equation 3.22 and 3.23 it follows that $\underline{\underline{l}}^{1/2} = \underline{\underline{U}}^T \cdot \underline{\underline{l_0}}^{1/2} \cdot \underline{\underline{U}}$ and hence $\underline{\underline{l}}^{1/2}$ is a rotation of $\underline{\underline{l_0}}^{1/2}$. The soft deformation, $\underline{\underline{\lambda}}_{\text{soft}}$, can be determined by substituting equation 3.22 and 3.23 into 3.20 ignoring $\underline{\underline{W}}_{\phi}$ since it is arbitrary: [40]

$$\begin{aligned} \underline{\underline{\lambda}}_{\text{soft}} &= \underline{\underline{l}}^{\frac{1}{2}} \cdot \underline{\underline{l_0}}^{-\frac{1}{2}} \\ &= \underline{\underline{U}}^T \cdot \underline{\underline{\lambda}}_{\text{m}} \cdot \underline{\underline{U}} \cdot \underline{\underline{\lambda}}_{\text{m}}. \end{aligned} \tag{3.24}$$

The implication of equation 3.24 is that LCEs can deform softly due to the existence of an isotropic reference state accessible through a deformation proportional to $\underline{\underline{\lambda}}_{\text{m}}$. [40] See figure 3.3 for a schematic of the soft deformations of nematic LCE due to an accessible isotropic reference state. From equation 3.24, the soft elastic deformation can be thought of as consisting of two parts; the first part is the virtual deformation of the anisotropic chain conformation to the accessible isotropic conformation via the deformation, $\underline{\underline{\lambda}}_{\text{m}}$; the second part is rotation, with no energetic cost, of the virtual intermediate isotropic state. Finally, the isotropic configuration, deforms by $\underline{\underline{\lambda}}_{\text{m}}$ into the final anisotropic configuration.

Semi-soft elasticity

In actuality, nematic LCEs will not deform completely softly due to the existence of 'non-idealities' introduced into the sample upon network formation which makes a completely isotropic reference state inaccessible. [40] One suggested cause for non-ideality in the network is a variation in chain lengths and backbone anisotropy; [111] this would be especially apparent, for example, in randomly a cross-linked network. As such the response is 'semi-soft' whereby: (a) a threshold strain is required for rotations of the director to occur and (b) the plateau of the response has a positive gradient (i.e. energetic cost of deformation) as opposed to the completely flat response of the ideal soft response. A schematic of the stress-strain curve and director behaviour of the semi-soft elastic response is shown in figure 3.4. The shapes of the representative curves are based on theory by Verwey

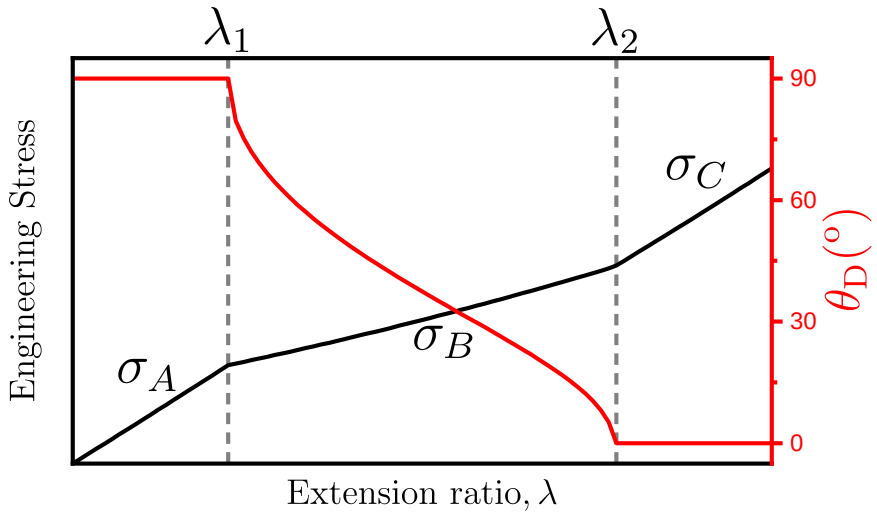

Figure 3.4: Schematic of the stress-strain behaviour and the director rotation of a nematic LCE strained perpendicular to the initial director and undergoing the semi-soft elastic response

et al. [40, 67] which are given below:

$$\begin{aligned}
\sigma_A &= \mu\left(\lambda^2 - \frac{1}{\lambda}\right) \text{ for } \lambda < \lambda_1, \\
\sigma_B &= \mu\lambda^2\left(1 - \frac{1}{\lambda_1^3}\right) \text{ for } \lambda_1 < \lambda < \lambda_2, \\
\sigma_C &= \mu\left(\lambda^2\left(1 - \frac{r-1}{\lambda_1^3 r}\right) - \frac{\sqrt{r}}{\lambda}\right) \text{ for } \lambda > \lambda_2, \\
\sin\left(\theta_D\right) &= \left(\frac{r(\lambda^2 - \lambda_1^2)}{(r-1)\lambda^2}\right)^{\frac{1}{2}} \text{ for } \lambda_1 < \lambda < \lambda_2,
\end{aligned} \tag{3.25}$$

where λ_1 is the threshold strain for the onset of the semi-soft response, λ_2 is the threshold strain for the end of the semi-soft response and θ_D is the angle of the nematic director.

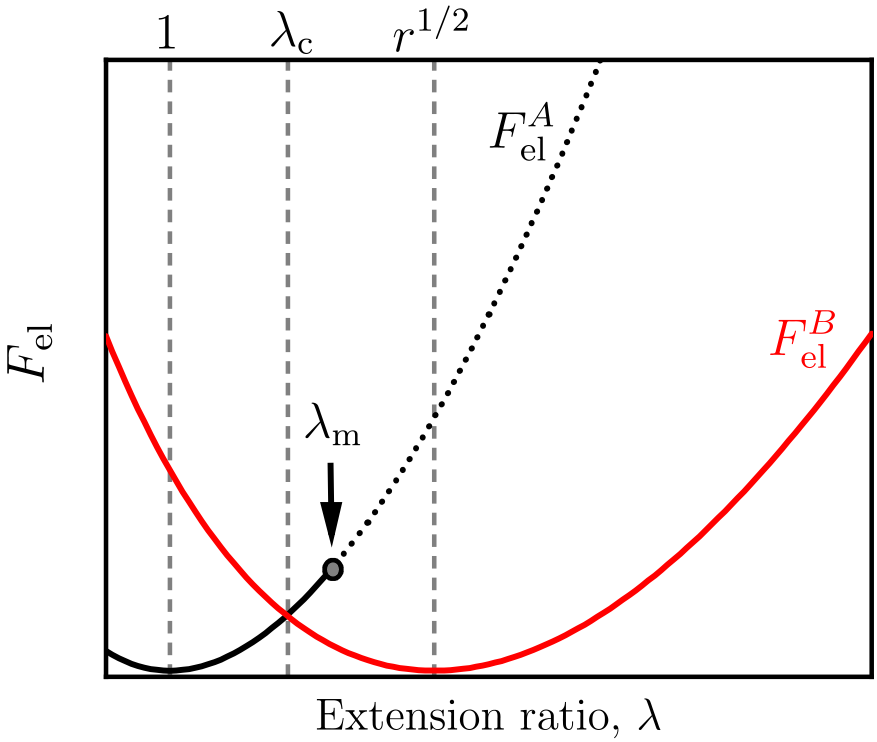

Figure 3.5: Free energy (F_{el}) against extension of an LCE in the unrotated state (F_{el}^A) and the rotated state (F_{el}^B). The free energies cross-over at λ_c.

3.4 Mechanical Fréedericksz transition

In addition to the 'semi-soft elastic' response, there have been reports in the literature of a different mechanical deformation exhibited by certain LCEs termed the 'Mechanical Fréedericksz transition' (MFT). [1, 40, 112] In the MFT, initially the director remains perpendicular to the applied strain, and after a critical threshold strain, then rotates sharply. Whilst there is theoretical work describing the director rotation and change in nematic order during the MFT [113, 114], as of writing, there is no known theoretical description of the stress-strain behaviour of the MFT. [2, 40] The theoretical frame-work of the MFT outlined herein follows the approach of the Warner & Terentjev book [40] and assumes that (a) the rotation of the director is instantaneous at the critical strain (λ_c) and (b) there is no change in nematic ordering before or after transition, therefore, the

$\mathbf{det}(\underline{\underline{l}})/\mathbf{det}(\underline{\underline{l_0}})$ term in equation 3.14 is ignored. The MFT has two free energy equations based on the two different scenarios of the director involved, one free energy equation before the director rotation (F_{el}^A), where the director is perpendicular to the applied strain, and one after the sharp rotation of the director (F_{el}^B) where the director is parallel to the applied strain. Extensions (λ) are applied in the x direction perpendicular to the initial nematic director which is aligned along z. The initial step-length tensor, before the rotation of the director, is given by $\underline{\underline{l_0}} = \text{Diag}(l_\perp, l_\perp, l_\parallel)$ and since there is no change in nematic ordering F_{el}^A is given by: [40]

$$F_{\text{el}}^A = \frac{1}{2}\mu\left(\lambda^2 + \left(\frac{1}{\lambda_{zz}\lambda}\right)^2 + \lambda_{zz}^2\right), \tag{3.26}$$

where the conservation of volume requires that $\lambda_{yy} = 1/\lambda_{zz}\lambda$. After the rotation of the nematic director, the step-length tensor has jumped to towards the strain axis (x) and the new step-length tensor is $\underline{\underline{l}} = \text{Diag}(l_\parallel, l_\perp, l_\perp)$. By substituting $\underline{\underline{l_0}}$ and $\underline{\underline{l}}$ into equation 3.14 F_{el}^B can be determined: [40]

$$F_{\text{el}}^B = \frac{1}{2}\mu\left(\frac{\lambda^2}{r} + \left(\frac{1}{\lambda_{zz}\lambda}\right)^2 + \lambda_{zz}^2 r\right). \tag{3.27}$$

Both F_{el}^A and F_{el}^B are minimised with respect to λ_{zz} which leads to the final equations: [40]

$$\begin{aligned} F_{\text{el}}^A &= \frac{1}{2}\mu\left(\lambda^2 + \frac{2}{\lambda}\right), \\ F_{\text{el}}^B &= \frac{1}{2}\mu\left(\frac{\lambda^2}{r} + \frac{2\sqrt{r}}{\lambda}\right). \end{aligned} \tag{3.28}$$

F_{el}^A and F_{el}^B have similar forms, however the natural state of F_{el}^B is at $\lambda = \sqrt{r}$ as opposed to $\lambda = 1$. The free energy functions are shown in figure 3.5 where it can be seen that F_{el}^A and F_{el}^B are the same at an extension defined as λ_{c}. The critical extension ratio can be determined by setting $F_{\text{el}}^A = F_{\text{el}}^B$ and solving for λ: [40]

$$\lambda_{\text{c}} = r^{\frac{1}{3}}\left(\frac{2}{\sqrt{r}+1}\right)^{\frac{1}{3}} = \lambda_{\text{m}}\left(\frac{2}{\sqrt{r}+1}\right)^{\frac{1}{3}}, \tag{3.29}$$

where $\lambda_m = r^{1/3}$ is the spontaneous deformation that occurs during the isotropic to nematic transition and $\lambda = \lambda_m$ is the limit of stability for F_{el}^{A}. [40]

In the approach above, it is assumed that the nematic ordering remains constant throughout the deformation. However, theoretical work on the MFT by Bladon *et al.* [113, 114] has shown that the free energy barrier of rotation can be reduced by a reduction in the uniaxial nematic ordering and the emergence of biaxial order along the strain axis before the transition has occurred. The reduction in uniaxial order has been observed by Roberts *et al.* using x-ray diffraction measurements. [70] The determination of order parameters using Raman spectroscopy performed in chapter 8 show a similar reduction in the uniaxial order and, additionally, an emergence in biaxial order parameters.

3.5 Summary

To summarise, the 'Trace formula', which is the free energy equation of an LCE under deformation, has been derived. The behaviour of LCEs under perpendicular strain is considered with two particular scenarios outlined. These are the semi-soft elastic (SSE) response and the Mechanical Fréedericksz transition (MFT). In the SSE, after an initial strain is reached (λ_1), the director rotates continuously and there is a softening in the stress-strain response. It is revealed that the soft elastic response arises due to the existence of an isotropic reference state accessible through the deformation tensor $\underline{\underline{\lambda_m}}$. However, in real LCEs, the reference state is not completely isotropic which leads to the semi-soft elastic response. [40, 111] In the MFT, the director rotates sharply at a critical strain (λ_c). In the approach of section 3.4 it is assumed that the nematic order of the system remains constant. However, theoretical work by Bladon *et al.* considers the change in order during the MFT revealing that there is a decrease in uniaxial order with the emergence of biaxial order. [113, 114] In addition to work by Bladon *et al.*, work by Finkelmann *et al.* considers anisotropic elasticity of a nematic LCE deformed without director rotation; [115] as such the work by Finkelmann *et al.* describes the situation of a real LCE under small deformations and an LCE exhibiting a MFT but before the director has rotated. The theoreti-

cal approach of Finkelmann *et al.* is introduced in chapter 8 when the emergence of biaxiality of a nematic LCE is investigated via Raman spectroscopy.

Chapter 4

Experimental I: Materials and LCE synthesis

This chapter describes the materials and synthesis steps required to produce the LCEs used throughout this thesis. The chemical composition of the LCE was designed by Mistry *et al.*, [2, 108] based on the LCE chemistry developed by Urayama *et al.* [116], with the aim to produced a precursor mixture that can be polymerised in the nematic phase at room temperature.

4.1 Cell assembly

To accurately characterise the behaviour of LCEs it is necessary that well-aligned, uniformly orientated samples with a uniform thickness are produced. To achieve this cells, which act as moulds for the final LCE samples, are assembled. The cell gap dictates the maximum thickness of the LCE produced and ensures that the final LCE sample has a uniform thickness. Additionally, if required, an alignment layer can be applied to the substrates of the cells to induce a uniform alignment in the final LCE sample. The cells are produced from two different substrates; 75mm × 25mm × 1mm (L×W×T) glass microscope slides and 60mm × 20mm × 100μm Melinex 401 films (DuPont Teijin Films). The melinex film is a flexible polymer based substrate; this substrate is used instead of glass as its flexibility allows it to be more easily removed from the polymerised LCE sample. Before

assembly the substrates are cleaned to remove any contaminants. The cleaning procedure is as follows:

- **Glass**: (i) sonicate with de-ionised water and decon 90 for 30 minutes, (ii) sonicate with de-ionised water for 30 minutes, (iii) sonicate with acetone for 30 minutes, (iv) sonicate with methanol for 30 minutes.
- **Melinex**: (i) rinse with de-ionised water to remove any visible debris, (ii) sonicate with methanol for 30 minutes.

The clean substrates are dried with an air gun to remove any remaining methanol after which assembly can begin.

If alignment is required both substrates are spin coated with a 0.5% polyvinyl alcohol (PVA) solution. PVA is desirable over other alignment layers for two reasons: (i) PVA can be dissolved into water which is not a solvent for the Melinex substrates and (ii) it is not necessary to bake PVA at elevated temperatures thus preventing the Melinex substrates from shrinking and warping. The PVA solution is created by dissolving 0.5g of PVA (molecular weight=>89,000) into 100ml of deionized water by constantly stirring with a magnetic stirrer at 100 rpm and 80°C. The PVA solution (0.5% wt) is pipetted onto the surface of each substrate ensuring that the whole surface is covered. Each substrate is spin-coated at 1800 rpm for 30 seconds followed by 40 seconds of spinning at 4200 rpm. The unaligned PVA layer is rubbed in the desired direction using the in-house rubbing machine *'Tippler'* in the following manner: Firstly, the substrates are secured onto a vacuum plate which is motorised to allow for lateral movement; the vacuum plate makes several passes underneath a rotating cylinder which is covered in velvet cloth and set at the correct height to allow for contact between the fibres of the cloth and the substrate surface. The contact of the velvet cloth fibres forces the PVA to align in the rubbing direction.

A cell is assembled by applying UVS 91 glue (Norland) along the long axis of the Melinex substrate. 100 μm Melinex ($\sim$2mm $\times$ 75mm) spacers are placed on top of the lines of adhesive and a further line of UVS 91 is placed along the spacers. The glass substrate is placed on top of the glue covered spacers ensuring that the rubbing directions of the substrates aligned in an anti-parallel manner.

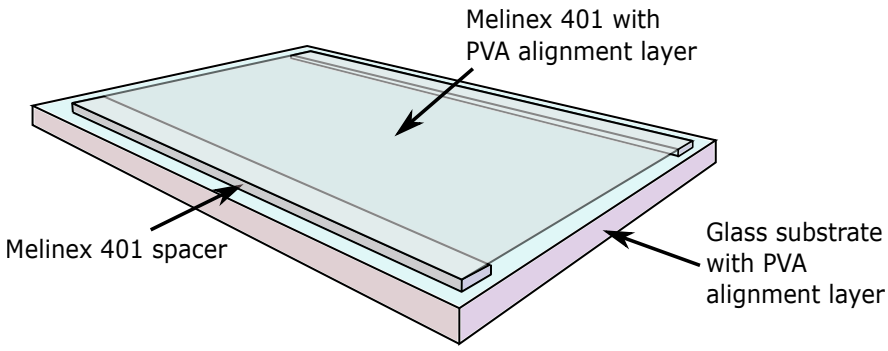

Figure 4.1: Schematic of an assembled cell. The steps required to assemble the cell are described in section 4.1.

The cell is placed onto a metal block and an even pressure is applied by magnets to ensure uniform thickness across the cell. The clamped cell is polymerised under a UV source ($\sim$2.5 mW^{-2}) for 10 minutes. A schematic of an assembled cell can be seen in figure 4.1.

4.2 LCE synthesis

The chemicals required to synthesise the LCE used throughout this thesis are: 1,4-bis-[4-(6-acryloyloxyhex-yloxy)benzoyloxy]-2-methylbenzene (RM82), 6-(4-cyano-biphenyl-4′-yloxy)hexyl acrylate (A6OCB), 2-ethylhexyl acrylate (EHA), 4-cyano-4-hexyloxybiphenyl (6OCB), and methyl benzoylformate (MBF). [2] The LCE network is formed from the bifunctional reactive mesogen, RM82, which acts as a cross-linker for the LCE network; the mono-functional reactive mesogen A6OCB; and the non-mesogenic spacer EHA. The non-reactive mesogen, 6OCB, is added to broaden the nematic phase of this mixture allowing for polymerisation at room temperature. [2, 108] Methyl benzoylformate (MBF) is a UV-photoinitiator. The chemical structures of RM82, A6OCB, EHA and 6OCB and MBF can be seen in figure 4.2 and the % mol of these chemicals can be seen in table 4.1.

Chemically identical LCEs can be synthesised in the isotropic, monodomain nematic and polydomain phase, the initial steps for each phase are as follows:

- A6OCB, 6OCB and RM82 are added into a clean glass vial containing the

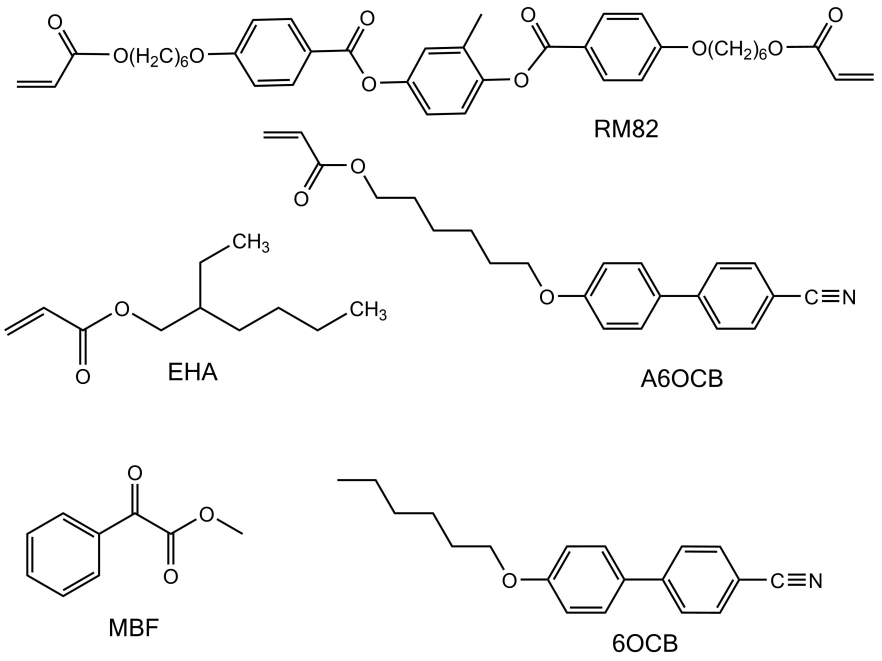

Figure 4.2: Structures of the constituent chemicals of the LCE.

magnetic stirrer bead. The mass of each material used is confirmed with a digital weighing scale it is ensured that there is a maximum difference of ±0.3 mg between the masses recorded and the desired masses. The sample vial containing A6OCB, 6OCB and RM82 is placed onto a hot plate at -110°C for 5 minutes to melt the materials.

- Using an Eppendorf pipette EHA and MBF are added to the sample vial. Since EHA and MBF are volatile materials the temperature of the hot plate is reduced to 40°C. The hot plate is set to stir at 70 rpm and left for 5 minutes to ensure the materials are well mixed. At this temperature the precursor mixture is in the isotropic phase. [2]

The solid LCE samples can be produced in the isotropic phase, the monodomain nematic phase or the polydomain nematic phase. However, in all cases the cells are capillary filled with the liquid precursor mixture in the isotropic phase to prevent issues with shear alignment. The following steps depends on the phase of the final LCE film required:

Component	% mol in monomer mixture	% mol in final LCE
A6OCB	14.6 ± 0.1	34.3 ± 0.3
6OCB	55.9 ± 0.3	-
RM82	7.1 ± 0.1	16.7 ± 0.3
EHA	20.9 ± 0.1	49.0 ± 0.1
MBF	1.56 ± 0.07	-

Table 4.1: Chemical composition of the LCE used throughout this thesis.

- **Isotropic LCE**: the precursor mixture is filled into an ***unaligned*** cell and placed on a hot stage at 60°C for 5 minutes. The precursor mixture is UV polymerised (source: ∼2.5 mW^{-2}) at 60°C for two hours.
- **Monodomain nematic LCE**: the precursor mixture is filled into an ***aligned*** cell at 40°C. The filled cell is removed from the hot stage and left at room temperature for 20 minutes to cool into the nematic phase. The precursor mixture is UV polymerised (source: ∼2.5 mW^{-2}) at room temperature for two hours.
- **Polydomain nematic LCE**: the precursor mixture is filled into an ***unaligned*** cell at 40°C. The filled cell is removed from the hot stage and left at room temperature for 20 minutes to cool into the nematic phase. The precursor mixture is UV polymerised (source: ∼2.5 mW^{-2}) at room temperature for two hours.

After polymerisation, the Melinex substrate is removed from the cell with a scalpel. The Melinex spacers are cut away and the LCE film is removed from the glass substrate. The sample is still swollen with the non-reactive mesogen 6OCB and MBF; these are washed out from the network by leaving the LCE in a ∼70:30 methanol/dichloromethane for a minimum of 12 hours. The now deswollen samples are left on a hot plate at 40°C for 2 hours to dry. A simplified schematic of the final LCE network is shown in figure 4.3. Figure 4.3 is included to show the acrylate backbone and constituent chemicals, however, the polymerisation of the network is random and the other possible network morphologies are not included in the schematic.

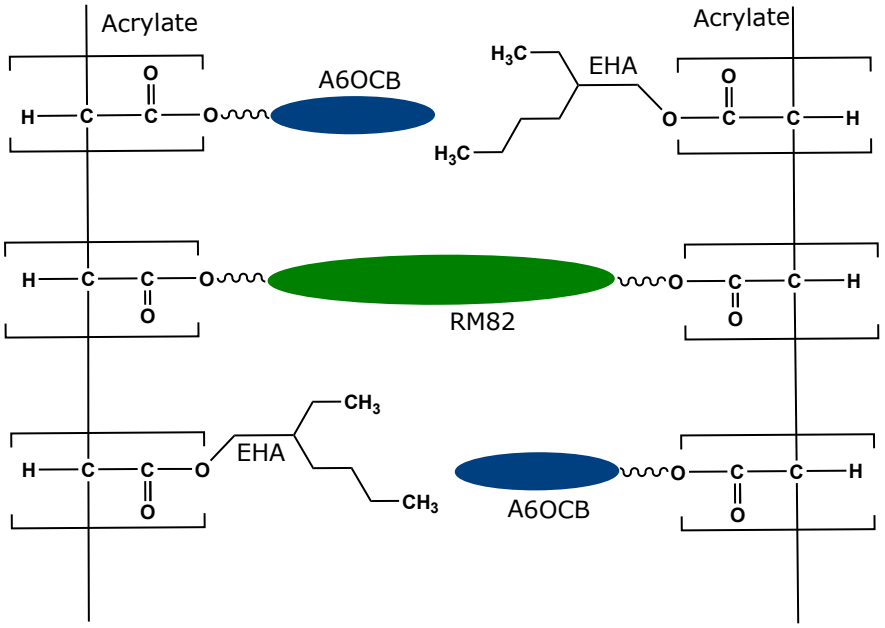

Figure 4.3: Schematic of the polymerised LCE network showing the constituent chemicals.

4.3 Summary

In this chapter, the constituent chemicals and synthesis steps required to produce acrylate LCE films of various alignments are outlined. The LCE described herein, in the monodomain nematic phase, displays an MFT to perpendicularly applied strain in addition to a molecular auxetic response. [1, 2] These interesting behaviours are explored in chapters 8 to 10 by performing various experiments on the LCE. Producing repeatable samples in the manner described above is an important part in understanding these behaviours.

Chapter 5

Experimental II: Raman spectroscopy

Raman scattering is the inelastic scattering of light that results from the interaction of incident light with the vibrational and rotational modes of the molecules in the medium being probed. [117–119] The wavelength of the scattered light is shifted by an amount related to the mode the light has interacted with and is therefore 'chemically specific'. [119, 120] This makes Raman scattering a useful probe into the microscopic and molecular nature of materials. Additionally, Raman scattering is polarisation dependent which allows for the determination of order parameters in liquid crystal and polymer systems. [79–87, 104, 118]

Other spectroscopic techniques have been employed to determine the order parameters in liquid crystals; namely x-ray diffraction and infrared (IR) spectroscopy. [89] Both Raman and IR spectroscopy are examples of vibrational spectroscopic techniques and are typically considered complementary techniques for complete chemical analysis, however, Raman and IR have different selection rules. [119] IR is better at determining asymmetric vibrations of polar groups whilst Raman is better at determining symmetric vibrations of non-polar groups; additionally Raman is not particularity affected by the presence of water unlike IR. IR can determine $\langle P_{200} \rangle$ (Q or often 'S') and biaxial order parameters (P, D, C). [103] However, Raman spectroscopy can determine uniaxial order parameters up to 4^{th} rank ($\langle P_{200} \rangle$ and $\langle P_{400} \rangle$) and, in principal, biaxial order parameters up to 4^{th} rank; [87, 103] this makes Raman spectroscopy a powerful technique in

liquid crystal research. The Raman scattering process occurs every 1 in 10^7 photons producing a relatively weak signal. [117, 118] However, with the invention of high power monochromatic lasers this technique has become a readily-available experimental technique.

This chapter begins by introducing the origins of Raman scattering in the simplified scalar case. The Raman tensor is then introduced and it is shown how this can be related to the order parameters of a liquid crystal phase through the orientational distribution function (ODF). The fitting functions on the Raman signal are presented for the uniaxial and biaxial nematic phases, the approach of this thesis closely follows the work presented in the thesis of Southern [83] and the thesis of Zhang. [85] Finally the experimental set up is shown.

5.1 Raman scattering

5.1.1 Scalar case

When an electromagnetic wave is incident on a material it induces an oscillating electrical dipole moment. This oscillating dipole re-emits EM waves which is the source of scattered light. Most light is scattered elastically which is known as Rayleigh scattering. Raman scattering is one of the inelastic scattering processes; the light is re-emitted with a shift in the wavelength (energy) when compared to the incident wavelength. The cause of this Raman shift is the interaction of incident light with the rotational and vibrational resonances of the molecules in the material [117–119]. Rotational Raman scattering is typical only significant in the gaseous phase therefore the remainder of this chapter will focus on vibrational Raman spectroscopy. Raman scattering can be understood by consideration the dipole moment of a material with light incident on it:

$$\mu = \alpha_{\mathrm{m}} E_0 \cos(2\pi\nu_0 t), \tag{5.1}$$

where μ is the induced dipole, α_{m} is the molecular polarisability, E_0 is the amplitude of the incoming EM radiation, ν_0 is the frequency of the incident light and t is time. The polarisability, α_{m}, is related to the oscillations of atoms about

their equilibrium position in molecules. By assuming simple harmonic motion, the displacement of the atoms as a function of time can be written as:

$$Q_{\mathrm{d}} = Q_{\mathrm{d},0}\cos(2\pi\nu_{\mathrm{vib}}t), \tag{5.2}$$

where Q_{d} is the displacement of the atom, $Q_{\mathrm{d},0}$ is maximum amplitude of displacement from equilibrium position and ν_{vib} is the vibration frequency. Since the polarisability depends on Q_{d}, we can perform a Taylor expansion of α_{m}: [117–119]

$$\begin{aligned}\alpha_{\mathrm{m}} &= \alpha_{\mathrm{m},0} + \left(\frac{\partial\alpha_{\mathrm{m}}}{\partial Q_{\mathrm{d}}}\right) \times Q_{\mathrm{d}} + ..., \\ \alpha_{\mathrm{m}} &= \alpha_{\mathrm{m},0} + \left(\frac{\partial\alpha_{\mathrm{m}}}{\partial Q_{\mathrm{d}}}\right) \times Q_{\mathrm{d},0}\cos(2\pi\nu_{\mathrm{vib}}t).\end{aligned} \tag{5.3}$$

By substituting equation 5.3 into equation 5.1:

$$\begin{aligned}\mu_{\mathrm{m}} &= \left[\alpha_{\mathrm{m},0} + \left(\frac{\partial\alpha_{\mathrm{m}}}{\partial Q_{\mathrm{d}}}\right)\right] \times E_0\cos(2\pi\nu_0 t), \\ &= \alpha_{\mathrm{m},0}E_0\cos(2\pi\nu_0 t) + \left(\frac{\partial\alpha_{\mathrm{m}}}{\partial Q_{\mathrm{d}}}\right) Q_{\mathrm{d},0}E_0\cos(2\pi\nu_{\mathrm{vib}}t)\cos(2\pi\nu_0 t).\end{aligned} \tag{5.4}$$

Using the double cosine rule equation 5.4 becomes:

$$\begin{aligned}\mu_{\mathrm{m}} &= \alpha_{\mathrm{m},0}E_0\cos(2\pi\nu_0 t) + \\ \frac{1}{2}&\left(\frac{\partial\alpha_{\mathrm{m}}}{\partial Q_{\mathrm{d}}}\right) Q_{\mathrm{d},0}E_0[\cos(2\pi t(\nu_0 - \nu_{\mathrm{vib}})) + \cos(2\pi t(\nu_0 + \nu_{\mathrm{vib}}))].\end{aligned} \tag{5.5}$$

In equation 5.5 there are 3 scattering process, these are the elastic Rayleigh (ν_0) scattering process and the inelastic Stokes ($\nu_0 - \nu_{\mathrm{vib}}$) and Anti-Stokes ($\nu_0 + \nu_{\mathrm{vib}}$) scattering processes. The Stokes and anti-Stokes scattering processes only occur in cases where vibrations change polarisability (i.e. $\partial\alpha_{\mathrm{m}}/\partial Q \neq 0$) [118] and typically the Stokes line is selected for Raman spectroscopy as it has a higher intensity than the anti-Stokes line. [117, 118] The Raman shift, in both the Stokes and anti-Stokes case, is given by:

$$\Delta\nu = \frac{1}{\lambda_0} - \frac{1}{\lambda_s}, \tag{5.6}$$

where λ_0 is the wavelength of the incident light, λ_s is the wavelength of the scattered light. From equation 5.6, we can see that the Stokes scattering process produces a positive Raman shift and anti-Stokes scattering produces a negative Raman shift. The intensity of the Raman peak is given by: [119]

$$I \propto \left(\frac{\partial \alpha_{\mathrm{m}}}{\partial Q_{\mathrm{d}}}\right)^2. \tag{5.7}$$

5.1.2 Tensorial case

In the above case, the polarisability is taken to be scalar. In fact the polarisability is tensorial. Equation 5.1 is therefore:

$$\vec{P} = \bar{\bar{\alpha}}_{\mathrm{m}} \times \vec{E}_0 \cos(2\pi\nu t), \tag{5.8}$$

where $\bar{\bar{\alpha}}_{\mathrm{m}}$ is the tensorial polarisability. Equation 5.7 states that the intensity of the Raman scattering process is proportional to the square of the differential polarisability. We now introduce the differential polarisability tensor for a particular mode:

$$\left(\frac{\alpha_{ij}}{\partial Q_{\mathrm{d}}}\right)^2 = \begin{pmatrix} \alpha'_{xx} & \alpha'_{xy} & \alpha'_{xz} \\ \alpha'_{yx} & \alpha'_{yy} & \alpha'_{yz} \\ \alpha'_{zx} & \alpha'_{zy} & \alpha'_{zz} \end{pmatrix}, \tag{5.9}$$

where α'_{ij} is short hand notion for the differential of α_{ij} with respect to Q. By selecting appropriate principal axes equation 5.9 simplifies into:

$$\left(\frac{\alpha_{ij}}{\partial Q_{\mathrm{d}}}\right)^2 = \begin{pmatrix} \alpha'_{xx} & 0 & 0 \\ 0 & \alpha'_{yy} & 0 \\ 0 & 0 & \alpha'_{zz} \end{pmatrix}. \tag{5.10}$$

Note that for a uniaxial system, $\alpha'_{xx} = \alpha'_{yy} = \alpha'$ and $\alpha'_{zz} = \alpha'_{zz}$. In general, for liquid crystal systems, $\alpha' \neq \alpha'_{zz}$. The anisotropy of the differential polarisability allows for the determination of order parameters of a liquid crystal phase. For a uniaxial system equation 5.10 can be rewritten in terms of the differential

polarisability ratio (p):

$$\left(\frac{\alpha_{ij}}{\partial Q_{\mathrm{d}}}\right)^2 = \begin{pmatrix} \alpha' & 0 & 0 \\ 0 & \alpha' & 0 \\ 0 & 0 & \alpha'_{zz} \end{pmatrix} = \alpha'_{zz} \begin{pmatrix} p & 0 & 0 \\ 0 & p & 0 \\ 0 & 0 & 1 \end{pmatrix}, \tag{5.11}$$

where the differential polarisability ratio is given by $r = \alpha'/\alpha'_{zz}$.

5.2 Selection of Raman peaks for calculation of order parameters in liquid crystal phases

In section 5.1.2 the differential polarisability tensor, or Raman tensor, was introduced. The generalised form of the Raman tensor is shown in equation 5.9. However, by defining a principal axis and assuming uniaxial anisotropy the Raman tensor is now equation 5.11 and the differential polarisability ratio (p) is introduced. The spectral range of Raman scattering events is typically between 200cm^{-1} and 3000cm^{-1}. [117, 119] Of particular interest are the 1606cm^{-1} and 2225cm^{-1} peaks. These represent the phenyl-stretching mode and the cyano-stretching mode, respectively. [120] Both of which are present in many liquid crystalline molecules (for example the n-CB series). A normalised Raman spectra of the acrylate LCE used within this thesis can be seen in figure 5.1.

Careful selection of the Raman band is necessary for useful determination of an order parameter. In polymeric materials, bond are typically selected which have a principal axis along coincident with the chain axis. [121] For liquid crystals, it is ideal to select a molecular vibration that best represents the nematic order parameter. For this to be the case the band selected needs satisfies some assumptions. These are, (i) that the molecular vibration itself is cylindrically symmetric and (ii) the bond vibration is parallel to the molecular long axis of the material. The 1606cm^{-1} (phenyl-stretching) and 2225cm^{-1} (cyano-stretching) peaks have be used to determine the order parameter in liquid crystal phases. [79, 80, 104, 122] The phenyl-stretching mode closely follows Maier-Saupe theory predictions for conventional nematic liquid crystal phases and therefore appears

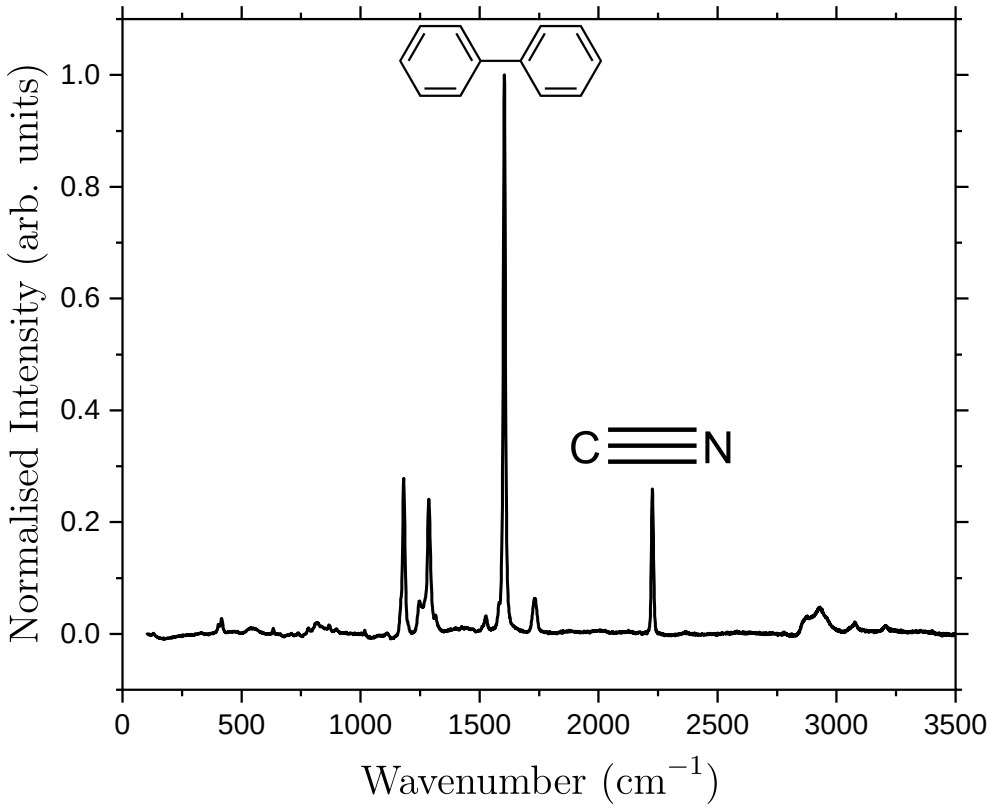

Figure 5.1: Typical Raman spectra for the acrylate LCE studied herein. The phenyl-stretching mode (1606 cm^{-1}) and the cyano-stretching (2250 cm^{-1}) are shown. These particular Raman modes are prevalent in many liquid crystalline systems.

to satisfies these assumptions reasonably well. [88] The cyano-stretching mode appears to not satisfy the assumption of cylindrical symmetry and therefore produces a miss-match in the calculated order parameter (particularly $\langle P_{400} \rangle$) when compared to theoretical predictions. [88]

5.3 Polarised Raman spectroscopy and the orientational distribution function (ODF)

Consider, as shown in figure 5.2a, a single molecule in a LC phase. The complete orientation of the molecule with respect to the nematic director (z_{D}) can be de-

scribed by the Euler angles (α,β,γ). The long axis of the molecule is orientated along z_{M}. When a cylindrically symmetric bond vibration is selected which has a vibration axis along the molecular long axis (z_{M}) equation 5.11 accurately describes the differential polarisability tensor of the molecule. Thus, the microscopic properties of the molecule can be related to the Raman intensity by substituting equation 5.11. into equation 5.7.

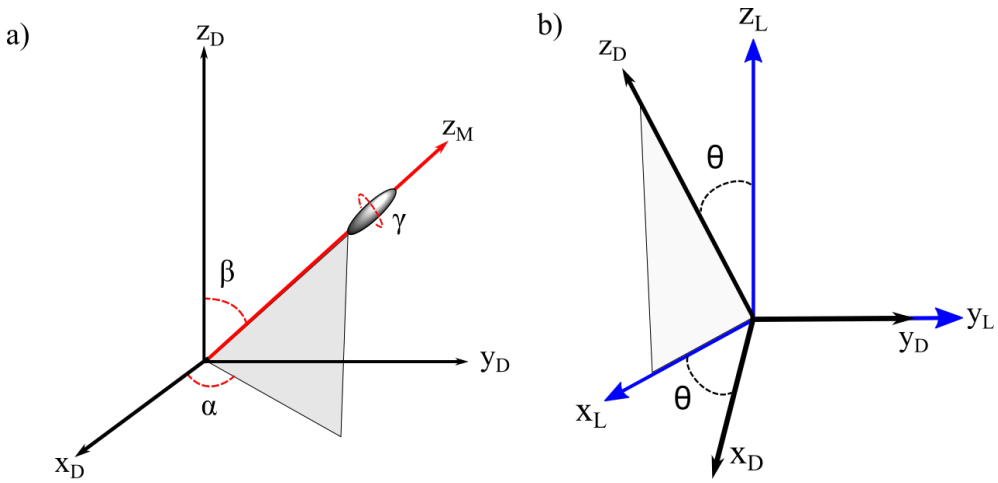

Figure 5.2: (a) Schematic showing the Euler angles (α, β, γ) of a liquid crystal molecule with its long axis (z_{M}) at an angle (β) from the director (z_{D}). z_{M} corresponds to the molecular long axis. (b) Shows the laboratory frame relating the angle between the incident laser polarisation and the director of nematic director (θ). In this case the laser travels along the y_{L} axis.

However, the incoming laser, and thus the back-scattered Raman intensity, has a finite sampling size. Raman spectroscopy therefore probes the macroscopic state of the LC phase not the individual molecule's microscopic properties. The intensity of a selected Raman peak is therefore a statistical average of the contribution from individual molecules which, as discussed in detail in 2.1, can be described through an orientational distribution function (ODF). The intensity of the Raman signal in the laboratory frame: [81–83, 85, 86]

$$I_{ij} \propto \langle \alpha'^2_{ij} \rangle = \int_0^{2\pi} d\alpha \int_0^{\pi} \sin\beta d\beta \int_0^{2\pi} d\gamma \alpha'^2_{L_{ij}} f(\alpha, \beta, \gamma), \tag{5.12}$$

where i and j denote the orientation of the analyser and polariser with respect to the planar aligned sample, $\langle ... \rangle$ is an ensemble average, $f(\alpha, \beta, \gamma)$ is the ODF and $\alpha'_{L_{ij}}$ is the components of the molecular polarisability measured in the laboratory frame. The 'laboratory frame' is shown in figure 5.2b and is the coordinate frame for any experimental measurement of the Raman intensity. In the laboratory frame the laser light is incident on the LC sample in y_{L} direction. The polarisation of the laser light occurs in the $x_{\mathrm{L}} - z_{\mathrm{L}}$ plane and makes an angle (θ) with the nematic director z_{D}.

In equation 5.12 the intensity of the Raman signal in the laboratory frame is related to the ODF. The form of the ODF depends on the symmetry of the LC phase and the molecules within the phase as is discussed in detail in section 2.1. In all cases the ODF can be constructed as a summation of order parameters, for example, the ODF of a uniaxial phase comprised of uniaxial molecules is given by:

$$f(\beta) = \frac{1}{8\pi^2}[1 + \frac{5}{2}\langle P_{200}\rangle(3\cos^2\beta - 1) + \frac{9}{8}\langle P_{400}\rangle(3 - 30\cos^2\beta + 35\cos^4\beta)], \quad (5.13)$$

where $\langle P_{200}\rangle$ and $\langle P_{400}\rangle$ are the uniaxial order parameters and P_{200} and P_{400} are Legendre polynomials. Therefore the Raman intensity holds, experimentally accessible, information of the LC order.

5.4 Determination of order parameters from polarised Raman spectroscopy

5.4.1 Full depolarisation method

The incident laser light is polarised at a well-defined angle, θ, and normal to a planar aligned liquid crystal sample (see figure 5.2b). However, the back-scattered light is scattered with polarisations at various angles with respect to the polarisation of the incident light. The full depolarisation method determines order parameters by recording back-scattered light parallel to the incident laser light ($I_{\parallel}$) and the intensity of the back-scattered light perpendicular to the incident laser light ($I_{\perp}$) as a function of θ for $0° \geq \theta \geq 360°$. A fitting procedure is then

performed to determined $\langle P_{200}\rangle$, $\langle P_{400}\rangle$ and p. The fitting equations for the full depolarisation method are: [80]

$$\begin{aligned} I_{\parallel}(\theta) = k(\alpha'_{s_{zz}})^2 \times (A + B\langle P_{200}\rangle + 3C\langle P_{400}\rangle - 3B\langle P_{200}\rangle \cos^2\theta \\ -30C\langle P_{400}\rangle \cos^2\theta + 35C\langle P_{400}\rangle \cos^4\theta), \end{aligned} \tag{5.14}$$

$$I_{\perp}(\theta) = k(\alpha_{s_{zz}})^2 \times (D - E\langle P_{200}\rangle - 4C\langle P_{400}\rangle + 35C\langle P_{400}\rangle \cos^2\theta \sin^2\theta), \tag{5.15}$$

with:

$$A = \frac{8p^2 + 4r + 3}{15}, \tag{5.16}$$

$$B = \frac{8p^2 + 2r - 6}{21}, \tag{5.17}$$

$$C = \frac{(p-1)^2}{35}, \tag{5.18}$$

$$D = \frac{(p-1)^2}{15}, \tag{5.19}$$

$$E = -\frac{(p-1)^2}{21}. \tag{5.20}$$

where k is an experimental constant which is related to the incident light intensity, the transmission of the instrument and the light collection efficiency. [80] By keeping the experimental conditions the same during collection of the $I_{\parallel}(\theta)$ and $I_{\perp}(\theta)$ spectra, the value k can be negated by fitting to the 'depolarisation ratio' or 'depol ratio', $R(\theta)$:

$$R(\theta) = \frac{I_{\perp}(\theta)}{I_{\parallel}(\theta)}. \tag{5.21}$$

Note that in equations 5.14 and 5.15 only the angle θ is considered as it is required that sample is planar aligned and normal to the incoming laser thus there are no components of tilt.

Figure 5.3 shows $R(\theta)$ of 5CB at 23°C using the 1606^{-1} bond vibration. The full depolarisation ratio method is used to determine $\langle P_{200}\rangle$, $\langle P_{400}\rangle$ and p. Values of $\langle P_{200}\rangle = 0.63 \pm 0.05$, $\langle P_{400}\rangle = 0.30 \pm 0.05$ and $p = -0.24$ are found.

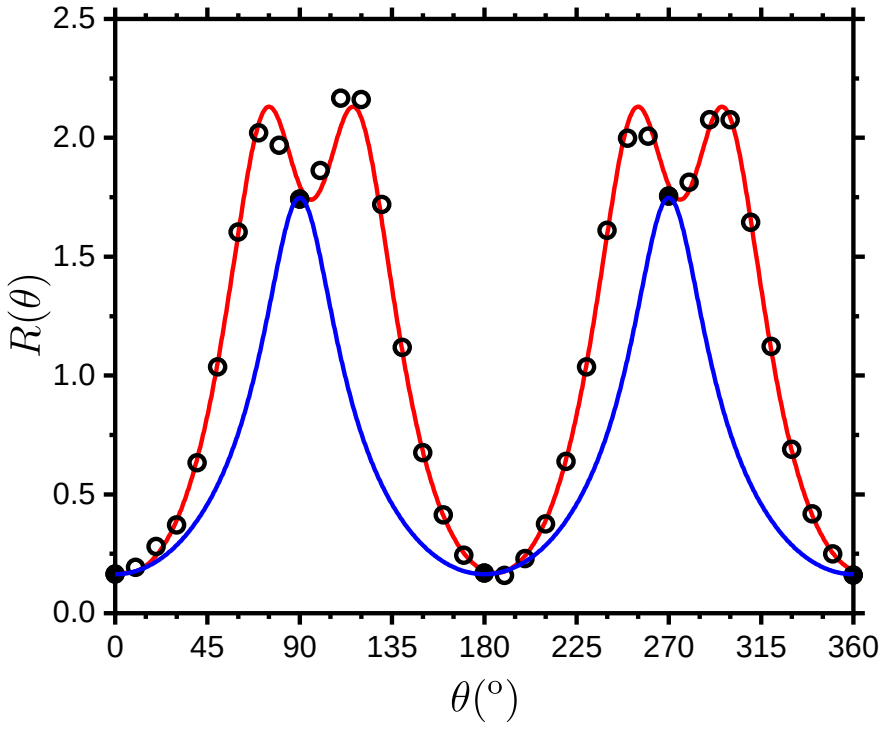

Figure 5.3: $R(\theta)$ of 5CB at 23°C determined from the 1606cm^{-1} peak. The red line shows the fitting to the data (black crosses) using the full depolarisation method; values of $\langle P_{200}\rangle = 0.63 \pm 0.05$, $\langle P_{400}\rangle = 0.30 \pm 0.05$ and $p = -0.24$ are deduced from the full depolarisation method. The blue line shows the fitting to the data using the '2 point method' where a value of $p = -0.04$ has been used as this is the value of p in the isotropic phase of 5CB; incorrect values of $\langle P_{200}\rangle = 0.53 \pm 0.05$, $\langle P_{400}\rangle = 0.11 \pm 0.05$ and $p = -0.04$ are deduced from the 2 point method.

5.4.2 Two point method

In principle, it is possible to determine the order parameters from polarised Raman spectroscopy (PRS) using only $R(\theta = 0°)$ and $R(\theta = 90°)$ provided that one of the required parameters ($\langle P_{200}\rangle$, $\langle P_{400}\rangle$, p) is known. Determining order parameters from only two points was pioneered by Jen *et al.* [104, 123] which is outlined fully in the appendix A. The Jen *et al.* method determines p from the depolarisation ratio in the isotropic phase R_{iso} and then $\langle P_{200}\rangle$ and $\langle P_{400}\rangle$ can be determined from $R(\theta = 0°)$ and $R(\theta = 90°)$. The Jen *et al.* has a key problem in that the value of p is often vastly different in the nematic phase and the

isotropic phase. [79, 81, 83, 85] Therefore, using p determined from the isotropic phase can result in incorrect values of order parameters; the value of $\langle P_{400} \rangle$ in particular can be erroneous, as it is more sensitive to the value p, with some early research reporting negative values of $\langle P_{400} \rangle$ in conventional nematic materials. [104, 123] The full depolarisation method results in more accurate and realistic values of $\langle P_{400} \rangle$; [79–81] as p is not assumed to be constant, instead, p is a fitting parameter which does not need to be determined via other means. In addition to, generally, more accurate values of $\langle P_{200} \rangle$ and $\langle P_{400} \rangle$, the full depolarisation method does not require the material to form an isotropic phase nor is there a need to apply Lax-Nelson corrections to the spectra (unlike in the 'two point method'). The Lax-Nelson corrections account for changes in the observed scattered signal intensity in anisotropic materials due to the non-collinearity of the laser and transmission losses at surfaces. [104, 124]

It should be noted that if p is predetermined correctly (i.e. not taken to be the value of p in the isotropic phase) the 'two point method' will produce sufficiently accurate values of $\langle P_{200} \rangle$ and $\langle P_{400} \rangle$. For example, when $p = -0.24$ is used the resulting fit for the 'two point method' for 5CB is $\langle P_{200} \rangle = 0.63 \pm 0.05$, $\langle P_{400} \rangle = 0.31 \pm 0.05$ which agrees with the values determined from the full depolarisation method (see figure 5.3) within error. In chapter 8, p is determined for an unstrained LCE using the full depolarisation method and then the two point method is used to study the change in order parameters as a function of strain. Doing so reduces the experimental time and therefore reduces the chance of sample breakage.

5.4.3 Phase biaxial order parameters from PRS

Thus far we have only considered cylindrically symmetric molecules which form uniaxial phases. In principle it is possible to determine biaxial order parameters in LC phases provided that some assumptions are made. The theory describing this was developed by Southern *et al.* and Zhang *et al.* [82, 83, 85, 87] with success determining the emergence of phase biaxiality in a bent-core LC biaxial SmA phase. [87] The approach in [87] considers a bent-core molecule with a bend angle with respect to the molecular long axis, however, in this thesis only linear

molecules need to be considered which simplifies the fitting functions greatly. The existence of biaxial phase order modifies the Raman fitting equations 5.14 and 5.15 as such: [87]

$$\begin{aligned} I_{\parallel}(\theta) &= \frac{4}{15}(3+4p+2p^2) \\ &- \frac{4}{21}\langle P_{200}\rangle(p-1)(3+4p)(1+3\cos 2\theta) \\ &+ \frac{1}{70}\langle P_{400}\rangle(p-1)^2(9+20\cos 2\theta+35\cos 4\theta) \\ &- \frac{16}{7}\langle P_{220}\rangle(p-1)(3+4p)\sin^2\theta \\ &+ \frac{24}{7}\langle P_{420}\rangle(p-1)^2(5+7\cos 2\theta)\sin^2\theta \\ &+ 8\langle P_{440}\rangle(p-1)^2\sin^4\theta, \end{aligned} \tag{5.22}$$

$$\begin{aligned} I_{\perp}(\theta) &= \frac{4}{15}(p-1)^2 \\ &+ \frac{4}{21}\langle P_{200}\rangle(p-1)^2 \\ &- \frac{1}{70}\langle P_{400}\rangle(p-1)^2(-3+35\cos 4\theta) \\ &+ \frac{8}{7}\langle P_{220}\rangle(p-1)^2 \\ &+ \frac{6}{7}\langle P_{420}\rangle(p-1)^2(1+7\cos 4\theta) \\ &+ 2\langle P_{440}\rangle(p-1)^2\sin^2 2\theta, \end{aligned} \tag{5.23}$$

where $\langle P_{200}\rangle$ and $\langle P_{400}\rangle$ are the uniaxial order parameters, $\langle P_{220}\rangle$, $\langle P_{420}\rangle$ and $\langle P_{440}\rangle$ are the phase biaxial order parameters, p is the molecular polarisability ratio, θ is the angle between the nematic director and the incident laser polarisation. It should be noted that whilst molecular biaxiality is ignored equations 5.22 - 5.23 still contain 6 fitting parameters ($\langle P_{200}\rangle$, $\langle P_{400}\rangle$, $\langle P_{220}\rangle$, $\langle P_{420}\rangle$, $\langle P_{440}\rangle$ and p). As such great care is required when fitting Raman data. In chapter 8 equations 5.22 - 5.23 are used to explore the emergence of biaxial ordering in a perpendicular strained LCE and the fitting the procedure to ensure sensible values of biaxial order is discussed fully.

5.4.4 Molecular biaxial order parameters from PRS

As discussed in chapter 2, non cylindrically symmetric molecules can be characterised by the molecular biaxial order parameters ($\langle P_{202}\rangle$, $\langle P_{402}\rangle$ and $\langle P_{404}\rangle$) which have a dependence on the Euler angle γ. One of the main assumptions in the Raman analysis described above is that the bond vibration has cylindrical symmetry [83, 85, 103] which means that the differential polarisability tensor (equation 5.11) can be represented by a single value of the differential polarisability ratio 'p'. However, if the molecular bond vibration has ellipsoidal symmetry the polarisability tensor is: [85, 88]

$$\left(\frac{\alpha_{ij}}{\partial Q_{\mathrm{d}}}\right)^2 = \begin{pmatrix} \alpha'_{xx} & 0 & 0 \\ 0 & \alpha'_{yy} & 0 \\ 0 & 0 & \alpha'_{zz} \end{pmatrix} = \alpha'_{zz} \begin{pmatrix} p_{xx} & 0 & 0 \\ 0 & p_{yy} & 0 \\ 0 & 0 & 1 \end{pmatrix}, \tag{5.24}$$

where $p_x x = \alpha'_{xx}/\alpha'_{zz}$ and $p_y y = \alpha'_{yy}/\alpha'_{zz}$ are the differential polarisability ratios in the xx and yy directions. The Raman fitting equations 5.14 and 5.15 for the uniaxial phase now contain the molecular biaxial order parameters: [88]

$$\begin{aligned} I_{\parallel} \propto\ & \frac{1}{15}(3 + 3p_{xx}^2 + 2p_{yy} + 3p_{yy}^2 + 2p_{xx}(1 + p_{yy})) \\ & - \frac{1}{42}\langle P_{200}\rangle(-6 + 3p_{xx}^2 - p_{yy} + 3p_{yy}^2 + p_{xx}(2p_{yy} - 1))(1 + 3\cos 2\theta) \\ & + \frac{1}{2240}\langle P_{400}\rangle(8 + 3p_{xx}^2 + 2p_{xx}(-4 + p_{yy}) - 8p_{yy} + 3p_{yy}^2) \\ & \times (9 + 20\cos 2\theta + 35\cos 4\theta) + \frac{1}{7}\langle P_{202}\rangle(p_{xx} - p_{yy})(1 + 3p_{xx} + 3p_{yy}) \\ & \times (1 + 3\cos 2\theta) - \frac{3}{112}\langle P_{402}\rangle(p_{xx} - p_{yy})(-2 + p_{xx} + p_{yy}) \\ & \times (9 + 20\cos 2\theta + 35\cos 4\theta) + \frac{1}{32}\langle P_{404}\rangle(p_{xx} - p_{yy})^2 \\ & \times (9 + 20\cos 2\theta + 35\cos 4\theta), \end{aligned} \tag{5.25}$$

$$
\begin{aligned}
I_{\perp} \propto & \frac{1}{15}(1+2p_{xx}^2-p_{yy}-p_{xx}(1+p_{yy})) \\
& -\frac{1}{42}\langle P_{200}\rangle(-2+p_{xx}^2-2p_{yy}+p_{yy}^2-p_{xx}(2-4p_{yy})) \\
& -\frac{1}{2240}\langle P_{400}\rangle(8+3p_{xx}^2+2p_{xx}(-4+p_{yy})-8p_{yy}+3p_{yy}^2) \\
& \times(-3+35\cos 4\theta)+\frac{1}{7}\langle P_{202}\rangle(p_{xx}-p_{yy})(-2+p_{xx}+p_{yy}) \\
& +\frac{3}{112}\langle P_{402}\rangle(p_{xx}-p_{yy})(-2+p_{xx}+p_{yy}) \\
& \times(-3+35\cos 4\theta)+\frac{1}{32}\langle P_{404}\rangle(p_{xx}-p_{yy})^2 \\
& \times(-3+35\cos 4\theta),
\end{aligned}
\tag{5.26}
$$

where $\langle P_{200}\rangle$, $\langle P_{400}\rangle$ are the uniaxial order parameters, $\langle P_{202}\rangle$, $\langle P_{402}\rangle$ and $\langle P_{404}\rangle$ are the molecular biaxial order parameters, θ is the angle between the nematic director and the incident laser polarisation. It is important to note that all the molecular biaxial terms ($\langle P_{202}\rangle$, $\langle P_{402}\rangle$, $\langle P_{404}\rangle$) contain a $(p_{xx}-p_{yy})$ term. Therefore, for bond vibrations with cylindrical symmetry, molecular biaxial order parameters, even if non-zero, do not contribute to the Raman depolarisation data. [85, 88] Throughout this thesis, the phenyl stretching mode is used to determine order parameters via PRS. The phenyl, stretching mode has been found to have near-cylindrical symmetry and provides the most physically realistic values of order parameter in the nematic phase. [85, 88] Due to the cylindrical symmetry of the phenyl stretching mode, molecular biaxial order parameters are not considered in the determination of order parameters in chapter 8.

5.5 Experimental set-up

The experimental set-up to determine the order parameters of an LC sample is shown in 5.4; this experimental set-up is used when measurement are performed with 'full depolarisation' or 'two point' method as the laboratory frame (figure 5.2b) is the same in both techniques. The whole system is encapsulated into a

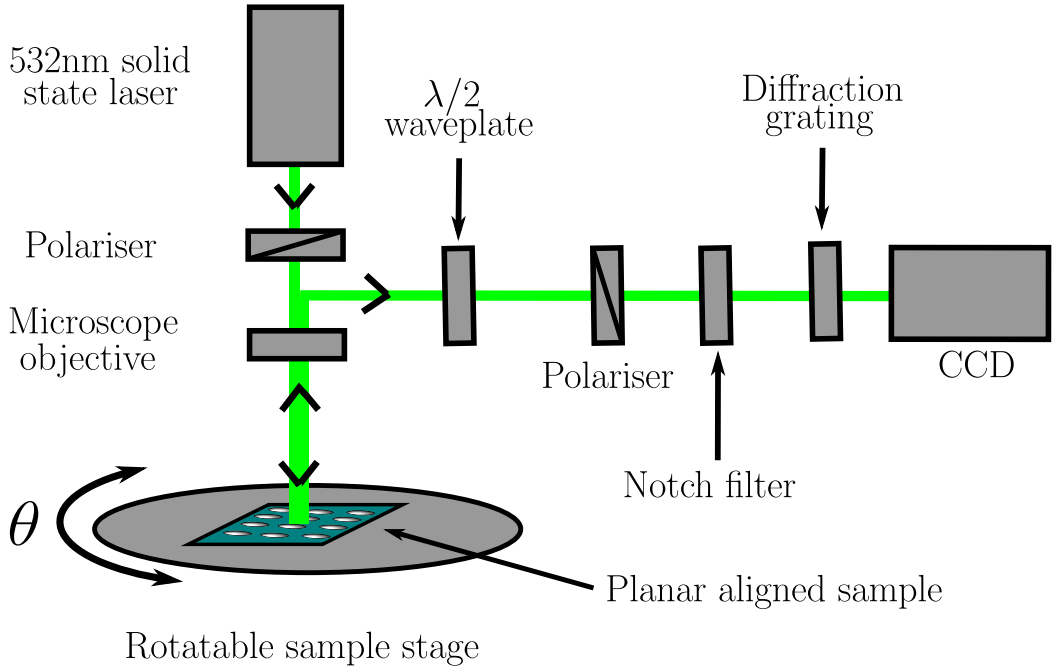

Figure 5.4: Schematic of the Raman spectrometer. The green line denotes the laser and the black arrows are the direction of the laser path which is in a back-scatter geometry. The whole Raman spectrometer as depicted is encapsulated in an polarised optical microscope.

polarised optical microscope, allowing for the simultaneous viewing of the sample and collection of the Raman spectra; additionally the polarised optical microscope allows one select and properly focus onto well-aligned regions of the sample. A 532.1nm 50mW solid state laser (Renishaw RLC532C) passes through a polariser, into a microscope objective and is incident on the sample; the laser power can be attenuated to prevent overexposure of light onto the sample. The sample is on a rotatable sample stage which allows for a change in θ. The light is reflected back up the microscope objective and passes through a second polariser. A $\lambda/2$ plate can be placed in front of the polariser to select for $I_{\parallel}$ ($\lambda/2$ plate out) or $I_{\perp}$ ($\lambda/2$ plate in). The backscattered light is then passed through a highly selective holographic notch filter which removes the Rayleigh scattering peak. Finally, the light is split by wavelength using a diffraction grating before terminating at charge-coupled device (CCD).

5.6 Summary

To summarise, the origin of the Raman scattering process is introduced. The tensorial nature of the Raman scattering process means that it carries information of the orientation of the Raman band. Since the intensity of a selected Raman band is averaged over a finite scattering volume, Raman spectroscopy measurements can be related to order parameters through the orientational distribution function (ODF). The assumptions of required for accurate determined of order parameters via Raman spectroscopy are discussed. Namely, these are the assumption of symmetrical bond vibration and the assumption that the vibration is aligned with the molecular long axis. With these assumption in mind it is suggested that the phenyl-stretching mode (1606 cm^{-1}) is selected for determination of order parameters. [88] Two techniques to determine order parameters via Raman spectroscopy are discussed, these are the 'full depolarisation' method and the 'two point' method. Finally, the modifications of the Raman intensity equations required to determined phase biaxial order parameters are discussed.

Chapter 6

Experimental III: Broadband dielectric spectroscopy

In chapter 1 the concept of a 'glass', which is a state of matter with non-equilibrium dynamics, is introduced. Glass formation can be understood in terms of the various molecular relaxations involved, therefore, to understand glassy behaviour it is desirable to probe these molecular relaxations and observe their temperature dependences. Broadband dielectric spectroscopy (BDS) is a technique in which an oscillatory electric field is applied to a sample and the subsequent dipole relaxations present in the material are recorded. BDS is a highly favoured technique due to the large dynamic window available which allows for the study of a large variety of dipole relaxations to be observed simultaneously. For example, the dielectric spectrometer used in this thesis has a dynamic window of 3×10^{-6} Hz - 4×10^{7} Hz. For polymeric materials, within the experimentally feasible frequency range, the dipole relaxations present are mainly related to the permanent or induced charge asymmetry of a particular molecular unit, hence, the study of dipole relaxations is related to molecular relaxations in the material. [125]

In this chapter the key principles of BDS are outlined. This chapter largely follows the approach of Kremer and Schönhals [27], Raju [126] and Böttcher and Bordewijk [127]. Once the fundamentals of BDS are outlined the experimental setup is discussed.

6.1 The dielectric response of materials

In this section the behaviour of a dielectric material in the presence of an electric field is discussed. It will be shown that the dielectric relaxation of a material in an oscillatory electric field results in a well-defined dipole relaxation frequency. First, the behaviour of a dielectric material in a static electric field is discussed to introduce concepts such as the dipole moment, dielectric constant and polarisation.

6.1.1 Static response

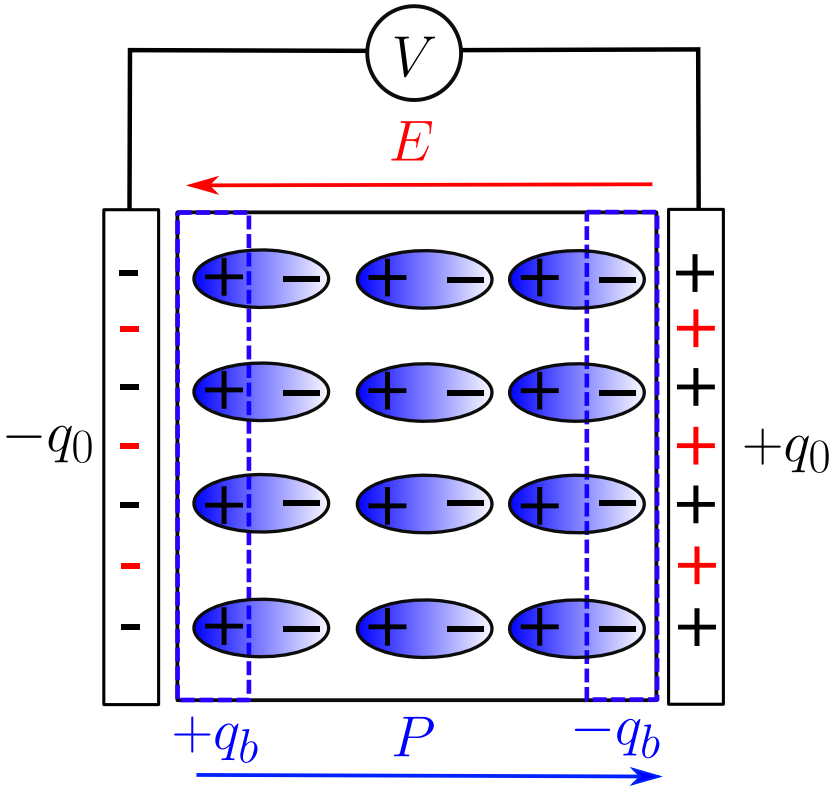

Figure 6.1: Schematic of a dielectric material placed between two capacitors with a charge build up, q_0, and a potential difference across the plates of V. There is a net polarisation, P, of dipoles in the dielectric material of and a build of bound charges, q_b, at the boundary of the dielectric material.

To understand the static behaviour of a dielectric material in an electric field consider two equally and oppositely charged plates of area A held at a separation d in a vacuum. There is a potential difference across the two parallel plates due to the presence of charges: [19, 126]

$$V_0 = \frac{q_0}{C_0}, \tag{6.1}$$

where V_0, q_0, C_0 are the potential difference, charge and capacitance in vacuum, respectively. For an empty capacitor, the capacitance is: [19, 126]

$$C_0 = \frac{\varepsilon_0 A}{d}, \tag{6.2}$$

where A is cross-sectional area of the capacitance plates and d is the distance between the capacitance plates. When a dielectric material is placed between two charged plates, there is a small displacement of the dipoles in the material which align with the electric field [128] as shown in figure 6.1. This results in 'bound' charges, q_b, at the surface of the dielectric material and a net polarisation, P, of the material. [19, 128] The 'true' charge, or total charge on the capacitor plate, q_0, remains unchanged and the difference between q_0 and q_b is known as the 'free' charge. If we assume that the potential difference is kept constant when a dielectric material is placed within the vacuum capacitor there must be an increase in true charge on the capacitor plate. [126] Using equation 6.1:

$$V = V_0 = \frac{q_0}{C_0} = \frac{q}{C}, \tag{6.3}$$

where C is the capacitance of the dielectric material and q is the charge on the parallel plates required to keep the potential difference constant for an empty capacitor and one with a dielectric material sandwiched between them. Rearranging for the difference in charge:

$$\begin{aligned} q - q_0 &= V_0(C - C_0) = V_0 C_0 \left(\frac{C}{C_0} - 1\right) \\ &= \frac{AV_0}{d}\varepsilon_0(\varepsilon - 1) = \varepsilon_0(\varepsilon - 1)AE, \end{aligned} \tag{6.4}$$

where $E = V/d$ is the electric field and ε is the dielectric constant of the material defined as: [19]

$$\varepsilon = \frac{C}{C_0}. \tag{6.5}$$

The increase in the charge required to generate the same potential difference is due to the presence of bound charges in the dielectric material through aligned dipoles. [126] The total dipole moment can therefore be defined as:

$$\mu = (q_1 - q_0)d = \varepsilon_0(\varepsilon - 1)AdE, \tag{6.6}$$

and the polarisation, or the net dipole moment per unit volume, of the dielectric material, P, can be defined as: [19, 126]

$$P = \frac{\mu}{Ad} = \varepsilon_0(\varepsilon - 1)E. \tag{6.7}$$

Polarisation of a dielectric material can occur via: [126, 129]

- Electronic polarisation - displacement of the electron cloud with respect to the nucleus.
- Orientational polarisation - the alignment of permanent dipoles.
- Atomic polarisation - displacement of atomic nuclei with respect to each other.
- Space charge polarisation - accumulation of charge within a boundary of an inhomogeneous system with differing conductivities or at the interfaces of the bulk material.

Electronic polarisation and atomic polarisation occurs in the frequency range of 10^{10} Hz - 10^{15} Hz [129] which exceeds the dynamic range of typical BDS measurements. However, within the dynamic range of a typical BDS measurement, one is likely to observe polarisation phenomena related to molecular relaxations within the material (orientational polarisation) or to the diffusion of ions within the material towards the electrodes (space charge polarisation). [125, 129]

6.1.2 Dynamics

Now that we have defined the terms in the case of a static electric field let us consider the case where the applied electric field is oscillatory. The applied electric field is of the form: [128]

$$E^*(\omega) = E_0 e^{i\omega t}, \tag{6.8}$$

where E_0 is the amplitude of the electric field, i is the imaginary number, ω is the angular frequency and t is time. The resulting polarisation and dielectric constant are therefore complex functions. Note, that since the complex dielectric constant has a frequency dependence it will be referred to as the complex (relative) dielectric permittivity from now on. [27, 130] The complex polarisation is of the form:

$$P^*(\omega) = \varepsilon_0 \left(\varepsilon^*(\omega) - 1\right) E, \tag{6.9}$$

where the complex dielectric permittivity is defined as: [27, 128]

$$\varepsilon^*(\omega) = \varepsilon^{'}(\omega) - i\varepsilon^{''}(\omega), \tag{6.10}$$

where $\varepsilon^{'}$ is the real part of the complex permittivity and is a measurement of the energy stored in the system per period and $\varepsilon^{''}$ is the imaginary part of the complex permittivity and is a measurement of the energy lost in the system per period. [27] Equation 6.7 holds true for steady electric fields and therefore must hold true in the limiting cases of $\lim(\omega \to 0)$ and $\lim(\omega \to \infty)$, hence: [27, 131]

$$\varepsilon^*(\omega \to 0) = \varepsilon_s, \tag{6.11}$$

$$\varepsilon^*(\omega \to \infty) = \varepsilon_\infty, \tag{6.12}$$

where ε_s and ε_∞ are the complex dielectric permittivity under steady and infinite frequency electric fields, respectively.

6.1.3 Debye single relaxation model

When an electric field is applied to a dielectric material, the polarisation of the material is not instantaneous but instead requires a finite time to reach a steady state polarisation value. [126, 128] Similarly, if the applied electric field is suddenly removed from the dielectric there is a decay in the polarisation. This lag in the dielectric response is often termed the *dielectric relaxation* [126]. The frequency dependence of the dielectric relaxation can be understood most simply by the 'Debye single relaxation model'.

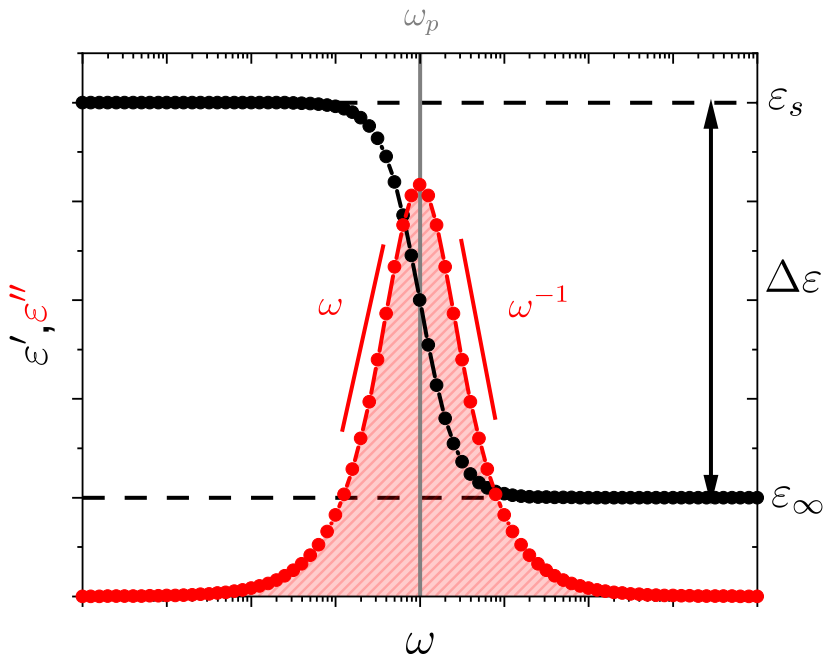

Figure 6.2: Frequency dependence of ε' and ε'' for the Debye single relaxation model.

The Debye single relaxation model assumes that the rate of change of the dielectric relaxation can be described by a single relaxation time: [27]

$$\frac{dP(t)}{dt} = -\frac{P(t)}{\tau_{\mathrm{D}}}, \tag{6.13}$$

where $P(t)$ is the time-dependent polarisation and τ_{D} is the 'Debye relaxation

time'. The solution to the differential in equation 6.13 is an exponential equation of the form: [19]

$$P(t) = P_\infty e^{-t/\tau_D}, \tag{6.14}$$

where P_∞ is the polarisation value of the material when polarised completely (i.e. under a strong electric field for an infinite amount of time). The relaxation of the polarisation can be expressed as a correlation function, Φ: [27, 131–133]

$$\Phi = \frac{P(t)}{P_\infty} = e^{-\tau_D/t}, \tag{6.15}$$

and the correlation function, Φ, can be related to the complex permittivity through the following equation: [27, 131–133]

$$\frac{\varepsilon^*(\omega) - \varepsilon_\infty}{\Delta\varepsilon} = 1 - i\omega \int_0^\infty \Phi(t) e^{-i\omega t} dt, \tag{6.16}$$

where $\varepsilon^*(\omega)$ is the complex dielectric permittivity in the frequency domain and $\Delta\varepsilon = \varepsilon_s - \varepsilon_\infty$ is the dielectric relaxation strength. Substitution of equation 6.15 into equation 6.16 can be solved via a known Laplace transform [27, 127] and leads to a complex permittivity of the following form:

$$\varepsilon^*(\omega) = \varepsilon_\infty + \frac{\Delta\varepsilon}{1 + i\omega\tau_D}. \tag{6.17}$$

Equation 6.17 is the key result of the Debye single relaxation model and the dependence of ε' and ε'' as a function of frequency is shown in figure 6.2. The Debye single relaxation model predicts the following behaviours: [27, 126]

- For frequencies well below the frequency of dielectric relaxation: $\varepsilon' \approx \varepsilon_s$ and $\varepsilon'' \approx 0$.
- For frequencies well above the frequency of dielectric relaxation: $\varepsilon'' \approx \varepsilon_\infty$ and $\varepsilon'' \approx 0$.
- ε'' peaks at a frequency, ω_p, called the 'peak relaxation frequency'.
- the gradient of the slopes either side of the peak are symmetric and follow a ω^1 or ω^{-1} power-law.

6.1.4 Empirical fitting: The Havriliak-Negami function

The idealised Debye single relaxation model generally does not describe real-world dielectric data particularly well. For example, the modulus of the power-law exponents of the ε'' peak is often smaller than unity and, therefore, the relaxation will have a peak breadth larger than that of the Debye response. [27, 134] Additionally, real-world dielectric data may have different values for the power-law exponents of the low-frequency and high-frequency flanks not described by the Debye model (i.e. the relaxation is asymmetric). [27, 134] The Havriliak-Negami (HN) function is an empirical fitting function which accounts for such deviations from the predictions by the Debye single model. [27, 135] The HN

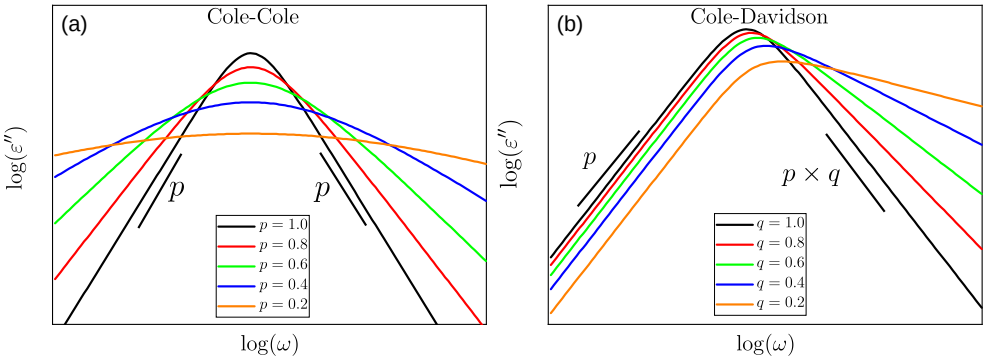

Figure 6.3: ε'' against frequency for (a) the Cole-Cole function ($p \neq 1, q = 1$) for various values of p and (b) the Cole-Davidson function ($p = 1, q \neq 1$) for various values of q.

function takes the form:

$$\varepsilon^*_{\mathrm{HN}}(\omega) = \varepsilon_\infty + \frac{\Delta\varepsilon}{(1 + (\omega\tau_{\mathrm{HN}})^p)^q}, \tag{6.18}$$

where τ_{HN} is the characteristic time scale of the HN function peak and p and q are shape parameters which correspond to the broadness and asymmetry of the dielectric response function. Specifically, p corresponds to the power-law exponent of the low-frequency flank of the peak and -$p \times q$ corresponds to the power-law exponent of the high-frequency flank of the peak. [27, 135] When $p = q = 1$ the function is equal to that of the Debye model function in equation

6.17. Additionally, there are two special cases of the HN function for when $p \neq 1, q = 1$ and $p = 1, q \neq 1$ which are the Cole-Cole function (CC) and Cole-Davidson (CD) function, respectively. [27] The shape of the CC and CD function for various values of p and q is shown in figure 6.3. A correction factor needs to be applied to determine the peak frequency of the relaxation, ω_{p}, as there is a shift in the frequency due to the asymmetry of the HN function: [27]

$$\omega_{\mathrm{p}} = \frac{1}{\tau_{\mathrm{HN}}} \left[\sin\left(\frac{p\pi}{2+2q} \right) \right]^{\frac{1}{p}} \left[\sin\left(\frac{pq\pi}{2+2q} \right) \right]^{-\frac{1}{p}}. \tag{6.19}$$

Note that for a CC function no correction is required as $q = 1$.

6.1.5 DC conductivity

The HN function can be used to fit the broad asymmetric dielectric data of real-world polymeric materials which typically deviate from the predictions of the Debye model. [134] In addition to this, polymeric materials typically contain various charge carriers within them which have not yet been considered. These charged species could be present due to ionic impurities in the material, or occasionally, as charge carriers added deliberately to the material for the study their ionic conductivity behaviour. [132, 136] When an electric field is a applied the charged species diffuse through the material towards the oppositely charged electrode which effects the dielectric spectra. [27, 125] The contribution of the DC conductivity, σ_{DC}, to the complex dielectric permittivity is given by: [27]

$$\varepsilon^*_{\mathrm{DC}}(\omega) = -i\frac{\sigma_{\mathrm{DC}}}{\varepsilon_0 \omega}. \tag{6.20}$$

Since equation 6.20 is an imaginary function DC conductivity is observed as a low-frequency flank in the ε'' data only.

The presence of DC conductivity can often obscure relaxation peaks in the ε'' spectra especially in the low frequency range and at high temperatures. [137] However, ε' and ε'' follow the Kramers-Kronig relationship which means that they can be transformed between each other. [27, 137] The ε' spectra when transformed into ε'' is ohmic-free (i.e. lacking contributions from DC conductivity) which

allows for the investigation of otherwise obscured peaks. [27, 137] The Kramers-Kronig equations need to be solved analytically, however, an approximate form of these relations is given by: [132, 137]

$$\varepsilon''_{\text{deriv}}(\omega) = -\frac{\pi}{2}\frac{\partial\varepsilon'(\omega)}{\partial\ln(\omega)}. \tag{6.21}$$

where $\varepsilon''_{\text{deriv}}$ is the dielectric loss spectra derived from ε' which closely approximates an ohmic free ε'' spectra.

In addition to the approximation of the ohmic free ε'' spectra given by equation 6.21 dielectric spectra can be analysed in the *complex dielectric modulus* representation to address obscuring of relaxations by DC conductivity. [137] The complex dielectric modulus, M^*, is given by: [137]

$$M^*(\omega) = \frac{1}{\varepsilon^*(\omega)}, \tag{6.22}$$

using the definition of the complex permittivity from equation 6.10 M^* can be rewritten into real and imaginary parts: [137]

$$M^*(\omega) = \frac{\varepsilon'(\omega)}{\varepsilon'^2(\omega)+\varepsilon''^2(\omega)} + i\frac{\varepsilon''(\omega)}{\varepsilon'^2(\omega)+\varepsilon''^2(\omega)} = M'(\omega) + iM''(\omega), \tag{6.23}$$

where $M'(\omega)$ is the storage dielectric modulus and $M''(\omega)$ is the loss dielectric modulus. In the dielectric modulus representation, the contribution by DC conductivity manifests as a peak in M'' spectra as opposed to a low-frequency power law flank observed in ε'' data. [137] The peak frequency of the DC conductivity contribution in the dielectric modulus representation is often quite separated from the peaks associated with molecular relaxation; thus any previously obscured peaks in the ε'' data can be observed and fitted with a modified Havriliak-Negami function. [137]

6.2 Experimental set-up

The broadband dielectric spectrometer (BDS) used throughout this thesis is the 'Novocontrol Alpha-A' analyser with the dynamic frequency window selected to

be 10^{-2} Hz - 10^{6} Hz. If required, the sample can be temperature controlled via the 'Novocontrol Quatro Cryosystem' which is a liquid nitrogen cryostat with a temperature range of -160°C - 400°C (113.15K - 673.15K) and an accuracy of ±0.01°C. For the LCEs used in this thesis BDS measurements were performed over -110°C - 100°C (163.15K - 373.15K).

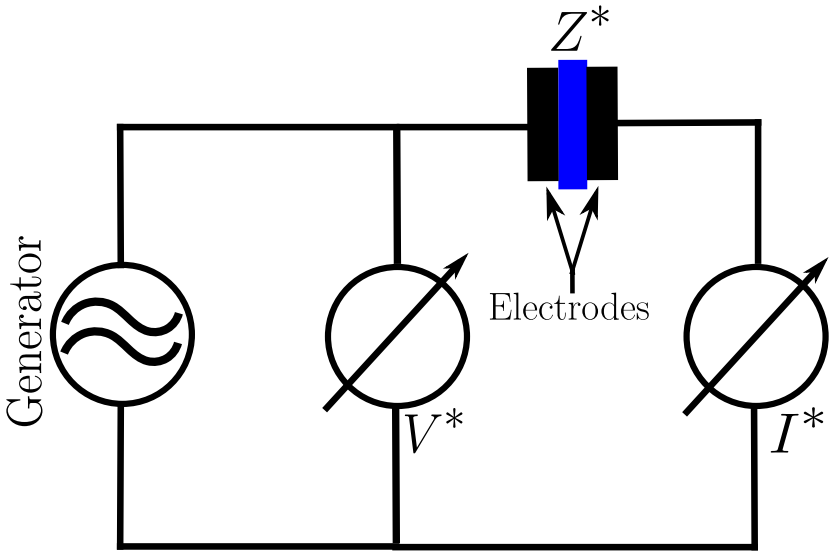

Figure 6.4: Simplified circuit diagram of a dielectric measurement. The sample is shown in blue and is sandwiched between the two electrodes.

The spectrometer functions by applying an oscillatory voltage across the sample cell of the form: [27, 131]

$$V^*(\omega) = V_0 e^{i\omega t}, \tag{6.24}$$

the corresponding current, I^*, is recorded and the complex impedance of the sample is determined: [27, 132]

$$Z^*(\omega) = \frac{V^*(\omega)}{I^*(\omega)} = Z'(\omega) + iZ''(\omega), \tag{6.25}$$

where Z' is the real component of the complex impedance relating to the resistive properties of the material and Z'' is the imaginary component relating to the capacitive properties of the material. [19] Note that any measurement of Z^*

will contain stray impedances due to the presence of wires within the circuit, contact impedance between the sample and electrodes; additionally, there will be capacitive edge effects due to the inhomogeneity of the field at the edge of the electrodes. [19, 130, 138] Throughout this thesis these effects are corrected for by setting the stray capacitance value to 1 pF. The complex dielectric permittivity is related to the complex impedance of the sample via the equation: [27]

$$\varepsilon^*(\omega) = -\frac{i}{\omega Z^*(\omega) C_0} \tag{6.26}$$

where C_0 is the capacitance of a vacuum capacitor defined in equation 6.2.

To perform BDS measurements on an LCE film the sample is placed between two parallel brass plates which is then housed within the Novocontrol BDS. It is typical to use silicon spacer rods between the brass plates when the sample forms a melt to ensure the cell gap remains constant. [131, 132] These spacer rods could be incorporated during LCE synthesis, however this disrupted the alignment of the nematic phase and often resulted in the samples breaking early if strain was applied. Since elastomeric materials remain solid above their glass transition temperature, i.e. do not form melts, spacer rods are not necessary to perform BDS measurements. [139, 140] The gap between the electrodes is simply the thickness of the solid LCE film which is measured using a digital micrometer. Whilst the thickness of the sample may change with changing temperature only the characteristic time-scales of observed relaxations are discussed which should be unaffected.

The dielectric spectra obtained is fitted in the ε'' representation using the 'Novocontrol WinFIT' software as a sum of dielectric response functions and, if required, a contribution from DC conductivity. The characteristic time-scale of any observed relaxation is $\tau_{\mathrm{p}} = 1/\omega_{\mathrm{p}}$ where ω_{p} is the corrected peak frequency described in 6.19. As described in more detail in chapter 9, the α relaxation, β relaxation and γ relaxation are observed in these LCEs in addition to a contribution from DC conductivity. The α relaxation is fit with the Havriliak-Negami function ($p \neq 1, q \neq 1$) whereas the β relaxation and γ relaxation are fit with the Cole-Cole function ($p \neq 1, q = 1$).

6.3 Summary

To summarise, the response of a dielectric material in a static field and the resulting polarisation of dipoles is described. It is shown that a dielectric material in an oscillatory electric field results in a frequency dependent complex permittivity, $\varepsilon^*(\omega)$, which has real and imaginary parts relating to the energy stored in the material per period and the energy dissipated in the material per period, respectively. [27] It is shown that molecular relaxations can be probed with BDS by measuring the frequency dependent response of ε^*. The dielectric response functions relating to the Debye single relaxation model and the empirical Havriliak-Negami function are introduced. Finally, the experimental set-up of the broadband dielectric spectrometer is outlined. BDS measurements as described here are used in chapter 9 and 10 to study the molecular relaxations present in LCEs and how they are influenced by (a) the phase of the LCE and (b) applied strain.

Chapter 7

Experimental IV: Rheology

In this chapter the key principles of rheology and the techniques involved with rheological measurements are outlined. Both dynamic mechanical analysis (DMA) and small amplitude oscillatory shear (SAOS) rheology have been used during this thesis. This chapter focuses on describing rheology in the context of DMA where axial strains are applied to a sample and the Young's modulus of the material, as a function of some external parameter, is investigated. The approach followed in this chapter is entirely interchangeable with shear rheological techniques (such as SAOS) where shear strains are applied to the material and the shear modulus of the material is investigated. Once the principles of rheology are outlined the experimental set-up of the rheological measurements are described.

7.1 Viscoelasticity

The two extremes in the behaviour of a material under deformation is that it behaves either as a 'Hookean solid' (i.e. perfectly elastic) or as a 'Newtonian fluid' (i.e. a perfectly viscous). The equations describing these two limiting cases are: [14, 130]

$$\sigma_{\text{Hookean}} = E\epsilon, \tag{7.1}$$

$$\sigma_{\text{Newtonian}} = \eta\frac{\partial\epsilon}{\partial t}, \tag{7.2}$$

where σ is stress, E is the Young's (or elastic) modulus, ϵ is strain, $\partial\epsilon/\partial t$ is the strain rate which is often denoted by $\dot{\epsilon}$ and η is viscosity. In reality most materials are said to be 'viscoelastic' and have behaviours between that of a Hookean solid and a Newtonian fluid. [130, 141] The extent of the elastic 'solid-like' and viscous 'liquid-like' behaviour in material is generally temperature and frequency dependent and is related to molecular interactions and motions within a material. [142] Thus the study of the viscoelastic behaviour of a material, or 'Rheology', provides key insight into its fundamental molecular behaviour. [130, 142]

7.2 The complex Young's modulus

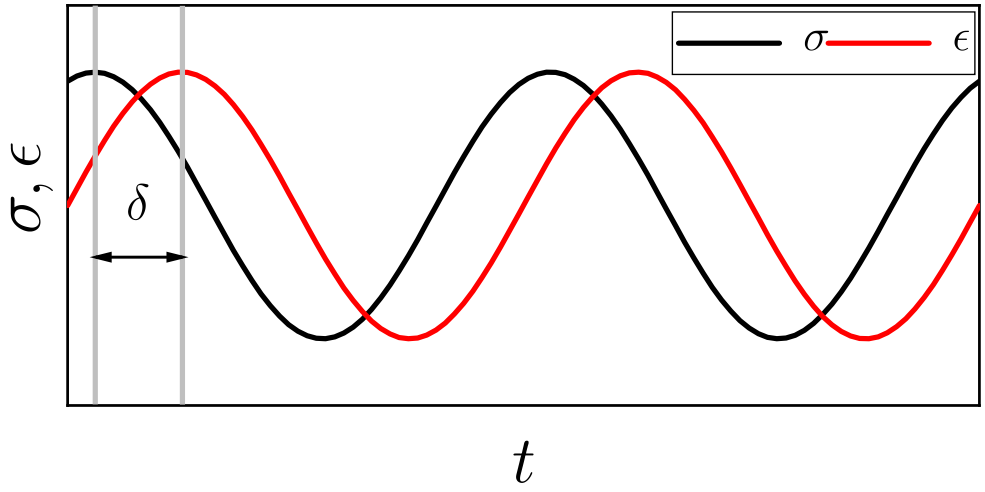

Figure 7.1: An oscillatory strain is applied to a sample. The resultant oscillatory stress is out of phase with the applied strain by the value δ.

Dynamic Mechanical Analysis (DMA) is a mechanical spectroscopy technique which probes the dynamic viscoelastic behaviour of a material by applying an oscillatory axial strain (or stress) to the sample. The DMA rheometer used in this thesis is strain controlled, hence let us consider an applied oscillatory strain, ϵ, of the form: [130]

$$\epsilon^* = \epsilon_o e^{i\omega t}, \tag{7.3}$$

where ϵ_o is the amplitude of the oscillatory strain, ω is the angular frequency of the oscillation and $i^2 = -1$. The resultant oscillatory stress, σ is given by: [130]

$$\sigma^* = \sigma_o e^{i(\omega t + \delta)}, \tag{7.4}$$

where σ_0 is the amplitude of the oscillatory stress and δ is a phase lag determined by the properties of the material and often referred to as the *loss angle*. [130] See figure 7.1 for a schematic of the oscillatory stress-strain response of a viscoelastic material. The complex Young's (or elastic) modulus, E^*, can be determined using equation 7.1: [130]

$$E^* = \frac{\sigma^*}{\epsilon^*} = \frac{\sigma_0}{\epsilon_o} e^{i\delta} = \frac{\sigma_o}{\epsilon_o}(\cos(\delta) + i\sin(\delta)). \tag{7.5}$$

The complex Young's modulus can be rewritten in the form:

$$E^* = E' + iE'' \tag{7.6}$$

where E' and E'' are known as the storage and loss moduli, respectively, and defined by:

$$E' = \frac{\sigma_o}{\epsilon_o}\cos\delta, \tag{7.7}$$

$$E'' = \frac{\sigma_o}{\epsilon_o}\sin\delta. \tag{7.8}$$

The storage modulus, E', is a measure of the elastic response of the material and E'' is a measure of the viscous response of the material. [130] As the names suggest, E' quantifies the materials ability to store energy during deformation and thus recover elastically, whilst E'' quantifies energetic loss from the system which typically occur as heat loss. [130, 142] Another useful quantity to define is the *loss tangent*:

$$\tan(\delta) = \frac{E''}{E'}, \tag{7.9}$$

which is the ratio of the viscous component of the material to the elastic component of the material. When $\tan(\delta) < 1$ the material has a greater elastic component to its dynamic behaviour and when $\tan(\delta) > 1$ the material has a greater viscous component to its dynamic behaviour.

7.3 DMA testing procedures

Now that the concept of the complex Young's modulus has been outlined it is useful to describe the testing procedures relevant to this thesis and how they are performed.

7.3.1 Strain sweep

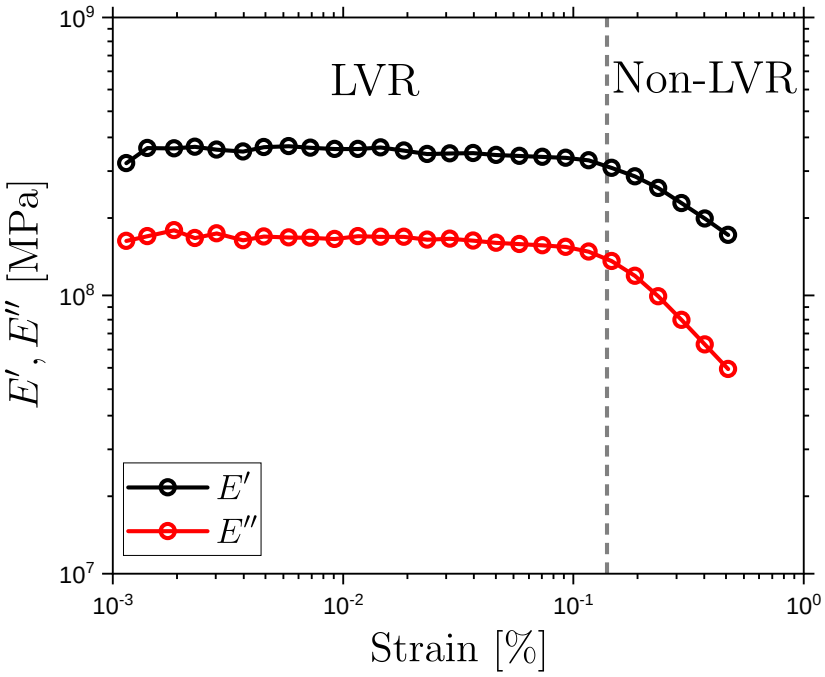

Figure 7.2: Strain sweep performed at 18°C and 1 Hz on a nematic LCE strained parallel to the director. The grey dashed line separates the linear viscoelastic regime and the non-linear viscoelastic regime.

In a strain sweep measurement the frequency and temperature are kept constant and E^* and $\tan(\delta)$ are recorded as function of strain amplitude. The strain sweep is important in determining the limits of the linear viscoelastic regime (LVR) of the sample. Within the LVR the stress-strain response of the material is linear and E' and E'' is independent of the applied strain. [130, 142] The end of the LVR is typically defined as the point where E' drops by ∼5% - 10% (depend-

ing on the international standard [143, 144]) from the initial plateau. Typically one wants to perform DMA measurements, such as temperature and frequency sweeps, within the LVR to ensure: (a) the complex Young's modulus of the material is being probed (b) the internal structure of the material remains intact and (c) the measurement of E' and E'' are independent of previous measurements. [130, 142] Shown in figure 7.2 is a strain sweep, performed at 18°C and 1 Hz, on a nematic LCE sample strained parallel to the director. We see from figure 7.2 that the upper limit of the LVR is ∼0.14% strain. If one is testing the sample over a large temperature (or frequency) range it is ideal to take strain sweeps over the full range and select a strain that is within the LVR for every measurement.

7.3.2 Frequency sweep

In a frequency sweep measurement, the strain amplitude and temperature are kept constant and the sample is subject to various frequencies of oscillatory strain. The strain amplitude is selected to be within the LVR to ensure that one is probing the complex Young's modulus of the material. This test is important to determine the time dependant properties of materials such as the frequency range of optimal damping properties and whether the sample fails at high frequencies. [142] Additionally, as described in chapter 1, the presence of chain modes in a polymeric material manifests in specific frequency dependent rheological behaviour, thus, performing frequency sweeps on a polymer can give key insight into the molecular motions of the material. [19, 20, 141] This behaviour spans many decades in frequency, far exceeding the experimentally available frequency window of rheometers ($1\times$ 10^{-3} Hz - 15 Hz for the Rheometrics RSA II), which means a single frequency sweep is not sufficient to investigate such behaviours in a meaningful capacity. The effective frequency window of an experiment can be extended by applying the time temperature superposition (TTS) principle allowing such behaviours to be captured.

7.3.3 Time temperature superposition

To perform time temperature superposition, frequency sweeps are performed over a range of discrete temperatures. A reference temperature is selected and the

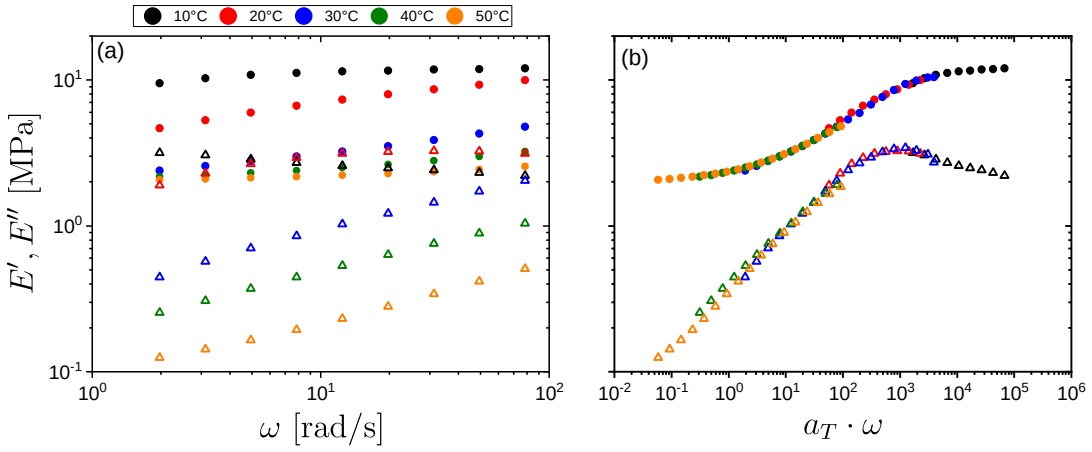

Figure 7.3: (a) Unshifted E' (solid circles) and E'' (empty triangles) data for the nematic LCE strained perpendicular to the director for a temperature range of 10°C - 50°C (b) Rheological master curve constructed with the TTS principle using $T_{\text{ref}} = 40$°C.

rheological data is shifted, with respect to the reference spectra, to construct a single master curve. The rheological data can be shifted both horizontally and vertically. The horizontal (or frequency) shift factor, a_T, is given by: [16, 19]

$$a_T = \frac{\omega(T_{\text{ref}})}{\omega(T)}, \tag{7.10}$$

where $\omega(T_{\text{ref}})$ is the unshifted angular frequency at the selected reference temperature and $\omega(T)$ is shifted angular frequency at another temperature. The vertical (or modulus) shift factor, b_T, is given by: [19]

$$b_T = \frac{\rho_{\text{ref}} T_{\text{ref}}}{\rho T} \tag{7.11}$$

where ρ_{ref} and ρ are the densities of the material at T_{ref} and T, respectively. Vertically shifting the rheological data requires that the temperature dependence of the material density is known. [19] Additionally, b_T is typically small and TTS can often be performed using only a_T. [145, 146] In the work of this thesis TTS could be performed using only a_T which demonstrates that the variation in b_T is negligible enough to be ignored.

The TTS principle is valid when a material is 'thermorheologically simple' which means that all relaxation processes in the spectra have the same temperature dependence. [147, 148] It is useful to be able to construct a curve of shift factors so that the expected horizontal shift factor for an arbitrary temperature can be estimated. It is typically the case that $a_T(T)$ for amorphous polymers follow the empirical Williams-Landel-Ferry (WLF) equation: [130, 149]

$$\log_{10}(a_T) = -\frac{C_1(T - T_{\text{ref}})}{C_2 + (T - T_{\text{ref}})}, \tag{7.12}$$

where C_1 and C_2 are positive empirical constants that depend on the material and the reference temperature selected. [130] It has been found that the empirical WLF equation results in values of $C_1 = 17K$ and $C_2 = 51K$ for many amorphous polymers when the reference temperature is selected to be near T_{g}. [19, 130, 149] Thus, C_1 and C_2 were originally thought to be universal constants, however, C_1 and C_2 deviate from these values when $T_{\text{ref}} \not\approx T_{\text{g}}$ or when the material is a particularity 'strong glass' or a particularity 'fragile glass'. [130, 150]

7.4 Experimental set-up

In this thesis, both DMA and shear rheology are performed on the LCE sample. The working principles of both are largely the same. In section 7.2 only the complex Young's modulus is discussed which is relevant to DMA measurements. Below, the experimental set-ups of both the DMA and SAOS rheometers are described.

7.4.1 Dynamic mechanical analyser

The dynamic mechanical analyser (DMA) used throughout this thesis is the 'Rheometrics RSA II' analyser which has a working frequency window of 10^{-3} Hz - 15 Hz. A schematic of the RSA II is shown in figure 7.4. The sample thickness is determined with a digital micrometer and the sample is loaded into the RSA II with the 'film tension clamp' attachment. A small loading force of $\sim$0.05 - 0.1 N is applied to the film to prevent buckling. Various DMA procedures are performed on the LCE throughout the thesis; these will be described

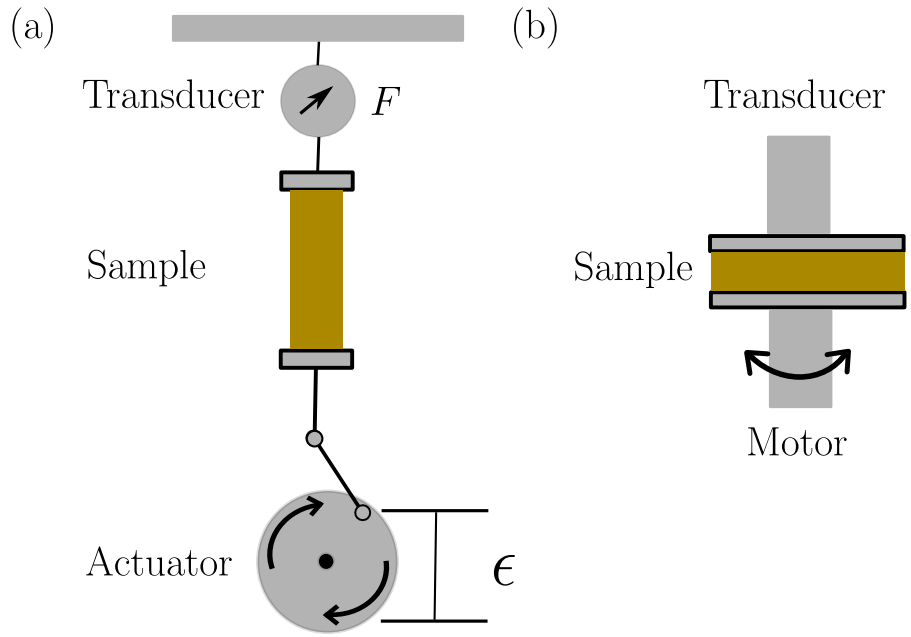

Figure 7.4: Schematic of rheological measurements on a sample using (a) the DMA performed with the tension film clamps attachment and (b) the shear rheometer in a parallel plate geometry.

in detail in the relevant results chapters. In all cases strain sweep measurements were performed beforehand to determine the LVR of the sample. The RSA II is a strain-controlled rheometer, hence, the sample is subjected to a user determined oscillatory strain. The corresponding oscillatory force, F^*, is measured by a transducer which is converted into an oscillatory stress by the relation:

$$\sigma^* = F^*/A \tag{7.13}$$

where A is the cross-sectional area of the sample. The input oscillatory strain and the output oscillatory stress can be used to determine E^* and $\tan\delta$ as described in section 7.2.

7.4.2 Shear rheometer

The shear rheometer used throughout this thesis is the Rheometrics Advanced Rheometric Expansion System 'ARES' which has a working frequency window

of 10^{-5} rad/s - 5×10^{2} rad/s. A schematic of the ARES is shown in figure 7.4. The sample is loaded into the ARES with the 'parallel plate' geometry. A slight overhang of the sample is required to ensure that the sample dimensions remain constant over the full temperature range of the experiment. The ARES is a strain-controlled rheometer, hence, the sample is subjected to a user determined oscillatory shear strain. The corresponding angular torque is measured by a transducer and converted into a complex shear stress for the given sample dimensions. The complex shear modulus, G^*, is determined via the following equation: [130]

$$G^* = \frac{\sigma^*}{\gamma^*} \tag{7.14}$$

where σ^* is the oscillatory shear stress and γ^* is the oscillatory shear strain.

7.5 Summary

The principles of rheology have been outlined. The approach taken has focused on DMA, however, it is interchangeable with shear rheological techniques. It has been shown that rheology can be used to investigate the frequency and temperature dependant behaviour of materials. The principle of time temperature superposition has been outlined which allows one to extend the frequency window of rheological measurements; this is important as the dynamic behaviour of polymeric and elastomeric materials can span many decades. Finally, the experimental set-ups of the DMA and the SAOS rheometers are described. Both rheological techniques are used in this thesis; in chapter 9 the glass transition and chain modes present in the unstrained nematic and isotropic LCE are investigated and in chapter 10 the effect of elongation on the viscoelastic behaviour of the nematic LCE is investigated.

Chapter 8

Results I: Order parameters of LCEs under strain: Insight into the auxetic response

8.1 Introduction

As discussed in chapter 1, some LCEs have been shown to display a molecular auxetic response (negative Poisson's ratio) when strains are applied perpendicularly to the nematic director. [1] The 'molecular' auxetic response in LCEs occurs without evidence of volume changes or the emergence of porosity making it potentially advantageous over the 'structural' auxetic response produced by designing structures into otherwise non-auxetic materials (i.e. positive Poisson's ratio in bulk). [75–77] While there are theoretical predictions of a negative Poisson's ratio for smectic-C LCEs [151], there is no theoretical description of the molecular auxetic response in nematic LCEs and this response is poorly understood. The auxetic response in the LCE can be described more fully, noting that it occurs in only one axis and beyond a threshold strain (the initial response at low strains is not auxetic). Strictly speaking, this makes the LCE a *partial auxetic*. The molecular auxetic LCEs identified in the literature thus far appear to deform exclusively via the MFT. [1, 2, 70] The MFT, discussed in detail in chapter 3, is characterised by a discontinuous rotation of the director that occurs after a critical strain is reached. From the discussions above, it would appear

the MFT is somewhat implicated in the molecular auxetic response observed in nematic LCEs.

Mistry *et al.* first reported the MFT in this LCE via simultaneous stress-strain measurements and cross-polarised microscopy. [2] The LCE is placed with its initial director in the $x-z$ plane with polarised light normal to the director. Stress-strain measurements were performed and the crossed polarisers were rotate about the y axis to determine the angle of the nematic director in the $x-z$ plane. [2] It was found that, initially the director remains perpendicular to the applied strain, however, at a threshold strain the director rotates sharply to align with the stress axis. [2] This is characteristic MFT behaviour and agrees with previous findings which investigated the MFT response using X-ray. [65, 70, 71] Mistry *et al* also studied the optical properties such as the interference colours of the sample as a function of strain. [2] It was found that the LCE sample remains optically clear throughout the full range of strain [2], thus suggesting a lack of 'stripe domains' as is typical of the SSE response; 'single director switching' was also observed by Roberts *et al.*, when polarised optical microscopy and X-ray scattering were used to study an LCE deforming via an MFT. [70, 71] Mistry et al. reported, for an LCE strain perpendicularly to its director, a change in the interference colours of the LCE as a function of strain. [2] Initially, when the LCE is strained perpendicularly to the director, the interference colours indicate a reduction in the retardance of the sample, which, if it is assumed that the director stays in the $x-z$ plane, indicates a reduction in the birefringence of the sample. [2] This reported reduction in the birefringence of the sample is consistent with findings by X-ray scattering, in which a reduction in the uniaxial order parameter of an LCE deforming via and MFT was reported. [70, 71] After the rotation of the director, the birefringence of the sample increases [2], again in agreement with previous findings via X-ray. [70, 71] Thus, current evidence suggests that the MFT is characterised by a sharp rotation of the director in which, before director rotation, the order of the system reduces and, subsequently, after the rotation of the director there is a recovery of some of the order. In all the outlined cases, no evidence of 'stripe domains', as is characteristic of the SSE, was found. [2, 70, 71]

In this chapter the order parameters of a nematic LCE, which deforms via an MFT and displays a molecular auxetic response, is studied via Raman spec-

troscopy to gain insight into these behaviour. The LCE is investigated in the parallel and the perpendicular geometry; in the parallel geometry the LCE is non-auxetic, however, in the perpendicular geometry the nematic LCE displays *partial* auxetic response (i.e. expands in one of its transverse axes). In the analysis of the Raman depolarisation data two different models are applied and their implications are discussed. The first model assumes that there is only *uniaxial order* in the system and *no biaxial order*. For the nematic LCE strained parallel to the director the order parameters follow predictions by Maier-Saupe theory, therefore, the mesogenic units can be described by a single Gaussian distribution throughout the whole deformation. However, the perpendicularly strained LCE deviates from Maier-Saupe predications which indicates the emergence of biaxiality. Therefore, in the second model, the *emergence of biaxial order* in the perpendicularly strained LCE is explored. The biaxial order parameters determined in the second model provide an explanation for the molecular auxetic response in the nematic LCE; construction of the orientational distribution functions using the determined order parameters result in out-of-plane rotations of mesogenic units which occur near the onset of the molecular auxetic response.

The majority of the content in this chapter has been published in the paper: T. Raistrick *et al.* "Understanding the physics of the auxetic response in a liquid crystal elastomer.", *Physical Review Research*, **3(2)**, 023191, 2021. [112] Much of this chapter is reproduced from said paper; unless specified any experimental work presented has been performed by T. Raistrick.

8.1.1 Predicted emergence of biaxiality

The MFT is the discontinuous rotation of the nematic director with applied strain. In chapter 3, the behaviour of the MFT is described starting from the *trace formula* assuming that the order of the system remains constant and that the rotation of the nematic director is instantaneous. However, evidence of a change in order in LCEs deforming via an MFT has been observed using X-ray scattering [70, 71] and polarised optical microscopy techniques. [2, 70] In the initial theoretical work by Bladon *et al.* describing the MFT, it was assumed that the nematic order of the LCE remains constant. [113] However, in later

publications the assumption of constant order was removed and it was found that during the MFT there is a change in the nematic order due to the coupling between the polymeric backbone and the mesogenic units; [114] it is found that before the rotation of the director, i.e. when strains are applied perpendicular to the director, te energy of the system is reduced by a decrease in the uniaxial order parameter ($Q = \frac{1}{2}\langle 3\cos^2(\beta) - 1\rangle$) and an emergence of biaxial ordering ($b = \frac{1}{4}\langle(1 - \cos^2(\beta))\cos(2\alpha)\rangle$) [40, 114] where the angles β and α are 2 of the 3 'Euler angles' as discussed in section 2.1. After the rotation of the director theory predicts that there is a collapse in the biaxial ordering and a return to a uniaxial ordering; however the macroscopic shape remains biaxial. [114] Note that in the Raman notation, as described in chapters 2 and 5, $\langle P_{200}\rangle = Q$ and $\langle P_{220}\rangle = b/6$. [103] The theoretical predictions of a reduction of uniaxial order, on increasing elongational strain until the rotation of the director, and a subsequent recovery of uniaxial order is consistent with experimental findings [2, 70]. However, the emergence of biaxial order parameter has not been investigated.

Finkelmann, Greve and Warner [115] developed theory describing the elastic anisotropy of strained nematic LCEs when there is no rotation of the nematic director; as is the case for small imposed strains and the MFT. In this work, a relationship between the changes in the uniaxial order and the biaxial order of an LCE when strained either parallel or perpendicular to the director is predicted. [115] Additionally, a relationship between the extent of the change in the uniaxial and biaxial order and the material properties of the LCE was discussed. [63] It is now useful to discuss this relationship in the context of the known material properties of the auxetic LCE which deforms via an MFT. The full analysis by Finkelmann *et al.* begins with the nematic trace formula where changes in the nematic order are accounted for in the step length tensor [63] and through Landau-de Gennes theory two moduli (or stiffnesses) are found; the uniaxial stiffness (F_Q'') quantifies how resistant the material is to changes in uniaxial order and the biaxial stiffness (F_b'') quantifies how resistant the material is to changes in biaxial order. The ratio of the uniaxial and biaxial stiffness is found to be related by the equation:

$$\frac{F_Q''}{F_b''} = \left(1 + \frac{2}{3}\left(\frac{T^* - T}{T_{\mathrm{ni}} - T^*}\right)\frac{Q_{\mathrm{ni}}}{Q_0(T)}\right), \tag{8.1}$$

where T_{ni} is the nematic-isotropic transition temperature of the material, Q_{ni} is the uniaxial order at T_{ni}, T is the temperature at measurement, $Q_0(T)$ is the uniaxial order parameter of the unstrained LCE at T, and T^* is the critical temperature and is typically close to T_{ni}. [40, 115] Thus the ratio of biaxial stiffness to uniaxial stiffness can be easily quantified by general properties of a material.

The properties required for equation 8.1 have already been indirectly determined for the nematic LCE in [2] which will now be used in relation to equation 8.1. The order parameter of certain LCEs is 'supercritical' meaning that, unlike a conventional LC, there is no weakly first-order transition into an isotropic phase upon heating. [52, 53, 57] Instead, the evolution of order with changing temperature is broadened and often continuous. [115, 152] The LCE investigated in this chapter shows evidence of supercritical behaviour. [2] The T_{ni} of this nematic LCE is very high (linearly extrapolated to be 345 ± 20°C) and actually above the sample's degradation temperature of 330°C. [2] The birefringence of the nematic LCE has been determined with a Berek compensator as a function of temperature. [2] Whilst not a direct measurement of order the relative value of birefringence, for a single material, and how this changes with temperature scales well with order parameter measurements. [84] At room temperature (20°C), the birefringence of the sample is 0.12 [2] which is a good indication of $Q_0(T)$. The supercritical nature of the LCEs makes determination of Q_{ni} difficult [115], however, the closest birefringence measurement to T_{ni} is 0.01. [2] If this is taken to be a good indication of Q_{ni}, and assuming that there are no density changes across the temperature range investigated, the $Q_{\mathrm{ni}}/Q_0(T)$ component of equation 8.1 at room temperature (20°C) will be of the order of 0.08. However, one could perform the same linear extrapolation that was performed to determine T_{ni} in Ref. [2] to arrive at a value of $Q_{\mathrm{ni}} = 0.004$ and a $Q_{\mathrm{ni}}/Q_0(T)$ component of equation 8.1 at room temperature (20°C) of the order of 0.03. T^* is the temperature of absolute stability of the isotropic phase. For conventional liquid nematic phases

$T_{ni} - T^* \approx 1$°C. [153] However, the order parameter of conventional nematic LCs evolve with a weakly first-order behaviour unlike the LCE presented. Finkelmann *et al.* determined T^* of a supercritical LCE and found that $T_{ni} - T^* \approx 1$°C [115], making it consistent with conventional nematic phases. [153] Thus, we take $T_{ni} - T^* = 1$°C to be a reasonable estimate for the LCE presented in Ref. [2] and discussed in this thesis. However, it is important to note that the LCE within this thesis has a $T_{ni} = 340 \pm 20$ [2] and the assumption that $T_{ni} - T^* = 1$°C may not hold true at such high temperatures. One could attempt to calculate a value of the critical temperature by assuming that the order parameters as a function of temperature follow, for example, Maier-Saupe theory [154], however, the LCE presented herein displays supercritical behaviour. Therefore taking T^* to be $\sim$ 1°C smaller than T_{ni} and setting T to 20 °C the component of equation 8.1 containing T_{ni}, T^*, and T will be of the order of 325. Substituting the values of the material one finds $F''_Q/F''_b \approx 27$ if $Q_{ni} = 0.01$ (taken from the smallest measured value of birefringence in Ref. [2]) or of the order of $F''_Q/F''_b \approx 10$ if $Q_{ni} = 0.004$ (deduced from a linear extrapolation of the birefringence values in Ref. [2]).

Therefore, given the assumptions made about the material properties and the value of T^* for this LCE, it is likely that the material is more susceptible to biaxial distortions in order than purely uniaxial distortions in order as the sample is well below T_{ni} ($T - T_{ni} = 325$ °C). Indeed, theoretical work by Bladon *et al.* suggests that for an LCE deforming via an MFT, it is energetically favourable for changes in the uniaxial order and the emergence of biaxial order. [114] It is therefore reasonable to investigate the emergence of biaxiality via Raman spectroscopy. Note that in the approaches of Bladon *et al.* and Finkelmann *et al.* only the low rank uniaxial and biaxial order parameters ($Q = \langle P_{200} \rangle$ and $b = 6\langle P_{220} \rangle$ [103]) are considered. However, Raman spectroscopy allows for the determination of additional higher rank order parameters ($\langle P_{400} \rangle$, $\langle P_{420} \rangle$ and $\langle P_{440} \rangle$) to get a more complete view of the orientational distribution of molecules in the phase. This is a distinction which will become important in relating biaxial order to the negative Poisson's ratio in these systems.

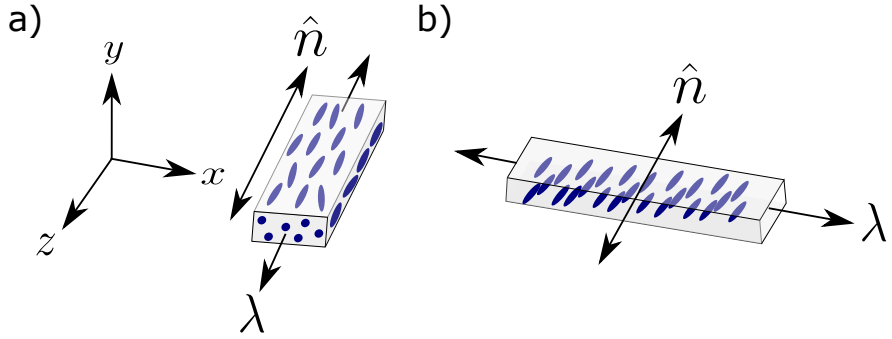

Figure 8.1: (a) Non auxetic parallel geometry refers to strain applied parallel to the initial nematic director (along z). (b) Auxetic perpendicular geometry refers to the strain being applied perpendicular to the initial nematic director (along x). The sample 'thickness' is in the y axis.

8.2 Experimental set-up

This chapter investigates both the uniaxial order parameters ($\langle P_{200}\rangle$ and $\langle P_{400}\rangle$) and the biaxial order parameters ($\langle P_{220}\rangle$, $\langle P_{420}\rangle$ and $\langle P_{440}\rangle$), however, initially all data are analysed assuming that only uniaxial order is present in the LCE; this is done as it is the simplest model to fit with the least parameters required. The possibility of biaxial order is explored later on in this chapter and the procedure required to do this is described in the relevant section.

The order parameters from the depolarisation ratio are determined as described in full in chapter 5. Briefly, the LCE order parameters are determined by placing a sample with a uniform director in the x-z plane normal to the direction of the incident laser light (incoming from y). The director and polarisation of the laser are in the same plane and measurements are taken. The sample is then rotated with respect to the initial laser polarisation (θ) and subsequent spectra are recorded. [81] The geometry of the LCE films in the laboratory frame of the Raman set-up can be seen in figure 8.1. Generally, the 'full depolarisation' method is used to determine order parameters where a fit is made to equations 5.14 and 5.15 with data recorded at small increments from $R(\theta = 0°)$ to $R(\theta = 360°)$ to determine $\langle P_{200}\rangle$, $\langle P_{400}\rangle$ and the differential polarisability ratio, p. However, order parameters can be determined from the 'two point' method (see appendix A) by considering only $R(\theta = 0°)$ and $R(\theta = 90°)$ provided that the molecu-

lar polarisability ratio (p) is known. [104]. In this chapter Raman spectra are therefore recorded as a function of strain using only $R(\theta = 0°)$ and $R(\theta = 90°)$. To check that p remains constant (within error), the full depolarisation ratio at intermediate strain steps of ∼0.2 is determined and fits are made. Doing this significantly speeds up the experimental procedure and reduces the possibility of sample failure under strain.

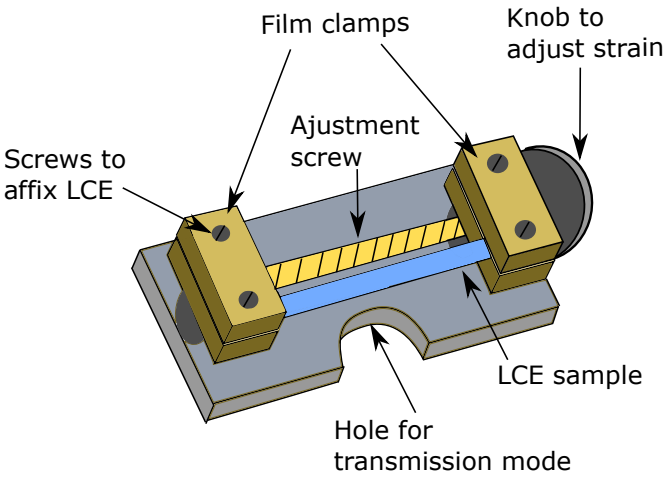

Figure 8.2: Schematic of the bespoke straining rig which is housed within the Raman spectrometer which allows one to determine order parameters of an LCE as a function of strain.

The Raman depolarisation data are collected using a polarised Raman system (Renishaw inVia) comprising of a 532 nm, 500 mW solid state laser (Renishaw) and a Leica polarising microscope equipped with a rotatable stage. A bespoke rig that allows the elastomer samples to be manually strained is fixed onto the rotatable stage (see figure 8.2 for a schematic of the bespoke straining rig). The LCEs are strained in 0.5 mm increments and are held for 5 minutes to allow for stress relaxation before the subsequent Raman spectra are measured. The sample is illuminated via a 20× lens resulting in a spot size of $\sim 7\mu m^2$. The laser intensity is selected to get the best signal to noise ratio for a given strain. Since p can change as a function of intensity [89], p is determined in the unstrained state for a given intensity so that fits could be made using the 2 point method.

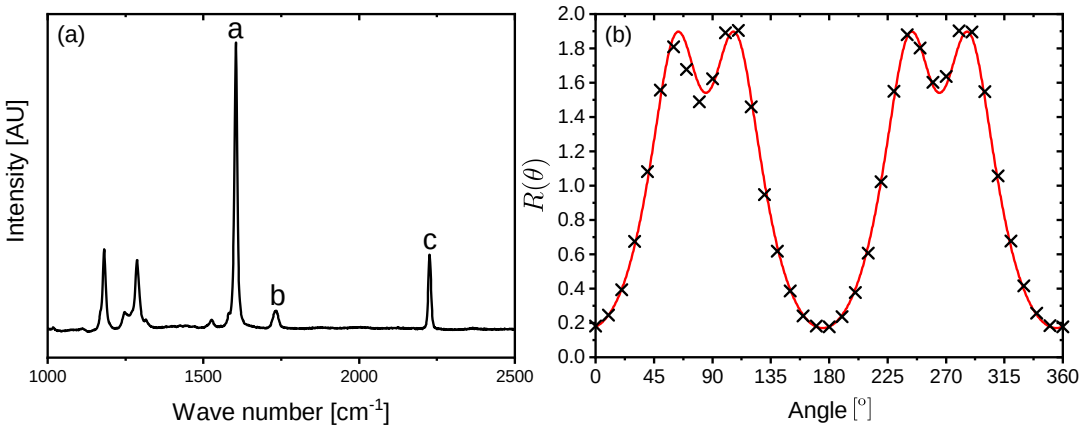

Figure 8.3: (a) Raman spectrum of the LCE film. Showing the symmetric phenyl stretch (a: 1606cm^{-1}), the carbonyl stretch (b: 1730cm^{-1}) and the cyano group stretch (c: 2250cm^{-1}). (b) Depolarisation ratio of an unstrained sample determined from the 1606cm^{-1} peak. The red line shows the fitting to the data (black crosses) with the values of $\langle P_{200} \rangle = 0.59 \pm 0.05$, $\langle P_{400} \rangle = 0.29 \pm 0.05$, $p = -0.23 \pm 0.05$ and $\theta = -5 \pm 0.5^{o}$ deduced from the fit.

As discussed in section 5.2, it is important to select an appropriate Raman peak for accurate determination of order parameters. [88] The phenyl stretching (1606cm^{-1}) mode is selected to determine order parameters as it best satisfies the theoretical assumptions of vibration along the molecular long axis and cylindrical symmetry. [88] The cyano stretching mode (2250cm^{-1}) is used to monitor the reorientation of the A6OCB side-chain group and the carbonyl stretching mode (1730cm^{-1}) is used to monitor the cross-linker RM82 as these are unique to the respective molecules. The behaviour of cyano stretching mode and the carbonyl stretching mode is compared to the phenyl stretching mode which is the combined reorientation of the mesogenic units as both A6OCB and RM82 contain this chemical group. The director angle with respect to the long axis of the sample (see figure 8.1) can be obtained from the full depolarisation data via the θ parameter in equations 5.14 and 5.15. The sample is loaded such that the long axis of the material is perpendicular to the incoming laser polarisation, θ is then a fitting parameter and is the angle of the nematic director in the x-z plane. Neither the cyano nor the carbonyl stretching modes were used to determine the order parameters as they return inaccurate values of $\langle P_{400} \rangle$. [88] Figure (a) shows a Raman

spectrum of the LCE with the (a) phenyl stretching (b) carbonyl stretching and (c) cyano stretching modes shown. Figure 8.3(b) shows the depolarisation data of the phenyl stretching mode for the unstrained sample, together with the fit to equations 5.14 and 5.15 and the relevant fitting parameters. Over the full strain range, the order parameters are calculated assuming that a nematic director lies in the $x-z$ plane and determined from backscattered Raman spectra taken from through the bulk of the sample (i.e. the determined order parameters are not from the surface). The analysis therefore assumes that there is an homogenous order parameter and director orientation throughout the thickness of the sample.

8.3 Results of the uniaxial model

In this section a uniaxial model assumption is applied to the depolarised Raman data for the strained LCEs and only the uniaxial order parameters ($\langle P_{200}\rangle$ and $\langle P_{400}\rangle$) are determined. Two geometries are investigated these are: the 'non auxetic' geometry (i.e. the nematic LCE strained parallel to the director) and the 'auxetic geometry' (i.e. the nematic LCE strained perpendicular to the director). These geometries are shown in figure 8.1. The resultant uniaxial order parameters are compared to tensile stress – strain measurements on the LCE published previously in [2] which are performed at 23°C and shown in the engineering stress – engineering strain representation. Additionally, the uniaxial order parameters are compared to relevant predictions of $\langle P_{400}\rangle$ for a given $\langle P_{200}\rangle$ from various models; these models are discussed in detail in section 2.

8.3.1 Strain parallel to the director

First, the uniaxial order parameters of the nematic LCE strained parallel to the nematic director are considered. In this geometry the LCE does not deform via an MFT nor is there an auxetic response. [1] In this geometry, the emergence of biaxial order is not predicted by theory [115], therefore, a uniaxial model is considered initially. The uniaxial order parameters are determined as described in section 8.2 using the 1606 cm^{-1} which is associated with the phenyl-stretching mode (see section 5.2 for discussion of Raman bond selection). Figure 8.4(a)

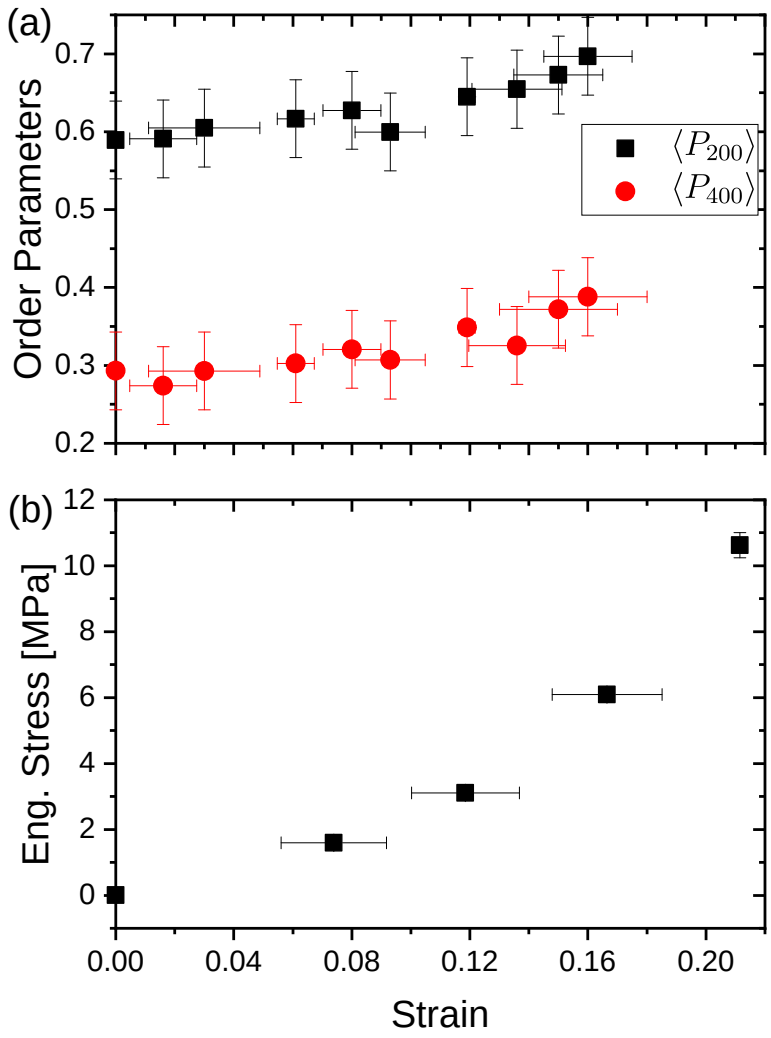

Figure 8.4: (a) Order parameters $\langle P_{200} \rangle$ and $\langle P_{400} \rangle$ as a function of strain applied parallel to the nematic director; error bars in order parameter data are the tolerances of the fitting procedure and error bars in strain are standard errors in measurements. (b) The stress-strain data for the LCE strained parallel to the director is taken from [2].

shows the change in the order parameters as a function of strain with a stress axis at 0° to the director. $\langle P_{200} \rangle$ and $\langle P_{400} \rangle$ increase from 0.58 ± 0.05 and 0.29 ± 0.05 to 0.69 ± 0.05 and 0.39 ± 0.05 respectively. Figure 8.4(b) shows the stress-strain response of the LCE strained in the parallel geometry. The stress-

strain response and uniaxial order parameters increase with increasing strain in agreement with prevailing theory. [40, 115]

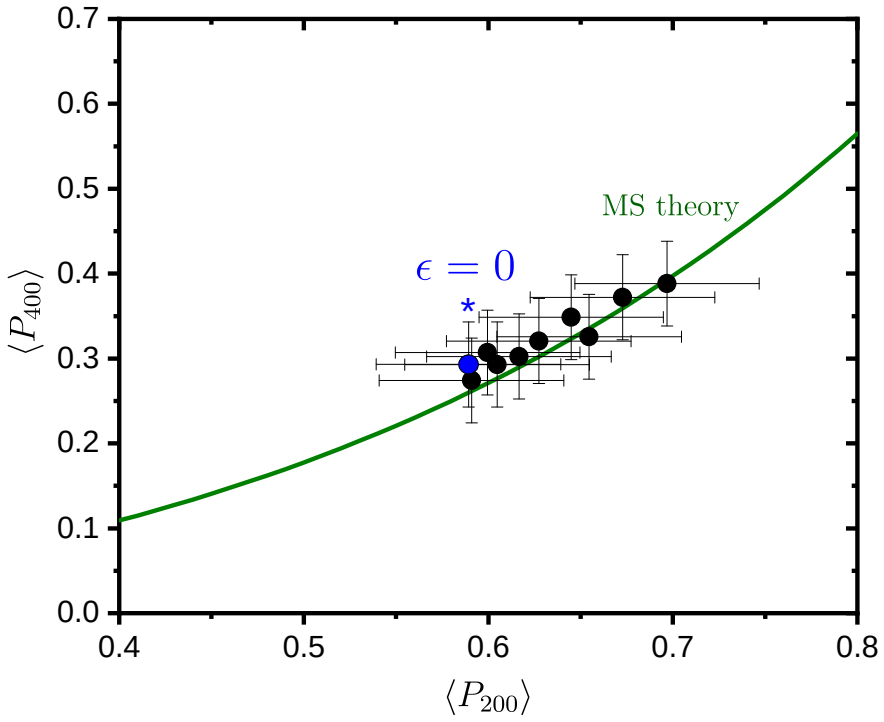

Figure 8.5: $\langle P_{400} \rangle$ against $\langle P_{200} \rangle$ for the LCE strained parallel to the nematic director; error bars in order parameter data are the tolerances of the fitting procedure. Maier-Saupe predictions of $\langle P_{400} \rangle$ for a given value of $\langle P_{200} \rangle$ is shown by the green line. The blue dot denotes the values of the order parameters for the unstrained LCE.

Figure 8.5 shows $\langle P_{400} \rangle$ against $\langle P_{200} \rangle$ for the LCE strained parallel to the nematic director. The green line is uniaxial order parameter prediction from Maier-Saupe theory (see section 2.2.2). Figure 8.5 shows good agreement between the determined order parameters and Maier-Saupe theory. Thus, the orientational distribution function of the mesogenic units follow a singly peaked Gaussian distribution centred at $\beta = 0$ and straining the LCE parallel to the director causes the distribution to move further up the Maier-Saupe line which signifies a narrowing of the ODF.

That the order parameter data follows the Maier-Saupe theory closely likely

means that the uniaxial model is a satisfactory model for the LCE strained in this geometry. Additionally, it suggests that contributions to the Raman data due to the molecular biaxiality of the molecules are small. Indeed, it has been reported previously that the phenyl-stretching mode, which is used consistently in this chapter to determine order parameters, has very close to uniaxial cylindrical symmetry [88] and therefore can not meaningfully probe molecular biaxial order parameters as the molecular vibration itself is invariant to γ. [88, 103] On the basis that the uniaxial model is satisfactory to deduce order parameters of the unstrained LCE and the LCE when strained parallel to the nematic director (where there is no emergence of phase biaxiality from symmetry arguments and predictions from theory [113, 114]), the order parameters of the LCE under perpendicularly applied strain can be investigated.

8.3.2 Strain perpendicular to the director

Now the uniaxial order parameters of the nematic LCE strained perpendicular to the nematic director are considered. In this geometry the LCE displays an MFT and a molecular auxetic response, additionally, it is predicted from theory that there will be an emergence of biaxial order. [115] However, initially a uniaxial model is considered as this is the simplest model and requires the least amount of fitting parameters. The uniaxial order parameters are determined as described in section 8.2 using the 1606 cm^{-1} which is associated with the phenyl-stretching mode (see section 5.2 for discussion of Raman bond selection).

Figure 8.6(a) shows the change in the order parameters as a function of strain, assuming a uniaxial model, for an LCE strain perpendicularly to its initial nematic director. Figure 8.6(b) shows the director reorientation, with an MFT at a strain of ∼1.0 and the stress-strain curve of the LCE. Figure 8.6(c) and 8.6(d) show the engineering stress – engineering strain response and the change in thickness of the nematic LCE taken from [2]. For strain values between 0 and 0.2, there is effectively no change in $\langle P_{200} \rangle$ and $\langle P_{400} \rangle$; this regime coincides with the first segment of the stress-strain curve (I) which has a relatively large modulus. In this region, there is very little change in the uniaxial order parameters and the orientation of the nematic director remains unchanged thus one would

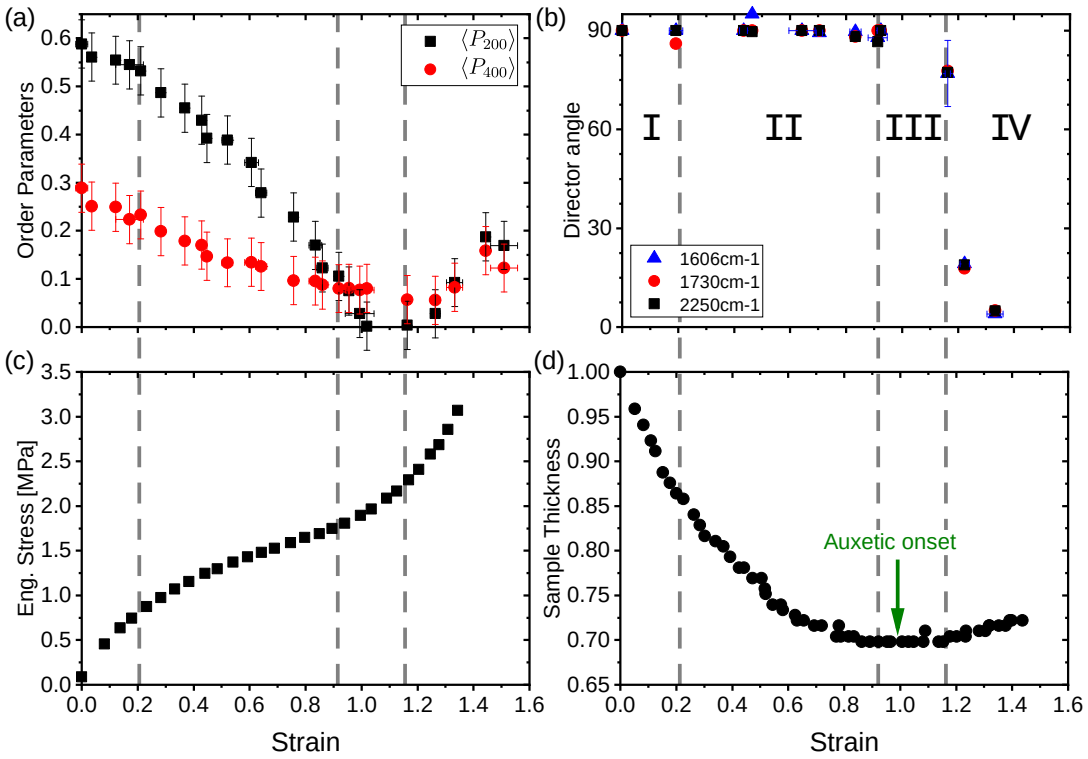

Figure 8.6: (a) $\langle P_{200} \rangle$ and $\langle P_{400} \rangle$ as a function of strain for the LCE strained perpendicular the initial nematic director; error bars in order parameter data are the tolerances of the fitting procedure and error bars in strain are standard errors from repeated measurements. (b) Reorientation of the director, determined from fitting to the full depolarisation Raman data, showing an MFT at a strain of 1.16; error bars are instrumental errors. (c) The stress-strain curve of the LCE showing a softening response between the strains of 0.2 and 0.9 and (d) Fractional sample thickness of the LCE sample showing the auxetic response emerging at strains near the MFT. The dotted grey lines show points of interest. The first line is the beginning of the softening of the stress response which coincides with the reduction in order clearly demonstrating the coupling of the nematic order and the polymer network. The second line shows the crossing of $\langle P_{400} \rangle$ and $\langle P_{200} \rangle$ and the end of the softened stress plateau. Director rotation occurs between the second and final line. The final line shows the re-emergence of $\langle P_{200} \rangle$ order and a sharp rotation of the director. See Mistry *et al.* [1, 2] for more details on stress-strain and thickness measurements.

expect a relatively large modulus in this region as per predictions by nematic elasticity. [40] After this initial regime, an overall decrease is seen in both $\langle P_{200} \rangle$ and $\langle P_{400} \rangle$ as a function of strain until a strain value of ~1.0. The overall director orientation again remains unchanged in this strain regime (figure 8.6(b)), but a softening of the stress-strain response is seen (figure 8.6(c)). Interestingly, while $\langle P_{200} \rangle$ decreases from 0.53 ± 0.05 to 0, $\langle P_{400} \rangle$ decreases more slowly and appears to plateau, with $\langle P_{400} \rangle$ eventually crossing over $\langle P_{200} \rangle$ at a strain of 0.81. $\langle P_{400} \rangle$ then remains larger than $\langle P_{200} \rangle$ until a strain of 1.33. A value of $\langle P_{400} \rangle$ greater than $\langle P_{200} \rangle$ would suggest an ODF in which there is a large distribution of molecules 90° to the overall director, which occurs here in a region well before the reorientation of the director. There is a re-emergence of non-zero $\langle P_{200} \rangle$ values at strains of 1.16; this coincides with the MFT where the director sharply reorients to become parallel to the stress axis. The reorientation of the nematic director coincides with the re-stiffening of the stress-strain curve. $\langle P_{200} \rangle$ continues to increase from 0 to a value of 0.17 ± 0.05 at a strain of 1.51.

8.3.3 The behaviour of different moieties in the LCE

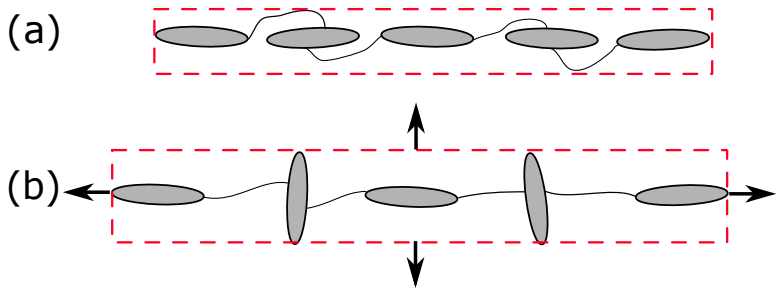

Figure 8.7: Proposed mechanism for an auxetic response in a liquid crystalline polymer. [155] (a) the LCP contains two types of repeating mesogenic units: one attached end-on and one attached laterally. (b) the LCP is strained which causes the laterally attached mesogenic unit to rotate.

A mechanism to elicit the auxetic response in liquid crystalline polymer systems has been suggested, however, experimental results failed to display an negative Poisson's ratio. [155] The proposed mechanism consists of a liquid crystalline

polymer containing 2 different mesogenic units; a mesogenic unit which is attached end-on to the polymer backbone and a mesogenic unit attached laterally to the polymer backbone. [155] The laterally attached mesogenic units would rotate with applied strain and it was suggested that the rotation of rigid units would elicit an auxetic response. [155, 156] See figure 8.7 for a schematic of the proposed mechanism.

Raman scattering is chemically specific so it is possible to investigate whether the two mesogenic units (cross-linker and side-chain) are decoupled in any way in their response to strain, analogous to the model suggested in [155]. Raman data from the 1606cm^{-1} line has contributions from both the side-chain and the cross-linking unit. However, one can also look at the behaviour of the 2250cm^{-1} peak, corresponding to the cyano group, present only in the side-chain and the 1730cm^{-1} peak, corresponding to the carbonyl group, present only in the cross-linker. It can be seen from figure 8.6(b) that the cross-linking units follow exactly the same reorientation profile as the side-chain units. Therefore, the mesogenic units respond identically to the strain, irrespective of whether they are doubly or singly coupled to the acrylate network. The 1730cm^{-1} and the 2250cm^{-1} vibrations are not used to determine order parameters as they do not satisfy the assumptions required for fitting order parameters via Raman; these are that the vibration is aligned with the long axis of the molecule and that it is a cylindrically symmetric vibration. [88]

8.4 Discussion

8.4.1 Uniaxial case: Insight into the mechanical Frèedericksz transition

The order parameter data shown in figure 8.4 and figure 8.6 are deduced using the assumption that the sample has uniaxial symmetry. Here, the extent to which the determined order parameters agree with uniaxial theory will be discussed. To begin with, let us consider the insight that the uniaxial order parameters provide into the nature of the director behaviour and stress – strain response of MFT (figure 8.6), noting the following points:

1. Initially, the mesogenic order is undisturbed and straining pulls on the polymer network, causing an approximately linear stress response. This is region I in figure 8.6.

2. During the flatter region of the stress response (which is similar in appearance to an SSE response, region II in figure 8.6), the director orientation is unchanged, but there is a marked decrease in both order parameters. The softening of the stress response therefore may be related to the increased disorder (and thus degree of freedom) of the mesogenic groups, which allows reorientation of the polymer network. This is a completely different mechanism from that of semi-soft elasticity, where the softening of the stress response occurs due to the continuous rotation of the overall nematic director. [40, 66] In the LCE investigated in this chapter, during the plateau regime, the order parameter data suggest that an increasing proportion of mesogenic units align with the strain axis, a point discussed further in the next sub-section where the order parameter data is compared to relevant theoretical models of $\langle P_{400} \rangle$ against $\langle P_{400} \rangle$. The non-zero value of $\langle P_{400} \rangle$ allows one to deduce that the observed black state is not isotropic as $\langle P_{400} \rangle = 0$ in the isotropic phase. In the analysis of order parameters from Raman spectroscopy it is a requirement for there to be a nematic director on the $x - z$ plane. [80, 83, 85] Thus it can be deduced that the black state is likely not due to the rotation of the director from the $x - z$ into the y axis as there is still a deduced none-zero order in the $x - z$ plane ($\langle P_{400} \rangle \neq 0$) and thus a director. In the sections that follow, it is argued that the atypical $\langle P_{200} \rangle$ and $\langle P_{400} \rangle$ is due to a failure of the uniaxial model for the LCE strained perpendicular to the initial nematic director.

3. As discussed in chapter 1.4.7, due to the near-zero birefringence of the sample near the MFT, it was deduced that there was zero ordering in the plane of observation and thus the LCE exhibited a negative order parameter. [1, 2] The determined order parameters, shown in figure 8.6, is consistent with these findings as $\langle P_{200} \rangle = 0$ near the MFT in the same plane as the birefringence measurements, however, it should be noted that there is a deduced non-zero value of $\langle P_{400} \rangle$ in this region.

4. Eventually, the overall director reorients to align with the strain axis, marking the end of the MFT. This occurs during region IV. There is a re-stiffening of the stress response as the material is pulled parallel to the director with a subsequent increase in order. Interestingly, the continued increase in order with strain in this scenario is quite different (and more marked) than the situation in figure 8.4, potentially explaining the difference in Young's moduli between a sample which has undergone an MFT, being strained parallel to the new director, and one strained parallel to the initial director. In the MFT case, an instantaneous Young's modulus of 5.7 MPa is found whereas an instantaneous Young's modulus of 23.1 MPa is found for a sample pulled parallel to the initial director. [2] One might expect that due to the different extents in changes of the order parameters in both these cases the elastic moduli would be different. [115, 157] The results of the uniaxial model suggests that the LCE deformation mechanism usually referred to as an MFT is far better described as an 'order modification transition' (OMT). This is because the analogy with the electric or magnetic-field cases implied by the term 'mechanical Fréedericksz transition' is unjustified; in the cases of electric and magnetic field Fréedericksz transitions in LCs, there is no change in order parameter, but instead a discontinuous threshold at which the director reorients, with the order staying constant. [158] Our results instead suggest that there is a continuous reduction in order as a function of strain with a subsequent sharp rotation of the director. This is a markedly different response to the continuous rotation of a director with counter rotating domains that is more typical of the SSE response. [40, 64, 67] It should be noted that determination of a single Young's modulus in the nematic LCE is difficult as the stress – strain response of the material is highly non-linear. In chapter 10 the mechanical behaviour of the nematic LCE is investigated via DMA to overcome such issues.

The order parameter measurements of the nematic LCE strained perpendicular to the director can be compared to those determined by Mitchell *et al.* [65] and Roberts *et al.* [70, 71], discussed in chapter 1, who performed X-ray scattering to measure $\langle P_{200} \rangle$ in a side-chain acrylate-based LCE that displayed an MFT.

Roberts *et al.* also found a large decrease in order and both the Mitchell LCE and the LCE studied in this thesis remain optically clear under strain. [2, 70] The Mitchell LCE was also studied at temperatures deep into the nematic phase, well below T_{ni}, and their discussion suggests that their system deforms through small continuous distributions of the director, rather than through highly localised abrupt changes.

8.4.2 Uniaxial case: Deviation from Maier-Saupe theory

Now let us consider how the order parameters, deduced assuming uniaxial symmetry, fit to theoretical predictions to investigate whether the initial approach of assuming uniaxial order (which is usual for nematic systems) is justified, or whether the addition of biaxial order parameters is required. Pottel *et al.* discussed the significance of the order parameters $\langle P_{200} \rangle$ and $\langle P_{400} \rangle$ to the overall ODF, defining the 7 distinct regions in the $\langle P_{200} \rangle / \langle P_{400} \rangle$ space. [94] These regions are discussed in detail in section 2.2.2. Since all the resultant order parameters assuming uniaxial symmetry are positive (see figure 8.6) only the 4 positive regions of figure 2.5 are included in figure 8.8.

Figure 8.8 reveals that initially (at low strains) the LCE behaviour lies near to Maier-Saupe predictions. However as the strain is increased, $\langle P_{200} \rangle$ decreases more rapidly than $\langle P_{400} \rangle$ and the behaviour deviates from Maier-Saupe predictions. The deviation from Maier-Saupe theory predictions continues towards the approach of the MFT (black circles). Eventually the order parameter data cross the 'lower limit' line and enter the region bounded by the this and $\langle P_4 \rangle$ model. In this region the order parameters describes an ODF with a large distribution of molecules perpendicular to the overall nematic director. During and after the MFT the deviation from Maier-Saupe predictions continues, in the opposite direction, along the same trend (red circles). This, for the nematic LCE the order parameter describe an initially Gaussian distribution of molecules centred at $\beta = 0^{\circ}$. On increasing strain a large population of molecules align perpendicular to the nematic director, this behaviour continues even after the MFT. See figure 8.9 for selected ODFs constructed by using information theory (see section 2.2.1) and the determined $\langle P_{200} \rangle$ and $\langle P_{400} \rangle$ data showing this behaviour.

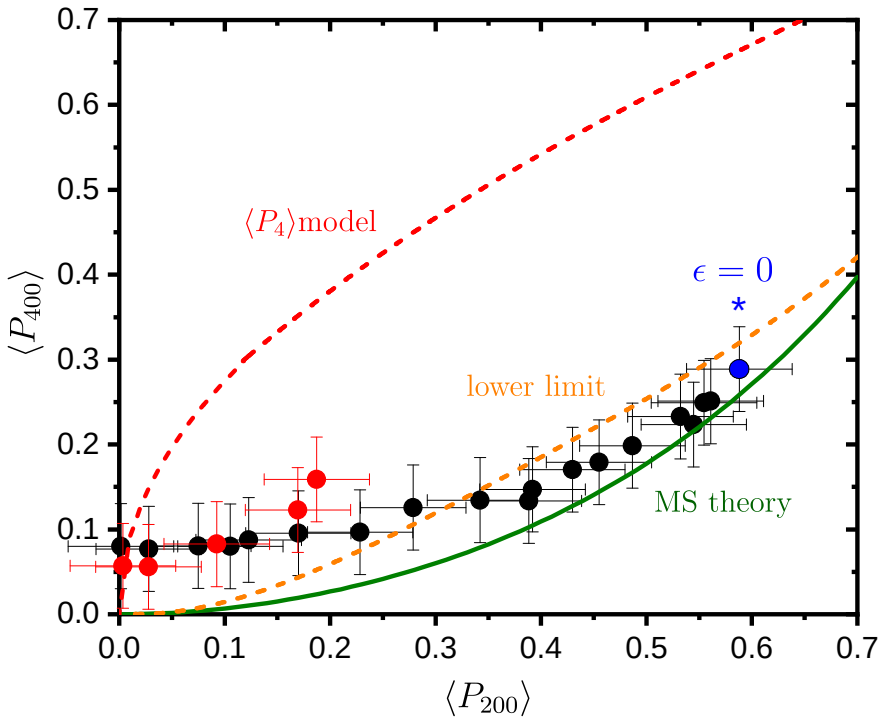

Figure 8.8: $\langle P_{400} \rangle$ plotted as a function of $\langle P_{200} \rangle$ for the LCE strained perpendicular to the initial director; error bars in order parameter data are the tolerances of the fitting procedure. The blue dot highlighted with the asterisk denotes the order parameters in unstrained state. The black dots signify the values of the order parameters on approach to the MFT (region I-III in figure 8.6). The red dots denote the order parameter values after the MFT (region IV in figure 8.6). Various models for $\langle P_{400} \rangle$ and $\langle P_{200} \rangle$ are included on the diagram which are discussed in detail in chapter 2 by Pottel *et al.*[94]

Figure 8.6(b) reveals that the cross-linking units follow the same reorientation profile as the side-chain units. This means that the region where $\langle P_{400} \rangle > \langle P_{200} \rangle$ cannot be explained by the two types of mesogenic units responding differently to strain. Consequently, any model in which the cross-linkers reorient before the side-chain, which could explain the observation that $\langle P_{400} \rangle > \langle P_{200} \rangle$, can be ruled out.

The key conclusion to make from figure 8.8 is that, within error, the order parameter data fits with Maier-Saupe theory at low strains. However, there is a systematic deviation from the Maier-Saupe theory at larger strains particu-

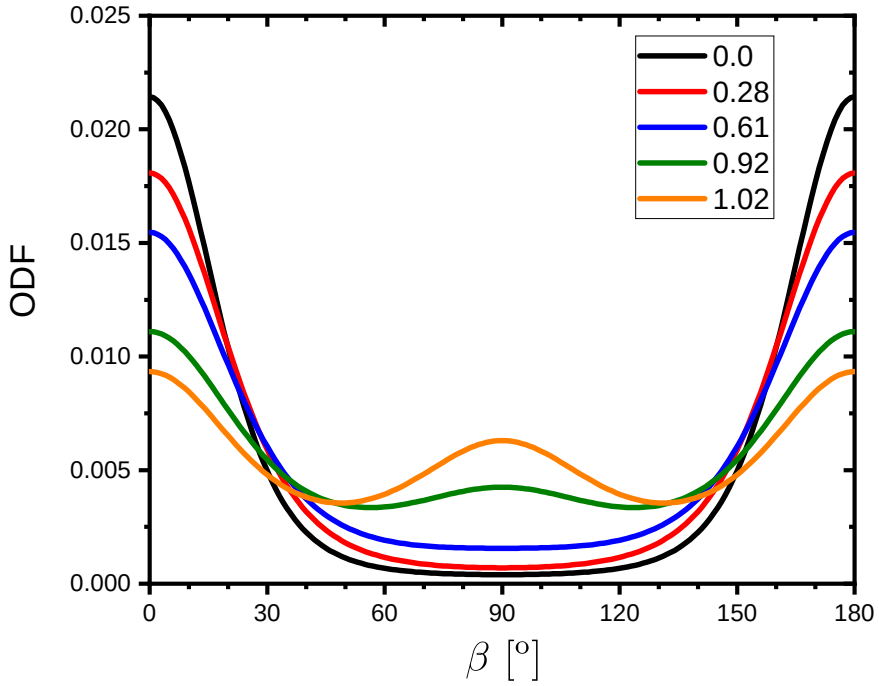

Figure 8.9: ODFs for the perpendicularly strained LCE constructed from the order parameter data deduced with the assumption of a uniaxial distribution of molecules (figure 8.6a.). Line colour corresponds to the strain. Increasing strain results in an increasing distribution of molecules perpendicular to the nematic director (i.e. $\beta = 90^{o}$)

larly around the MFT. The behaviour described a large proportion of molecules aligning perpendicular to the nematic director which cannot be explained by a difference in response to strain between the side-chain A6OCB or the cross-linker RM82. It is interesting to note, that such deviation from Maier-Saupe theory predictions is not observed in the LCE strained parallel to the nematic director (figure 8.4). Based on the difference in the evolution of order parameters observed via Raman spectroscopy in the two geometries and predictions from theory [114, 115] (that deforming the LCE parallel to the nematic director could result in changes in the uniaxial order only, whereas deforming the LCE perpendicular to the nematic director could result in changes in both the uniaxial and biaxial order parameters), the emergence of biaxiality in the nematic LCE should be explored.

8.4.3 The emergence of biaxiality

Conventional nematic liquid crystals form uniaxial phases and the approach taken so far to deduce the order parameters of the nematic LCE has continued to assume that the system is uniaxial. However, as mentioned previously, theory by Finkelmann *et al.* [115] describes the case of straining a LCE without rotation of the director, predicting a decrease in the uniaxial order parameters with the emergence of biaxiality. Additionally, it has been reported in low molar mass liquid crystals that a deviation from Maier-Saupe theory can be explained by the emergence of biaxial order. [87] Since the order parameter data, assuming a uniaxial model, deviate from Maier-Saupe predictions (see figure 8.8) the emergence of phase biaxiality in the nematic LCE will be explored. The phase biaxial order parameters, discussed in section 2.3, are defined as:

$$\begin{aligned} \langle P_{420} \rangle &= \frac{1}{24} \langle (7\cos^2(\beta) - 1) \\ &\times \quad (1 - \cos^2(\beta))\cos(2\alpha) \rangle, \qquad (8.2) \\ \langle P_{440} \rangle &= \frac{1}{16} \langle (1 - \cos^2(\beta))^2 \cos(4\alpha) \rangle, \qquad (8.3) \\ \langle P_{220} \rangle &= \frac{1}{4} \langle (1 - \cos^2(\beta))\cos(2\alpha) \rangle, \qquad (8.4) \end{aligned}$$

where P_{Lm0} are a set of the associated Legendre polynomials. As already noted, $\langle P_{220} \rangle = b/6$ is the biaxial order parameter introduced earlier in the LCE theory. Raman scattering can in principle be employed to determine the biaxial order parameters. [82, 88] However, in practice, it is not possible to directly determine the absolute biaxial contribution to the order parameters from Raman depolarisation data, though qualitative biaxial behaviour can be deduced by careful analysis of the data. [87] The approach, outlined below, has been used to successfully observe the emergence of biaxial order in a biaxial SmA system; [87] the same approach will be used to determine the biaxial order parameters in the nematic LCE.

Throughout the analysis of the Raman depolarisation data to investigate the emergence of phase biaxial order parameters ($\langle P_{420} \rangle$, $\langle P_{440} \rangle$, $\langle P_{220} \rangle$) the molecular biaxial order parameters ($\langle P_{402} \rangle$, $\langle P_{404} \rangle$, $\langle P_{202} \rangle$) are ignored and explicitly set

to 0. [87] This is done for two reasons: (i) to reduce the number of fitting parameters in the analysis and (ii) because the phenyl stretching mode is used during the analysis. The phenyl stretching mode, which is used consistently in this chapter to determine order parameters, has very close to uniaxial cylindrical symmetry [88] and therefore cannot meaningfully probe molecular biaxial order parameters as the molecular vibration itself is invariant to γ. [88, 103] Since the molecular biaxial order parameters are set to 0, the ODF is rotationally invariant to γ but now has dependencies on β and α. To deduce values of the biaxial order parameters idealised depolarisation data is constructed from the experimental values of $\langle P_{200} \rangle$ and $\langle P_{400} \rangle$ using the experimentally determined value of p in the unstrained state ($p = -0.23$). This smooths the data and allows one to extrapolate between experimental values. It is then assumed that the anomalously large values of $\langle P_{400} \rangle$ that causes the data to deviate from Maier-Saupe behaviour (figure 8.8) can be attributed to biaxiality. This is reasonable as it is predicted by theory [113–115] and the retardation of the sample becomes zero at the MFT [2] which is consistent with the birefringence of the material becoming zero if the director remains in the $x-z$ plane. New values of $\langle P_{400} \rangle$ are calculated from $\langle P_{200} \rangle$ by assuming that the uniaxial contributions, $\langle P_{200} \rangle$ and $\langle P_{400} \rangle$, follow Maier-Saupe theory predictions as seen in figure 8.10(a). These values are then fixed and a new fit is made to the reconstructed depolarisation data using the full expression, including biaxial terms (equation 5.22 and equation 5.23), thus obtaining values for $\langle P_{420} \rangle$, $\langle P_{440} \rangle$ and $\langle P_{220} \rangle$ which can be seen in figure 8.10(b). The qualitative behaviour, and relative values, of the biaxial order parameters provided using this approach is reasonable, however, due to the degeneracy of the fitting procedure and the assumptions made their absolute values are not. [87] It is important to check the values of $|\langle P_{420} \rangle|$, $|\langle P_{440} \rangle|$ and $|\langle P_{220} \rangle|$ are all within physically meaningful limits (0.0563, 0.0625 and 0.25 respectively) when using this approach to ensure that, even though the absolute values of the phase biaxial order cannot be relied upon, they fall within reason. The tolerance of fit for the uniaxial model is ± 0.05, however, given the number of fitting terms and the complexity of the fitting function when biaxial order is included, the errors in the fit are hard to systemically determine. Hence, the errors in the fitting procedure are not considered nor are conclusions drawn from the values of the

biaxial order parameters, instead, the evolution of the biaxial order parameters are discussed and whether or not biaxial order provides a reasonable mechanism for the auxetic response.

It is interesting to now consider the emergence of biaxiality in the LCE under strain (figure 8.10). The analysis returns very small values for the biaxial order parameters in the linear elastic region (strains <0.2), where it was already apparent that $\langle P_{200} \rangle$ and $\langle P_{400} \rangle$ followed Maier-Saupe behaviour. However, it can be seen that with increasing strain (and decreasing $\langle P_{200} \rangle$ and $\langle P_{400} \rangle$ values) there is a clear increase in the magnitude of the biaxiality of the phase, as predicted by theory. [115] The absolute values of all the biaxial order parameters increase until the MFT (strain ∼1.0), following which they decrease. Interestingly, and relevantly, the value of $\langle P_{220} \rangle$ becomes increasingly large and negative. The biaxial behaviour is consistent with theoretical predictions, where the biaxial order emerges prior to the MFT. [115] Bladon *et al.* also predicted that after the MFT there is a collapse of the biaxial order and re-emergence of uniaxial order. [114] $\langle P_{220} \rangle$ and the other biaxial order parameters show a decrease in magnitude after the MFT, coinciding with the re-emergence of uniaxial ordering, in apparent agreement with predictions for the reorientation event. [114] However, while there is a reduction in the biaxial order parameters after reorientation of the director, the biaxial order parameters do not collapse to zero as predicted theoretically. While theoretical approaches typically assume that the strains imposed are small and that the polymer chains are Gaussian [113–115], this has been shown to not necessarily be the case [159] and is certainly not the case here with strains $> 100\%$. Hence, even after the MFT the system remains biaxial, which may have an implication in the mechanical properties of the material. [40, 160]

8.4.4 Relating biaxiality to the auxetic behaviour

The theory predicting biaxiality in LCEs considers only the $b = 6\langle P_{220} \rangle$ order parameter; however, Raman spectroscopy can determine $\langle P_{220} \rangle$, $\langle P_{420} \rangle$ and $\langle P_{440} \rangle$. The ability for Raman spectroscopy to probe higher order biaxial terms gives insight into the mechanism for the auxetic response in this LCE, which occurs

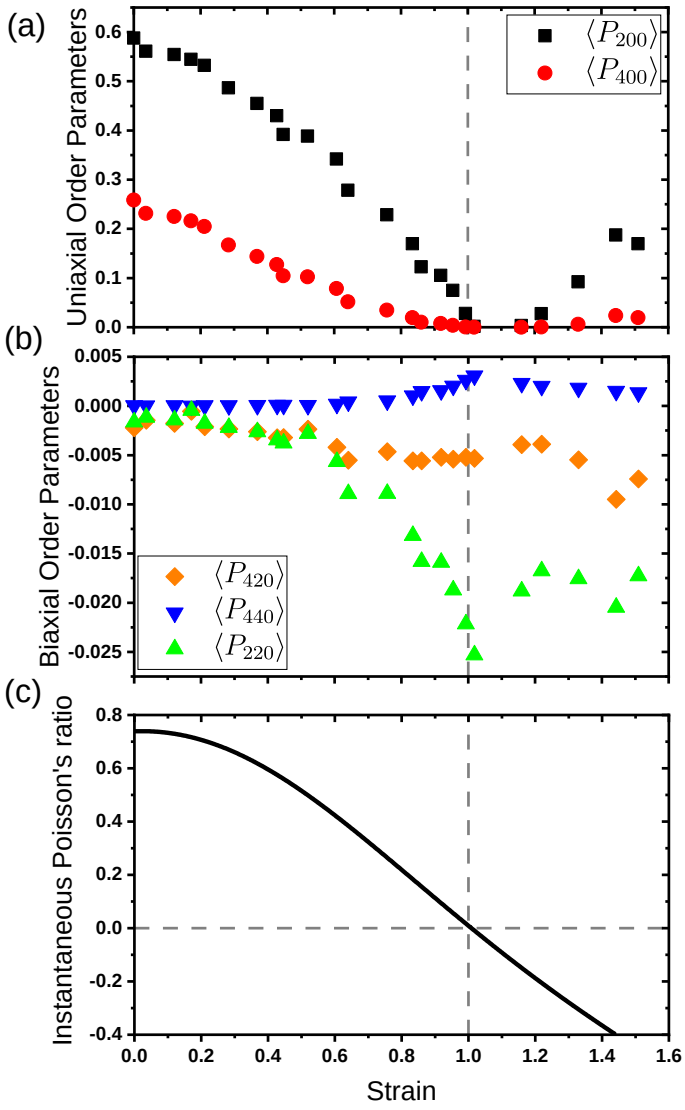

Figure 8.10: (a) Uniaxial order parameters ($\langle P_{200}\rangle$: black squares, $\langle P_{400}\rangle$: red circles) used in the fitting of the biaxial order parameters. The values for $\langle P_{400}\rangle$ are obtained using Maier-Saupe predictions. (b) Biaxial order parameters ($\langle P_{420}\rangle$: purple diamonds, $\langle P_{440}\rangle$: blue downwards triangles $\langle P_{220}\rangle$: green upwards triangles) as a function of strain. (c) Instantaneous Poisson's ratio of the auxetic LCE as a function of strain which becomes negative at a strain of ∼1.00. See Mistry *et al.* [1, 2] for more details on stress-strain and thickness measurements.

above a threshold strain of ∼1.0. Figure 8.10 shows that the biaxial order parameters emerge rather slowly until a strain of ∼0.6 when $\langle P_{220} \rangle$ rapidly decreases towards -0.025 at a strain ∼1.0. $\langle P_{420} \rangle$ changes little during the full strain range. However, $\langle P_{440} \rangle$ remains relatively constant until a strain of ∼0.8 were it becomes increasingly positive. The increase in $\langle P_{440} \rangle$ occurs briefly before the onset of a negative Poisson's ratio [1]. Interestingly, the magnitude of $\langle P_{220} \rangle$ and $\langle P_{440} \rangle$ are maximal at the point where the Poisson's ratio becomes negative. Therefore, it is likely that the increase of $\langle P_{440} \rangle$ may provide a possible explanation for the emergence of molecular auxeticity, as follows.

The distribution of molecules (ODF) can be calculated from the order parameters $\langle P_{200} \rangle$, $\langle P_{400} \rangle$, $\langle P_{420} \rangle$, $\langle P_{440} \rangle$ and $\langle P_{220} \rangle$. It should be noted that since Raman spectroscopy can only determine order parameters up to the 4th rank, that reconstructed ODFs will be inexact, but nonetheless give insight into the molecular distribution of the system. [8] Figure 8.11 shows the distribution of molecules for strain values of 0 and ∼0.99; the larger strain near the beginning of the auxetic response.

Figure 8.11 can be understood as follows. The sample has an initial director oriented along the z axis and is strained along the x axis. In the unstrained state, the molecular distribution is uniaxial with the highest probability found for molecules aligning along the z-direction (red region). However, in the auxetic regime there is now a large distribution of molecular orientations in the x direction, which is along the strain axis. This is a consequence of the contributions of the $\langle P_{220} \rangle$ order parameter and agrees with prevailing theory. [115] Also seen is a growing distribution of molecules towards the y axis in the yz plane, presumably a consequence of the combination of $\langle P_{420} \rangle$ and $\langle P_{440} \rangle$. The redistribution of molecules towards the y axis on a macroscopic scale would increase the dimensions in that direction, providing an explanation for the emergence of a negative Poisson's ratio in this sample in the y-direction. Such out-of-plane deformations have been suggested to achieve a molecular auxetic response in liquid crystalline polymers, however this was not realised experimentally. [155, 156] Early work on microporous foams has also suggested a similar mechanism, albeit with the formation of voids [161], unlike the LCE used here which conserves volume and remains void-less. [1]

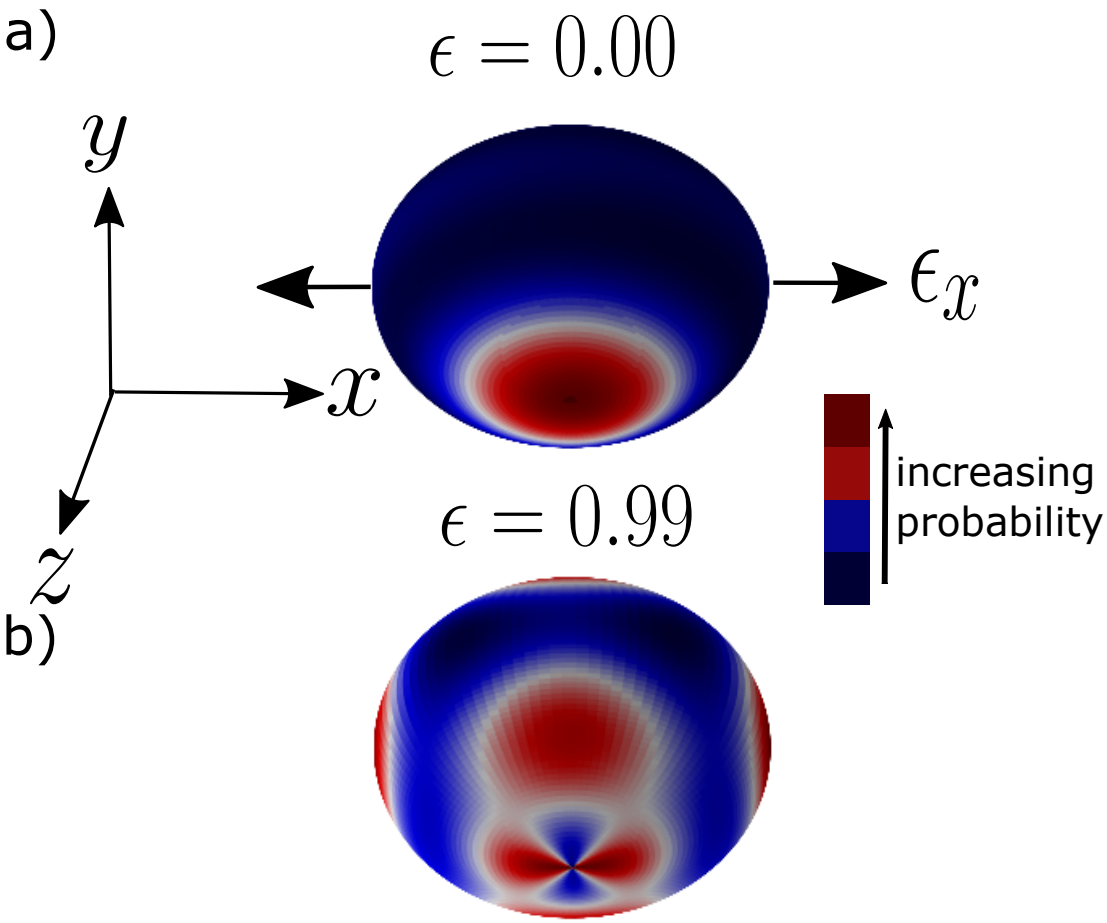

Figure 8.11: Truncated ODF plot showing distribution of molecules in the unstrained state (a) and at the beginning of the auxetic response (b). The initial director orientation is along z and the strain axis is in the x direction. The macroscopic sample's 'thickness' occurs is in the y-dimension. The red regions correspond to the highest density of molecules and black/blue the lowest.

It should be emphasised that only the relative values of the biaxial order parameters have been deduced, and while their qualitative dependence on strain is robust, it is not feasible to determine the absolute values of these parameters. That means that while the data shows how the emergence of biaxiality can in principle result in an auxetic response perpendicular to both the initial director and the strain axis, it cannot quantify the extent of the negative Poisson's ratio.

8.5 Conclusion

In this chapter the change in order parameter of a nematic LCE which displays an auxetic response with applied strain is investigated. The motivation for chapter is twofold. Firstly, to understand the mechanism of the auxetic response in the material. Secondly, as a link was implied experimentally between the MFT and the auxetic response, to understand the apparent contradiction in the mechanical behaviour of a LCE that underwent a mechanical Fréedericksz transition; in particular why the stress-strain curve is reminiscent of an SSE response.

The evolution of the order parameters of the LCE is determined and related these to the mechanical behaviour of the material under strain. The nematic order parameter $\langle P_{200} \rangle$ clearly decreases to zero at the point of the MFT, which is consistent with previous measurements via X-ray spectroscopy [65, 71] and with the determination of zero birefringence which lead to the assumption of a negative order parameter. [1] It is clear from this work of this chapter that the order changes continuously in the system and that the elastic softening of the material coincides with the reduction in order. The deformation mechanism is not analogous with a Fréedericksz transition, and it may be appropriate to consider this behaviour as an order modification transition (OMT) in future, rather than a mechanical Fréedericksz transition (MFT).

It is demonstrated that fitting the Raman data acquired for this system assuming uniaxial symmetry reveals inconsistencies in the relationship between $\langle P_{200} \rangle$ and $\langle P_{400} \rangle$ – they do not follow Maier-Saupe theory. However, by constraining them to do so, it is shown that stretching the LCE induces biaxial order. The emergence of a negative $\langle P_{220} \rangle$ describes a distribution of molecules around the azimuthal angle and in line with the direction of strain, which is an intuitive result.

However, the emergence of a significant population of molecules perpendicular to the strain is observed, which is in the same direction of the molecular auxetic response. The rotation of mesogenic units occurs at the onset of the observed the auxetic threshold and provides a tangible explanation for this response. It is important to note that the theory predicting biaxiality in these systems considers only the $b = \langle P_{220} \rangle$ term [115] whereas here it is argued that the higher rank biaxial terms ($\langle P_{420} \rangle$ and $\langle P_{440} \rangle$) are the drivers of the auxetic response. Thus, it may prove useful for future theoretical approaches to consider the higher rank terms.

Questions arise as to whether the uniaxial order parameters become negative [1], a state which cannot be meaningfully probed using conventional polarised Raman spectroscopy in this geometry, and the conventional analysis used to derive the order parameters, as it is required that the nematic director and the laser polarisation are in the same plane. [83, 85] Certainly, $\langle P_{200} \rangle = 0$ in the plane investigated can be indicative of a negative order state, however the non-zero biaxial order parameters in this region should be noted. In any case, the potential negatively ordered state occurs in a very small strain range [1, 2] and there is clearly rich order parameter behaviour occurring before and after the transition, due to imposed strains. LCEs have been developed which have a stable negative ordering [13] in the unstrained state and further experiments will be required to understand whether a negative order parameter that then evolves with strain also results in an negative Poisson's ratio.

Finally, it is noteworthy that the material studied here, in which the auxetic response was first measured, satisfies the condition in equation 8.1 for biaxiality to dominate as $T_{\mathrm{ni}} > 330$°C [2] and measurements are taken at $T = 20$°C, therefore one expects the biaxial stiffness of the material to be much lower than the uniaxial stiffness. Thus, it could be suggested that an auxetic response in LCEs is more likely to occur around room temperature in LCEs with a high T_{ni} and it will be seen above the glass transition temperature where the system can behave elastically. This describes the acrylate systems that have been reported to exhibit an MFT, at least one of which [2, 70] appears to undergo an auxetic response. Questions remain about whether the magnitude and threshold of the auxetic

response can be predicted, but the first important steps in determining what elicits an auxetic response in LCEs have now been taken.

Chapter 9

Results II: Influence of phase on the molecular dynamics of LCEs

9.1 Introduction

In this chapter, the molecular relaxations of an unstrained LCE is studied via BDS and rheological techniques. LCEs display interesting and complex mechanical behaviours such as stress-optical coupling, soft-elasticity, enhanced damping properties and, in some cases, a molecular auxetic response to strain; [1, 40, 162] studying the dynamic response of these materials is interesting as it may provide insight into these properties. As discussed in chapter 1 and 3 nematic LCEs display an SSE response or an MFT when strain is applied perpendicularly to the director. There have been numerous investigations of the molecular relaxation behaviour of LCEs that deform via the SSE using rheological techniques, however, the molecular relaxation behaviour of LCEs which deform via the MFT remains to be studied. [163–166] Furthermore, the general relaxation dynamics and glass-formation in nematic liquid crystals is of fundamental interest. [167, 168] As described in chapter 4, the LCE used in this thesis can be synthesised, as chemically identical samples, in either the nematic or the isotropic phase by polymerisation. [61] The existence of the nematic or isotropic phase for the LCE has been confirmed by studying the order parameters of the respective sample via Raman spectroscopy in [61] and chapter 8. For the LCEs used in this thesis, there is no evidence of a thermally driven nematic-isotropic phase transition up to the point

of sample degradation, therefore, the phase selected for the sample is locked in during synthesis. [2, 61] For these reasons, the LCE is an interesting and useful candidate for studying glassy behaviour of a chemically identical samples in the isotropic and nematic phase over a wide range in temperatures.

The majority of the content in this chapter has been published in the paper: T. Raistrick *et al.* "Influence of Liquid Crystallinity and Mechanical Deformation on the Molecular Relaxations of an Auxetic Liquid Crystal Elastomer.", *Molecules*, **26(23)**, 7313, 2021. [169] Much of this chapter is reproduced from said paper; unless specified any experimental work presented has been performed by T. Raistrick; V_{corr} analysis was performed by M. Reynolds using data obtained from BDS measurements performed by T.Raistrick, SAOS measurements were performed in collaboration with M. Reynolds.

9.2 Nomenclature of molecular relaxations in LCEs

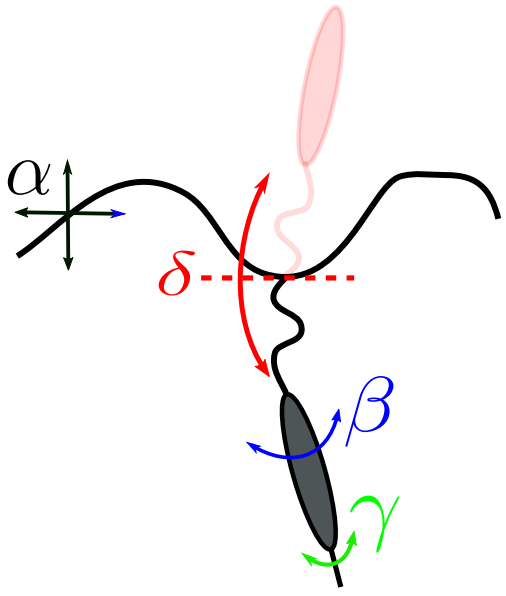

Figure 9.1: Schematic of possible dielectric relaxations in a side-chain liquid crystalline polymer.

In chapter 1, the dynamics involved with general glass formation are outlined. For molecular glass-formers and conventional polymeric glass-formers relaxations are often named in order of appearance on cooling. [27] However, in the study of the molecular relaxations in LCEs, while there have been relatively few studies [163, 170, 171], the nomenclature follows that used for side-chain liquid crystal polymers (SCLCPs) where relaxations are attributed to specific motions. In SCLCPs, 4 relaxation processes are typically observed: δ, α, β and γ, named in order of increasing relaxation frequency for a fixed T. [27] The possible mechanisms of these relaxations are shown in figure 9.1 and are described as follows:

1. the α relaxation in SCLCPs involves the backbone polymer segments and is directly related to the glass transition. [27]

2. the δ process has been observed in both SCLCPs [27, 172, 173] and LCEs [163, 170, 171] and is typically slower than the α relaxation, follows a VFT dependence, and is attributed to reorientation of the mesogenic units around the polymer backbone.

3. the β relaxation is typically assigned to fluctuations of the mesogen around its own long axis. [27, 172, 174, 175]

4. the γ relaxation is assigned to motions of either the spacer unit, or the terminal group of the side-chain mesogenic unit. [172, 176]

As described in chapter 1 the α relaxation shows a cross-over in dynamic behaviour at temperatures T_B and T_A ($T_A > T_B$): at T_B there is a cross-over from one Vogel-Fulcher-Tammann (VFT) behaviour to a more fragile VFT behaviour (i.e. less Arrhenius-like) which typically coincides with the bifurcation of the α relaxation and β relaxation; T_A is the high temperature cross-over from VFT behaviour to Arrhenius behaviour, however, for polymeric materials T_A is often higher than the degradation temperature of the sample and the cross-over is not observed. [16] In SCLCPs a cross-over in the dynamic behaviour $\tau_\alpha(T)$ has also been observed. However, in contrast to the non-LC glass-formers, SCLCPs display a cross-over from VFT behaviour to Arrhenius behaviour, on increasing T, at a crossover temperature of $T^* = 1.1 - 1.3 \times T_g$. [173, 177] Interestingly,

the cross-over from VFT to Arrhenius in SCLCPs at T^* is similar to the cross-over form VFT to a more fragile VFT in non-LC glass-formers which occurs at $T_B \approx T_{\alpha\beta}$ and $T_B = 1.2 - 1.6 \times T_g$ [27, 37], suggesting similarities in their origins. This cross-over to Arrhenius behaviour is typically only observed for polymers that form LC phases and not observed in chemically similar polymers that show no LC behaviour. For example, the existence of LC phase behaviour was removed from a SCLCP by the substitution of a hydrogen on the biphenyl mesogenic group with the bulkier methoxy (-OCH3) group which resulted in a loss of the crossover from VFT to Arrhenius at T^* and τ_α could instead be described by a single VFT. [173] This observation suggests that fluctuations related to LC phases are required for this behaviour to occur.

9.3 Experimental set-up

9.3.1 Sample preparation

The isotropic and nematic LCE samples are prepared as described in chapter 4. The LCE samples are cut into the required dimensions. For the BDS measurements sample dimensions of 1.5cm × 1.5 cm × 100 μm (L × W × T) are used. For the DMA measurements sample dimensions of 5 cm × 2 mm × 100 μm are used. For SAOS measurements a diameter of 5 mm and a sample thickness of 500 μm (5× 100 μm samples stacked on top of each other) is used.

9.3.2 Broadband dielectric spectroscopy

Broadband dielectric spectroscopy (BDS) is performed as described in chapter 6. Briefly, BDS using a Novocontrol Alpha-A dielectric analyser. The LCE samples are sandwiched between two 10 mm diameter brass electrodes. The temperature is controlled using a Novocontrol Quatro Cryosystem for -150°C $< T <$ 100°C. The molecular relaxations of the LCEs are investigated by fitting the dielectric data, for each T, as sum of relaxation contributions as described in chapter 6. To obtain the time-scale corresponding to the peak maximum of each observed relaxation, τ_p, the τ_{HN} time-scales are corrected.

9.3.3 Rheology

DMA and SAOS rheology are performed as described in chapter 7. Briefly, DMA is performed with the film tension clamp attachment using a Rheometrics solid analyser (RSAII) with a oscillatory strain amplitude of 0.1%. This strain amplitude is within the LVR of the material as confirmed by prior strain sweeps. The DMA frequency sweeps are performed from 1 Hz to 12.5 Hz (6.3 and 78.5 rad/s) from $T = 22$ °C to 48 °C in 2 °C steps. SAOS is performed with the parallel plate attachment using a Rheometrics ARES rheometer. Samples are loaded between 5 mm diameter parallel plates with a shear strain of 0.07%. This shear strain is within the LVE regime of the material as confirmed by prior strain sweeps. The SAOS frequency sweeps are performed between 0.1 and 100 rad/s from $T = 80$ °C to 0 °C in 5 °C steps. Upon lowering the temperature, the gap is reduced to ensure that the sample remained in the correct shape, and the strain was reduced to ensure an optimum torque (stress) response.

9.4 Results: Broadband dielectric spectroscopy

In this section, the molecular relaxations of the LCE, in both the isotropic and nematic phase, are probed via broadband dielectric spectroscopy. Thus, the effects of the nematic phase on the glass formation of chemically identical samples can be investigated.

9.4.1 Relaxation dynamics of the isotropic and nematic LCE

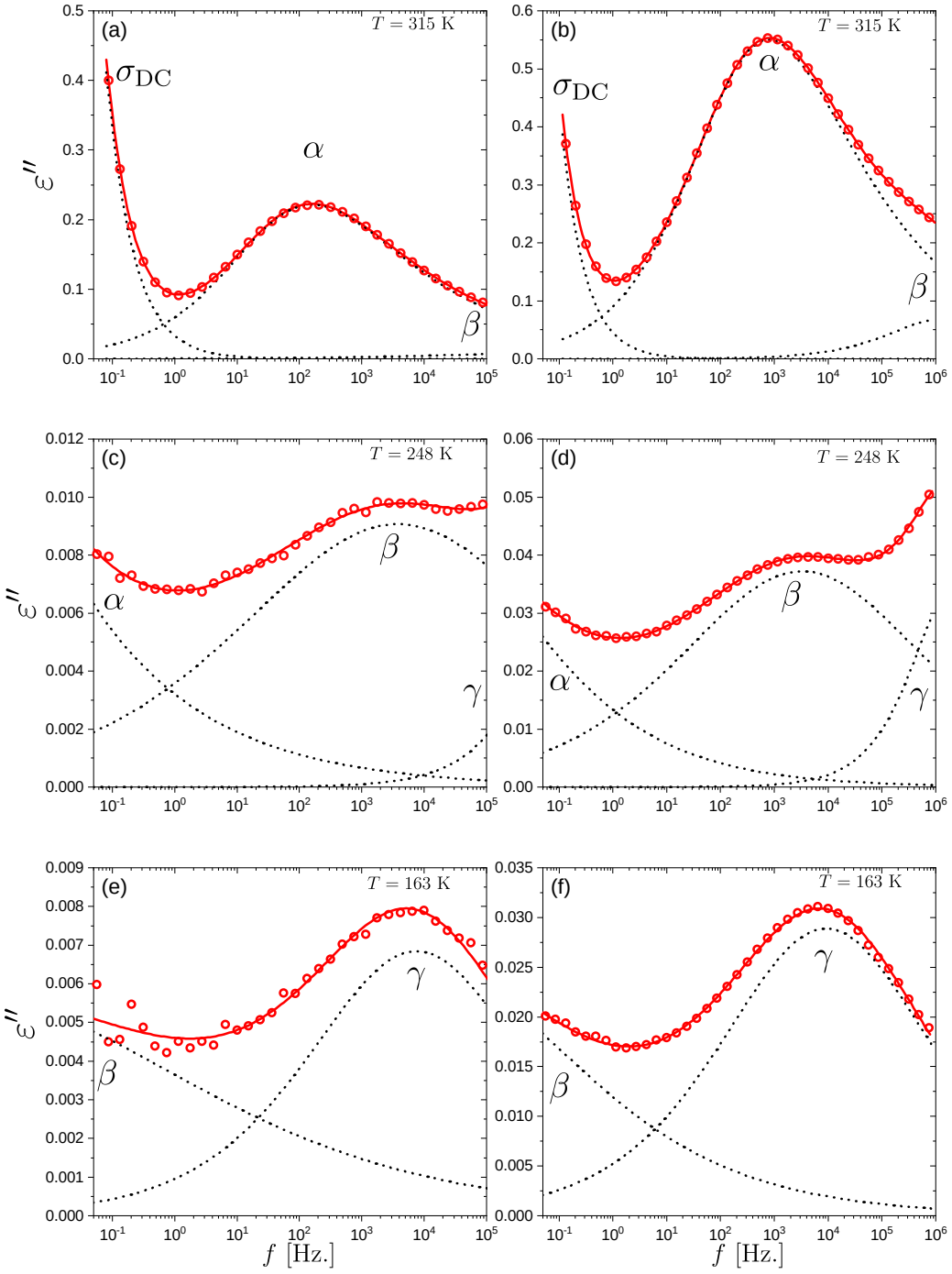

Figure 9.2: Dielectric loss (ε'') versus frequency (f) for the isotropic (a, c, e) and nematic (b, d, f) LCE samples at $T = 315$ K, $T = 248$ K and $T = 163$ K. The overall fits to the data are shown in solid red lines, and the individual contributions from the α, β and γ relaxations, as well as the DC conductivity (σ) are labelled and shown in dashed lines. Errors associated with equipment ($\Delta\varepsilon''\pm < 1\%$) are smaller than the symbol size.

Figure 9.2 shows the ε'' data and fitting of relaxation processes for the isotropic (a, c, e) nematic (b, d, f) LCE for selected temperatures. In both the nematic and isotropic LCE samples, three relaxation processes are identified: α, β and γ, where α denotes the structural relaxation, directly related to the glass-transition, and β and γ, correspond to more local motions, and are thus characterised by shorter time-scales. In section 6.1.4 the β relaxation and γ relaxation will be assigned to specific motions by evaluating the activation energies of the relaxation. In addition to the observed molecular relaxations, there is a clear contribution from ionic DC-conductivity, as evidenced by the power-law contribution $\varepsilon'' \propto f^{-1}$, observed at low frequencies and high temperatures in (a) and (b) of figure 9.2.

9.4.2 Existence of the δ relaxation?

The LCEs previously investigated in literature typically show a 'δ relaxation' that is slower than the α relaxation and associated with the motions of the mesogenic unit around its short axis. [163, 170, 171] This slow δ relaxation may be obscured by the large DC conductivity contribution observed in figure 9.2. The presence of any dielectrically active molecular relaxation obscured by DC conductivity is investigated by the two approaches described in chapter 6. In the first approach, the ohmic-free dielectric loss spectra are determined from the ε' spectra using a well-established approximation of the Kramers–Kronig transformation as described in section 6.1.5. [137] In the second approach, the dielectric modulus representation $M^* = 1/\varepsilon^*$ is used in which any contribution from conductivity is suppressed (also described in section 6.1.5). [137]

Figure 9.3 shows that for both these approaches a relaxation is seen in the dynamic window slower than the α relaxation. In the M^* representation, the relaxation is Debye-like and this Debye-relaxation coincides with the presence of electrode polarization as evidenced by a low-frequency increase in ε' which is shown in figure 9.4. Thus the Debye-like relaxation peak observed in the LCE is likely to be the so-called 'conductivity relaxation' [137, 178], due to electrode polarization, and thus not to a molecular relaxation; electrode polarization is due to charge accumulation at the sample-electrode interface. [27] Thus, in our LCE system, there is no evidence of the so-called δ relaxation within the temperature

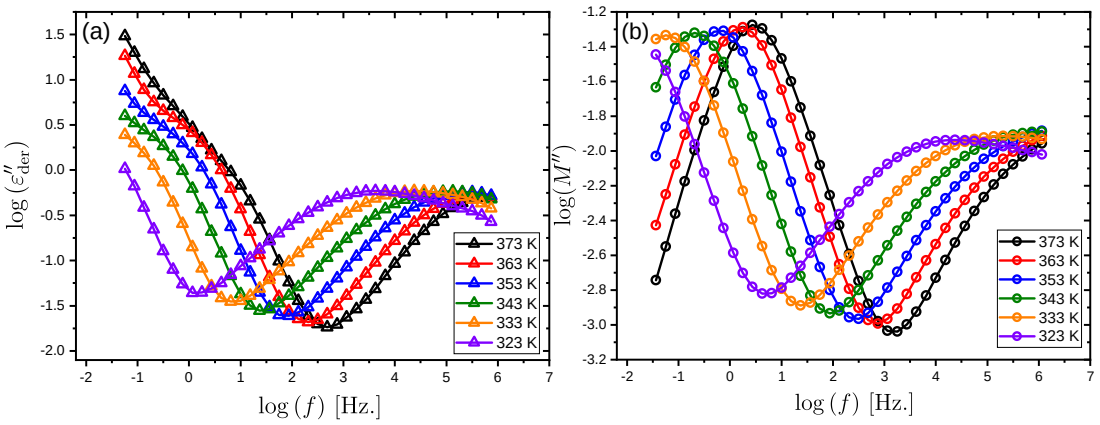

Figure 9.3: A slow Debye-like relaxation is observed in (a) the $\varepsilon''_{\mathrm{der}}$ and (b) the M'' representation for selected temperatures.

and frequency range investigated. The LCEs studied previously display δ relaxations and additionally a transition from an isotropic phase to an LC phase upon cooling. [163, 170, 171] Conversely, our LCE displays no such δ relaxation and additionally shows no such transition from isotropic to nematic phase (or vice-versa) [2, 61]. This suggests that despite the presence of side-chain mesogenic units, the larger-scale motions of the mesogenic units are hindered in both the isotropic and nematic phases of our LCE. The cross-link density of our LCE, based on its chemical composition, is 7.1 mol%. This cross-linking density is comparable to the 7.5 mol% cross-link density in a previous study of an LCE with a comparable T_{g} value, which did show a δ relaxation [170], suggesting that the level of cross-linking in our LCE might not be enough to trap the large-scale movements of the mesogenic units. Thus, the presence of the non-mesogenic pendant units, EHA, in our LCE could entrap the mesogenic A6OCB side-chain, in turn preventing the larger-scale motions corresponding to the δ relaxation. Interestingly, although speculatively, the lack of the δ relaxation in our LCE may be somewhat related to the MFT that occurs in our LCE when strains are applied perpendicular to the director. The 'Finkelmann-type' LCE, which displays the SSE response to applied strain, has been shown to display a δ relaxation. [163] The ability of the mesogenic units to rotate around their short axis may be related to the large

scale motions of the rotation of the nematic director required for the SSE. Thus, the MFT may be related to an LCE system in which the mesogenic units have to deform via small scale changes in the nematic order, as described in chapter 8, as opposed to macroscopic director rotation. However, as mentioned this is speculative and would require more investigations of the molecular relaxations of LCEs of both the SSE and MFT type before a conclusion could be drawn.

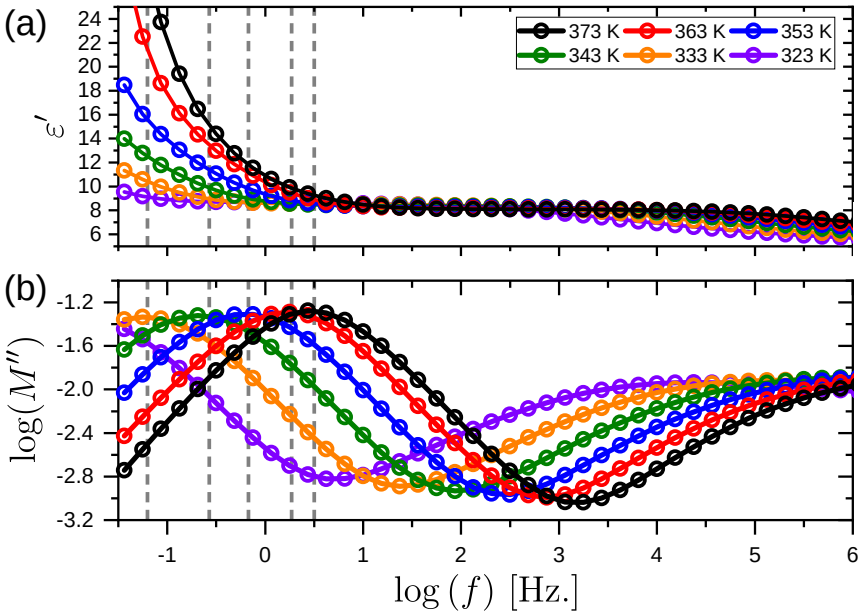

Figure 9.4: An increase in (a) ε' coincides with the presence of the Debye-like relaxation in the (b) M'' representation. The is evidence that the observed relaxation is the 'conductivity relaxation'.

9.4.3 T-dependant behaviour of observed relaxations

The T-dependence of the observed molecular relaxations, α, β and γ, is investigated by fitting of the molecular relaxations as described in chapter 6. The α relaxation time-scales, both the isotropic and nematic LCE, are well described by the HN function ($q \neq 1$, $p \neq 1$) whilst the β and γ relaxation are well described by the symmetric Cole-Cole function ($p = 1$, $q \neq 1$). The T-dependent characteristic relaxation times for the α, β and γ relaxations are shown in an Arrhenius

plot in figure 9.5. The α relaxations for the isotropic (Iso) and nematic (Nem) LCE samples are fitted using a VFT expression, whereas the β and γ relaxations are fitted using an Arrhenius expression. The fitting parameters are provided in table 9.1.

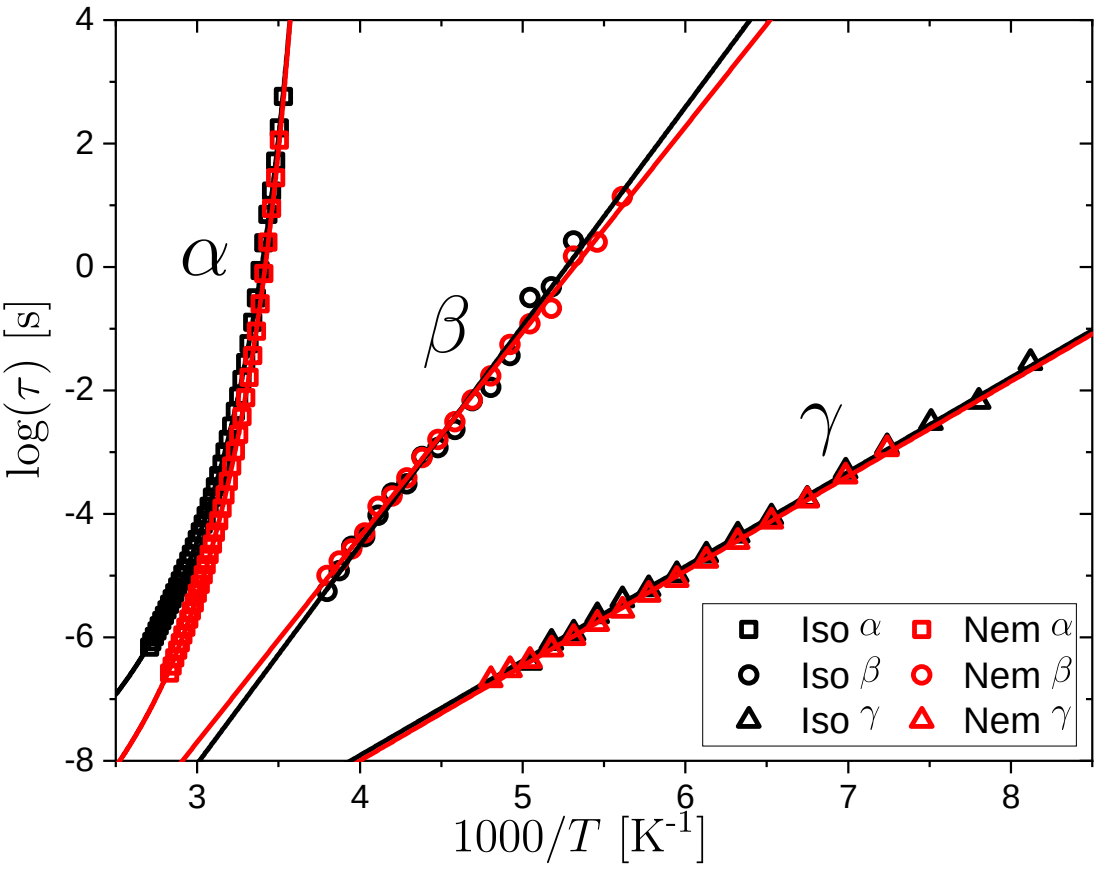

Figure 9.5: Characteristic relaxation times for the α (squares), β (circles) and γ (triangles) relaxations identified for the isotropic (black) and nematic (red) LCE samples. The results of a VFT fit to the α relaxation data, and Arrhenius fits the β and γ relaxation data are shown in solid lines. Errors associated with the fitting tolerances are smaller than the symbol size.

As seen from the fits in figure 9.5 and the corresponding parameters in table 9.1, the β and γ relaxations have very similar T-dependencies in the isotropic and nematic states. The corresponding activation energies ΔE_{A} for the β relaxation

Sample	Process	$\log(\tau_0)$ [s]	ΔE_A [kJmol^{-1}]	D	T_0 [K]	T_g [K]
Isotropic	α	-10.3±0.1	-	5.0±0.1	243±1	286±1
	β	-18.7±0.7	67.9±0.2	-	-	-
	γ	-14.0±0.1	29.3±0.3	-	-	-
Nematic	α	-11.8±0.1	-	5.6±0.1	243±1	285±1
	β	-17.7±0.2	63.6±0.7	-	-	-
	γ	-14.1±0.1	29.4±0.3	-	-	-

Table 9.1: Results of Arrhenius and VFT fits to relaxations in the isotropic and LCE nematic samples. Errors are associated with the fitting tolerance of the VFT fits to data.

are 67.9 kJmol^{-1} and 63.6 kJmol^{-1} for the isotropic and nematic LCE, respectively. The corresponding ΔE_A results for the γ relaxation are 29.3 kJmol^{-1} and 29.4 kJmol^{-1}, respectively. The results of the Arrhenius fits thus demonstrate that the LCE phase has little effect on the β and γ relaxations. This may be due to the relatively short characteristic length scales of these relaxations, in comparison to the relevant length scale of the LC phase. It is interesting to compare our LCE results to those of other LC systems in the literature. A collection of activations energies, ΔE_A, for β relaxations in polyacrylate and polymethacrylate SCLCPs are found in work by Kremer and Schönhals [27] and Schönhals and Hans-Eckart Carius, [176] ΔE_A values within the range 46.5–68.9 kJmol^{-1} were reported. The exact ΔE_A value depends on the terminal group attachment of the mesogenic unit and the length of the alkyl spacer between the backbone and the mesogenic unit. The acrylate-based LCE used in this thesis has a spacer length of 6. The activation energy of the SCLCP with the closest chemistry to this LCE (acrylate backbone, spacer length of 6) is 62.8 kJmol^{-1}, which is close to the ΔE_A values, determined in figure 9.5, of 67.9 kJmol^{-1} and 63.6 kJmol^{-1} for the isotropic and nematic LCE respectively. Thus, the observed β relaxation follows the literature assignment and is therefore assigned to fluctuations of the mesogenic units around its long axis. Literature values of the γ relaxation, typically assigned to motions of the alkyl spacer units, have ΔE_A values in the range ∼33-35 kJmol^{-1}, [172, 179, 180] which is close to the ΔE_A of ∼29 kJmol^{-1} determined for the γ relaxation in the isotropic and nematic LCE. Hence, based on comparison to literature data, the γ process for the LCE as determined in figure 9.5 is likely due to motions of

the 6-alkyl chain connecting A6OCB to the acrylate backbone.

9.4.4 Dynamic cross-over of the α relaxation

As discussed in chapter 1, for molecular glass-formers the T-dependence of the α relaxation is often not described by a single VFT equation and dynamic cross-overs in behaviour are often observed over extended temperatures. To further investigate the T-dependence of $\tau_\alpha(T)$ the derivative-based analysis, or 'Stickel analysis', as described in 1.3 is performed. [34, 35] The result of the Stickel analysis is shown in figure 9.6

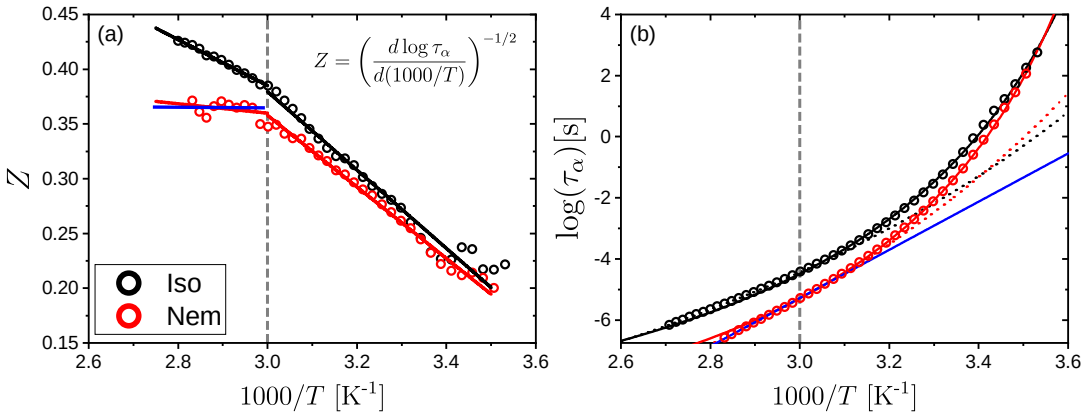

Figure 9.6: Stickel analysis of $\tau_\alpha(T)$ data of the isotropic (black) and nematic (red) LCE samples. A crossover behaviour is observed at T^* ≈333 K, as shown with a dashed line. Linear fits of the data are shown both for temperatures above and below T^*. For the nematic samples the data for $T > T^*$ can be well described using a horizontal line (corresponding to Arrhenius behaviour). (b) Arrhenius plot of $\tau_\alpha(T)$ vs. inverse temperature for the isotropic and nematic samples. For $T < T^*$, the VFT fits to the data are shown in solid lines. For $T > T^*$ VFT fits are shown in dashed lines for the isotropic (black) and nematic (red) sample. An Arrhenius fit is also applied to the nematic data before $1000/T$=3.0 (blue solid line).

As shown in figure 9.6(a), both the isotropic and nematic LCE samples undergo a change in $\tau_\alpha(T)$ at a temperature $T^* \approx 333$ K, corresponding to $1000/T^* \approx 3.0$. For $T < T^*$, the gradients of the linear fits are similar (-0.36 and -0.33 for the isotropic and nematic samples, respectively). However, for

Sample	$1000/T$	$\log(\tau_0)$ [s]	ΔE_A [kJmol^{-1}]	D	T_0 [K]	T_g [K]
Isotropic	< 3.0	-13.3	-	16.6	183	270
	> 3.0	-10.6±0.3	-	5.4±0.3	241±1	286±1
Nematic	< 3.0	-15.6	-	17.2	193	275
	< 3.0	-28.9	151.0	-	-	-
	> 3.0	-11.42±0.1	-	5.1±0.1	245±1	285±1

Table 9.2: Results of the VFT and Arrhenius fits for the isotropic and nematic LCE. Due to the small range of data points for $1000/T < 3.0$ the errors of the fitting procedure are not considered, instead the values serve to investigate the possibility of Arrhenius behaviour as evidence by the Stickel analysis discussed in the main text.

$T > T^*$, the gradients are clearly significantly different (-0.21 and -0.04) thus $\tau_\alpha(T)$ has different behaviour in the isotropic and nematic samples above T^*. It is also clear from figure 9.6(a) that the gradient for the nematic samples for $T > T^*$ is very near zero and can thus be well described by an Arrhenius behaviour. To further investigate $\tau_\alpha(T)$, the data are fit with separate VFTs, for $T < T^*$ (solid lines) and $T > T^*$ (dashed lines), as shown in figure 9.6(b). For the nematic data, for $T > T^*$, the data are also fit using an Arrhenius expression for comparison. The results of the fits are outlined in table 9.2. From the fit result of the dielectric data, the T_g values can be determined from $T_g = T(\tau_\alpha = 100\text{s})$, which results in T_g values of 286 K and 285 K, respectively. The similar VFT parameters D=5.4 and D=5.1 reflect that $\tau_\alpha(T)$ behave in a very similar manner for temperatures approaching T_g and that the fragility of the two samples is thus similar. The fragility parameter (m) for the isotropic and nematic LCEs can also be determined from the VFT parameters, using equation 1.27, the results of which are m=110 and m=130 for the isotropic and nematic LCE, respectively. This demonstrates that both LCE phases are fragile glass-formers with fragility values consistent with those of polymers. [37, 39] For $T > T^*$, however, both the isotropic and nematic LCEs are less fragile which is demonstrated by the VFT parameters D=16.6 and D=17.2. The Stickel analysis demonstrates that the nematic LCE can be well described by an Arrhenius equation (gradient of 0 on Stickel plot) in this T-range as the gradient of the Stickel plot for $T > T^*$ is -0.04 for the nematic LCE. Thus, an Arrhenius fit is also applied to this region

of the data of the nematic LCE (figure 9.6(b), solid blue line). The result of the Arrhenius fit is $\tau_\alpha \sim 10^{-29}$ s and 151 kJmol^{-1}. Interestingly, the isotropic LCE also becomes more Arrhenius-like above T^*, as evidence by a reduction in the gradient on the Stickel plot.

T^* is situated well above T_g (T^*/T_g ≈1.17) and corresponds to $\tau_\alpha(T^*)$= 3.8×10^{-5} s and 5.0×10^{-6} s for the isotropic and nematic LCE samples, respectively. The ratio T^*/T_g for the cross-over in behaviour observed in the LCEs is close to the ratio T_B/T_g observed for conventional glass formers (T_B/T_g = 1.2-1.6) [37] suggesting a related origin. However, as described in chapter 1, conventional non-LC glass formers typically display a transition to more markedly non-Arrhenius (more fragile) behaviour for $T > T_B$, whereas for LCE the opposite trend is observed for $T > T^*$. Additionally, for non-LC glass-formers, a bifurcation of the Johari–Goldstein β relaxation from the α relaxation is often observed at $T_{\alpha\beta} \approx T_B$. [27, 36] Neither of the two dielectrically active secondary relaxations, β or γ, observed in figure 9.5 show any relation with T^*. However, it should be noted that it is not possible to rule out the presence of another secondary relaxation that is not dielectrically active (and thus not detected via BDS), which demonstrates a bifurcation behaviour near T^*.

In SCLCPs, a qualitatively similar $\tau_\alpha(T)$ behaviour to that of the LCE is observed for the α relaxation where the data is described by an Arrhenius behaviour for $T > T^*$ and a VFT behaviour for $T < T^*$. [173, 177, 181] Temperature ratios of T^*/T_g = 1.1 - 1.3 have been observed in nematic and smectic SCLCPs [173, 177], which is close to the ratios observed in the isotropic and nematic LCE. In studies of a homologous series of methacrylate-based SCLCPs with systematically varying side-chain lengths, the T^*/T_g ratio was found to be fixed and independent of the phase transition temperatures. [173, 177] The activation energy, ΔE_A, for the α relaxation of SCLCPs in the high-T Arrhenius regime typically ranges from 80-127 kJmol^{-1} [173] is comparable to the value of 151 kJmol^{-1} of the nematic LCE. Thus, the behaviours observed in SCLCPs are generally very similar to the observations for the nematic LCE.

9.4.5 Suggested cause of the dynamic cross-over in this LCE

As the glass transition is approached, the α relaxation is characterised by the presence of dynamic heterogeneities (i.e. regions in space with dynamics different from their surroundings). Additionally, the motions relating to the α relaxation become increasingly cooperative on cooling. The length-scale of the cooperative motions often discussed in terms of the 'cooperatively rearranging region' or CRR which is the smallest region within the material that can change its configuration independently of its surrounding neighbours. [27] The cross-over behaviour of the α relaxation observed in SCLCPs at T^* has been suggested to be related to a matching between the characteristic length-scale of correlated motions of the α relaxation and a length-scale characterising microphase separation of mesogen-rich and polymer-rich domains. [27, 173, 177] Microphase separation has been observed in polysiloxane SCLCPs that readily phase separate [182] and in SCLCPs which form layers due to smectic phase behaviour. [177] However, cross-over behaviour at T^* is seen in both the nematic LCE and isotropic LCE; microphase separation is certainly not present in the isotropic LCE, the origin of the observed crossover behaviour lies elsewhere. A possible mechanism for the cross-over behaviour is discussed below.

The $\tau_\alpha(T)$ data undergoes a crossover to more Arrhenius-like behaviour for $T > T^*$ for both the nematic and isotropic LCE, which is opposite to the crossover to more non-Arrhenius behaviour for non-LC glass-formers. [35] It is therefore interesting to determine any length-scales related to 'liquid crystalline' behaviour in the 'isotropic' LCE which may be involved in this cross-over. The most pertinent length-scale is the static correlation-length, ξ, of pre-transitional nematic domains. [183] The correlation length of the pre-transitional nematic regions, ξ, in an isotropic phase follows the equation: [183]

$$\xi = \xi_0 \sqrt{\frac{T_c}{T - T_c}}, \tag{9.1}$$

where ξ_0 is the bare correlation length of the pre-transitional nematic regions, which is typically $\xi_0 \approx 0.5$ nm in simple molecular LCs, [183] and T_c is is the temperature of absolute stability of the isotropic phase which is typically $\sim$1 K

lower than T_{ni}. [153] The isotropic phase is templated into the LCE and after polymerisation there is no evidence of a phase change in the isotropic LCE as investigated by DSC. [61] Thus it can be assumed that the pre-transitional nematic regions are frozen-in during polymerisation, a phenomenon similar to 'frozen-in order' near cross-linking points and 'quenched disorder' previously observed in LCEs. [58, 184] The isotropic LCE is polymerised at 60°C and the T_{ni} of the precursor mixture is 36°C; [2, 61] therefore by substituting these values into equation 9.1, an expected correlation length of the order of 3.5 ξ_0 is found. Using the typical value of $\xi_0 = 0.5$ nm, the correlation length of the nematic domains in the isotropic LCE to is expected to be of the order of $\xi_0 = 1.8$ nm. The size of the spatial regions of correlated motion has been determined for both non-polymeric and polymeric liquids and the determined length-scale characterising correlated motions is typically ∼1–5 nm [185–187] in the vicinity of T_g, where the detailed behaviour depends on the specifics of the system, such as its dynamic fragility. This is comparable to the length scale of the nematic domains in the isotropic LCE as determined by equation 9.1. Thus, it seems plausible that the difference in $\tau_\alpha(T)$ in the isotropic and nematic phase is related to the interplay between length-scales characterising the correlated molecular motions of the α relaxation and the correlation length of the pre-transitional phenomena in the form of nematic fluctuations of the isotropic LCE. Previous measurements on SCLCPs, which displayed only an isotropic phase, thus lacking pre-transitional nematic fluctuations, have shown that $\tau_\alpha(T)$ can be described with a single VFT, [173] as is also typical for polymeric materials with a sufficiently long chain-length. [32] In contrast, the precursor mixture presented herein has a nematic to isotropic transition and thus, in the isotropic phase, will have pre-transitional nematic regions present.

In principle it is possible to estimate the characteristic length scale of the α relaxation from BDS measurements. [132, 185] Whilst not the focus of this thesis chapter, this analysis has been performed by Matthew Reynolds on the $\tau_\alpha(T)$ data and published in [169] and is provided in brief below. The volume of the correlated motions can be estimated from the characteristic time-scale of the α

relaxation from the following equation: [188]

$$V_{\mathrm{corr}} \propto \frac{k_{\mathrm{B}}}{\rho \Delta c_{\mathrm{p}}} T^2 \left(\frac{d \ln (\tau_\alpha)}{dT} \right)^2 , \tag{9.2}$$

where c_{p} is the isobaric configurational specific heat associated with the α relaxation and here is determined from the specific heat step at T_{g} using DSC; ρ is the mass density of the LCE calculated by measuring the sample mass with a Mettler Toledo ME weighing scale and measuring the corresponding dimensions of the LCE sample using a Mituoyo Quantamike IP65 digital micrometer. [169] Using these determined values the volume of the correlated motions, V_{corr}, can be estimated from the $\tau_\alpha(T)$ data in figure 9.5. The result of this is shown in figure 9.7.

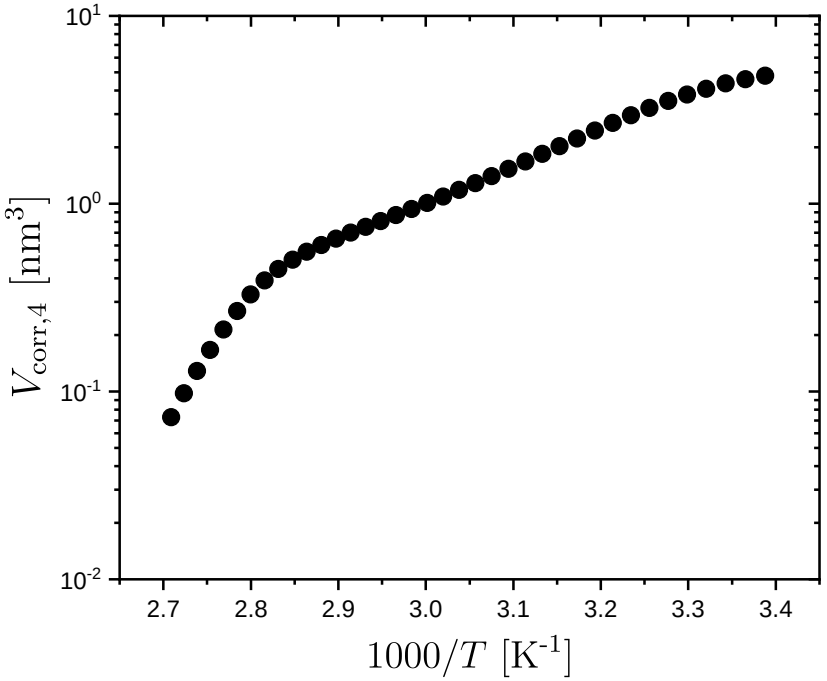

Figure 9.7: Volume of correlated molecular motions for the isotropic LCE sample as a function of inverse temperature. [169]

The behaviour seen in figure 9.7 is typical for glass-formers with an increasing V_{corr} for decreasing T and the stronger T-dependence at higher temperatures,

which significantly reduces near T_g. [185, 189] It should be noted that the most significant change in T-dependence of V_{corr} takes place at around 350 K ($1000/T \sim 2.86$), which is above $T^* = 333$ K where a change in $\tau_\alpha(T)$ is observed. However, importantly it is found that the volume of correlated motions for the isotropic LCE at the transition temperature T^* of ~ 1 nm^3 which corresponds to a length-scale of $l_\alpha(T^*) \sim 1$nm. l_α is therefore comparable to the expected length scale of the nematic regions in the isotropic LCE. Therefore it is feasible that the difference in $\tau_\alpha(T)$ in the isotropic and nematic LCE could be understood by the presence of pre-transitional nematic regions and nematic correlations, respectively, and the relative size of these with respect to the length-scale of correlated motions of the α relaxation as discussed above.

9.4.6 Ionic Conductivity Behaviour of the Isotropic and Nematic LCE

There is strong interest in developing polymer-based materials for applications in energy materials e.g. as electrolytes for batteries. [190, 191] Polymer-based electrolytes could provide both the safety, mechanical flexibility and rigidity needed for ion-transporting membranes to act simultaneously as ion conductors and electrode separators. Elastomers, in particular, show promise since cross-linking impart mechanical stability. However, polymer-based materials still have relatively high T_g values which means that, if ion transport is strongly coupled to the α relaxation, sufficient ion transport is very difficult to achieve. [136, 192] Thus, it is of significant interest for future applications to understand and control the coupling of ion transport and the α relaxation. Polymer systems with LC functionalities have been identified as interesting candidates for battery applications [193, 194] due to the additional structural control provided, which can affect both the nature and efficiency of the ion transport, as well as allow for anisotropic control of charge transfer. LCEs are potentially interesting in this respect due to their cross-linked nature which results in a combination of mechanical rigidity and liquid crystalline functionalities, however, there have been few studies on LCEs in this regard. [195, 196]

In this section the decoupling of DC conductivity from the α relaxation is investigated in the isotropic LCE and the nematic LCE. DC conductivity is related to the mobility of the ionic units present in the sample and is therefore dictated by the Stokes-Einstein (SE) relation: [16]

$$D_{\mathrm{DC}} = \frac{k_{\mathrm{B}}T}{a_{\mathrm{D}}\eta r_{\mathrm{D}}} \tag{9.3}$$

where D_{DC} is the Stokes-Einstein coefficient, η is the viscosity of the material, r_{D} is the hydrodynamic radius of the diffusing molecule and a_{D} is a constant. η is approximately proportional to τ_α, therefore the SE coefficient can be discussed in terms of the α relaxation: [16]

$$D_{\mathrm{DC}} \propto \tau_\alpha^{-k_{\mathrm{D}}}, \tag{9.4}$$

where k_{D} is a constant. When $k_{\mathrm{D}} = 1$ the DC conductivity is completely coupled to the α relaxation (i.e. the Stokes-Einstein relation is obeyed) which is generally the case for $T >> T_{\mathrm{g}}$. [16] However, on the approach to T_{g}, a 'fractional Stokes-Einstein' behaviour, is observed whereby $k_{\mathrm{D}} < 1$, signifying that DC conductivity and the α relaxation are decoupled. [16, 197, 198] Whilst there have been different mechanisms proposed for the breakdown of the SE-relation, [16, 199] a common explanation for the decoupling is that it is related to onset of dynamic heterogeneities (i.e. spatial regions in the material with different characteristic relaxation times). [200, 201] whilst this is not completely understood the breakdown of SE may be related to how D_{DC} and τ_α are averaged over the distribution of dynamics. An alternative explanation for the breakdown of SE is that the relationship is affected by emergence of a secondary relaxation or that D_{DC} and τ_α couple differently to spatial variations in intermolecular cooperativity. [202]

Conducting ions have not been specifically added to the LCEs to study the decoupling behaviour, however, the LCE samples contain a small number of ionic impurities present from synthesis. Therefore, the corresponding ionic DC-conductivity, from ionic impurities, can be investigated to see how this correlates with the α relaxation, and importantly identify any effects the LC phase has on this behaviour. To study the extent of the decoupling of the DC conductivity

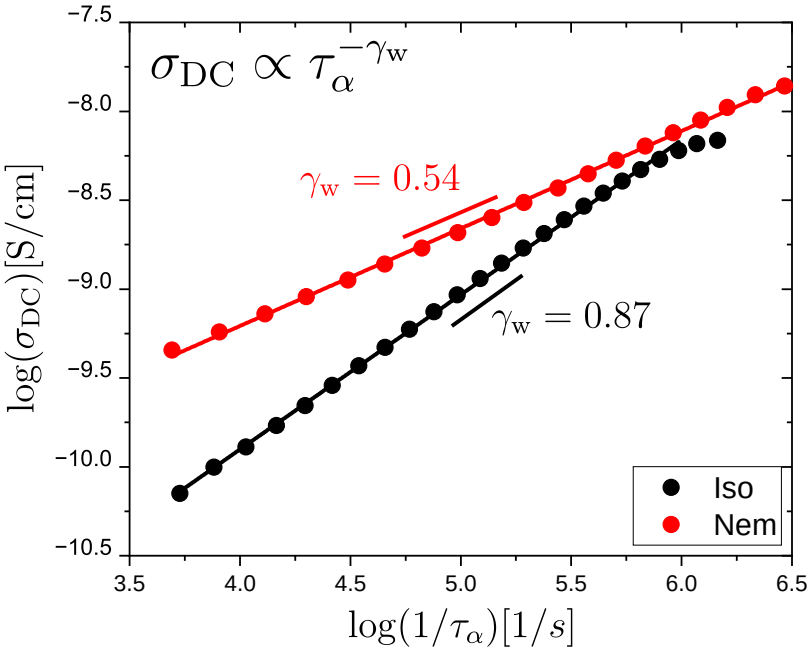

Figure 9.8: Plot of $\log(\sigma_{DC})$ vs. $\log 1/\tau_\alpha$ for the isotropic and nematic LCE samples. Also shown is the γ_w coupling coefficient from the equation σ_{DC}, which is related to the extent of coupling between the α relaxation and the ionic conductivity.

from the α relaxation the data is plotted as a modified 'Walden plot'. [191] The 'Walden plot' is a plot of conductivity against $1/\eta$, however, here the measured DC conductivity is plotted against $1/\tau_\alpha$ in a double-logarithmic representation. [191] The gradient of the data in the Walden plot representation is the 'decoupling parameter', γ_w:

$$\sigma_{DC} \propto \tau_\alpha^{-\gamma_w}. \tag{9.5}$$

When $\gamma_w = 1$ the DC conductivity and the α relaxation is completely coupled and when $\gamma_w < 1$ there is decoupling between the DC conductivity and α relaxation. Figure 9.8 shows the resulting Walden plot for the isotropic and nematic LCE sample. It can be seen that the isotropic LCE is relatively well coupled with a coupling parameter of $\gamma_w = 0.87$, whereas the nematic LCE is significantly less coupled, corresponding to a $\gamma_w = 0.54$. The fragility of the isotropic and nematic LCE is m=110 and m=130, respectively. These two fragility values are

quite similar, but it should be noted that a higher fragility is typically associated with a stronger decoupling in conventional polymeric materials. [136] For LC-based materials, a number of studies have investigated the coupling between ion conduction and the α relaxation. [168, 203, 204] For 5CB, in the isotropic phase on the approach of T_{ni}, a strong deviation from a Walden plot gradient of 1 was observed, indicating significant decoupling, which was explained as due to the presence of pre-transitional nematic fluctuations. [205] The addition of nanoparticles to the isotropic phase of 5CB was shown to reduce the decoupling between DC-conductivity and the α relaxation and the behaviour was attributed to the nanoparticle-induced disruption of pre-transitional nematic fluctuations in the isotropic phase. [204] The nematic phase shows a distribution of nematic domains with slightly varying order parameters and orientations throughout the sample, and is therefore likely to be more dynamically heterogeneous than the isotropic phase, which contains only pre-transitional nematic effects. Thus, explanations focused on the presence and strength of dynamic heterogeneities, and how these influence both the α relaxation and ionic conductivity, might explain the observations of a greater decoupling in the nematic than in the isotropic phase observed in our LCE system and LC systems in general. Finally, it is important to note that for the nematic LCE, the mesogenic units are arranged in an ordered manner which could in itself affect the transport of ions. Effects on ionic transport, and the relationship between the DC-conductivity and the α relaxation, due to induced spatial anisotropies have also been observed for the non-LC polymer poly(ethylene oxide), PEO, where the PEO chains were aligned either by mechanical stretching or by magnetic and electric fields. [206, 207] The observed effects were interpreted as due to molecular structure-induced changes in conduction pathways. For LC-based systems, the structural organization characterising some phases, could thus directly affect both the efficiency of the ion transport, as well as the coupling between the ion transport and the α relaxation. What is clear from figure 9.8 is that LCEs containing relevant ion-coordinating chemistries should be highly interesting materials for which the LC phases can be utilized to tune the ion transport properties.

9.5 Results: Rheological behaviour of LCEs

In this section, the rheological behaviour the LCE is investigated via DMA and SAOS. The rheological behaviour of LCEs is fundamentally interesting due to the coupling of the mesogenic units to the polymeric network. Whilst there have been previous studies on the dynamic rheological behaviour of LCEs these have largely been performed on LCEs with polysiloxane backbones and/or LCEs which deform via the SSE response. [164–166, 208] Herein, the rheological behaviour of an LCE, which in contrast to these literature studies have an acrylate-based backbone and (in the mono-domain nematic phase) deforms via the MFT, is investigated. Note that for the SAOS measurements on the nematic LCE, the LCE is prepared with a polydomain alignment (see chapter 4 for details of synthesis) as opposed to the monodomain nematic alignment so as to study the effect of nematic interactions on polymer dynamic behaviour without worrying about orientational effects.

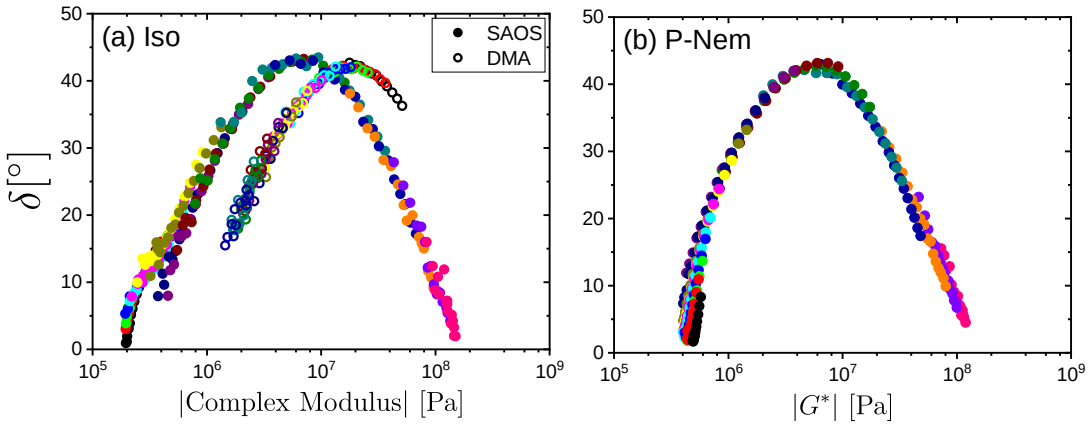

Figure 9.9: (a) van Gurp-Palmen plots of the SAOS (filled circles) and DMA (hollow circles) data for the isotropic LCE. (b) van Gurp-Palmen of the SAOS data for the polydomain nematic LCE.

To obtain data over a wide frequency range, the time temperature superposition (TTS) principle is employed to construct master curves. The validity of TTS is first investigated by plotting the data in a van Gurp–Palmen (vGP) representation, which is a plot of $\tan(\delta)$ against the complex modulus shown in figure 9.9. The vGP representation removes all explicit time-dependence from the

unshifted rheological data and therefore, shows if accurate TTS using frequency shifts is possible. [148] Since the SAOS technique requires the stacking of samples to produce a thick enough sample the SAOS rheological is compared to DMA, performed on a single isotropic LCE film, to check that there is no complications due to the inter-facial layers of the SAOS samples. In the vGP representation, the DMA and SAOS data of the isotropic LCE fall on a single line (respectively), and, for the nematic LCE the SAOS data fall onto a single line, thus TTS can be adequately performed on these samples.

For TTS, a reference temperature of $T_{\text{ref}} = 40$ °C is selected, for both the isotropic and nematic LCE, and a horizontal shift factor is applied to the data at other temperatures to form a master curve. The resulting rheological master curves for the isotropic and the polydomain nematic LCE are shown in figure 9.10 and 9.11, respectively. SAOS is used to determine the complex shear modulus, $G^*(\omega) = G'(\omega) + iG''(\omega)$, ($G'$ = green circles, G'' = blue circles) and DMA is used to determine the complex Young's modulus $E^*(\omega) = E'(\omega) + iE''(\omega)$ (E' = hollow black circles, E'' = hollow red circles). The DMA data are shifted (shifted E' = black circles, shifted E'' = red circles) to directly compare the SAOS and DMA data to each other. As seen in figure 9.10, E' and E'' can be collapsed onto G' and G'' (vertical shift of -0.37 applied). Therefore there appears to be little effect of the stacking of LCE sample, within the T and ω range of the complimentary SAOS and DMA measurements, on the shape of the rheological master curve; therefore, the SAOS data which has a larger dynamic frequency window than the DMA measurement can be discussed.

The rheological data, for the isotropic LCE (figure 9.10) and the polydomain nematic LCE (figure 9.11), includes the structural α relaxation response in the high-frequency range ($\sim 10^7 - 10^{10}$ rad/s). At a lower frequency range, a power law-like regime is observed where $G' \approx G'' \propto \omega^{0.5}$ ($\sim 10^2 - 10^4$ rad/s for the isotropic LCE and ($\sim 10^1 - 10^3$ rad/s for the polydomain nematic LCE). This scaling is more pronounced for G'' due to the transition towards a rubber-like plateau in G' at low frequencies resulting from the presence of permanent cross-links. The observed $G' \approx G'' \propto \omega^{0.5}$ scaling is evidence of a Rouse-like spectrum. [14, 209] A Rouse-like mode spectrum has similarly been reported in isotropic, nematic and smectic LCE systems. [164–166, 208]

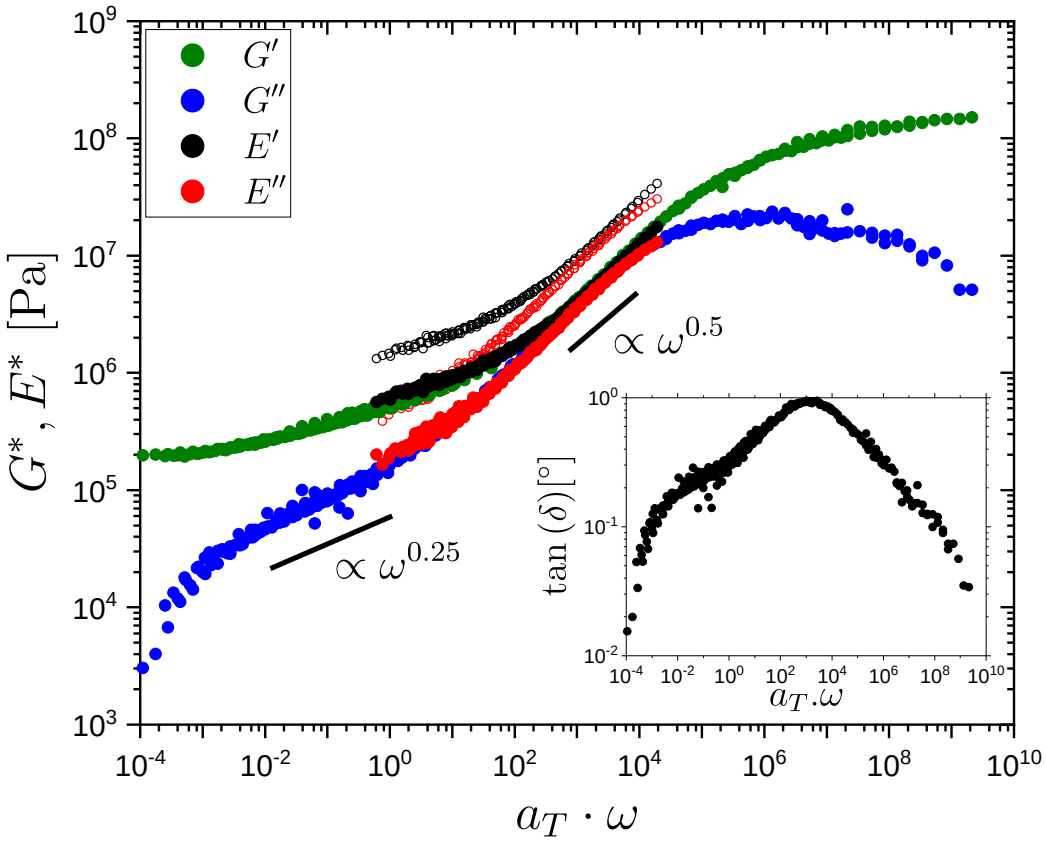

Figure 9.10: TTS master curves of the isotropic LCE for shear storage modulus (G', green circles), shear loss modulus (G'' , blue circles), unshifted storage modulus (E', hollow black circles), unshifted loss modulus (E'', hollow red circles), shifted storage modulus (E', black circles) and shifted loss modulus (E'', red circles). A vertical shift of -0.37 (on the log-scale) is applied between G^* and E^* demonstrating a very good agreement between the two data sets. Approximate power-law scalings of $\omega^{0.5}$ and $\omega^{0.25}$ discussed in the text are illustrated. Inset: phase angle, $\tan(\delta)$, against TTS shifted angular frequency ($a_T.\omega$) for the SAOS data.

In the isotropic LCE, towards lower frequencies ($10^1 - 10^{-2}$ rad/s), a flatter approximately power-law-like regime of $G'' \propto \omega^{0.25}$ is observed. This contribution is also observed as a shoulder in the low-frequency flank of $\tan(\delta)$ shown in figure 9.10 (inset, $\tan(\delta) = G''/G'$). Similarly, a low-frequency power law of $G' \approx G'' \propto \omega^{0.3}$ has been observed in the SmA phase of LCE systems, whereas it

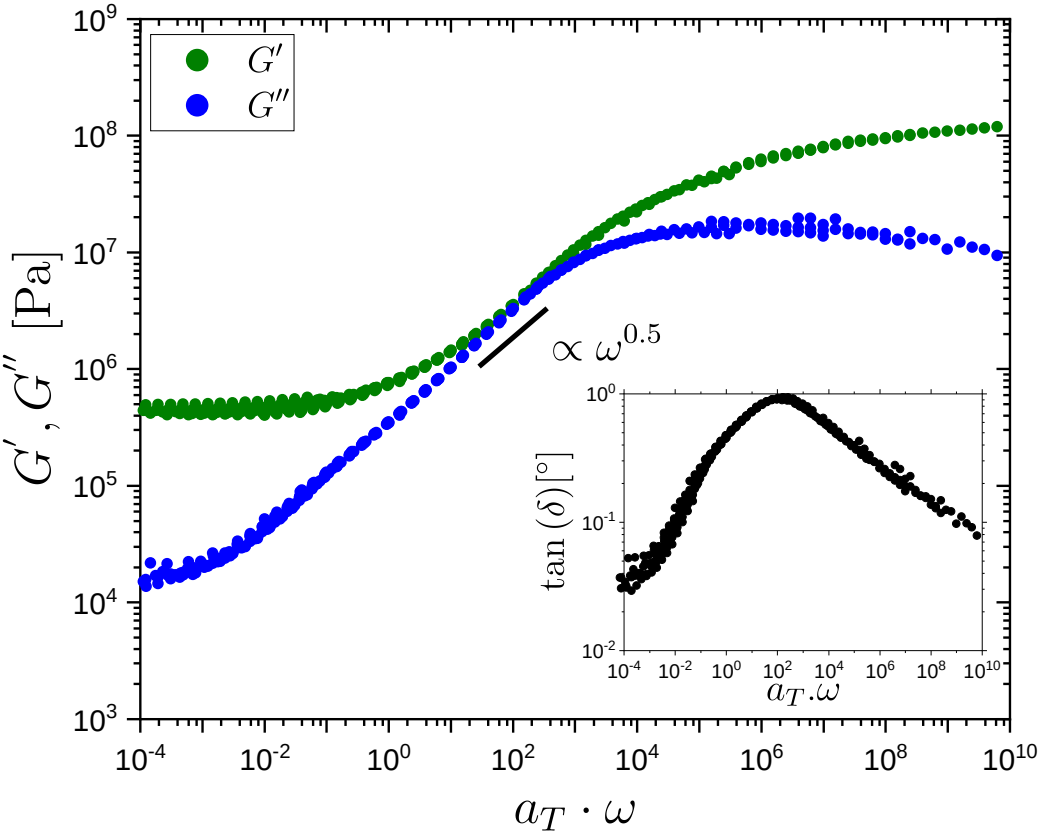

Figure 9.11: TTS master curves of the polydomain nematic LCE for shear storage modulus (G', green circles), shear loss modulus (G'' , blue circles). Approximate power-law scaling of $\omega^{0.5}$ discussed in the text is illustrated. Inset: phase angle ($\tan(\delta)$) against TTS shifted angular frequency ($a_T.\omega$) for the SAOS data.

was not observed for the corresponding isotropic phase. [164, 208] This scaling in SmA LCEs was interpreted as due to the presence of smectic layers which influence the otherwise separated polymer backbones. [164, 208, 210] However, for the isotropic LCE in figure 9.10 this situation is clearly not the same, and the observed behaviour must have a different origin. Note that a change in rheological behaviour is also observed in the nematic LCE, evidence by a shoulder in $\tan(\delta)$ in figure 9.11 at $\omega \approx 10^{-1}$, however, it is more subtle than the isotropic case. Both the isotropic and nematic LCE are randomly cross-linked networks containing the pendant units A6OCB and EHA, based on this, two

possible mechanisms for the low frequency behaviour are proposed. Firstly, the observed response could be related to the motion of free chains (i.e. chains which, due to random cross-linking, are not chemically connected to the LCE network) through the network. A $G'' \propto \omega^{0.2-0.3}$ dependence has indeed been reported in cross-linked poly(dimethylsiloxane) (PDMS) networks where linear 'free' PDMS chains were present. [211] Secondly, the relaxation could be due to the motions of the dangling pendant chains within the network. This has been observed for poly(butyl acrylate) networks, where it has been interpreted as due to chain motions linked to pendant arm retraction, [25] and in PDMS networks with pendant chains where the details of the loss contribution depended on the pendant chain length. [212] The difference in the shoulder of the low-frequency flank of tan (δ) for the isotropic and nematic LCE may therefore be understood by a reduction in entanglements in the network due to nematic alignment, or the slowing down of the reptation time, τ_{rep}, of the nematic network when compared to the isotropic phase of the network; both of which have been observed in conjugated polymers which display a nematic and isotropic phase. [213]

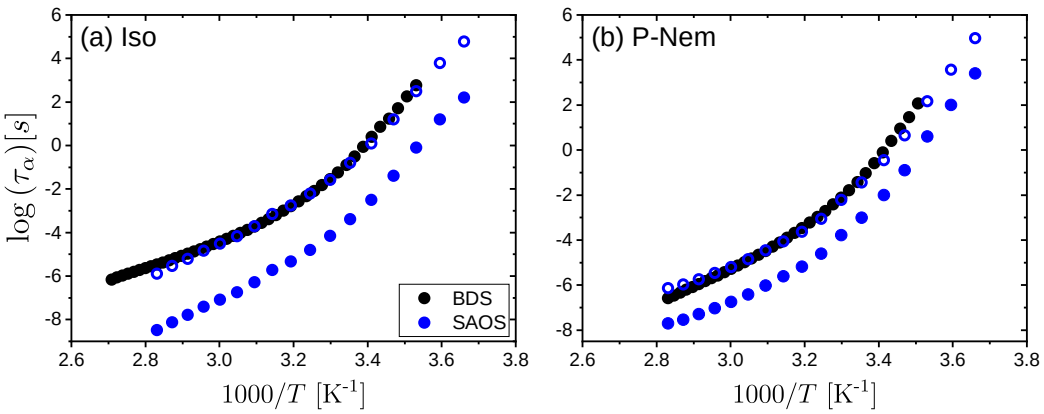

Figure 9.12: Arrhenius plot showing the α relaxation time, $\tau_\alpha(T)$ vs. inverse T for the (a) isotropic LCE and (b) polydomain nematic LCE as measured via BDS (filled black circles) and SAOS (filled blue circles). Also shown is the SAOS vertically shifted (hollow blue circles) to show good agreement between $\tau_\alpha(T)$ between the BDS and SAOS measurements.

The TTS shift-factors can be used to directly obtain information about the T-dependent characteristic time-scale for the LCE within the investigated T-range.

The α relaxation time-scale at T_{ref} (40 °C) is determined from the peak maximum in the G'' data in figure 9.10; this is found via the '*find peaks/valleys*' function in the '*TA orchestrator*' software. The corresponding α relaxation time-scale at T_{ref}, $\tau_\alpha(T_{\text{ref}})$, is 2.2×10^5 s and 1.6×10^5 s for the isotropic LCE and the polydomain nematic LCE respectively. Subsequently, $\tau_\alpha(T)$, from the rheological data, is determined using the following equation:

$$\tau_\alpha(T) = a_T \cdot \tau_\alpha(T_{\text{ref}}), \tag{9.6}$$

where a_T are the horizontal shift factors from TTS. The temperature dependence of the α relaxation determined from rheology is compared to the results for BDS in figure 9.12. Here, vertical shifts of 2.58 and 1.56 (on the log scale) are applied to the isotropic LCE and polydomain nematic LCE, respectively. A shift of the relaxation time scales is expected between rheological and dielectric measurements [214] and based on this analysis, good agreement is found for $\tau_\alpha(T)$ determined via BDS and SAOS for both samples. The close correspondence between the two data sets supports the validity of the TTS approach used in the construction of the rheological master curves.

9.6 Conclusion

In this chapter, the molecular relaxations of the isotropic and nematic phases of an acrylate-based LCE are determined using a combination of broadband dielectric spectroscopy (BDS), small amplitude oscillatory shear (SAOS) rheology and tensile dynamic mechanical analysis (DMA). Due to the lack of phase transitions across a wide T-range, once polymerised, this LCE constitutes an excellent model system for investigating the effects of nematic order on the glass-transition-related molecular relaxation behaviour. For the unstrained LCEs, it is shown that both the isotropic and nematic LCE samples show a similar T-dependence of their characteristic α relaxation time-scales, τ_α, near their glass transition temperatures T_g which is reflected in the similar T_g-values (T_g = 286K and 285K) and dynamic fragilities (D=5.4 and D=5.1; m=110 and m=130) for the two phases;

both phases of the LCE therefore are 'fragile glass-formers' and have fragility values consistent with those of conventional polymers. [32, 33, 39] Importantly, for both phases, $\tau_\alpha(T)$ qualitatively changes T-dependence at a crossover $T^* \approx 333$ K. For $T < T^*$, both the nematic and isotropic LCE follow a VFT dependence, however, for $T > T^*$, the nematic LCE has a $\tau_\alpha(T)$ well described by the Arrhenius equation. In the isotropic LCE, a cross-over in behaviour is observed for $T > T^*$ where $\tau_\alpha(T)$ transitions from markedly non-Arrhenius (i.e. fragile) to more Arrhenius-like (i.e. becomes less fragile). A similar change from non-Arrhenius to Arrhenius at a crossover temperature, T^*, is often observed for SCLCPs with nematic phases. [173, 177]

For comparison, a change in the T-dependence of τ_α is typically observed in non-LC glass-formers at a temperature $T_\mathrm{B} \approx 1.2 - 1.6 \times T_\mathrm{g}$ [37], which is comparable to the $T^* \approx 1.17 \times T_\mathrm{g}$, observed in the LCEs herein. However, for non-polymeric non-LC glass-formers, $\tau_\alpha(T)$ is typically less Arrhenius-like (more fragile) above, than below, T_B and the change in T-dependence often disappears all together for polymeric systems. [35] Thus, the behaviour observed for many nematic systems displays both similarities and clear differences to that of non-LC systems. For the LCE, which can be synthesised in chemically identical isotropic or nematic phases, the change of phase does not significantly affect the value of T^*, but it strongly affects how Arrhenius-like the T-dependence of $\tau_\alpha(T)$ is for $T > T^*$. Herein, it is argued that these observations could be related to the existence of pre-transitional phenomena in the form of nematic regions in the isotropic LCE, which are locked in by the polymerisation. The size of these regions are estimated to be of the order $\sim$1 nm as determined from the T_ni of the LCE precursor mixture and the curing temperature of the isotropic sample. This is found to be similar to the length scale of the correlated motions of the α relaxation at T^* as determined by analysis of the BDS data on the isotropic LCE. Thus validating the proposition that the change in dynamic behaviour could be related to a matching of the length-scales of these two phenomena. In addition to the α relaxation, two further dielectrically active relaxations (β and γ) are observed in both LCE phases. They both demonstrate Arrhenius behaviour within the glassy state and are not significantly affected by the LCE phase; these

motions are assigned to motions of the mesogen side-chain around its long axis (β), and motions of the alkyl spacer (γ). [27, 176]

The extent of decoupling between the ionic conductivity and the α relaxation is investigated by 'Walden analysis'. It is found that the ionic conductivity is significantly more decoupled from the α relaxation in the nematic LCE than in the isotropic LCE. It is suggested that differences in dynamic heterogeneity in the two LCE phases could be an important contributing factor in these results. Additionally, and perhaps more importantly, the structural anisotropy induced by the nematic order could in itself play a role in driving the observed decoupling with parallels being drawn, for example, from conventional polymers aligned in magnetic fields. [206, 207]

Finally, a rheological investigation of the isotropic LCE and the (polydomain) nematic LCE provided evidence for both a Rouse-like mode contribution on time-scales slower than the α relaxation, and an additional relaxation contribution. The additional relaxation is suggested to be due either to free chains moving within the elastomer network, [211] or to the motion of pendant network chains [25, 212]; the additional relaxation is affected by the presence of the nematic phase as evidence by a reduction of this contribution in the rheological data.

Chapter 10

Results III: Effect of applied strain on the molecular dynamics of LCEs

10.1 Introduction

In this chapter the effect of strain, applied perpendicularly to the director, on the viscoelastic behaviour and molecular relaxations of a nematic LCE is investigated. In this geometry the nematic LCE displays a molecular auxetic response. [1] In chapter 8 it was shown that there is a relationship between the applied strain and the order parameters of the mesogenic units in the LCE, i.e. there is a reduction in uniaxial order ($\langle P_{200} \rangle$ and $\langle P_{400} \rangle$) and an emergence of biaxial order ($\langle P_{220} \rangle$, $\langle P_{420} \rangle$ and $\langle P_{440} \rangle$). In chapter 8 it is argued that the molecular auxetic response is a consequence of out-of-plane rotation of mesogenic units as evidenced by the emergence of the $\langle P_{440} \rangle$ order parameter near the onset of the auxetic response. The order parameters determined in chapter 8 are in effect static measurements which give a 'snap-shot' insight into the state of the mesogenic order of the LCE at that given strain. It is important to also probe the changes in the viscoelastic behaviour and the molecular relaxations of the LCE in this geometry to gain additional insight into how the dynamic behaviour of the LCE changes during the auxetic response and the MFT.

This chapter begins by describing the experimental set-up used to perform these measurements and how the strain is applied to the LCE. First, the viscoelastic behaviour of the LCE is investigated using DMA. It is found that initially the viscoelastic behaviour of the LCE is unchanged for relatively small (true) strains. However, there is an increase in both E' and E'' occurring near the onset of the molecular auxetic response. Similarly, changes in the characteristic time-scale of the α relaxation are found near the onset of the molecular auxetic response. It is suggested that the molecular auxetic response is driven by constraints imposed on the polymer backbone at large strains or related to the finite extensibility of the network.

The majority of this chapter has been published in the paper: T. Raistrick *et al.* "Influence of Liquid Crystallinity and Mechanical Deformation on the Molecular Relaxations of an Auxetic Liquid Crystal Elastomer.", *Molecules*, **26 (23)**, 7313, 2021. [169] Much of this chapter is reproduced from this paper; unless specified any experimental work presented has been performed by T. Raistrick.

10.2 Experimental methods

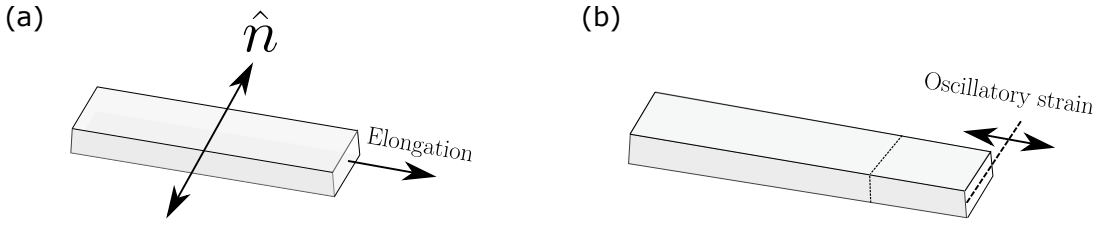

Figure 10.1: Schematic showing how DMA measurements were performed under strain. (a) The nematic LCE sample in the DMA with the nematic director perpendicular to the axis of oscillatory strain. The sample is elongated to the desired strain and stress-relaxed. (b) an oscillatory strain is applied to the sample and the complex elastic modulus is measured E^*.

The complex Young's modulus ($E^* = E' + iE''$) is determined via the Rheometrics Solid Analyser II DMA (see chapter 7) with film tension clamps by applying an oscillatory strain onto an already elongated LCE sample. The nominal

dimensions of the unstrained nematic LCE are 5 cm × 0.2 cm × 100 μm and the samples are placed into the DMA such that the initial nematic director is aligned perpendicular to the applied strain. The LCE film is subjected to varying elongations. The elongational strain of the LCE sample is shown in true-strain (ϵ_t) representation:

$$\epsilon_t = \ln\left(\frac{L_f}{L_i}\right) \tag{10.1}$$

where L_f is the length of the sample after elongation, and L_i is the initial sample length. After the elongation is applied, the LCE is left to stress-relax for 2 minutes. This relaxation time is selected as it is short enough to avoid sample breakage, yet long enough to not affect the auxetic response of the material. [1] Similar relaxation times are used in chapter 8 to determine the order parameters of the nematic LCE under strain thus using this relaxation time allows for a direct comparison of results. Additionally, a relaxation time of 2 minutes has been used in literature when reporting the stress-strain response of the nematic LCE. [2] For all DMA measurements an oscillatory strain amplitude of 0.1% is selected as this is confirmed to be in the linear viscoelastic regime of the nematic LCE. A schematic illustrating how the DMA was performed under strain can be seen in figure 10.1.

To perform BDS measurements under strain, the nematic LCE sample is stretched to the desired strain and affixed to a 20 mm brass plate with Kapton tape. The sample dimensions are nominally 7 cm × 1.5 cm × 100 μm (L×W×T) and a brass plate of 5 mm is placed on top of the sample to allow for BDS measurements. BDS measurements are recorded with the Novocontrol Alpha-A dielectric analyser and, if required, temperature is controlled via the Novocontrol Quatro cryosystem (see chapter 6). It is confirmed that the Kapton tape is placed sufficiently far away from the electrodes to not influence the measurements. After mounting, the sample is left to stress-relax for 2 minutes before measurement were performed.

10.3 Effect of applied strain on the complex elastic modulus

In this section, the effect of strain on the viscoelastic behaviour of the LCE when strains are applied perpendicular to the nematic director is investigated. Studying the changes in viscoelastic behaviour under elongational strain provides key insight into the behaviour of a material under strain. [215, 216] An increase in both the storage and loss moduli has been observed in natural rubber and styrene butadiene elastomers for strains larger than 70% ($\epsilon_t > 0.53$), whereas at strains smaller than 70% ($\epsilon_t < 0.53$) the storage and loss moduli was similar to the unstrained values. [217] The increase in storage and loss moduli is related to an increase in the effective constraints on the molecular orientations within the elastomer network due to the applied strain [218], and to the finite extensibility of the network. [219] In addition to this, changes in loss moduli or $\tan(\delta)$ as a function of strain can indicate the breaking of bonds or molecular slippage occurring within the network or, alternatively, the onset of plastic deformation. [215, 216]

10.3.1 Effect of applied strain on DMA master curve data

Initially, the effect of applied external strain is investigated for the nematic LCE by performing frequency sweeps over a temperature range. This allows one to construct rheological master curves via the time-temperature superposition (TTS) principle as discussed in detail in chapter 7. A frequency range of 1 Hz - 12 Hz and a temperature range of 20 °C - 40 °C (2 °C steps) is chosen. Measurements were performed on pre-elongated samples as described in section 10.2. Master curves are constructed from the data using horizontal shifting only (a_T) with a reference temperature of $T_{\text{ref}} = 22^{\circ}\text{C}$. The horizontal shift factors are fitted with the empirical Williams-Landel-Ferry (WLF) equation:

$$\log_{10}(a_T) = -\frac{C_1(T - T_{\text{ref}})}{C_2 + (T - T_{\text{ref}})} \tag{10.2}$$

where C_1 and C_2 are positive experimental parameters that depend on the material and the reference temperature (see chapter 7 for details).

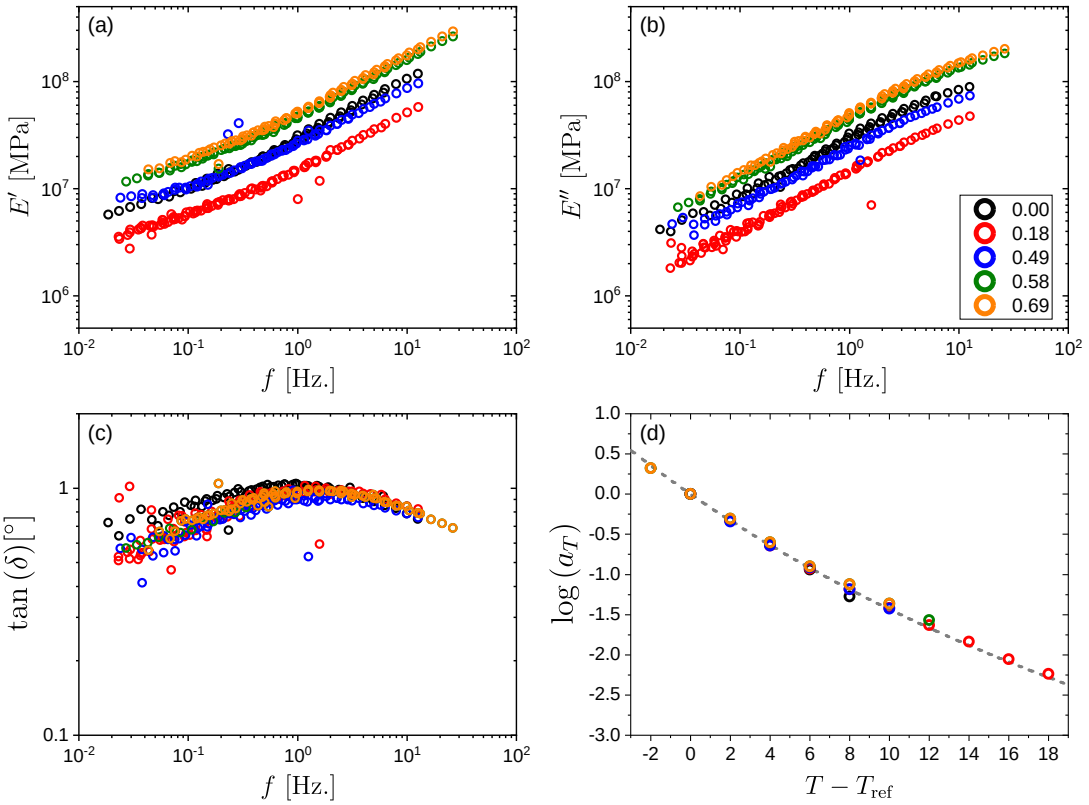

Figure 10.2: (a) E', (b) E'', (c) $\tan(\delta)$ master curves constructed from DMA measurements for the nematic LCE as a function of perpendicularly applied strain (see legend in (b)). (d) horizontal shift factors (a_T) against $T - T_{\mathrm{ref}}$ where $T_{\mathrm{ref}} = 22^{\mathrm{o}}\mathrm{C}$. The grey dashed line is a fit to the WLF model with $C_1 = 9 \pm 1\mathrm{K}$ and $C_2 = 50 \pm 10\mathrm{K}$.

In figure 10.2 the result of the TTS master curves for the (a) storage modulus, E', (b) loss modulus, E'' and (c) $\tan(\delta)$ are shown revealing that for all strains ($\epsilon_{\mathrm{t}} = 0.00$ to 0.69) the general shape of the E' and E'' is unchanged and in all cases the nematic LCE is, over the frequency and temperature range investigated, within the 'leathery transition region' (or glass-rubber transition). [130] There is no obvious trend observed in the magnitude of E' and E'' with the lower strain data ($\epsilon_{\mathrm{t}} = 0.18$ to 0.49) having smaller values than the unstrained LCE and the

higher strain data ($\epsilon_t = 0.58$ to 0.69) having larger values than the unstrained LCE. However, the magnitude of $\tan(\delta) = E''/E'$ remains unchanged over the strain range investigated suggesting that (a) the material is behaving elastically throughout and (b) the variations in E' and E'' observed for the different samples under strain is likely due to the variations within the different samples. The maximum strain achieved when attempting to construct master curve is $\epsilon_t = 0.69$ which is below the auxetic threshold of $\epsilon_t = 0.74$, thus, to properly investigate the effect of strain on the dynamic modulus one needs to perform the measurement on a single sample.

Finally, from figure 10.2(d) it can be seen that the horizontal shifting factors, a_T from the TTS master curves fall onto a single line with a resultant WLF fit of $C_1 = 9 \pm 1$K and $C_2 = 50 \pm 10$K. That the horizontal shift factors for all strains falls onto a single line suggests that the temperature dependence of the mechanical relaxation processes present in the nematic LCE, within the frequency and temperature range investigated, are unaffected by the application of strain. [220, 221] The DMA measurements are performed close to the glass transition temperature of the nematic LCE ($T_g \approx 12$°C as determined in chapter 9), therefore, it is likely that the α relaxation is, in part, captured within this data as reflected by the peak in $\tan(\delta)$ observed in figure 10.2(c). Thus the temperature dependence, $\tau_\alpha(T)$ is likely independent of elongational strain, within the investigated frequency and temperature range measured, as evidenced by a_T collapsing onto a single WLF curve. However, direct measurement of the LCE when elongated within the glassy regime was not possible as the samples would break when cooled below T_g. The temperature dependence of τ_α will be discussed later in section 10.4.1 where the α relaxation can be measured directly via BDS.

10.3.2 Effect of applied strain on E^* at fixed frequency and temperature

In section 10.3.1 an attempt is made to determine the effect of perpendicularly applied strain on the nematic LCE by constructing master curves via TTS. The issue with performing measurements in this manner is that, during the various frequency and temperature sweeps required to construct master curves, the

strained sample would eventually break. Thus for each strain the measurements are performed on different samples and the variation in magnitudes of E' and E'' between samples is too large to accurately determine the effect of applied strain. Another issue with the measurements performed in section 10.3.1 is that strains large enough to probe the behaviour of the auxetic response could not be reached. However, what is clear from section 10.3.1 is that the shape of E', E'' is largely unaffected by applied strain. Additionally, the temperature dependence of the mechanical relaxation processes present in the nematic LCE, within the frequency and temperature range investigated, are unaffected by the application of strain as evidenced by the horizontal shift factors, a_T in figure 10.2(d). As such, it is expected that any effect of strain on the nematic LCE will be relatively independent of frequency and temperature (over the range that is experimentally feasible). Thus, the effect of applied strain on the complex Young's modulus of the nematic LCE is investigated at single frequency and temperature; in doing so this reduces the time of the experiment and the likelihood of sample failure and will allow strains to be reached within the auxetic response of the material to investigate changes in the viscoelastic behaviour of the LCE. In this section, the storage ($E'(f_0)$) and loss modulus ($E''(f_0)$) is determined at $f_0 = 1$ Hz ($\omega \approx 6.3$ rad/s) and $T = 23$ °C for each elongation by applying oscillatory strains with amplitudes of 0.1% to the pre-elongated nematic LCE sample. The result of this experiment can be seen in figure 10.3.

Figure 10.3 shows the evolution of E' and E'' for the nematic LCE as a function of external strain applied perpendicular to the nematic director. In the inset, tensile stress-strain measurements performed at 23°C are shown for comparison; these tensile measurements are taken from Mistry *et al.* [2]. The tensile stress-strain data is shown in the true-stress – true-strain representation with the true-stress defined as:

$$\sigma_{\mathrm{t}} = F/A \tag{10.3}$$

where F is the force measured on the sample and A is the cross-sectional area of the sample after the application of strain. To calculate the true-stress from the engineering-stress reported in [2] the cross-sectional area of the LCE as function of strain is calculated by assuming the volume of the LCE is constant. This

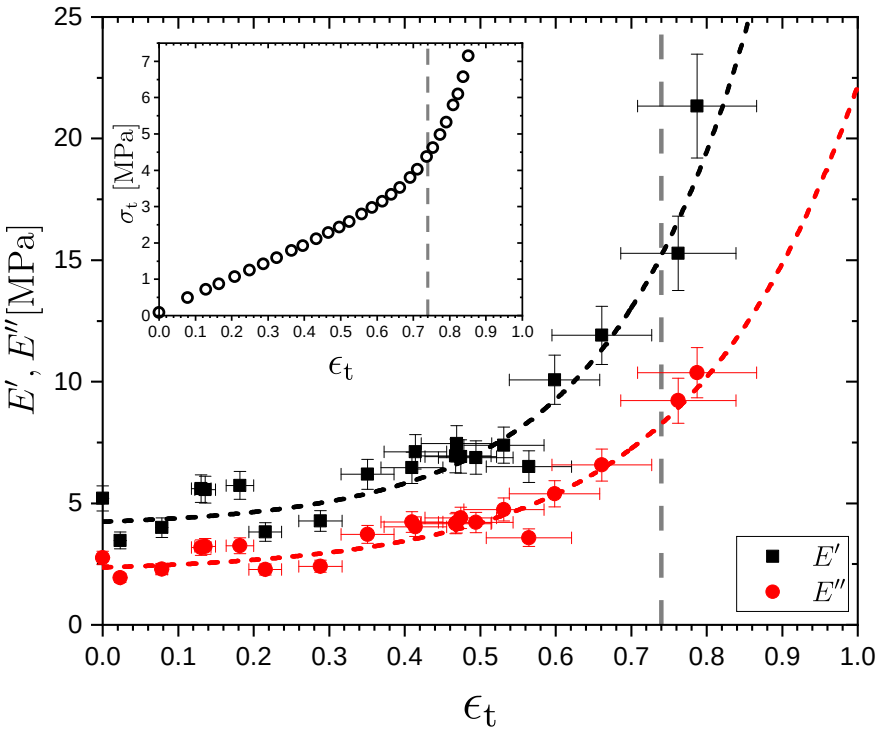

Figure 10.3: Storage and loss moduli determined at 1 Hz and T = 23°C, as a function of true-strain applied perpendicular to the nematic director; errors in E', E'' and ϵ_t are standard errors from multiple measurements. Inset: non-dynamic tensile tests showing the true-stress (hollow circles) σ_t [MPa] as function of true strain ϵ_t (raw data taken from [2]). The grey dashed line marks the threshold for the onset of the molecular auxetic response.

assumption has been shown to be a good approximation for this LCE via direct measurement. [1] The true-strain is calculated from the engineering-strain using equation 10.1.

The grey dashed line in figure 10.3 denotes the threshold for the onset of the molecular auxetic response. [1, 2] In chapter 8 it is found that the molecular auxetic response is related to out-of-plane rotations of the mesogenic units. The black and red dashed lines are exponential growth functions which serve as guides to the eye. At low values of applied strain ($\epsilon_t < 0.22$), $E'(f_0)$ and $E''(f_0)$ are relatively constant with average values of 4.9 ± 0.2 MPa and 2.7 ± 0.1 MPa respectively; the elastic modulus determined from the gradient of the true-stress

– true-strain data in this region ($\epsilon_t < 0.22$) is 4.6 MPa showing an excellent agreement with E' (f_0). Between ϵ_t=0.22 and ϵ_t=0.53 average values of $E' = 7.7 \pm 0.6$ MPa and $E'' = 4.7 \pm 0.4$ MPa are observed as compared to 4.9±0.2 MPa and 2.7±0.1 MPa for $\epsilon < 0.22$; therefore in this regime ($\epsilon_t < 0.55$) there is a small dependence of dynamic moduli on strain. Figure 10.4 shows $\tan(\delta) = E''/E'$ as a function of ϵ_t. It can be see that $\tan(\delta)$ is constant, within error ($\tan(\delta) = 0.55 \pm 0.03$ for $\epsilon_t < 0.22$ and $\tan(\delta)$=0.60±0.07 for $0.22 < \epsilon_t < 0.55$), which suggest that the LCE is deforming elastically (albeit non-linearly) throughout this strain region.

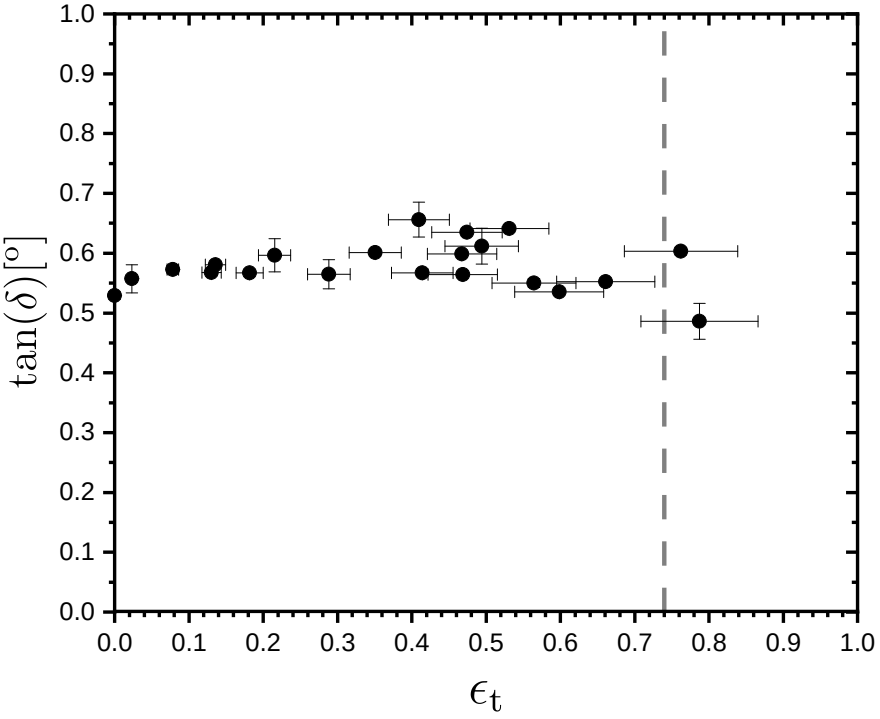

Figure 10.4: $\tan(\delta)$ as a function of true-strain applied perpendicularly to the nematic director; errors in $tan(\delta)$ and strain are standard errors from multiple measurements.

At larger values of strain ($\epsilon_t > 0.55$) a stiffening of the stress-strain response is observed in the true-stress – true-strain representation, additionally a significant increase in $E'(f_0)$ and $E''(f_0)$ is observed. At the strain corresponding to sample

breakage ($\epsilon_t \approx 0.78$), $E'(f_0) = 21.3$ MPa which is consistent with the value of the elastic modulus $E \approx 24$ MPa determined from the gradient of the true-stress – true-strain data in this region. The upturn in the true-stress – true-strain response, and the corresponding increases in $E'(f_0)$ and $E''(f_0)$ occurs just before the sharp rotation of the director at the mechanical Fréedericksz transition, and the emergence of molecular auxetic response (signified by the grey vertical line). In figure 10.4 it can be seen that $\tan(\delta)$ remains constant throughout the full operational range of the LCE, thus, the MFT and the molecular auxetic response cannot be related to a transition from elastic to plastic behaviour, or involve significant bond breakages/molecular slippage, which would signify a fundamental change in the network. [215, 216] The increase in both E' and E'' is therefore consistent with findings in vulcanised rubber and styrene butadiene elastomers, where it is attributed to an increase in the effective constraints on the molecular orientations within the elastomer network due to the applied strain [218], and to the finite extensibility of the network. [219]

10.4 Effect of applied strain on the α relaxation

In this section, we consider the effect of strain on the behaviour of the α relaxation of the LCE when strains are applied perpendicular to the nematic director. Studying the behaviour of the α relaxation is fundamentally interesting to understanding glassy behaviour and provides key insight into the behaviour of the material under strain. [222–225] However, the relationship between the α relaxation and strain is not simple. For example, the non-cross-linked glass forming linear polymer, poly(methyl methacrylate) (PMMA) under constant load or constant strain-rate shows an increase in the time-scale of the α relaxation by a factor of up to 1000 when measurements are performed below the yield stress. This increase in mobility is argued to be related to the tilting of the potential energy landscape due to applied load or strain which leads to a lowering of activation barriers. [222, 223] Post-yield, the mobility of α relaxation in PMMA is found to be positively correlated with increasing stress or strain-rate. [223, 224] The effect of elongational strain, up to 400% ($0 \leq \varepsilon_{\mathrm{t}} \leq 1.39$), on the α relaxation

has been studied on a lightly cross-linked (6.5% mol/m^3) polyisoprene-based elastomer and polyurethane-based elastomer composed of 32.5 wt.% hard segments (4,4'-diphenylmethane diisocyanate and 1,4-butanediol) [225], both of which are non-liquid crystal elastomers. In the polyisoprene elastomer, there was no effect of elongational strain on the α relaxation as investigated by BDS. In the polyurethane elastomer, the α relaxation was shown to slow down and broaden with applied strain, additionally, an increase in the fragility parameter (m) was observed. Similar behaviour to the polyurethane elastomer has been reported in a polyurea-based elastomer. [226] In both cases, the changes in the α relaxation observed in the strained elastomers was attributed to increasing constraints imposed on the soft segments of the elastomers due to a deformation-induced reduction in microphase separation. [225, 226]

10.4.1 Effect of applied strain on $\tau_\alpha(T)$

Initially, the effect of elongational strain on the α relaxation is investigated by performing BDS over a range of temperatures. The BDS measurements were performed, as described in 10.2, on cooling from 50°C to 15°C in 5°C steps. In the temperature range investigated, one observes contributions associated with DC conductivity (σ_{DC}), the α relaxation and, at the lower temperatures, the low-frequency flank of the β relaxation. The complex permittivity at each temperature is fitted as a sum of peaks associated with these relaxations as described in chapter 6. The temperature dependence of the time-scale of the α relaxation, $\tau_\alpha(T)$, is shown in figure 10.5(a). $\tau_\alpha(T)$ is fitted with the Vogel-Fulcher-Tamman (VFT) function: [27]

$$\tau_\alpha(T) = \tau_0 \exp\left(\frac{DT_0}{T - T_0}\right) \tag{10.4}$$

where τ_0 is a microscopic relaxation time, T_0 is the temperature at which τ_α tends to infinity and D is the 'strength parameter' which described the extent of deviation of τ_α from Arrhenius behaviour. Whilst the β relaxation is present in the spectra, for most temperatures, the peak is outside of the frequency window, therefore, only $\tau_\alpha(T)$ can be accurately determined. The result of the VFT fitting is given in table 10.1. The $\tau_\alpha(T)$ data and VFT fits for the unstrained ($\epsilon_{\mathrm{t}} =$

0.00) nematic LCE are from table 9.2 in chapter 9. Note that in chapter 9, a cross-over of $\tau_\alpha(T)$ from VFT to Arrhenius behaviour at a critical temperature (T^* ≈60°C) is observed, however, these measurement are performed below the cross-over temperature so only the VFT fit is required.

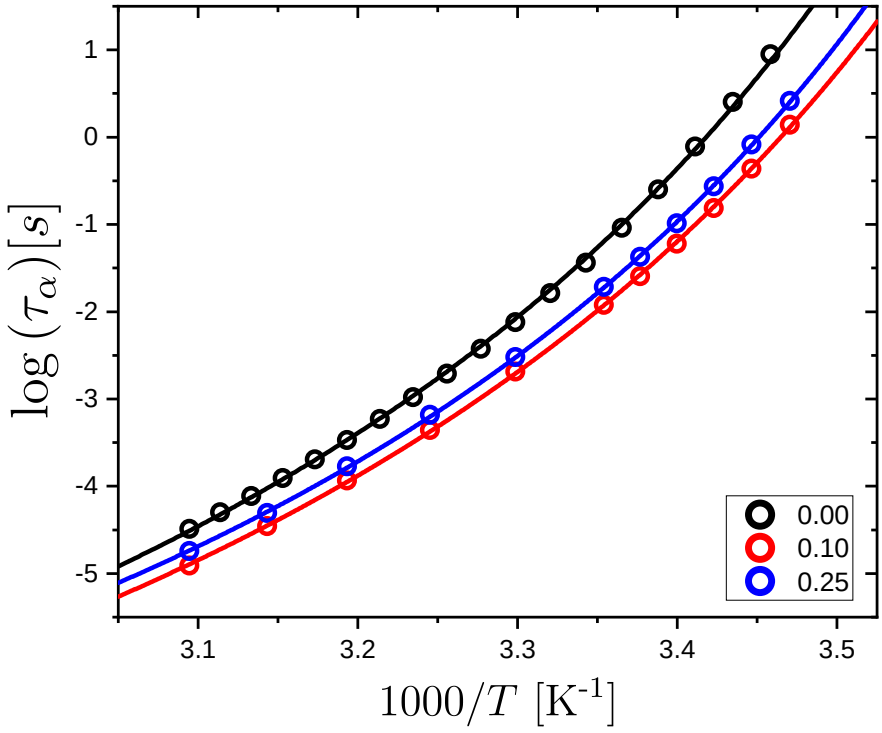

Figure 10.5: $\tau_\alpha(T)$ against $1000/T$ for the nematic LCE under strain. The solid lines are fits to the data with the VFT equation. Errors associated with the fitting tolerances are smaller than the symbol size.

ϵ_t	$\log(\tau_0)$ [s]	D	T_0 [°C]	T_g [°C]
0.00	-11.4±0.1	5.1±0.1	-28±1	12±1
0.10	-11.8±0.2	5.6±0.3	-34±1	9±1
0.25	-11.4±0.2	5.2±0.2	-31±1	9±1

Table 10.1: Results of the VFT fits to the α relaxation as a function of perpendicular strain applied to the nematic LCE. Errors shown are associated with the fitting tolerances of the VFT equation.

It can be seen from the VFT fitting parameters in table 10.1 that applying perpendicular strain to the nematic LCE has little effect on $\tau_\alpha(T)$ reflected in the values of the D strength parameter. Whilst the strains applied in figure 10.5 are relatively small ($\epsilon_t < 0.25$), the effect of strain on $\tau_\alpha(T)$ is in agreement with those observed in figure 10.2(d) where it is shown that the TTS horizontal shifting factors collapse onto a single curve described by $C_1 = 9\pm1$K and $C_2 = 50\pm10$K. Both these results suggest that, over the frequency and temperature range investigated, externally applied strain has little effect on the ***temperature dependence*** of the α relaxation. However, much like the attempt to construct master curves using the TTS principle, BDS measurements over a wide temperature range have a high sample failure rate which means that the auxetic threshold could not be reached. Additionally, because different samples were used the variation in τ_0 and T_0 observed under strain is likely due to the variations within the different samples. Thus, to properly investigate the effect of strain on the α relaxation one needs to perform the measurement on a single sample.

10.4.2 Effect of applied strain on τ_α at a fixed temperature

In section 10.4.1 an attempt is made to determine the affect applied strain on τ_α by performing BDS measurements as a function of strain and temperature. As such, one could probe changes in glass forming behaviour by fitting to $\tau_\alpha(T)$. The main issue is that during these measurements the sample would often break which meant that (a) strains large enough to probe the auxetic response were not reached and (b) for each strain the measurements are performed on different samples and the compositional variation between samples made accurately determining the effect of applied strain on the α relaxation difficult. To overcome these issues, in this section, the BDS measurements are performed at a single temperature on as few samples as possible. A temperature of 23°C was selected for direct comparison to the complex Young's modulus data in section 10.3.2.

Despite efforts to perform the BDS measurements on a single sample this was not experimentally feasible. Instead two nematic LCE samples were used, one taken to 'low' values of elongational strain ($\epsilon_t < 0.44$) and one taken to 'high' values ($\epsilon_t > 0.6$); the latter of which is subjected to strains above the auxetic

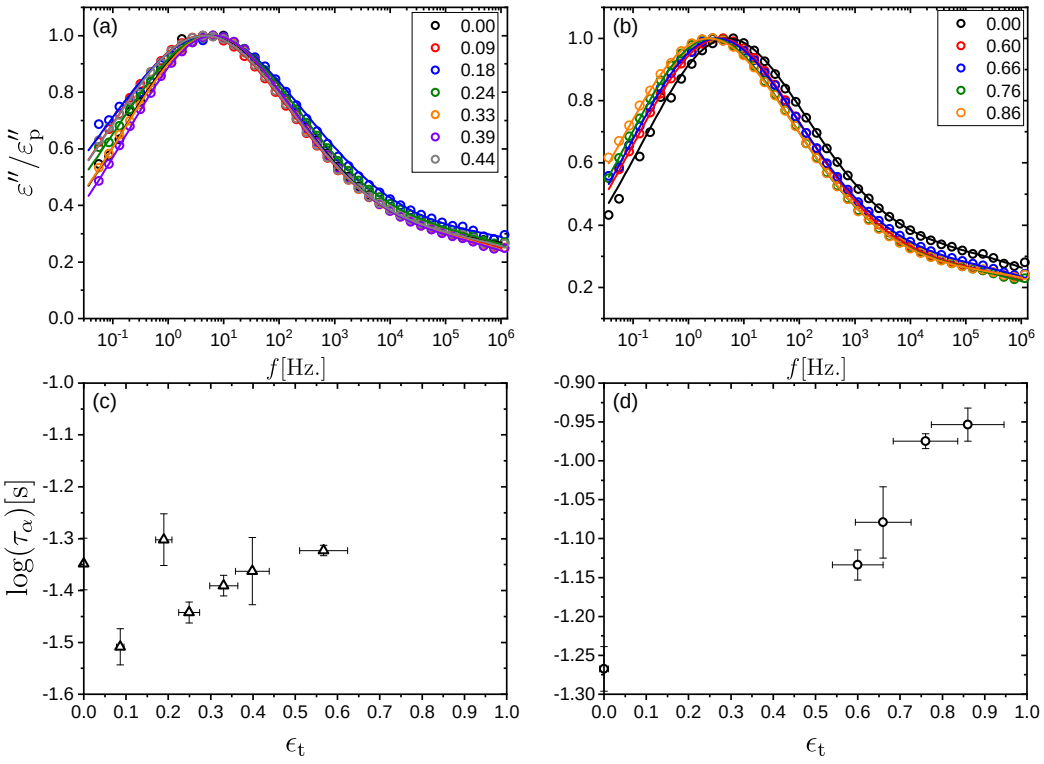

Figure 10.6: Normalised BDS loss data taken at T =23°C as a function of applied true-strain (ϵ_t) ranging from (a) 0.00 to 0.44 and (b) 0.00 to 0.86. (c) and (d) the corresponding α relaxation times from fitting with a HN function; errors in τ_α are fitting tolerances and errors in strain are standards errors from multiple measurements.

threshold. Figure 10.6 shows the frequency-dependent dielectric loss $\varepsilon''(f)$ data for the 'low' strain (figure 10.6(a)) and 'high' strain (figure 10.6(b)) nematic LCE samples. Ensuring the same electrode contact was achieved for a given sample whilst applying strain was not feasible hence the data in 10.6(a) and (b) is normalised by the maximum of the relaxation peak corresponding to the α relaxation, ε''_p. Within the measured dynamic range ($10^{-2} < f < 10^6$ Hz), the α relaxation is observed together with the low-frequency side of the β relaxation. The data are thus fit using a sum of an HN function (α relaxation) and a CC function (β relaxation). Since the β relaxation contribution is only partly covered in the dynamic window only the effect of elongational strain on the α relaxation is considered. It

is clear from figure 10.6(b) that the general shape of the α relaxation remains the same even at large values of applied strain. Figure 10.6(c) and 10.6(d) show the raw α relaxation time-scale for the 'low' and 'high' strain samples, respectively. Due to slight differences in the unstrained α relaxation timescale between the two samples the $\tau_\alpha(\epsilon_t)$ data are normalized by the unstrained timescale ($\tau_\alpha(\epsilon_t = 0)$, the result of which is shown in figure 10.7. For the sample subjected only to lower values of strain (open triangles) there is no obvious trend, within error, in the τ_α timescales. However, in the sample taken to higher true-strains (open circles) there is a clear shift in the α relaxation to slower relaxation times. The results are therefore consistent with findings of a polyurethane elastomer containing rigid units and the polyurea elastomer, which were attributed to increased strain-induced constraints on the polymeric backbone. [225, 226]

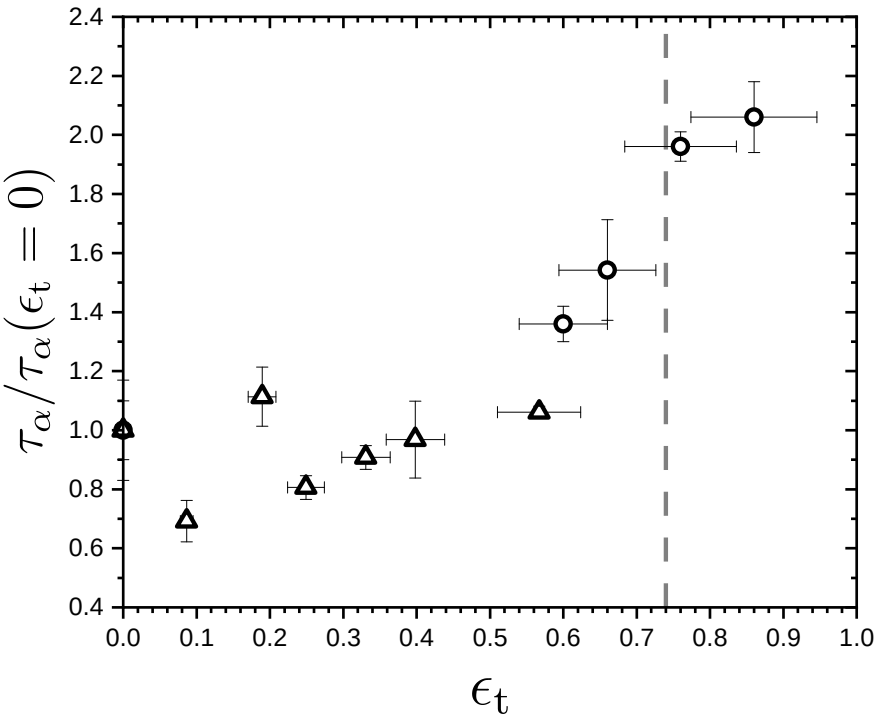

Figure 10.7: Normalised α-relaxation times, τ_α, versus applied true-strain; errors in τ_α are fitting tolerances and errors in strain are standards errors from multiple measurements. The grey dashed line marks the threshold for the onset of the molecular auxetic response.

10.5 Conclusion

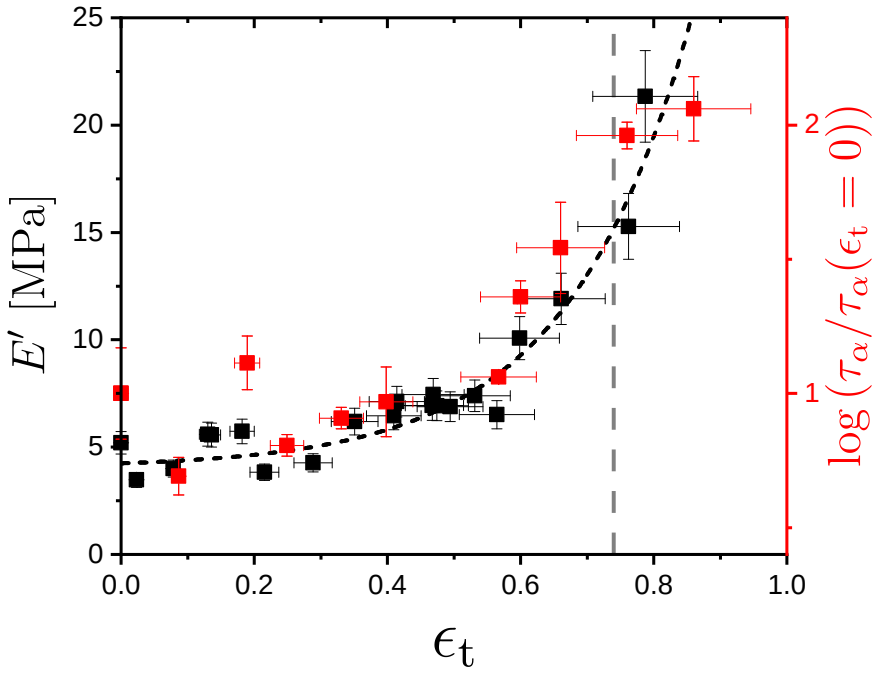

Figure 10.8: Storage modulus, E' and normalised α-relaxation times, τ_α, versus applied true-strain. The grey dashed line marks the threshold for the onset of the molecular auxetic response.

In this chapter the effect of elongational strain on the viscoelastic behaviour and the characteristic time-scale of the α relaxation of a nematic LCE is investigated. The complex Young's modulus of the material is investigated as a function of strain by imposing an additional oscillatory strain onto an elongated, and stress-relaxed, LCE. The characteristic time-scale of the α relaxation is investigated via BDS. It is found that both $E'(f_0)$ and $E''(f_0)$ and the characteristic time-scale of the α relaxation are relatively constant until a large strain ($\epsilon_t \approx 0.55$) is reached, after which an increase in E' and E'' is observed and, correspondingly, the α relaxation begins to slowdown. Both these effects likely can be understood in terms of a strain-induced increase of constraints [225], and the finite extensibility of the network. [219] The increases in E', E'' and τ_α occur near the MFT and the onset of the molecular auxetic response. [2] The increase in the E' and

τ_α as a function of strain is similar as evidenced by figure 10.8. In chapter 8, it is argued that the molecular auxetic response is related to the emergence of biaxial order and out-of-plane rotations of the mesogenic units. Based on the changes in the viscoelastic response and the α relaxation reported in here, it could be argued that the out-out-plane rotations of mesogenic (which likely facilitate the auxetic response in this system) arises due to the strain-imposed configurational restrictions on the polymer backbone.

Chapter 11

Conclusion and outlook

The overall aim of this thesis was to understand the behaviour of a class of LCEs which deform via an MFT and also display a molecular auxetic response. The underlying behaviour of the LCE is probed in two different, and somewhat complementary, ways. In the first approach, the order of the system is probed via Raman spectroscopy to investigate the evolution of order parameters as a function of strain. This approach provides a 'snap-shot' static view of the state of order in the material and, since the phenyl mode is selected, only the mesogenic units of the LCE are probed. In the second approach, the LCE is probed via broadband dielectric spectroscopy (BDS) and rheological techniques. These techniques provide information regarding the dynamics of the LCE. The results of these complimentary approaches are discussed below.

In chapter 8, the order parameters of the LCE are investigated via Raman spectroscopy. Experiments are performed in the 'non-auxetic geometry' and the 'auxetic geometry': in the former, strains are applied parallel to the nematic director; in the latter, strains are applied perpendicular to the nematic director. In the non-auxetic geometry, a uniaxial model is used to derive the relevant order parameters, $\langle P_{200} \rangle$ and $\langle P_{400} \rangle$, from the Raman depolarisation data. It is revealed that both $\langle P_{200} \rangle$ and $\langle P_{400} \rangle$ increase, in agreement with predictions. [40] Additionally, the order parameter data when represented in a $\langle P_{400} \rangle$ vs. $\langle P_{200} \rangle$ plot follow predictions by Maier-Saupe theory, thus, throughout the full deformation the orientational distribution function (ODF) can be described by a Gaussian distribution (which narrows with increasing strain). The 'auxetic geometry' (i.e.

strain applied perpendicular to the nematic director) is investigated in two ways. Initially, the auxetic geometry is investigated with a uniaxial model assumption. In the uniaxial approach $\langle P_{200} \rangle$ and $\langle P_{400} \rangle$ decrease on increasing strain signifying a reduction in the order of the system. At small strains of $\epsilon < 0.3$, relative to the auxetic response and the MFT, $\langle P_{400} \rangle$ vs. $\langle P_{200} \rangle$ begins to deviate from Maier-Saupe predictions. Eventually, $\langle P_{400} \rangle > \langle P_{200} \rangle$ which signifies that there is a large distribution of molecules perpendicular to the initial nematic director. [8] It is interesting to note, that such deviation from Maier-Saupe theory predictions is not observed in the LCE strained parallel to the nematic director (figure 8.4). Based on the difference in the evolution of order parameters observed via Raman spectroscopy in the two geometries and predictions from theory [114, 115] (that deforming the LCE parallel to the nematic director could result in changes in the uniaxial order only, whereas deforming the LCE perpendicular to the nematic director could result in changes in both the uniaxial and biaxial order parameters), the emergence of biaxiality in the nematic LCE is explored. In this approach the uniaxial order parameters ($\langle P_{200} \rangle$ and $\langle P_{400} \rangle$) and biaxial order parameters ($\langle P_{220} \rangle$, $\langle P_{420} \rangle$, $\langle P_{440} \rangle$) are determined. It is found that $\langle P_{220} \rangle$ becomes increasingly negative signifying an increase in the number of molecules aligning with the strain axis. The $\langle P_{420} \rangle$ order parameter is initially relatively constant, however, at strains near to the onset of the molecular auxetic response $\langle P_{420} \rangle$ rapidly becomes positive. When the ODF is reconstructed from the experimentally determined order parameters it is revealed that the mesogenic units rotate out-of-plane and into the thickness direction (i.e. the axis in which the auxetic response is observed) at strains close to the auxetic threshold. Due to the coupling of mesogenic order to the polymer conformation it is suggested that this out-of-plane rotation of mesogenic units is the cause of the molecular auxetic response observed in the LCE.

In chapter 9, the molecular relaxations of the LCE in the isotropic and nematic phase are investigated via BDS and rheology. In both phases the α relaxation, β relaxation and γ relaxation are present in the spectra. The observed β relaxation is assigned to fluctuations of the mesogenic unit around its long axis. The observed γ relaxation is assigned to motions of the alkyl chain connecting A6OCB to the acrylate backbone. Whilst the δ relaxation has been observed in

other LCEs in literature [163, 170, 171] it is not observed in our LCE in either the isotropic or nematic phase. The δ relaxation is associated with the motion of the mesogenic units around the polymer backbone. [27, 172] One of LCEs previously studied is the 'Finkelmann' type known to display an SSE response with applied strain. [51, 163] In chapter 9, it is argued that the lack of the δ relaxation may be related to the MFT response in the auxetic nematic LCEs (i.e. the hindered motion of the mesogenic units around the polymeric backbone means that the 'soft mode' of deformation is not accessible), however, this is speculative and requires more investigation. The temperature dependence of the characteristic time-scale of the α relaxation, $\tau_\alpha(T)$, is investigated using a temperature derivative 'Stickel' analysis to investigate any changes in its dynamic behaviour. [34] It is found that both the isotropic and nematic LCE show a change in the dynamic behaviour of $\tau_\alpha(T)$ at $T^* \approx 1.17 \times T_g$. The isotropic LCE shows a change from a VFT behaviour to a less fragile VFT behaviour on heating. The nematic LCE shows a cross-over of $\tau_\alpha(T)$ from a VFT behaviour to an Arrhenius behaviour. In conventional (non-LC) glass formers a cross-over in $\tau_\alpha(T)$ from a VFT behaviour to a more fragile VFT behaviour, upon heating, is observed at $T_B \approx 1.2 - 1.6 \times T_g$. [27, 37] This temperature typically coincides with the bifurcation temperature of the α relaxation with the Johari-Goldstein β relaxation. Additionally, in SCLCP glass formers that also display liquid crystalline phases a cross-over in $\tau_\alpha(T)$ from VFT behaviour to Arrhenius behaviour is observed at $T^* \approx 1.1 - 1.3 \times T_g$. [173, 177] In SCLCPs the cross-over behaviour is argued to be related to the length-scale of the correlated motions of the α relaxation in relation to the length-scale of the microphase separation of the polymeric backbone and mesogenic units. [27, 173, 177] However, a cross-over in $\tau_\alpha(T)$ is observed in the isotropic LCE, which does show any microphase separation. Therefore, the underlying cause for the cross-over of $\tau_\alpha(T)$ in our LCE needs to be investigated.

The most pertinent length-scale, to compare to the length-scale of the correlated motions of the α relaxation, is the size of the pre-transitional nematic regions in the isotropic phase. Assuming that the pre-transitional nematic regions remain in the isotropic LCE after polymerisation, the nematic domains have a length scale of the order of 1.8 nm at T^*. This is close to the length scale of the correlated motions of the α observed in typical glass formers at T_g. [185–187] The

length-scale of correlated motions in the isotropic LCE is estimated from the BDS measurements and found to be of the order of 1 nm at T^*. Thus, the length-scales of the pre-transitional nematic regions and the correlated motions of the α relaxation are comparable. It is therefore suggested that a matching in length-scale of the pre-transitional nematic regions in the isotropic LCE and the length-scale of the correlated motions of the α relaxation is the driver for the cross-over in behaviour in $\tau_\alpha(T)$ at T^*. Finally, the chain modes present in the isotropic and nematic LCE are investigated via rheology. In both the isotropic and nematic LCE sample a Rouse-like spectrum is present as evidenced by a $G' \approx G'' \propto \omega^{0.5}$ scaling in the spectra. [14] An additional contribution assigned to either the reptation of 'free chains' through the LCE network or the arm retraction of the pendant chains is found in the low frequency domain.

In chapter 10, the effect of strain on the complex Young's modulus and the characteristic time-scale of the α relaxation is investigated via DMA and BDS. For true strains of $\epsilon_t < 0.55$, it was found that E', E'' and τ_α are constant. However, for true strains $\epsilon_t > 0.55$ it is found that E', E'' and τ_α increase. $\epsilon_t = 0.55$ is close to the sharp rotation of the director as determined by cross-polarised microscopy ($\epsilon_t \approx 0.74$, $\epsilon \approx 1.1$) [2] and is close to the onset of the molecular auxetic response. [1] The increase in these values is argued to be related to a strain-induced increase in the constraints of the polymeric backbone and the finite extensibility of the network. [218, 219, 225] Additionally, it is argued that the increase in constraints on the polymeric backbone may be the driver of the auxetic response as follows: from chapter 8 it was found that the auxetic response is related to the out-of-plane rotation of mesogenic units into the thickness direction. Based on the changes in the viscoelastic response and the α relaxation reported it chapter 10, it is argued that the out-out-plane rotations of mesogenic (which likely facilitate the auxetic response in this system) arises due to the strain-imposed configurational restrictions on the polymer backbone.

This thesis provides the first tangible explanation for the molecular auxetic response observed in a class of LCEs that also deform via an MFT. The explanation, as investigated using Raman spectroscopy, rheology and BDS can be summarised as follows: 'the emergence of out-of-plane rotations of mesogenic units due to the increase in constraints on the polymer backbone with imposed strain'. Ideally, to

investigate the validity of this explanation one would perform similar measurements on a range of LCEs which display the auxetic response. Additionally, the absence of the δ relaxation in an LCE that deforms via an MFT as a possible explanation as to why certain LCEs deform via an SSE and others deform via an MFT requires further investigation. Indeed, the absence of the δ relaxation may explain the auxetic response in some part. The δ relaxation is associated with the motion of the mesogenic units around the polymer backbone. [27, 172] The absence of the δ relaxation means that the mesogenic unit cannot freely rotate around the polymeric backbones, instead, it is likely that the mesogenic units are coupled to the α relaxation, which is the relaxation related to the polymeric backbone and the glass transition. When the LCE is deformed in the perpendicular geometry, the polymer chains deform biaxially with the imposed strain and the number of configurational states of the polymeric network are reduced. Due to the lack of the δ relaxation, the mesogenic units must distort with the polymeric backbone and a change in order is observed. The out-of-plane rotations, which in this thesis is argued to be the driver of the auxetic, could be related to the lack of mobility of the mesogenic units around the polymeric backbone as evidenced by the lack of a δ relaxation. A simplified schematic outlining the proposed behaviour is shown in figure 11.1.

Further work could include studying the director fluctuations of an LCE deforming via the MFT through dynamic light scattering measurements. Dynamic light scattering measurements performed on an LCE deforming via an SSE revealed that the characteristic time-scale of the director fluctuation is minimum at the onset of the softening response. [227, 228] It would therefore be interesting to compare how the characteristic time-scale of director fluctuations behave as a function of strain during the MFT and compare these results to the SSE behaviour. The DMA measurements as a function of strain, performed in chapter 10, probe the dynamic behaviour along the same axis for which the strain is applied and therefore only provides insight into one element of the elastic modulus tensor of the LCE. However, since the mechanical properties of the LCE are anisotropic, and the molecular auxetic response results in a negative Poisson's ratio in an axis not investigated by the experimental setup in chapter 10, it would be useful to study the complete elastic modulus tensor of the LCE. A

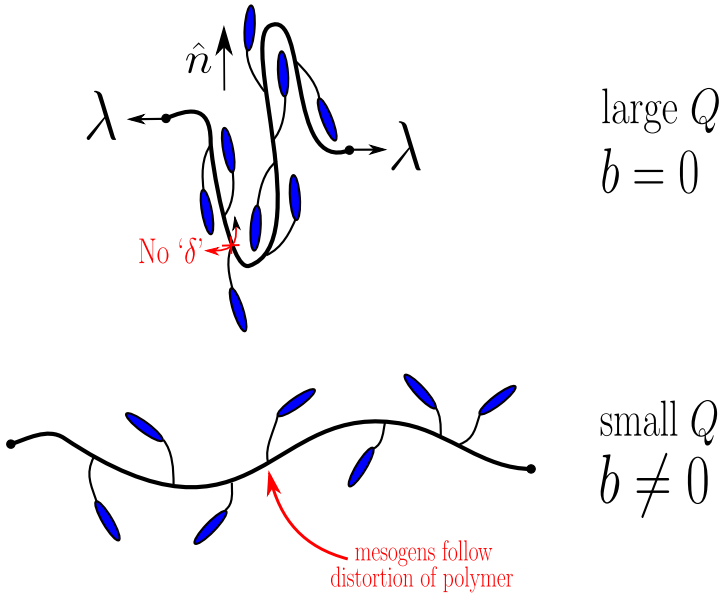

Figure 11.1: Schematic of the proposed auxetic mechanism, due to the lack of a δ relaxation, the mesogenic units are constrained to follow the distortions of the polymer network. The network is deformed perpendicular to the nematic director which results in a biaxial conformation of the polymer. The overall configurational entropy of the polymer is reduced. Configurations in which there are out-of-plane rotations of the mesogenic become increasingly likely due to a reduction in the overall configurational states available. The out-of-plane rotations drive the auxetic behaviour.

useful technique in this regard is Brillouin spectroscopy as the complete elastic modulus tensor can be determined from these measurements. [229]

To summarise, this thesis has investigated the MFT and molecular auxetic response in a nematic LCE. The first tangible explanation for the molecular auxetic response is provided as follows 'the emergence of out-of-plane rotations of mesogenic units due to the increase in constraints on the polymer backbone with imposed strain'. Much further work is required to investigate this behaviour, however, the first important steps have now been taken.

Appendix A

Raman Spectroscopy: Jen *et al.* [104] method

The earliest attempt to determine order parameters from polarised Raman spectroscopy was by Jen and co-workers. In 1977, Jen *et al.* published a paper describing a method to determine the order parameters of uniaxial nematic phases. [104] Using a planar aligned homogenous nematic cell, 2 scattering intensities were taken with the laser polarisation and nematic director parallel to each other. These are with the analyser parallel (I_{zz}) and perpendicular (I_{zx}) to the incident laser polarisation. The notation I_{ij} here means that the laser is polarised at i and the analyser is polarised at j. The sample is then rotated such that the laser polarisation and the nematic director are perpendicular. Scattering intensities are taken with the analyser parallel (I_{xx}) and perpendicular (I_{xz}) to the incident laser polarisation. (Note that for uniaxial phases $I_{zx} = I_{xz}$ so this method can be achieved with 3 measurements). From these scattering intensities depolarisation ratios can be calculated:

$$R_1 = \frac{I_{xz}}{I_{zz}} = \frac{I_{zx}}{I_{zz}}, \tag{A.1}$$

$$R_2 = \frac{I_{zx}}{I_{xx}} = \frac{I_{xz}}{I_{xx}}. \tag{A.2}$$

Equation A.1 and A.2 are equivalent to $R(\theta = 0°)$ and $R(\theta = 90°)$, respectively, as defined in equation 5.21. The differential polarisability ratio in these scattering

geometries are related to the molecular polarisability in the laboratory frame by:

$$p_1 = \frac{\langle (a'_{L_{xz}})^2 \rangle}{\langle (a'_{L_{zz}})^2 \rangle} = \frac{\langle (a'_{L_{zx}})^2 \rangle}{\langle (a'_{L_{zz}})^2 \rangle}, \tag{A.3}$$

$$p_2 = \frac{\langle (a'_{L_{zx}})^2 \rangle}{\langle (a'_{L_{xx}})^2 \rangle} = \frac{\langle (a'_{L_{xz}})^2 \rangle}{\langle (a'_{L_{xx}})^2 \rangle}. \tag{A.4}$$

These are related to the recorded depolarisation measurements via the Lax-Nelson equations:

$$R_1 = C_n p_1, \tag{A.5}$$

$$R_2 = \frac{p_2}{C_n}, \tag{A.6}$$

where C_n is a correction factor given by:

$$C_n = \left(\frac{n_{\text{out}} + n_{zz}}{n_{\text{out}} + n_{xx}} \right)^2, \tag{A.7}$$

where n_{out} is the refractive index of the glass cover slide and n_{zz} and n_{xx} are the refractive indices along the z and x axis.

The Jen *et al.* method requires that one of the fitting parameters ($\langle P_{200} \rangle$, $\langle P_{400} \rangle$ and p) is determined in another manner. Typically, this is done by determining the depolarisation ratio of the sample in the isotropic phase, R_{iso}. Doing this allows one to determine, p_{iso} as $\langle P_{200} \rangle = \langle P_{400} \rangle = 0$. The equation for R_{iso}, assuming uniaxial bond vibration, is given by:

$$R_{\text{iso}} = \frac{(1-p)^2}{3 + 4p + 8p^2}. \tag{A.8}$$

It is then assumed that $p_{\text{iso}} = p_{\text{nem}}$ and that p remains constant within the nematic phase with no temperature dependence. This assumption has been proven to be invalid and, as discussed in section 5.4.2, is one of the causes for the discrepancy in the $\langle P_{400} \rangle$ value determined using this method. [80, 81] The definitions of

molecular polarisabilites in the laboratory frame are given by: [104]

$$A_2^{-2}\langle(a'_{L_{xx}})^2\rangle = \frac{1}{9} + \frac{3}{16}B_2 + \frac{1}{4}C_2 + \frac{1}{18}D_2 + \frac{11}{288}D_2^2 + (\frac{1}{8}B_2 + \frac{1}{2}C_2 - \frac{1}{6}D_2 - \frac{5}{48}D_2^2)\langle\cos^2\beta\rangle + (\frac{3}{16}B_2 - \frac{3}{4}C_2 + \frac{3}{32}D_2^2)\langle\cos^4\beta\rangle, \tag{A.9}$$

$$A_2^{-2}\langle(a'_{L_{zz}})^2\rangle = \frac{1}{9} + \frac{1}{2}B_2 - \frac{1}{9}D_2 + \frac{1}{36}D_2^2 - (B_2 + 2C_2 - \frac{1}{3}D_2 - \frac{1}{6}D_2^2)\langle\cos^2\beta\rangle + (\frac{1}{2}B_2 - 2C_2 + \frac{1}{4}D_2^2)\langle\cos^4\beta\rangle, \tag{A.10}$$

$$A_2^{-2}\langle(a'_{L_{xz}})^2\rangle = \frac{1}{4}B_2 + \frac{1}{4}C_2 - (\frac{3}{4}C_2 - \frac{1}{8}D_2^2)\langle\cos^2\beta\rangle - (\frac{1}{4}B_2 - C_2 + \frac{1}{8}D_2^2)\langle\cos^4\beta\rangle, \tag{A.11}$$

with the constants:

$$A_2 = 1 + 2p, \tag{A.12}$$

$$B_2 = \frac{1}{4(1+2p)^2}[(1-p)^2\sin^4\beta_0], \tag{A.13}$$

$$C_2 = \frac{1}{(1+2p)^2}[(1-p)^2\sin^2\beta_0\cos^2\beta_0], \tag{A.14}$$

$$D_2 = \frac{1}{(1+p)}[(1-p)\sin^2\beta_0 - 1], \tag{A.15}$$

where β_0 is the angle made between the long axis of the molecule and the bond vibration dipole. [104]

To summarise the Jen *et al.* method, p is determined using the isotropic phase depolarisation ratio data; A_2, B_2, C_2 and D_2 are then calculated using β_0 as a fitting parameter. From this $\langle\cos^2\beta\rangle$ and $\langle\cos^4\beta\rangle$ can be determined from equations A.9 - A.11 and equations A.5 - A.6 using the Lax-Nelson correction factor, C_n. C_n is calculated by determining the refractive indices of the sample via other means; for example via Pulfrich refractometry [104] or Abbé refractometry. The calculated values of $\langle\cos^2\beta\rangle$ and $\langle\cos^4\beta\rangle$ are used to calculate $\langle P_{200}\rangle$ and $\langle P_{400}\rangle$ using the definitions in equations 2.29. It should be noted that if p is

determined accurately, fitting with the 'two point' method will produce accurate and reasonable values of $\langle P_{200} \rangle$ and $\langle P_{400\rangle}$ as is discussed in detail in section 5.4.2. In chapter 8, p is determined for an unstrained LCE using the full depolarisation method and then the two point method is used to study the change in order parameters as a function of strain. Doing so reduces the experimental time and therefore reduces the chance of sample breakage.

References

[1] D. Mistry, S. D. Connell, S. L. Mickthwaite, P. B. Morgan, J. H. Clamp, and H. F. Gleeson. Coincident molecular auxeticity and negative order parameter in a liquid crystal elastomer. *Nature communications*, 9(1):1–9, 2018. xiv, xix, xx, 1, 5, 23, 24, 56, 65, 104, 113, 117, 120, 128, 129, 131, 132, 134, 163, 165, 170, 183

[2] D. Mistry, P. B. Morgan, J. H. Clamp, and H. F. Gleeson. New insights into the nature of semi-soft elasticity and "mechanical-fréedericksz transitions" in liquid crystal elastomers. *Soft Matter*, 14(8):1301–1310, 2018. xviii, xix, xx, xxiii, 1, 21, 22, 23, 24, 56, 60, 62, 63, 65, 104, 105, 106, 107, 108, 109, 113, 114, 116, 117, 120, 121, 122, 126, 128, 132, 135, 141, 149, 165, 169, 170, 178, 183

[3] D. Dumnar and T. Kazuhisha. Physical properties. In D. Demus, J. W. Goodby, and G. W. Gray, editors, *Handbook of Liquid Crystals*, volume 1, pages 189–594. John Wiley & Sons, 1999. 2

[4] K. Abe, A. Usami, K. Ishida, Y. Fukushima, and T. Shigenari. Dielectric and fluorescence study on phase transitions in liquid crystal 5CB and 8CB. *J. Korean Phys. Soc*, 46:220–223, 2005. 2

[5] P. J. Wojtowicz, P. Sheng, and E. B. Priestley. *Introduction to liquid crystals*. Springer, 1975. 2, 3

[6] J. W. Goodby and G. W. Gray. Guide to the nomenclature and classification of liquid crystals. In D. Demus, J. W. Goodby, and G. W. Gray, editors,

Handbook of Liquid Crystals, volume 1, pages 17–23. John Wiley & Sons, 1999. 2

[7] P. G. De Gennes and J. Prost. Long and short range order in nematics. In *The physics of liquid crystals*, pages 41 – 92. Oxford University Press, Berlin, 1993. 3, 4

[8] C. Zannoni. Order parameters and orientational distributions in liquid crystals. In *Polarized Spectroscopy of Ordered Systems*, pages 57–83. Springer Netherlands, Dordrecht, 1988. 3, 28, 29, 30, 31, 32, 33, 37, 38, 39, 40, 41, 129, 181

[9] C. Zannoni. Distribution functions and order parameters. In *The Molecular Physics of Liquid Crystals*, pages 51 – 81. Academic Press, London, 1979. 3, 28, 29, 30, 31, 32, 33, 40, 41

[10] W. Tsvetkov. Über die molecülanordnung in der anisotrop-flüssigen phase (on molecular order in the anisotropic liquid phase). *Acta Physicochimica U.R.S.S*, 15:132–147, 1942. (*transl.*) T. J. Sluckin, D. A. Dunmur and H. Stegemeyer. *Crystals That Flow*, pages 368 - 379. CRC Press, 2004. 3, 4

[11] W. Maier and A. Saupe. Eine einfache molekulare theorie des nematischen kristallinflüssigen zustandes. *Zeitschrift für Naturforschung A*, 13(7):564–566, 1958. 4, 37

[12] L. M. Blinov. *Structure and properties of liquid crystals*, volume 123. Springer Science & Business Media, 2010. 4

[13] V. S. R. Jampani, R. H. Volpe, K. R. de Sousa, J. F. Machado, C. M. Yakacki, and J. P. F. Lagerwall. Liquid crystal elastomer shell actuators with negative order parameter. *Science advances*, 5(4):eaaw2476, 2019. 5, 132

[14] M. Rubinstein and R. H. Colby. *Polymer physics*, volume 23. Oxford university press New York, 2003. 5, 6, 7, 8, 9, 10, 11, 12, 47, 95, 156, 183

[15] R. F. Landel and L. E. Nielsen. *Mechanical properties of polymers and composites*. CRC press, 1993. 5

[16] C. M. Roland. *Viscoelastic behavior of rubbery materials*. Oxford University Press, Oxford, 2011. 5, 8, 14, 15, 16, 100, 136, 152

[17] J. E. Mark and B. Erman. Elastomers and rubberlike elasticity. In *The Oxford Handbook of Soft Condensed Matter*, pages 333 – 365. Oxford University Press, Oxford, 2015. 6

[18] P. E. Rouse Jr. A theory of the linear viscoelastic properties of dilute solutions of coiling polymers. *The Journal of Chemical Physics*, 21(7): 1272–1280, 1953. 8, 9, 11

[19] N. G. McCrum, B.E. Read, and G. Williams. *Anelastic and dielectric effects in polymeric solids*. Wiley, 1967. 10, 14, 84, 85, 88, 92, 93, 99, 100, 101

[20] M. T. Shaw and W. J. MacKnight. *Introduction to polymer viscoelasticity*. John Wiley & Sons, 2018. 10, 11, 99

[21] G. R. Strobl. *The physics of polymers*, volume 2. Springer, 1997. 11, 12

[22] M. Doi and S. F. Edwards. Dynamics of concentrated polymer systems. part 1.—brownian motion in the equilibrium state. *Journal of the Chemical Society, Faraday Transactions 2: Molecular and Chemical Physics*, 74: 1789–1801, 1978. 11

[23] S. T. Milner and T. C. B. McLeish. Reptation and contour-length fluctuations in melts of linear polymers. *Physical Review Letters*, 81(3):725, 1998. 11, 12, 13

[24] P. G. De Gennes. Reptation of a polymer chain in the presence of fixed obstacles. *The journal of chemical physics*, 55(2):572–579, 1971. 11

[25] H. Yamazaki, M. Takeda, Y. Kohno, H. Ando, K. Urayama, and T. Takigawa. Dynamic viscoelasticity of poly (butyl acrylate) elastomers containing dangling chains with controlled lengths. *Macromolecules*, 44(22):8829–8834, 2011. 13, 159, 162

[26] E. D. Zanotto and J. C. Mauro. The glassy state of matter: Its definition and ultimate fate. *Journal of Non-Crystalline Solids*, 471:490–495, 2017. 13

[27] F. Kremer and A. Schönhals. *Broadband dielectric spectroscopy*. Springer Science & Business Media, 2002. 14, 15, 16, 82, 86, 87, 88, 89, 90, 91, 92, 93, 94, 136, 137, 140, 144, 147, 148, 162, 173, 182, 184

[28] K. L. Ngai and S. Capaccioli. Relation between the activation energy of the johari-goldstein β relaxation and T_g of glass formers. *Physical Review E*, 69(3):031501, 2004. 14

[29] A. Kudlik, C. Tschirwitz, S. Benkhof, T. Blochowicz, and E. Rössler. Slow secondary relaxation process in supercooled liquids. *Europhysics Letters*, 40(6):649, 1997. 14

[30] F. Kremer and A. Loidl. *The scaling of relaxation processes*. Springer, 2018. 14, 15

[31] G. P. Johari and M. Goldstein. Viscous liquids and the glass transition. ii. secondary relaxations in glasses of rigid molecules. *The Journal of chemical physics*, 53(6):2372–2388, 1970. 15

[32] R. Casalini, C. M. Roland, and S. Capaccioli. Effect of chain length on fragility and thermodynamic scaling of the local segmental dynamics in poly (methylmethacrylate). *The Journal of chemical physics*, 126(18):184903, 2007. 15, 16, 149, 161

[33] L. M. Wang, C. A. Angell, and R. Richert. Fragility and thermodynamics in nonpolymeric glass-forming liquids. *The Journal of chemical physics*, 125 (7):074505, 2006. 15, 161

[34] F. Stickel, E. W. Fischer, and R. Richert. Dynamics of glass-forming liquids. I. temperature-derivative analysis of dielectric relaxation data. *The Journal of chemical physics*, 102(15):6251–6257, 1995. 16, 145, 182

[35] F. Stickel, E. W. Fischer, and R. Richert. Dynamics of glass-forming liquids. II. detailed comparison of dielectric relaxation, dc-conductivity, and viscosity data. *The Journal of chemical physics*, 104(5):2043–2055, 1996. 16, 145, 148, 161

[36] K. L. Ngai, P. Lunkenheimer, C. Leon, U. Schneider, R. Brand, and A. Loidl. Nature and properties of the johari–goldstein β-relaxation in the equilibrium liquid state of a class of glass-formers. *The Journal of Chemical Physics*, 115(3):1405–1413, 2001. 16, 147

[37] A. Schönhals. Evidence for a universal crossover behaviour of the dynamic glass transition. *EPL (Europhysics Letters)*, 56(6):815, 2001. 16, 137, 146, 147, 161, 182

[38] J. Mattsson, R. Bergman, P. Jacobsson, and L. Börjesson. Chain-length-dependent relaxation scenarios in an oligomeric glass-forming system: from merged to well-separated α and β loss peaks. *Physical review letters*, 90(7): 075702, 2003. 16

[39] C. M. Roland. Relaxation phenomena in vitrifying polymers and molecular liquids. *Macromolecules*, 43(19):7875–7890, 2010. 16, 146, 161

[40] M. Warner and E. M. Terentjev. *Liquid crystal elastomers*, volume 120. Oxford University Press, Oxford, 2007. 17, 18, 19, 20, 21, 45, 46, 47, 49, 50, 52, 53, 54, 55, 56, 57, 58, 107, 108, 115, 118, 120, 121, 127, 134, 180

[41] W. H. De Jeu. *Liquid crystal elastomers: materials and applications*, volume 250. Springer, 2012. 17

[42] H. Hirschmann, P.M.S. Roberts, F.J. Davis, W. Guo, C.D. Hasson, and G.R. Mitchell. Liquid crystalline elastomers: the relationship between macroscopic behaviour and the level of backbone anisotropy. *Polymer*, 42 (16):7063–7071, 2001. 18, 20

[43] G. R. Mitchell, F. J. Davis, W. Guo, and R. Cywinski. Coupling between mesogenic units and polymer backbone in side-chain liquid crystal polymers and elastomers. *Polymer*, 32(8):1347–1353, 1991.

[44] W. Guo, F. J. Davis, and G. R. Mitchell. Side-chain liquid-crystal copolymers and elastomers with a null coupling between the polymer backbone and the mesogenic groups. *Polymer*, 35(14):2952–2961, 1994. 19

[45] H. Finkelmann, W. Kaufhold, L. Noirez, A. Ten Bosch, and P. Sixou. Chain conformation in nematic elastomers. *Journal de Physique II*, 4(8):1363–1373, 1994. 18, 19

[46] J. P. Cotton and F. Hardouin. Chain conformation of liquid-crystalline polymers studied by small-angle neutron scattering. *Progress in polymer science*, 22(4):795–828, 1997. 19

[47] K. Urayama, E. Kohmon, M. Kojima, and T. Takigawa. Polydomain- monodomain transition of randomly disordered nematic elastomers with different cross-linking histories. *Macromolecules*, 42(12):4084–4089, 2009. 19

[48] F. Brömmel, D. Kramer, and Finkelmann H. Preparation of liquid crystalline elastomers. In *Liquid Crystal Elastomers: Materials and Applications*, pages 1 – 48. Advances in Polymer Science., Springer, Berlin, 2012. 19

[49] K. Urayama, R. Mashita, Y. O. Arai, and T. Takigawa. Swelling and shrinking dynamics of nematic elastomers having global director orientation. *Macromolecules*, 39(24):8511–8516, 2006. 19

[50] K. Urayama, R. Mashita, I. Kobayashi, and T. Takigawa. Stretching-induced director rotation in thin films of liquid crystal elastomers with homeotropic alignment. *Macromolecules*, 40(21):7665–7670, 2007. 19

[51] J. Küpfer and H. Finkelmann. Nematic liquid single crystal elastomers. *Die Makromolekulare Chemie, Rapid Communications*, 12(12):717–726, 1991. 19, 20, 182

[52] G. Cordoyiannis, A. Lebar, B. Zalar, S. Žumer, H. Finkelmann, and Z. Kutnjak. Criticality controlled by cross-linking density in liquid single-crystal elastomers. *Physical review letters*, 99(19):197801, 2007. 20, 108

[53] G. Cordoyiannis, A. Lebar, B. Rozic, B. Zalar, Z. Kutnjak, S. Žumer, F. Brömmel, S. Krause, and H. Finkelmann. Controlling the critical behavior of paranematic to nematic transition in main-chain liquid single-crystal elastomers. *Macromolecules*, 42(6):2069–2073, 2009. 20, 108

[54] T. Ostapenko, D. B. Wiant, S. N. Sprunt, A. Jákli, and J. T. Gleeson. Magnetic-field induced isotropic to nematic liquid crystal phase transition. *Physical review letters*, 101(24):247801, 2008. 20

[55] W. Helfrich. Effect of electric fields on the temperature of phase transitions of liquid crystals. *Physical Review Letters*, 24(5):201, 1970.

[56] I. Lelidis and G. Durand. Electric-field-induced isotropic-nematic phase transition. *Physical Review E*, 48(5):3822, 1993. 20

[57] A. Lebar, Z. Kutnjak, S. Žumer, H. Finkelmann, A. Sánchez-Ferrer, and B. Zalar. Evidence of supercritical behavior in liquid single crystal elastomers. *Physical review letters*, 94(19):197801, 2005. 20, 108

[58] L. Petridis and E. M. Terentjev. Nematic-isotropic transition with quenched disorder. *Physical Review E*, 74(5):051707, 2006. 20, 149

[59] H. Finkelmann, H. J. Kock, W. Gleim, and G. Rehage. Investigations on liquid crystalline polysiloxanes, 5. orientation of lc-elastomers by mechanical forces. *Die Makromolekulare Chemie, Rapid Communications*, 5(5): 287–293, 1984. 20

[60] K. Hammerschmidt and H. Finkelmann. Stress-optical and thermomechanical measurements on liquid crystalline elastomers. *Die Makromolekulare Chemie: Macromolecular Chemistry and Physics*, 190(5):1089–1101, 1989.

[61] D. Mistry, M. Nikkhou, T. Raistrick, M. Hussain, E. I. L. Jull, D. L. Baker, and H. F. Gleeson. Isotropic liquid crystal elastomers as exceptional photoelastic strain sensors. *Macromolecules*, 2020. 134, 135, 141, 149

[62] B. R. Donovan, H. E. Fowler, V. M. Matavulj, and T. J. White. Mechanotropic elastomers. *Angewandte Chemie*, 131(39):13882–13886, 2019. 20

[63] H. Finkelmann, E. Nishikawa, G. G. Pereira, and M. Warner. A new opto-mechanical effect in solids. *Physical Review Letters*, 87(1):015501, 2001. 20, 107

[64] I. Kundler and H. Finkelmann. Strain-induced director reorientation in nematic liquid single crystal elastomers. *Macromolecular rapid communications*, 16(9):679–686, 1995. 20, 52, 121

[65] G. R. Mitchell, F. J. Davis, and W. Guo. Strain-induced transitions in liquid-crystal elastomers. *Physical review letters*, 71(18):2947, 1993. 21, 22, 105, 121, 131

[66] M. Warner, P. Bladon, and E. M. Terentjev. "soft elasticity"—deformation without resistance in liquid crystal elastomers. *J. Phys. II. France.*, 4(1): 93–102, 1994. 21, 120

[67] G. C. Verwey, M. Warner, and E. M. Terentjev. Elastic instability and stripe domains in liquid crystalline elastomers. *Journal de Physique II*, 6 (9):1273–1290, 1996. 21, 52, 55, 121

[68] J. Küpfer and H. Finkelmann. Liquid crystal elastomers: influence of the orientational distribution of the crosslinks on the phase behaviour and reorientation processes. *Macromolecular chemistry and physics*, 195(4):1353–1367, 1994. 21

[69] I. Kundler and H. Finkelmann. Director reorientation via stripe-domains in nematic elastomers: influence of cross-link density, anisotropy of the network and smectic clusters. *Macromolecular Chemistry and Physics*, 199 (4):677–686, 1998. 21, 52

[70] P. M. S. Roberts, G. R. Mitchell, and F. J. Davis. A single director switching mode for monodomain liquid crystal elastomers. *Journal de Physique II*, 7 (10):1337–1351, 1997. 22, 24, 58, 104, 105, 106, 107, 121, 122, 132

[71] P. M. S. Roberts, G. R. Mitchell, F. J. Davis, and J. A. Pople. Mechanical switching and soft elasticity in liquid crystal elastomers. *Mol. Crys. Liq.*

Crys. Sci. Tech. Mol. Crys. Liq. Crys., 299(1):181–186, 1997. 22, 105, 106, 121, 131

[72] T. C. T. Ting and T. Chen. Poisson's ratio for anisotropic elastic materials can have no bounds. *The quarterly journal of mechanics and applied mathematics*, 58(1):73–82, 2005. 22

[73] K. W. Wojciechowski. Poisson's ratio of anisotropic systems. *Computational methods in science and technology*, 11(1):73–79, 2005. 22

[74] I. M. Ward and J. Sweeney. *An Introduction to the Mechanical Properties of Solid Polymers*. Wiley, West Sussex, 2 edition, 2004. ISBN 0471496251. 22

[75] K. E. Evans and A. Alderson. Auxetic materials: functional materials and structures from lateral thinking! *Adv. Mater.*, 12(9):617–628, 2000. 22, 104

[76] X. Ren, R. Das, P. Tran, T. D. Ngo, and Y. M. Auxetic metamaterials and structures: a review. *Smart Mater. Struct.*, 27(2):023001, 2018. 22

[77] K. K. Saxena, R. Das, and E. P. Calius. Three decades of auxetics research-materials with negative poisson's ratio: a review. *Adv. Eng. Mater.*, 18(11): 1847–1870, 2016. 22, 104

[78] M. Van Gurp. The use of rotation matrices in the mathematical description of molecular orientations in polymers. *Colloid and polymer science*, 273(7): 607–625, 1995. 28, 29, 30, 31, 40, 41

[79] W. J. Jones, D. K. Thomas, D. W. Thomas, and G. Williams. Raman scattering studies of homogeneous and twisted-nematic liquid crystal cells and the determination of $\langle P2 \rangle$ and $\langle P4 \rangle$ order parameters. *Journal of molecular structure*, 614(1-3):75–85, 2002. 28, 31, 66, 70, 76

[80] W. J. Jones, D. K. Thomas, D. W. Thomas, and G. Williams. On the determination of order parameters for homogeneous and twisted nematic liquid crystals from raman spectroscopy. *Journal of molecular structure*, 708(1-3):145–163, 2004. 28, 70, 74, 120, 187

[81] C. D. Southern and H. F. Gleeson. Using the full raman depolarisation in the determination of the order parameters in liquid crystal systems. *The European Physical Journal E*, 24(2):119–127, 2007. 28, 32, 72, 76, 110, 187

[82] C. D. Southern, P. D. Brimicombe, S. D. Siemianowski, S. Jaradat, N. Roberts, V. Görtz, J. W. Goodby, and H. F. Gleeson. Thermotropic biaxial nematic order parameters and phase transitions deduced by raman scattering. *EPL (Europhysics Letters)*, 82(5):56001, 2008. 31, 76, 125

[83] C. D. Southern. *Order Parameter Measurements and Phase Behaviour in Bent Core Liquid Crystal Systems*. Ph.D. thesis, University of Manchester, 2008. 41, 67, 72, 76, 78, 120, 132

[84] H. F. Gleeson, C. D. Southern, P. D. Brimicombe, J. W. Goodby, and V. Görtz. Optical measurements of orientational order in uniaxial and biaxial nematic liquid crystals. *Liquid Crystals*, 37(6-7):949–959, 2010. 28, 108

[85] Z. Zhang. *Research into Order Parameters and Graphene Dispersions in Liquid Crystal Systems using Raman Spectroscopy*. Ph.D. thesis, University of Manchester, 2014. 28, 41, 42, 67, 72, 76, 78, 79, 120, 132

[86] Z. Zhang, V. P. Panov, M. Nagaraj, R. J. Mandle, J. W. Goodby, G. R. Luckhurst, J. C. Jones, and H. F. Gleeson. Raman scattering studies of order parameters in liquid crystalline dimers exhibiting the nematic and twist-bend nematic phases. *Journal of Materials Chemistry C*, 3(38):10007–10016, 2015. 32, 72

[87] Z. Zhang, S. Kaur, B. Kundu, B. K. Sadashiva, and H. F. Gleeson. Observing the emergence of phase biaxiality in a polar smectic a system via polarised raman spectroscopy. *Journal of Materials Chemistry C*, 5(5): 1195–1205, 2017. 66, 76, 77, 125, 126

[88] Z. Zhang and H. F. Gleeson. Understanding liquid crystal order parameters deduced from different vibrations in polarised raman spectroscopy. *Liquid Crystals*, 46(2):219–233, 2019. 28, 32, 42, 43, 71, 78, 79, 81, 112, 116, 119, 125, 126

[89] A. Sanchez-Castillo, M. A. Osipov, and F. Giesselmann. Orientational order parameters in liquid crystals: a comparative study of x-ray diffraction and polarized raman spectroscopy results. *Physical Review E*, 81(2):021707, 2010. 32, 66, 111

[90] F. Lagugné Labarthet, T. Buffeteau, and C. Sourisseau. Orientation distribution functions in uniaxial systems centered perpendicularly to a constraint direction. *Applied Spectroscopy*, 54(5):699–705, 2000. 32

[91] E. T. Jaynes. Information theory and statistical mechanics. *Physical review*, 106(4):620, 1957.

[92] B. J. Berne, P. Pechukas, and G. D. Harp. Molecular reorientation in liquids and gases. *The Journal of Chemical Physics*, 49(7):3125–3129, 1968. 32

[93] C. Zannoni, A. Arcioni, and P. Cavatorta. Fluorescence depolarization in liquid crystals and membrane bilayers. *Chemistry and Physics of Lipids*, 32(3):179 – 250, 1983. ISSN 0009-3084". 33, 39

[94] H. Pottel, W. Herreman, B. W. Van der Meer, and M Ameloot. On the significance of the fourth-rank orientational order parameter of fluorophores in membranes. *Chemical physics*, 102(1-2):37–44, 1986. xx, 34, 35, 122, 123

[95] D. I. Bower. Orientation distribution functions for uniaxially oriented polymers. *Journal of Polymer Science: Polymer Physics Edition*, 19(1):93–107, 1981. 35

[96] F. Jenz, M. A. Osipov, S. Jagiella, and F. Giesselmann. Orientational distribution functions and order parameters in "de vries"-type smectics: A simulation study. *The Journal of Chemical Physics*, 145(13):134901, 2016. 36

[97] G. R. Luckhurst and C. Zannoni. Why is the maier–saupe theory of nematic liquid crystals so successful? *Nature*, 267(5610):412–414, 1977. 37, 38

[98] C. Zannoni. Mean field theory of a model anisotropic potential of rank higher than two. *Molecular Crystals and Liquid Crystals*, 49(8):247–253, 1979. 37

[99] M. A. Cotter. Molecular theories of nematic liquid crystals. *Molecular Crystals and Liquid Crystals*, 97(1):29–47, 1983. 37

[100] R. L. Humphries, P. G. James, and G. R. Luckhurst. Molecular field treatment of nematic liquid crystals. *Journal of the Chemical Society, Faraday Transactions 2: Molecular and Chemical Physics*, 68:1031–1044, 1972. 37

[101] C. Chiccoli, P. Pasini, F. Biscarini, and C. Zannoni. The P4 model and its orientational phase transition. *Molecular Physics*, 65(6):1505–1524, 1988. 39

[102] C. Chiccoli, P. Pasini, and C. Zannoni. Phase diagram and orientational order of a system with second and fourth rank interactions. *International Journal of Modern Physics B*, 11(16):1937–1944, 1997. 39

[103] G. R. Luckhurst and T. J. Sluckin. *Biaxial Nematic Liquid Crystals: Theory, Simulation, and Experiment*. John Wiley & Sons, 2015. 40, 43, 66, 78, 107, 109, 116, 126

[104] S. Jen, N. A. Clark, P. S. Pershan, and E. B. Priestley. Polarized raman scattering studies of orientational order in uniaxial liquid crystalline phases. *The Journal of Chemical Physics*, 66(10):4635–4661, 1977. xii, 40, 66, 70, 75, 76, 111, 186, 188

[105] M. A. Morrison and G. A. Parker. A guide to rotations in quantum mechanics. *Australian journal of physics*, 40(4):465–498, 1987. 41

[106] J.W. Emsley, G.R. Luckhurst, and C.P. Stockley. The deuterium and proton-{deuterium} nmr spectra of the partially deuteriated nematic liquid crystal 4-n-pentyl-4′-cyanobiphenyl. *Molecular Physics*, 44(3):565–580, 1981. 43

[107] J. S. Biggins. *Soft and Hard Elasticity of Liquid Crystal Elastomers*. Ph.D. thesis, University of Cambridge, 2010. 45

[108] D. A. Mistry. *Synthetic lenses for the ageing eye: a motivation for developing the mechanical applications of Liquid Crystal Elastomers*. Ph.D. thesis, University of Leeds, 2018. 46, 53, 60, 62

[109] L. R. G. Treloar. *The physics of rubber elasticity*. Oxford University Press, USA, 1975. 47

[110] P. D. Olmsted. Rotational invariance and goldstone modes in nematic elastomers and gels. *Journal de Physique II*, 4(12):2215–2230, 1994. 52

[111] G. C. Verwey and M. Warner. Compositional fluctuations and semisoftness in nematic elastomers. *Macromolecules*, 30(14):4189–4195, 1997. 54, 58

[112] T. Raistrick, Z. Zhang, D. Mistry, J. Mattsson, and H. F. Gleeson. Understanding the physics of the auxetic response in a liquid crystal elastomer. *Physical Review Research*, 3(2):023191, 2021. 56, 106

[113] P. Bladon, E. M. Terentjev, and M. Warner. Transitions and instabilities in liquid crystal elastomers. *Physical Review E*, 47(6):R3838, 1993. 56, 58, 106, 116, 126, 127

[114] P. Bladon, M. Warner, and E. M. Terentjev. Orientational order in strained nematic networks. *Macromolecules*, 27(24):7067–7075, 1994. 56, 58, 107, 109, 116, 124, 127, 181

[115] H. Finkelmann, A. Greve, and M. Warner. The elastic anisotropy of nematic elastomers. *The European Physical Journal E*, 5(3):281–293, 2001. 58, 107, 108, 109, 113, 115, 116, 121, 124, 125, 126, 127, 129, 132, 181

[116] K. Urayama, Y. O. Arai, and T. Takigawa. Volume phase transition of monodomain nematic polymer networks in isotropic solvents accompanied by anisotropic shape variation. *Macromolecules*, 38(8):3469–3474, 2005. 60

[117] H. F. Gleeson. Raman spectroscopy. In J. P. F. Lagerwall, editor, *Liquid Crystals with Nano and Microparticles*, volume 1 of *6*, chapter 7, pages 255–276. World Scientific, 1 edition, 2016. 66, 67, 68, 70

[118] M. Amer. *Raman spectroscopy for soft matter applications*. John Wiley & Sons, Hoboken, 2009. 66, 67, 68

[119] P. Larkin. *Infrared and Raman spectroscopy: principles and spectral interpretation*. Elsevier, 2017. 66, 67, 68, 69, 70

[120] G. Socrates. *Infrared and Raman characteristic group frequencies: tables and charts*. John Wiley & Sons, 2004. 66, 70

[121] M. Tanaka and R. J. Young. Review polarised raman spectroscopy for the study of molecular orientation distributions in polymers. *Journal of Materials Science*, 41(3):963–991, 2006. 70

[122] K. Miyano. Raman depolarization ratios and order parameters of a nematic liquid crystal. *The Journal of Chemical Physics*, 69(11):4807–4813, 1978. 70

[123] S. Jen, N. A. Clark, P. S. Pershan, and E. B. Priestley. Raman scattering from a nematic liquid crystal: orientational statistics. *Physical review letters*, 31(26):1552, 1973. 75, 76

[124] M. Lax and D. F. Nelson. Light scattering in crystals with surface corrections. In B. Bendow, J. L. Birman, and Vladimir M. Agranovich, editors, *Theory of Light Scattering in Condensed Matter*, pages 371–390, Boston, MA, 1976. Springer US. 76

[125] J. W. Schultz. Dielectric spectroscopy in analysis of polymers. *Encyclopedia of Analytical Chemistry: Applications, Theory and Instrumentation*, 2006. 82, 85, 90

[126] G. G. Raju. *Dielectrics in electric fields: Tables, Atoms, and Molecules*. CRC press, 2017. 82, 84, 85, 87, 88

[127] C. J. F. Böttcher and P. Bordewijk. *Theory of electric polarization*, volume 2. Elsevier Science Limited, 1996. 82, 88

[128] H. Fröhlich. *Theory of dielectrics: dielectric constant and dielectric loss*, volume 190. Clarendon Press, 1958. 84, 86, 87

[129] K. C. Kao. *Dielectric Phenomena in Solids: with emphasis on physical concepts of electronic processes*. Academic Press, San Diego, 2004. 85

[130] J. D. Menczel and R. B. Prime. *Thermal analysis of polymers: fundamentals and applications*. John Wiley & Sons, 2009. 86, 93, 95, 96, 97, 98, 99, 101, 103, 167

[131] D. L. Baker. *Relaxation dynamics in molecular glass-formers with systematic structure modifications*. Ph.D. thesis, University of Leeds, 2014. 86, 88, 92, 93

[132] M. Reynolds. *Chain-length dependent rheology and relaxation dynamics in glass-forming polymers*. Ph.D. thesis, University of Leeds, 2018. 90, 91, 92, 93, 149

[133] C. P. Gainaru. *Dielectric Properties of Molecular Glass Formers; from the Liquid State to the Tunneling Regime*. Ph.D. thesis, Universität Bayreuth, 2008. 88

[134] S. Havriliak Jr and S. J. Havriliak. Results from an unbiased analysis of nearly 1000 sets of relaxation data. *Journal of non-crystalline solids*, 172: 297–310, 1994. 89, 90

[135] S. Havriliak and S. Negami. A complex plane analysis of α-dispersions in some polymer systems. In *Journal of Polymer Science Part C: Polymer Symposia*, volume 14, pages 99–117. Wiley Online Library, 1966. 89

[136] A. L. Agapov and A. P. Sokolov. Decoupling ionic conductivity from structural relaxation: a way to solid polymer electrolytes? *Macromolecules*, 44 (11):4410–4414, 2011. 90, 151, 154

[137] M. Wübbenhorst and J. Van Turnhout. Analysis of complex dielectric spectra. i. one-dimensional derivative techniques and three-dimensional modelling. *Journal of non-crystalline solids*, 305(1-3):40–49, 2002. 90, 91, 140

[138] G. C. Ives, J. A. Mead, and M. M. Riley. *Handbook of plastics test methods*. Iliffe Books, 1971. 93

[139] L. J. Romasanta, P. Leret, L. Casaban, M. Hernández, A. Miguel, J. F. Fernández, J. M. Kenny, M. A. Lopez-Manchado, and R. Verdejo. Towards materials with enhanced electro-mechanical response: CaCu3Ti4O12–polydimethylsiloxane composites. *Journal of Materials Chemistry*, 22(47): 24705–24712, 2012. 93

[140] J. G. Meier, J. W. Mani, and M. Klüppel. Analysis of carbon black networking in elastomers by dielectric spectroscopy. *Physical review B*, 75(5): 054202, 2007. 93

[141] J. D. Ferry. *Viscoelastic properties of polymers*. John Wiley & Sons, 1980. 96, 99

[142] K. P. Menard and N. R. Menard. *Dynamic mechanical analysis*. CRC press, 2020. 96, 97, 98, 99

[143] ISO 6721. Plastics — determination of dynamic mechanical properties. Technical report, ISO, 2019. 99

[144] ASTM D4065. Plastic dynamic mechanical properties. Technical report, ASTM, 2020. 99

[145] F. J. Stadler, S. Chen, and S. Chen. On "modulus shift" and thermorheological complexity in polyolefins. *Rheologica Acta*, 54(8):695–704, 2015. 100

[146] S. Naya, A. Meneses, J. Tarrío-Saavedra, R. Artiaga, J. López-Beceiro, and C. Gracia-Fernández. New method for estimating shift factors in time–temperature superposition models. *Journal of thermal analysis and calorimetry*, 113(2):453–460, 2013. 100

[147] D.J. Plazek. 1995 bingham medal address: Oh, thermorheological simplicity, wherefore art thou? *Journal of rheology*, 40(6):987–1014, 1996. 101

[148] M. Van Gurp and J. Palmen. Time-temperature superposition for polymeric blends. *Rheol. Bull*, 67(1):5–8, 1998. 101, 156

[149] M. L. Williams, R. F. Landel, and J. D. Ferry. The temperature dependence of relaxation mechanisms in amorphous polymers and other glass-forming liquids. *Journal of the American Chemical society*, 77(14):3701–3707, 1955. 101

[150] C. A. Angell. Why C_1= 16–17 in the WLF equation is physical—and the fragility of polymers. *Polymer*, 38(26):6261–6266, 1997. 101

[151] A. W. Brown and J. M. Adams. Negative poisson's ratio and semisoft elasticity of smectic-c liquid-crystal elastomers. *Phys. Rev. E.*, 85(1):011703, 2012. 104

[152] J.V. Selinger, H.G. Jeon, and B.R. Ratna. Isotropic-nematic transition in liquid-crystalline elastomers. *Physical review letters*, 89(22):225701, 2002. 108

[153] E. F. Gramsbergen, L. Longa, and W. H. de Jeu. Landau theory of the nematic-isotropic phase transition. *Physics Reports*, 135(4):195–257, 1986. 109, 149

[154] W. H. De Jeu. *Physical properties of liquid crystalline materials*, volume 1. CRC Press, 1980. 109

[155] C. He, P. Liu, P. J. McMullan, and A. C. Griffin. Toward molecular auxetics: Main chain liquid crystalline polymers consisting of laterally attached para-quaterphenyls. *Phys. Status Solidi B*, 242(3):576–584, 2005. xix, 118, 119, 129

[156] J. N. Grima, A. Alderson, and K. E. Evans. Auxetic behaviour from rotating rigid units. *Phys. Status Solidi B*, 242(3):561–575, 2005. 119, 129

[157] Z. Zeng, L. Jin, and Y. Huo. Strongly anisotropic elastic moduli of nematic elastomers: Analytical expressions and nonlinear temperature dependence. *The European Physical Journal E*, 32(1):71–79, 2010. 121

[158] B. J. Frisken and P. Palffy-Muhoray. Freedericksz transitions in nematic liquid crystals: The effects of an in-plane electric field. *Phy. Rev. A.*, 40 (10):6099, 1989. 121

[159] D. Rogez and P. Martinoty. Mechanical properties of monodomain nematic side-chain liquid-crystalline elastomers with homeotropic and in-plane orientation of the director. *Eur. Phys. J. E*, 34(7):1–13, 2011. 127

[160] M. Warner and S. Kutter. Uniaxial and biaxial soft deformations of nematic elastomers. *Phys. Rev. E*, 65(5):051707, 2002. 127

[161] K. E. Evans and B. D. Caddock. Microporous materials with negative poisson's ratios. ii. mechanisms and interpretation. *J. Phys. D: Appl. Phys.*, 22(12):1883, 1989. 129

[162] D. R. Merkel, N. A. Traugutt, R. Visvanathan, C. M. Yakacki, and C. P. Frick. Thermomechanical properties of monodomain nematic main-chain liquid crystal elastomers. *Soft Matter*, 14(29):6024–6036, 2018. 134

[163] S. Lal, S. K. Tripathi, N. Sood, and S. Khosla. Study of dielectric parameters of liquid crystal elastomer. *Liquid Crystals*, 41(10):1402–1409, 2014. 134, 136, 140, 141, 182

[164] J. J. Zanna, P. Stein, J. D. Marty, M. Mauzac, and P. Martinoty. Influence of molecular parameters on the elastic and viscoelastic properties of side-chain liquid crystalline elastomers. *Macromolecules*, 35(14):5459–5465, 2002. 155, 156, 158

[165] P. Stein, N. Assfalg, H. Finkelmann, and P. Martinoty. Shear modulus of polydomain, mono-domain and non-mesomorphic side-chain elastomers: Influence of the nematic order. *The European Physical Journal E*, 4(3): 255–262, 2001.

[166] D. Rogez, G. Francius, H. Finkelmann, and P. Martinoty. Shear mechanical anisotropy of side chain liquid-crystal elastomers: Influence of sample preparation. *The European Physical Journal E*, 20(4):369–378, 2006. 134, 155, 156

[167] A. Drozd-Rzoska. Glassy dynamics of liquid crystalline 4'-n-pentyl-4-cyanobiphenyl in the isotropic and supercooled nematic phases. *The Journal of chemical physics*, 130(23):234910, 2009. 134

[168] A. Drozd-Rzoska. Heterogeneity-related dynamics in isotropic n-pentylcyanobiphenyl. *Physical Review E*, 73(2):022501, 2006. 134, 154

[169] T. Raistrick, M. Reynolds, H. F. Gleeson, and J. Mattsson. Influence of liquid crystallinity and mechanical deformation on the molecular relaxations of an auxetic liquid crystal elastomer. *Molecules*, 26(23):7313, 2021. xxi, 135, 149, 150, 164

[170] F. Brömmel, W. Stille, H. Finkelmann, and A. Hoffmann. Molecular dynamics and biaxiality of nematic polymers and elastomers. *Soft Matter*, 7 (6):2387–2401, 2011. 136, 140, 141, 182

[171] D. Shenoy, S. Filippov, F. Aliev, P. Keller, D. Thomsen, and B. Ratna. Vogel-Fulcher dependence of relaxation rates in a nematic monomer and elastomer. *Physical Review E*, 62(6):8100, 2000. 136, 140, 141, 182

[172] R. Zentel, G. R. Strobl, and H. Ringsdorf. Dielectric relaxation of liquid crystalline polyacrylates and polymethacrylates. *Macromolecules*, 18(5): 960–965, 1985. 136, 144, 182, 184

[173] A. Schönhals, D. Wolff, and J. Springer. Temperature dependence of the relaxation rates of α and δ relaxation in liquid-crystalline side-group polymethacrylates. *Macromolecules*, 31(25):9019–9025, 1998. 136, 137, 147, 148, 149, 161, 182

[174] K. L. Ngai and A. Schönhals. Interpretation of the observed influence of mesophase structures on the β-relaxation in side chain liquid crystal polymers. *Journal of Polymer Science Part B: Polymer Physics*, 36(11): 1927–1934, 1998. 136

[175] S. U. Vallerien, F. Kremer, and C. Boeffel. Broadband dielectric spectroscopy on side group liquid crystal polymers. *Liquid Crystals*, 4(1):79–86, 1989. 136

[176] A. Schönhals and Hans-Eckart Carius. Dielectric properties of thermotropic polymer liquid crystals. *International Journal of Polymeric Materials*, 45 (3-4):239–276, 2000. 136, 144, 162

[177] G. Turky, D. Wolff, and A. Schönhals. Confinement effects on the molecular dynamics of liquid-crystalline polymethacrylates—a broadband dielectric spectroscopy study. *Macromolecular chemistry and physics*, 213(22):2420–2431, 2012. 136, 147, 148, 161, 182

[178] F. Salehli, S. Yildiz, H. Ozbek, E. Uykur, Y.H. Gursel, and Y. Y. Durmaz. Peculiarities of δ-and α-relaxations in thermotropic side chain liquid crystalline polymers with and without nematic reentrant phase. *Polymer*, 51 (6):1450–1456, 2010. 140

[179] U. W. Gedde, F. Liu, A. Hult, F. Sahlen, and R. H. Boyd. Dielectric relaxation of liquid crystalline side-chain poly (vinyl ether) s. *Polymer*, 35 (10):2056–2062, 1994. 144

[180] A. Martínez-Felipe, L. Santonja-Blasco, J. D. Badia, C. T. Imrie, and A. Ribes-Greus. Characterization of functionalized side-chain liquid crystal methacrylates containing nonmesogenic units by dielectric spectroscopy. *Industrial & Engineering Chemistry Research*, 52(26):8722–8731, 2013. 144

[181] C. Schick, D. Sukhorukov, and A. Schönhals. Comparison of the molecular dynamics of a liquid crystalline side group polymer revealed from temperature modulated dsc and dielectric experiments in the glass transition region. *Macromolecular chemistry and physics*, 202(8):1398–1404, 2001. 147

[182] L. Zhang, W. Yao, Y. Gao, C. Zhang, and H. Yang. Polysiloxane-based side chain liquid crystal polymers: From synthesis to structure–phase transition behavior relationships. *Polymers*, 10(7):794, 2018. 148

[183] J. J. Krich, M. B. Romanowsky, and P. J. Collings. Correlation length and chirality of the fluctuations in the isotropic phase of nematic and cholesteric liquid crystals. *Physical Review E*, 71(5):051712, 2005. 148

[184] H. R. Brand and K. Kawasaki. On the macroscopic consequences of frozen order in liquid single crystal elastomers. *Macromolecular rapid communications*, 15(3):251–257, 1994. 149

[185] C. Dalle-Ferrier, C. Thibierge, C. Alba-Simionesco, L. Berthier, G. Biroli, J. P. Bouchaud, F. Ladieu, D. L'Hôte, and G. Tarjus. Spatial correlations in the dynamics of glassforming liquids: Experimental determination of their temperature dependence. *Physical Review E*, 76(4):041510, 2007. 149, 151, 182

[186] E. Donth. The size of cooperatively rearranging regions at the glass transition. *Journal of Non-Crystalline Solids*, 53(3):325–330, 1982.

[187] E. Hempel, G. Hempel, A. Hensel, C. Schick, and E. Donth. Characteristic length of dynamic glass transition near T_g for a wide assortment of glass-forming substances. *The Journal of Physical Chemistry B*, 104(11):2460–2466, 2000. 149, 182

[188] M. Reinecker, V. Soprunyuk, M. Fally, A. Sánchez-Ferrer, and W. Schranz. Two glass transitions of polyurea networks: Effect of the segmental molecular weight. *Soft Matter*, 10(31):5729–5738, 2014. 150

[189] S. Capaccioli, G. Ruocco, and F. Zamponi. Dynamically correlated regions and configurational entropy in supercooled liquids. *The Journal of Physical Chemistry B*, 112(34):10652–10658, 2008. 151

[190] M. A. Ratner, P. Johansson, and D. F. Shriver. Polymer electrolytes: ionic transport mechanisms and relaxation coupling. *Mrs Bulletin*, 25(3):31–37, 2000. 151

[191] Y. Wang, F. Fan, A. L. Agapov, X. Yu, K. Hong, J. Mays, and A. P. Sokolov. Design of superionic polymers—new insights from walden plot analysis. *Solid State Ionics*, 262:782–784, 2014. 151, 153

[192] V. Bocharova and A. P. Sokolov. Perspectives for polymer electrolytes: a view from fundamentals of ionic conductivity. *Macromolecules*, 53(11): 4141–4157, 2020. 151

[193] M. Funahashi, H. Shimura, M. Yoshio, and T. Kato. Functional liquid-crystalline polymers for ionic and electronic conduction. In *Liquid crystalline functional assemblies and their supramolecular structures*, pages 151–179. Springer, 2007. 151

[194] K. Kishimoto, T. Suzawa, T. Yokota, T. Mukai, H. Ohno, and T. Kato. Nano-segregated polymeric film exhibiting high ionic conductivities. *Journal of the American Chemical Society*, 127(44):15618–15623, 2005. 151

[195] C. Feng, C. P. H. Rajapaksha, J. M. Cedillo, C. Piedrahita, J. Cao, V. Kaphle, B. Lüssem, T. Kyu, and A. Jákli. Electroresponsive ionic liquid crystal elastomers. *Macromolecular rapid communications*, 40(19):1900299, 2019. 151

[196] M. Chambers, B. Zalar, M. Remškar, J. Kovač, H. Finkelmann, and S. Žumer. Investigations on an integrated conducting nanoparticle–liquid crystal elastomer layer. *Nanotechnology*, 18(41):415706, 2007. 151

[197] H. C. Price, J. Mattsson, and B. J. Murray. Sucrose diffusion in aqueous solution. *Physical Chemistry Chemical Physics*, 18(28):19207–19216, 2016. 152

[198] G. L. Pollack. Atomic test of the stokes-einstein law: Diffusion and solubility of xe. *Physical Review A*, 23(5):2660, 1981. 152

[199] Y. H. Bin, W. W. Hua, B. H. Yang, and S. Konrad. The β-relaxation in metallic glasses. *National Science Review*, 1(3):429–461, 2014. 152

[200] M. D. Ediger. Can density or entropy fluctuations explain enhanced translational diffusion in glass-forming liquids? *Journal of non-crystalline solids*, 235:10–18, 1998. 152

[201] M. D. Ediger, P. Harrowell, and L. Yu. Crystal growth kinetics exhibit a fragility-dependent decoupling from viscosity. *The Journal of chemical physics*, 128(3):034709, 2008. 152

[202] H .B. Yu, W. H. Wang, H. Y. Bai, and K. Samwer. The β-relaxation in metallic glasses. *National Science Review*, 1(3):429–461, 2014. 152

[203] A. Drozd-Rzoska, S. J. Rzoska, M. Paluch, S. Pawlus, J. Zioło, P. G. Santangelo, C. M. Roland, K. Czupryński, and R. Dabrowski. Mode coupling behavior in glass-forming liquid crystalline isopentylcyanobiphenyl. *Physical Review E*, 71(1):011508, 2005. 154

[204] A. Drozd-Rzoska, S. Starzonek, S. J. Rzoska, and S. Kralj. Nanoparticle-controlled glassy dynamics in nematogen-based nanocolloids. *Physical Review E*, 99(5):052703, 2019. 154

[205] A. Drozd-Rzoska and S. J. Rzoska. Anomalous decoupling of the dc conductivity and the structural relaxation time in the isotropic phase of a rod-like liquid crystalline compound. In *Metastable Systems under Pressure*, pages 141–149. Springer, 2010. 154

[206] D. Golodnitsky, E. Strauss, E. Peled, and S. Greenbaum. On order and disorder in polymer electrolytes. *Journal of The Electrochemical Society*, 162(14):A2551, 2015. 154, 162

[207] Y. G. Andreev and P. G. Bruce. Polymer electrolyte structure and its implications. *Electrochimica Acta*, 45(8-9):1417–1423, 2000. 154, 162

[208] J. Weilepp, J. J. Zanna, N. Assfalg, P. Stein, L. Hilliou, M. Mauzac, H. Finkelmann, H.R. Brand, and P. Martinoty. Rheology of liquid crystalline elastomers in their isotropic and smectic a state. *Macromolecules*, 32(14):4566–4574, 1999. 155, 156, 158

[209] W. L. Vandoolaeghe and E. M. Terentjev. Constrained rouse model of rubber viscoelasticity. *The Journal of chemical physics*, 123(3):034902, 2005. 156

[210] J. L. Gallani, L. Hilliou, P. Martinoty, F. Doublet, and M. Mauzac. Mechanical behavior of side-chain liquid crystalline networks. *Journal de Physique II*, 6(3):443–452, 1996. 158

[211] K. Urayama, K. Yokoyama, and S. Kohjiya. Viscoelastic relaxation of guest linear poly (dimethylsiloxane) in end-linked poly (dimethylsiloxane) networks. *Macromolecules*, 34(13):4513–4518, 2001. 159, 162

[212] D. C. Agudelo, L. E. Roth, D. A. Vega, E. M. Vallés, and M. A Villar. Dynamic response of transiently trapped entanglements in polymer networks. *Polymer*, 55(4):1061–1069, 2014. 159, 162

[213] R. Xie, M. P. Aplan, N. J. Caggiano, A. R. Weisen, T. Su, C. Müller, M. Segad, R. H. Colby, and E. D. Gomez. Local chain alignment via nematic ordering reduces chain entanglement in conjugated polymers. *Macromolecules*, 51(24):10271–10284, 2018. 159

[214] B. Jakobsen, K. Niss, C. Maggi, N. B. Olsen, T. Christensen, and J. C. Dyre. Beta relaxation in the shear mechanics of viscous liquids: Phenomenology and network modeling of the alpha-beta merging region. *Journal of Non-Crystalline Solids*, 357(2):267–273, 2011. 160

[215] S. Basu, J. L. Hay, J. E. Swindeman, and W. C. Oliver. Continuous dynamic analysis: evolution of elastic properties with strain. *MRS Communications*, 4(1):25–29, 2014. 166, 172

[216] Z. Lv, J. Ren, S. Lin, Y. Pei, Z. Shao, and S. Ling. Understanding the continuous dynamic mechanical behavior of animal silk. *Macromolecules*, 54(1):249–258, 2020. 166, 172

[217] E. A. Meinecke. Dynamisches verhalten von elastomeren bei großen dehnungen überlagerten kleinen schwingungen. *Rheologica Acta*, 10(2):302–309, 1971. 166

[218] N. Suphadon, A. G. Thomas, and J. J. C. Busfield. Viscoelastic behavior of rubber under a complex loading. *Journal of applied polymer science*, 113 (2):693–699, 2009. 166, 172, 183

[219] P. Mason. The viscoelastic behavior of rubber in extension. *Journal of Applied Polymer Science*, 1(1):63–69, 1959. 166, 172, 178, 183

[220] H. Li and R. Xiao. Glass transition behavior of wet polymers. *Materials*, 14(4):730, 2021. 168

[221] M. E. Yildiz and J. L. Kokini. Determination of williams–landel–ferry constants for a food polymer system: Effect of water activity and moisture content. *Journal of Rheology*, 45(4):903–912, 2001. 168

[222] H. Eyring. Viscosity, plasticity, and diffusion as examples of absolute reaction rates. *The Journal of chemical physics*, 4(4):283–291, 1936. 172

[223] B. Bending, K. Christison, J. Ricci, and M.D. Ediger. Measurement of segmental mobility during constant strain rate deformation of a poly (methyl methacrylate) glass. *Macromolecules*, 47(2):800–806, 2014. 172

[224] H. N. Lee, K. Paeng, S. F. Swallen, and M. D. Ediger. Direct measurement of molecular mobility in actively deformed polymer glasses. *Science*, 323 (5911):231–234, 2009. 172

[225] H. Lee, D. Fragiadakis, D. Martin, A. Milne, J. Milne, and J. Runt. Dynamics of uniaxially oriented elastomers using broadband dielectric spectroscopy. *Macromolecules*, 43(7):3125–3127, 2010. 172, 173, 177, 178, 183

[226] T. Choi, D. Fragiadakis, C. M. Roland, and J. Runt. Microstructure and segmental dynamics of polyurea under uniaxial deformation. *Macromolecules*, 45(8):3581–3589, 2012. 173, 177

[227] A. Petelin and M. Čopič. Observation of a soft mode of elastic instability in liquid crystal elastomers. *Physical review letters*, 103(7):077801, 2009. 184

[228] A. Petelin and M. Čopič. Strain dependence of the nematic fluctuation relaxation in liquid-crystal elastomers. *Physical Review E*, 82(1):011703, 2010. 184

[229] M. Philipp, U. Müller, R. Sanctuary, P. Seck, and J.K. Krüger. Scanning brillouin microscopy: acoustic microscopy at gigahertz frequencies. *Archives des Sciences Naturelles, Physiques et Mathématiques*, (Special volume), 2012. 185